



Étude théorique de complexes de Fer par la théorie de la fonctionnelle de la densité: Application au problème de piégeage de spin

Antony Fouqueau

► To cite this version:

Antony Fouqueau. Étude théorique de complexes de Fer par la théorie de la fonctionnelle de la densité: Application au problème de piégeage de spin. Autre. Université Joseph-Fourier - Grenoble I, 2005. Français. NNT: . tel-00256593

HAL Id: tel-00256593

<https://theses.hal.science/tel-00256593>

Submitted on 15 Feb 2008

HAL is a multi-disciplinary open access archive for the deposit and dissemination of scientific research documents, whether they are published or not. The documents may come from teaching and research institutions in France or abroad, or from public or private research centers.

L'archive ouverte pluridisciplinaire **HAL**, est destinée au dépôt et à la diffusion de documents scientifiques de niveau recherche, publiés ou non, émanant des établissements d'enseignement et de recherche français ou étrangers, des laboratoires publics ou privés.

THÈSE

Soutenue le 3 mars 2005 devant

L'UNIVERSITÉ JOSEPH FOURIER

au Laboratoire d'Études Dynamiques et Structurales de la Sélectivité, LEDSS

en vue de l'obtention du titre de

DOCTEUR DE L'UNIVERSITÉ JOSEPH FOURIER

Spécialité : Chimie Physique Moléculaire et Structurale

présentée par

Antony Fouqueau

Étude théorique de complexes de Fer

par la théorie de la fonctionnelle de la densité :

Application au problème de piégeage de spin

Jury

Rapporteurs	Claude DAUL Andreas HAUSER	Professeur à l'Université de Fribourg, Suisse Professeur à l'Université de Genève, Suisse
Examinateurs	Pascale MALDIVI Carlo ADAMO Andréas SAVIN Mark E. CASIDA	Ingénieur CEA de Grenoble Professeur à L'ENSCP Directeur de recherche, Université Pierre-et-Marie-CURIE Professeur à l'Université de Grenoble, directeur de thèse

Remerciements

Je remercie mes proches pour m'avoir encouragé pendant cette thèse. Je remercie Mark Casida pour m'avoir encadré dans mes travaux de recherche. Enfin, je remercie l'ensemble du personnel du LEDSS et plus particulièrement les membres du service informatique.

Résumé

Ce travail a consisté à étudier des complexes de Fer (II) et plus particulièrement à décrire le phénomène de piégeage d'états de spin excités par la lumière. La taille des molécules présentant cette propriété étant d'une centaine d'atomes, la théorie de la fonctionnelle de la densité (DFT) a été la méthode de choix. Au travers de cette étude, les limites d'application de la DFT aux complexes de Fer (II) ont été évaluées en les comparant à des calculs *ab initio* puis à des données expérimentales. Il a été mis en évidence que le terme d'échange des fonctionnelles d'échange-corrélation influence le plus la capacité à décrire ΔE_{HL} et Δr_{HL} . La fonctionnelle OLYP de type GGA a permis d'obtenir la meilleure description de ces complexes. Les énergies à décrire étant de l'ordre de la précision chimique ($\text{kcal} \cdot \text{mol}^{-1}$), les fonctionnelles d'échange doivent être encore améliorées pour obtenir des résultats plus fiables.

Abstract

This work was a study of iron (II) complexes and specially, consist to describe the light induced excited spin state trapping (LIESST) phenomena. The size of the molecules showing this property was around 100 atoms, so the density functional theory (DFT) was the method of choice. In this study, the limit of applications of the DFT to iron(II) complexes was evaluated by comparing this DFT results with ab initio results and then with experimental results. It was shown that the exchange term of the exchange-correlation functionals most influence the capacity to well describe ΔE_{HL} and Δr_{HL} . The OLYP functional (GGA functional) allow the better description of this complexes. The energies to be described being in the order of the chemical precision ($\text{kcal} \cdot \text{mol}^{-1}$), the exchange functional should be improved in order to give more accurate results.

Table des matières

Remerciements	i
Résumé	iii
Abstract	v
Introduction	1
Bibliographie	3
1 Généralités	5
1.1 La chimie des complexes de coordination	5
1.1.1 Qu'est-ce qu'un complexe?	5
1.1.2 Un peu de nomenclature	6
1.1.3 Élément de transition	6
1.1.3.1 Structure électronique à l'état fondamental	7
1.1.3.2 Règle des 18 électrons - Indice de coordination	7
1.2 Structure et propriétés des complexes en théorie du champ des ligands	8
1.2.1 Levée partielle de dégénérescence du niveau <i>d</i> de valence de l'élément central	9
1.2.1.1 Symétrie sphérique	9
1.2.1.2 Symétrie octaédrique	10
1.2.1.3 Autres symétries	11
1.2.2 Facteurs influençant Δ_0 , série spectrochimique	12
1.2.3 Complexes à champ fort et à champ faible	12
1.2.3.1 Cas d'un complexe octaédrique de configuration d^6 .	13
1.2.4 Propriétés magnétiques	14
1.2.5 Effet Jahn-Teller	15
1.2.6 Limites de cette théorie	15
1.2.6.1 Paramètres de Racah et diagramme de Tanabe-Sugano	16
1.2.6.2 Estimations des paramètres principaux	17

1.3	Le phénomène de transition de spin	17
1.3.1	Un brin d'histoire	17
1.3.2	Comment induire une transition de spin ?	18
1.3.2.1	Transition de spin induite par la température	18
1.3.2.2	Transition de spin induite par la pression	21
1.3.2.3	Transition de spin induite par un champ magnétique	21
1.3.2.4	Transition de spin induite par la lumière	21
1.3.3	Rôle des interactions intermoléculaires	22
1.3.3.1	Approche moléculaire	23
1.3.3.2	Approche macroscopique	23
1.4	Le phénomène LIESTT	24
1.4.1	En phase liquide	24
1.4.2	En phase solide	25
1.4.2.1	Le retour à l'état fondamental : la relaxation HS → LS	27
1.4.2.2	Cas des systèmes peu coopératifs	28
1.4.2.3	Cas des systèmes coopératifs	28
1.5	Conclusion	29
	Bibliographie	30
2	Aspects Théoriques	35
2.1	Les méthodes <i>ab initio</i>	35
2.1.1	L'équation de Schrödinger	35
2.1.1.1	Hamiltonien moléculaire	36
2.1.1.2	Unités atomiques	37
2.1.1.3	L'approximation Born-Oppenheimer	38
2.1.1.4	Quelques propriétés de la fonction d'onde	39
2.1.2	L'approximation Hartree-Fock	40
2.1.2.1	Les Orbitales Moléculaires	40
2.1.2.2	Les orbitales	41
2.1.2.3	Les fonctions de bases	42
2.1.2.4	Le principe variationnel	43
2.1.2.5	Les équations de Roothaan-Hall	43
2.1.2.6	La corrélation électronique	46
2.1.3	Les méthodes Post-Hartree-Fock	47
2.1.3.1	La théorie des perturbations à plusieurs corps	47
2.1.3.2	Les méthodes multi-configurationnelles	50
2.1.3.3	Interaction de Configuration	50
2.1.3.4	<i>Complete Active Space Self-Consistent Field</i>	51

2.1.3.5	Calcul perturbationel des effets dynamiques : CASPT2	52
2.2	La théorie de la fonctionnelle de la densité	52
2.2.1	Les théorèmes de Hohenberg-Kohn	52
2.2.1.1	Le premier théorème de Hohenberg-Kohn	53
2.2.1.2	Le deuxième théorème de Hohenberg-Kohn	55
2.2.1.3	La recherche avec contrainte de Levy	56
2.2.1.4	L'approche Kohn-Sham	57
2.2.2	Les différentes classes de fonctionnelles	58
2.2.2.1	Le trou d'échange-corrélation	58
2.2.2.2	La connection adiabatique	60
2.2.2.3	L'approximation locale de la densité	61
2.2.2.4	L'approximation du gradient généralisé	62
2.2.2.5	Les fonctionnelles meta-GGA	64
2.2.2.6	Les fonctionnelles hybrides	65
2.2.2.7	Les fonctionnelles très paramétrées	67
2.2.2.8	Autres fonctionnelles	67
2.3	Conclusion	67
	Bibliographie	67
3	Étude des complexes $[\text{Fe}(\text{H}_2\text{O})_6]^{2+}$ et $[\text{Fe}(\text{NH}_3)_6]^{2+}$	71
	Bibliographie	73
3.1	<i>Comparison of Density Functionals for Energy and Structural Differences Between the High $[^5T_{2g} : (t_{2g})^4(e_g)^2]$ and Low $[^1A_{1g} : (t_{2g})^6(e_g)^0]$ Spin States of the Hexaquoferrrous Cation, $[\text{Fe}(\text{H}_2\text{O})_6]^{2+}$</i>	73
I	Introduction	75
II	Density Functionals	78
III	Computational Details	83
A	<i>Ab Initio</i> Calculations	83
1	Programs and Basis Sets	84
2	CASSCF and CASPT2 Calculations	84
3	SORCI Calculations	85
4	SCF Convergence	86
B	DFT Calculations	86
1	Atomic DFT Calculations	87
IV	Results	88
A	Optimized Geometries	88
1	<i>Ab Initio</i> : HS results	89
2	DFT: HS Results	90

3	LS: <i>Ab Initio</i> and DFT results	91
B	Energetics	92
1	Atomic Limit	92
2	Molecular Energy Differences	94
C	Comparison of STO and GTO-Based DFT Calculations	96
V	Conclusion	97
	Bibliography	99
VI	Appendix : Multiplet Sum Method	105
3-2	<i>Comparison of Density Functionals for Energy and Structural Differences Between the High- [$^5T_{2g} : (t_{2g})^4(e_g)^2$] and Low- [$^1A_{1g} : (t_{2g})^6(e_g)^0$] Spin States of Iron(II) Coordination Compounds : II. More Functionals and the Hexaminoferrous Cation, $[Fe(NH_3)_6]^{2+}$</i>	111
I	Introduction	113
II	Density Functionals and the pairing energy problem	114
III	Ligand Field Theory	118
IV	<i>ab initio</i> reference calculations	121
A	CASSCF and CASPT2 calculations	122
1	Computational details	122
2	Results	122
B	SORCI calculations	123
1	Computational details	123
2	Results	125
V	Validation of Density Functionals	127
A	Computational details	127
B	Optimized Geometries	128
C	Energetics	131
VI	Conclusion	134
	Bibliography	137
4	Étude des complexes $[Fe(bpy)_3]^{2+}$ et $[Fe(L)('NHS4')]$	145
	Bibliographie	147
4-1	Comparison of density functionals for energy and structural differences between the high-[$^5T_{2g}(t_{2g}^4e_g^2)$] and low-[$^1A_{1g}(t_{2g}^6e_g^0)$] spin states of iron(II) coordination compounds : III. The low-spin iron(II) <i>tris</i> (2,2'-bipyridine) complex and assessment of density functionals through the comparison of calculated values and the experimental estimate of the high-spin/low-spin energy difference	147
I	Introduction	149

II	The HS→LS relaxation and the zero-point energy difference	152
III	Theoretical framework	156
	A Outline of the density-functional formalism	157
	B DFT characterisation of LS and HS states of iron(II) complexes	161
IV	Computational details	164
V	Results and Discussion	164
	A LS and HS states	164
	B Optimised geometries	171
	1 Geometries in the LS state	171
	2 Geometries in the HS states	174
	C Structural changes with regard to the analysis of the low- temperature relaxation dynamics	175
	D The HS-LS energy gap	176
VI	Concluding remarks	183
	Bibliography	186
4-7	Comparison of Density Functionals for Energy and Structural Diffe- rences Between the High [$^5T_{2g} : (t_{2g})^4(e_g)^2$] and Low [$^1A_{1g} : (t_{2g})^6(e_g)^0$] Spin States of Iron(II) Coordination Compounds : IV. Comparison of Density-Functional and Experimental Results for the Ferrous Com- plexes [Fe(L)(‘NHS ₄ ’)], where ‘NHS ₄ ’ = 2,2'-Bis(2-mercaptophenylthio)diethylamine Dianion, and L = NH ₃ , N ₂ H ₄ , PMe ₃ , CO, and NO ⁺	198
I	Introduction	202
II	Thermodynamic Calculations	206
III	Density Functionals	209
	A Jacob’s Ladder	210
	B Exchange and the DFT Spin-Pairing Energy Problem	213
IV	Computational Details	216
V	Results	217
	A Thermodynamic Data	218
	B Hartree-Fock and Half-And-Half Functionals	218
	C Hybrid Functionals	218
	D LDA, GGA and meta-GGA Functionals	220
	E Geometry optimization	223
	F Quantitative Assessment of Functionals: Comparison of ΔE_{HL}^{DFT} vs. $\Delta E_{HL}^{ab initio}$ and ΔE_{HL}^{exp}	224
VI	Conclusion	227

Bibliography	228
VII Appendix : Density Functionals	232
Conclusion	235
Annexes	237
1 Processus multiphonon non-adiabatique	237
2 Conversion d'énergies	238
3 <i>Size consistency</i> et <i>size extensivity</i>	239
4 Fonction et fonctionnelle	240

Introduction

Dans l'histoire industrielle, la microélectronique présente une croissance économique et technique sans précédent depuis le premier microprocesseur (Intel 4004) en 1971. Ces dernières années, la célèbre loi de Moore [1] s'est accélérée afin de passer d'une technologie à la suivante tous les deux ans contre trois auparavant. De plus, la forte miniaturisation, possible suivant une règle simple de réduction d'échelle, a assuré la transition d'une génération à la suivante sans réelle rupture technologique, et ce jusqu'à la technologie actuelle basée sur celle du silicium.

Actuellement, la taille des éléments actifs est de 120 nm. La réduction des composants électroniques utilisés dans les technologies courantes CMOS (pour l'anglais *Complementary Metal Oxide Semiconductor*) devrait se poursuivre jusqu'à 22 nm. A l'approche de cette dimension, les difficultés technologiques à résoudre deviennent de plus en plus nombreuses, et les limites physiques du transistor MOS d'architecture conventionnelle (poly-Si/SiO₂/Si) imposent le développement de nouveaux matériaux ou procédés.

La thermodynamique de ces systèmes sub-micronique diffère de celle des systèmes macroscopiques. Dès lors, des problèmes de dissipation de chaleur, d'interfaces, d'interférences,..., limitent cette expansion réductrice. C'est dans ce contexte que l'électronique moléculaire a pris toute son importance.

Elle se définit par "l'utilisation de molécules comme fils et composants dans la construction de circuits électroniques [2]". Ainsi, il est possible de concevoir des édifices moléculaires possédant des fonctions électroniques telles que les diodes, les transistors et les résistances. Cependant, l'électronique moléculaire ne consiste pas seulement à élaborer des "nanocomposants", mais également à stocker des informations.

Dans ce but, les composés à transition de spin présentent des commutateurs modèles possédant des propriétés intéressantes. Ces matériaux ont la caractéristique de pouvoir exister dans deux états différents. La commutation d'un état à l'autre est réalisable à l'aide d'une perturbation extérieure comme la lumière, la température, la pression ou le magnétisme. Parmi l'ensemble des ions métalliques présentant une

transition de spin, les composés à base d'ions Fe(II) sont particulièrement intéressants. La commutation se fait entre un état magnétique (état haut spin, HS, pour l'anglais *High Spin*) et un état non magnétique (état bas spin, LS pour l'anglais *Low Spin*). Le passage d'un état à l'autre s'accompagne d'un changement de couleur et de volume.

Deux voies sont envisageables pour atteindre l'échelle moléculaire. La première consiste à étudier des systèmes macroscopiques puis à réduire leur taille. Cette méthode est celle utilisée actuellement mais à chaque réduction d'échelle, de nouveaux problèmes surviennent. La seconde est l'étude directe des phénomènes mis en jeu au niveau moléculaire.

Cette dernière approche est celle à laquelle nous nous sommes intéressés dans cette thèse. Nous avons décrit les deux états HS et LS impliqués dans le phénomène de transition de spin à l'aide des méthodes de la chimie quantique. L'objectif principal étant la compréhension du phénomène LIEST (pour l'anglais *Light-Induced Excited Spin-State Trapping*) pour lequel la transition de spin est induite par la lumière. Cet intérêt pour les processus photo-induits se justifie par son avantage sur la commutation thermique : plus rapide et plus locale.

La première partie de ce manuscrit sera consacrée à la présentation générale des propriétés des composés du Fe(II) à transition de spin. La présentation des moyens théoriques mis à notre disposition pour comprendre ce phénomène seront alors décrits.

La deuxième partie rapportera l'étude de deux systèmes modèles de Fe(II), le complexe hexaaqua fer (II), $[Fe(H_2O)_6]^{2+}$ et le complexe hexaammine fer (II), $[Fe(NH_3)_6]^{2+}$. Nous comparons les résultats de calculs *ab initio* très poussés avec ceux obtenus par la Théorie de la Fonctionnelle de la Densité (DFT pour l'anglais *Density Functional Theory*) afin de déterminer une méthodologie pour étudier des complexes d'intérêts pratiques.

La troisième partie rapportera l'étude de systèmes d'intérêts expérimentaux, le complexe *tris*(2,2'-bipyridine) fer (II), $[Fe(bpy)_3]^{2+}$ et la famille de complexes 2,2'-*bis*(2-mercaptophenylthio)diethylamine dianion, $[Fe('NHS4')](L)$ avec L = NH₃, N₂H₄, CO, et NO⁺. Nous comparerons les résultats issus de calculs DFT avec l'expérience.

Enfin, nous conclurons puis nous proposerons des perspectives pour continuer ce travail.

Bibliographie

- [1] G.E. Moore, Electronics **38**, 8 (1965).
- [2] traduit de “<http://encyclopedia.thefreedictionary.com/Molecular%20electronics>”

Chapitre 1

Généralités

1.1 La chimie des complexes de coordination

Le but de cette thèse est de modéliser des complexes de métaux de transition. Dans un premier temps, quelques rappels sur la chimie de ces composés vont être effectués [1, 2].

1.1.1 Qu'est-ce qu'un complexe ?

Un **complexe** est un édifice polyatomique constitué d'un atome ou d'un ion central auquel sont liés des molécules (H_2O , CO , NH_3 , ...) ou des ions (Cl^- , Br^- , CN^- , ...) appelés ligands. Il est caractérisé par sa géométrie dépendant de son indice de coordination.

L'**atome** ou l'**ion central** d'un complexe est un acide de Lewis. Selon la définition de Lewis, un acide est une entité dans laquelle un atome est déficitaire d'au moins une paire électronique. Il présente alors une tendance naturelle à pallier cette insuffisance. C'est un accepteur de doublet d'électrons. La plupart des atomes des complexes dits de coordination sont des éléments de transition, comme Cu^{2+} , Fe , Fe^{2+} , Fe^{3+} , Co , Co^{2+} , Ni , Ni^{2+} . Cependant, d'autres ions comme Ca^{2+} , Mg^{2+} peuvent aussi donner des complexes.

Les **ligands** sont des atomes ou groupes d'atomes liés à un atome ou à un ion central, généralement métallique, dans une entité moléculaire polyatomique. Ce sont des bases de Lewis. Selon la définition de Lewis, une base est un donneur de doublet d'électrons. Ils possèdent au moins un doublet d'électrons libres. Un ligand lié à l'atome ou à l'ion central par une seule liaison est un ligand monodentate, c'est le cas de l'eau, de l'ammoniac, de l'ion hydroxyde, de l'ion chlorure. Ceux comportant plusieurs liaisons sont polydentates tel que le ligand 2,2'-bipyridine. Il est bidentate

car il se lie par les deux doublets non liants des 2 atomes d'azote de la molécule. L'ion éthylènediaminetétraacétate (EDTA), souvent noté Y^{4-} , est un ligand hexadentate.

Le nombre de liaisons simples formées par l'atome ou l'ion central avec les ligands est appelé **l'indice de coordination**. Il est égal au nombre de ligands entourant l'atome ou ion central lorsque ceux-ci sont monodentates.

Dans ces travaux, nous nous restreindrons à l'étude de complexes des ions métalliques de transition.

1.1.2 Un peu de nomenclature

Le nom des complexes indique la nature de l'atome ou de l'ion central, son nombre d'oxydation, la nature et le nombre de ligands. Il précise également si le complexe est une molécule neutre, un anion ou un cation. Son nom s'établit en suivant les règles suivantes :

1. Les noms des ligands sont cités en premier ; le nom de l'atome ou de l'ion central est placé en dernier en indiquant le nombre d'oxydation de celui-ci.
2. Les noms des cations complexes et des complexes neutres n'ont pas de terminaison caractéristique, en revanche les anions complexes sont caractérisés par la terminaison *-ate*.
3. Les ligands anioniques sont cités avant les ligands neutres ou cationiques et les ligands minéraux avant les ligands organiques.
4. Les préfixes bi, di, tri, tétra, penta, hexa, etc, sont utilisés pour indiquer le nombre de ligands identiques présents dans le complexe. Cependant, lorsque le nom du ligand contient déjà l'un de ces préfixes (par exemple **bipyridine**) le nombre de ligands est précisé à l'aide des préfixes bis, tris, tétrakis, ...

Quelques exemples : $[\text{Fe}(\text{CN})_6]^{4-}$, ion hexacyanoferrate (II) ; $[\text{Fe}(\text{H}_2\text{O})_6]^{2+}$, ion hexaaqua fer (II) ; $[\text{Fe}(\text{NH}_3)_6]^{2+}$, ion hexaammine fer (II) ; $[\text{Fe}(\text{bpy})_3]^{2+}$, ion trisbipyridine fer (II).

1.1.3 Élément de transition

Le terme générique d'élément de transition désigne théoriquement tous les éléments de la classification périodique caractérisés par une sous-couche *d* ou *f* partiellement remplie, soit à l'état élémentaire, soit dans son état d'oxydation stable. Il est important de rappeler, pour la suite de ces travaux, la structure électronique de tels éléments.

1.1.3.1 Structure électronique à l'état fondamental

Établir la configuration électronique d'un atome ou d'un ion monoatomique dans un état donné consiste à indiquer la répartition, dans cet état, des électrons dans les différentes spin-orbitales monoélectroniques (1s, 2s, 2p ...). Pour déterminer la structure électronique à l'état fondamental, les trois règles et principes suivants sont à appliquer :

- **Règle de Klechkowski**

Dans un atome polyélectronique, l'ordre de remplissage des orbitales caractérisées par les nombres n (nombre quantique principal n , entier strictement positif) et l (nombre quantique secondaire ou azimuthal l , entier positif ou nul tel que $l < n$) est celui où la somme $n + l$ est croissante. Quand deux orbitales différentes ont la même valeur pour la somme $n + l$, l'Orbitale Atomique (OA) occupée en premier est celle dont le nombre quantique principal n est le plus petit.

- **Principe d'exclusion de Pauli**

Deux électrons d'un même atome ne peuvent avoir leurs 4 nombres quantiques n , l , m_l et m_s identiques. m_l est le nombre quantique magnétique, entier relatif compris entre $-l$ et $+l$ et m_s est appelé nombre quantique magnétique de spin et vaut pour un électron $1/2$ ou $-1/2$.

- **Règle de Hund**

Quand un niveau d'énergie est dégénéré et que le nombre d'électrons n'est pas suffisant pour saturer ce niveau, l'état de plus basse énergie est obtenu en utilisant le maximum d'orbitales, les spins des électrons non appariés étant les mêmes.

Dans le cas des éléments de transition, conformément à la règle de Klechkowski, le niveau 4s est occupé avant le niveau 3d. Ainsi l'occupation du niveau 3d ne commence qu'après saturation du niveau 4s. En revanche, la formation des cations correspondants correspond toujours au départ des électrons de l'orbitale atomique ns.

Intéressons-nous maintenant à la détermination de la structure électronique des ions d'éléments de transition dans l'état fondamental.

1.1.3.2 Règle des 18 électrons - Indice de coordination

La règle de l'octet est généralement vérifiée pour les deux premières périodes de la classification périodique mais au delà, elle ne s'applique plus directement. En effet, les électrons d ou les orbitales atomiques d peuvent intervenir dans les liaisons

chimiques et doivent alors être pris en compte au même titre que leurs homologues *s* et *p*.

Comme la réactivité de tout élément repose fondamentalement sur la recherche de la structure électronique du gaz noble le plus proche, structure électronique la plus stable, les éléments de la quatrième ou cinquième période ayant un numéro atomique $Z > 18$ (après l'argon) tendent à acquérir la configuration électronique du type $ns^2(n-1)d^{10}np^6$, soit 18 électrons de valence.

A partir de la quatrième période ($Z>18$), un élément tend à constituer des liaisons en nombre telles qu'elles confèrent dix-huit électrons à sa couche de valence.

Ainsi les cations métalliques, par liaison avec les ligands, reçoivent des électrons et tendent vers la structure électronique du gaz noble qui les suit. Par exemple, le fer au degré d'oxydation +II contient 6 électrons *d*. Pour vérifier la règle des 18 électrons, les complexes seront hexacoordinés. C'est effectivement le cas de $[\text{Fe}(\text{H}_2\text{O})_6]^{2+}$ et $[\text{Fe}(\text{NH}_3)_6]^{2+}$.

Cependant cette règle, du fait de sa simplicité, souffre de nombreuses exceptions. Par exemple, pour l'ion Cu^+ (10 électrons *d*), l'indice de coordination est de 4, alors que les complexes observés renferment seulement deux ligands : $[\text{CuCl}_2]^-$ et $[\text{Cu}(\text{NH}_3)_2]^{2+}$.

1.2 Structure et propriétés des complexes en théorie du champ des ligands

En 1929, Bethe [3] a proposé un modèle électrostatique pour décrire la distribution électronique dans les sous-couches *d* ou *f* de l'atome dans des entourages de diverses symétries. Cette théorie, dite du “champ cristallin”, est fondée sur les hypothèses énoncées suivantes :

- les interactions entre l'atome coordinateur et les ligands sont purement électrostatiques. Elles sont la cause des liaisons de coordination et déterminent la stabilité d'un complexe.
- Les ligands sont considérés comme des charges ponctuelles (ou dans certain cas comme des dipôles) dont la disposition autour de l'atome central conditionne la symétrie du champ électrostatique extérieur agissant sur cet ion.
- La configuration électronique de l'ion central est prise en compte explicitement.

Avant de poursuivre, il est important d'aborder la notion de levée de dégénérescence des niveaux *d* de l'ion central liée à l'interaction électrostatique avec les ligands.

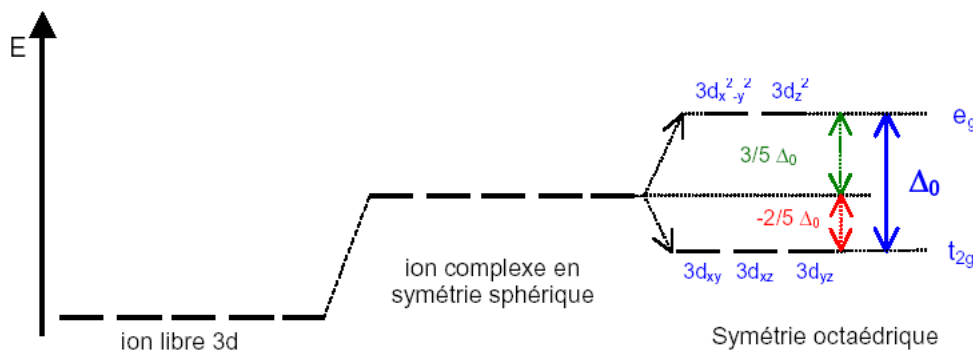


FIG. 1.1: Influence du champ cristallin octaédrique sur les niveaux d'énergies 3d.

1.2.1 Levée partielle de dégénérescence du niveau *d* de valence de l'élément central

A l'état d'ion libre, les cinq orbitales atomiques *d* (fonctions de la forme d_{z^2} , $d_{x^2-y^2}$, d_{xy} , d_{yz} , d_{xz}) des ions des métaux de transition possèdent toutes la même énergie : elles sont dégénérées (cf. figures 1.1).

Mais cette dégénérescence est partiellement levée par interaction avec le champ électrostatique extérieur créé par la disposition spatiale des ligands. L'effet produit sur les énergies de ces orbitales atomiques dépend de la configuration géométrique du complexe.

1.2.1.1 Symétrie sphérique

Si le champ cristallin est à symétrie sphérique, la valeur de l'énergie du niveau *d* s'avère modifiée par rapport à l'ion libre à cause de l'interaction avec le champ des ligands, mais la dégénérescence subsiste. Le niveau d'énergie des orbitales *d* est élevé, mais aucune dégénérescence n'est levée. En effet, l'introduction de l'ion métallique libre dans le composé de coordination, c'est-à-dire dans le champ électrostatique généré par les ligands, provoque une augmentation de l'énergie des orbitales *d* (déstabilisation) en raison de la répulsion entre les charges des électrons *d* et celles des ligands.

Cependant, le champ, lié à la disposition et au nombre de ligands, est de symétrie plus faible. Les complexes sont souvent octaédriques (coordinence 6), tétraédriques (coordinence 4) ou adoptent encore d'autres dispositions.

1.2.1.2 Symétrie octaédrique

Supposons maintenant qu'un ion M^{n+} soit introduit au centre d'un octaèdre régulier dont les sommets sont occupés par des ligands L^{q-} pour former un complexe octaédrique $[ML_6]^{(n-6q)+}$. Un octaèdre régulier est beaucoup moins symétrique qu'une sphère. La dégénérescence des orbitales atomiques d est donc en partie levée. Mais comment ?

Sous l'effet d'interactions électrostatiques, les cinq orbitales d de l'ion central ne sont alors plus équivalentes vis-à-vis des 6 ligands. Les orbitales d_{z^2} et $d_{x^2-y^2}$ possèdent des lobes dirigés le long des axes de coordonnées, alors que les orbitales d_{xy} , d_{yz} et d_{xz} ont des lobes dirigés suivant les bissectrices des axes de coordonnées. Les premières sont donc déstabilisées par la présence des charges négatives des ligands et leur niveau énergétique relevé. Par contre les secondes sont stabilisées et, pour des raisons liées à la conservation de l'énergie du système, leur niveau énergétique est abaissé.

Ainsi dans une symétrie octaédrique, les orbitales atomiques d se séparent en deux niveaux d'énergie : d'une part le niveau d'énergie, triplement dégénéré, noté t_{2g} (d_{xy} , d_{yz} et d_{xz}), stabilisé, d'autre part le niveau d'énergie, doublement dégénéré, noté e_g (d_{z^2} et $d_{x^2-y^2}$), déstabilisé.

L'éclatement du champ cristallin Δ_0 ou $10Dq$ exprime, par définition, la séparation énergétique entre les niveaux e_g et t_{2g} :

$$\Delta_0 = 10Dq = E(e_g) - E(t_{2g}). \quad (1.1)$$

Les termes D et q sont des quantités qui appartiennent à la description mathématique formelle du modèle électronique. Ils dépendent de la charge de l'ion métallique, de la distribution radiale des électrons d et de la distance métal-ligand a . Le facteur 10 de $10Dq$ correspond spécifiquement à un électron isolé dans un potentiel électrostatique de géométrie octaédrique. En effet, le potentiel total électrostatique (extérieur) créé par des ligands de charge Ze en $\pm a$ (origine : centre de l'octaèdre) selon les trois directions x , y et z , moyennant des approximations, peut s'écrire selon cette forme :

$$U_{octa} = \frac{6Ze}{4\pi\epsilon_0 a} + \frac{35}{4} \frac{Ze}{4\pi\epsilon_0 a^5} (x^4 + y^4 + z^4 - \frac{3}{5}r^4) + \dots . \quad (1.2)$$

Le premier terme est de symétrie sphérique et ne fait qu'élever le niveau d'énergie des orbitales de l'ion libre (d'environ 20 à 40 eV) sans lever aucune dégénérescence. Le deuxième terme de U_{octa} est de symétrie octaédrique. On pose $D = \frac{35}{4} \frac{Ze}{4\pi\epsilon_0 a^5}$.

D dépend de la charge des ligands et de la distance a . Le paramètre q n'apparaît qu'après des calculs de perturbation et ne dépend que de l'atome ou de l'ion central.

La conservation de l'énergie, faisant appel à la règle du barycentre, se traduit par la compensation entre l'énergie gagnée par les orbitales du niveau t_{2g} et celle perdue par les orbitales du niveau e_g . Ainsi, si le niveau énergétique des orbitales d dans le champ à symétrie sphérique est pris pour référence, les orbitales t_{2g} ont leur niveau abaissé de $4 Dq$ ou $(2/5) \Delta_0$ et les orbitales e_g ont leur niveau élevé de $6 Dq$ ou $(3/5) \Delta_0$, d'où le diagramme énergétique 1.1.

Prenons le cas le plus simple, c'est-à-dire un ion tel que Ti^{3+} ou V^{4+} ne comportant qu'un seul électron d , soit de configuration d^1 .

Dans un champ de symétrie sphérique, l'électron d occupe indifféremment n'importe laquelle des 5 orbitales d . Dans un champ de symétrie octaédrique, l'électron d ne peut occuper que l'une des trois orbitales correspondant au niveau t_{2g} . Il gagne une énergie appelée *Énergie de Stabilisation du Champ Cristallin* (E^{LFSE} pour l'anglais *Ligand Field Stabilisation Energy*) telle que

$$E^{LFSE} = E_{t_{2g}} - E_{\text{sphérique}} = -(2/5)\Delta_0 = -4Dq . \quad (1.3)$$

L'énergie E^{LFSE} , pour une configuration d^n donnée, se calcule en faisant la somme de toutes les E^{LFSE} individuelles de chacun des n électrons :

$$E^{LFSE} = \sum_{i=1}^n E_i^{LFSE} . \quad (1.4)$$

Le cas des configurations d^n sera explicité plus en détail dans la partie 1.2.3.

1.2.1.3 Autres symétries

Dans le cas d'un ion tétracoordiné dans une symétrie tétraédrique, la levée de dégénérescence est différente. Les orbitales sont réparties en deux niveaux : d_{xy} , d_{yz} et d_{xz} (appelées t_2), et d_{z^2} et $d_{x^2-y^2}$ (appelées e). Par rapport au niveau correspondant à la symétrie sphérique, les orbitales e ont leur niveau abaissé et les orbitales t_2 leur niveau élevé. En comparaison avec la symétrie octaédrique, les deux niveaux sont donc inversés. L'intervalle énergétique entre les deux niveaux est plus réduit : $\Delta_{\text{tétra}} = (4/9)\Delta_0$.

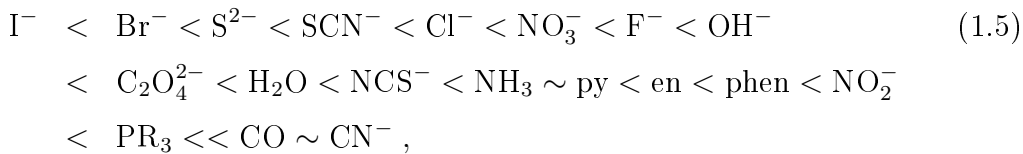
Les levées de dégénérescence varient suivant la symétrie du champ électrostatique des ligands.

Nous allons par la suite nous focaliser essentiellement sur les complexes octaédriques.

1.2.2 Facteurs influençant Δ_0 , série spectrochimique

Les valeurs de Δ_0 dans les complexes octaédriques varient de 1 à 4 eV pour différents ions centraux et ligands, voire plus pour des atomes coordinateurs des cinquième et sixième périodes. Ces énergies peuvent être mesurées par l'observation de bandes d'absorption spectrales de 8000 à 35000 cm⁻¹ pour la transition $t_{2g} \rightarrow e_g$. Ces bandes d'absorption sont peu intenses. En effet, les transitions électroniques $d \rightarrow d$ sont normalement interdites. Mais les vibrations des liaisons de coordination ligands-ion central induisent une modification de la symétrie à chaque instant. Par le biais de ces déformations, de faibles bandes d'absorption sont observées.

L'observation de ces nombreux spectres d'absorption pour des complexes octaédriques a permis de formuler la règle de la série spectrochimique. Quel que soit l'atome ou l'ion central, la valeur de Δ_0 augmente lorsque l'on passe du ligand I⁻ au ligand CN⁻, dans la série spectrochimique suivante :



où py = pyridine (hétérocycle C₅H₅N), en = éthylènediamine (H₂N-CH₂-CH₂-NH₂) et phen=1,10-phénanthroline. Cette séquence n'a pas de valeur absolue et est à employer avec prudence car des inversions plus ou moins importantes peuvent se produire selon le cation métallique.

La nature et la charge de l'ion central influencent aussi la valeur de Δ_0 . Celle-ci est plus forte pour les ions des métaux de transition des périodes élevées. De fait, au sein d'une même colonne, Δ_0 augmente quand Z croît. Par exemple, [Cr(H₂O)₆]²⁺ a un Δ_0 d'environ 14000 cm⁻¹ et [W(H₂O)₆]²⁺ a un Δ_0 d'environ 30000 cm⁻¹.

De même, on constate que dans une ligne donnée, Δ_0 diminue quand Z augmente.

Pour un ligand donné, Δ_0 augmente avec le nombre d'oxydation du métal ou sa charge, car l'interaction électrostatique augmente aussi. Par exemple, Δ_0 est de 9700 cm⁻¹ pour [Co(H₂O)₆]²⁺ et d'environ 18200 cm⁻¹ pour [Co(H₂O)₆]³⁺.

D'une manière générale, nous avons : $\Delta_0 = 7800$ à 11000 cm⁻¹ pour [M(H₂O)₆]²⁺ et $\Delta_0 = 13700$ à 25000 cm⁻¹ pour [M(H₂O)₆]³⁺.

1.2.3 Complexes à champ fort et à champ faible

Considérons à présent des complexes où l'ion central a plusieurs électrons d . Les interactions entre électrons rendent l'étude plus ardue. Qualitativement, comme pour

les atomes à plusieurs électrons, deux effets principaux se produisent :

- les électrons tendent à former une sous-couche complète,
- ils forment préférentiellement une configuration électronique à nombre maximal de spins non appariés (règle de Hund).

La règle de multiplicité maximale de Hund traduit le fait que, dans un atome isolé, le couplage parallèle des spins électroniques apporte un gain d'énergie au système. Inverser le spin d'un électron nécessite donc un apport d'énergie suffisant pour vaincre le terme d'échange.

Par définition, l'énergie d'appariement P ($P > 0$) représente l'énergie minimale à fournir à un atome pour créer un doublet à spins antiparallèles à partir d'une paire d'électrons à spins parallèles. L'énergie totale E_{tot} d'une configuration d^n sera donc la somme de deux termes ; l'un de signe négatif, fonction de l'éclatement Δ_0 du champ cristallin, l'autre, positif ou nul selon les cas, fonction du nombre n de paires de spins formées :

$$E_{tot} = \sum_{i=1}^n E_i^{LFSE} + nP . \quad (1.6)$$

1.2.3.1 Cas d'un complexe octaédrique de configuration d^6

Pour une configuration d^6 , la répartition des électrons dans les orbitales d peut se faire suivant deux manières :

- Soit dans le niveau déstabilisé e_g , en respectant la règle de Hund (cas a). Le moment de spin total correspondant vaut $S = 5(1/2) + 1(-1/2) = 2$ et est identique à celui de l'ion libre.

$$E_{tot}^{(a)} = E^{LFSE} + 1P = 4(-2/5\Delta_0) + 2(3/5\Delta_0) + P = -0.4\Delta_0 + P \quad (1.7)$$

- Soit dans le niveau stabilisé t_{2g} , ce qui oblige à inverser son spin (cas b). Le moment de spin total est réduit à la valeur $S = 3(1/2) + 3(-1/2) = 0$.

$$E_{tot}^{(b)} = E^{LFSE} + 3P = 6(-2/5\Delta_0) + 3P = -2.4\Delta_0 + 3P . \quad (1.8)$$

Selon les valeurs relatives Δ_0 et de P , deux types de représentation sont ainsi envisageables en champ octaédrique :

- Le 1er cas (a) s'observe si $E_{tot}^{(a)} < E_{tot}^{(b)}$, soit $\Delta_0 < P$. La configuration électronique globale, de spin $S=2$, est appelée état à spin fort (ou état *High Spin*) HS ; elle s'écrit $t_{2g}^4 e_g^2$.
- Le 2ème cas (b) s'observe si $E_{tot}^{(a)} > E_{tot}^{(b)}$, soit $\Delta_0 > P$. La configuration électronique globale, de spin $S=0$, est appelée état à spin faible (ou état *Low Spin*) LS.

LS ; elle s'écrit $t_{2g}^6 e_g^0$.

Si seulement un, deux ou trois électrons d sont présents, alors les seules configurations électroniques possibles sont t_{2g}^1 , ou t_{2g}^2 , ou t_{2g}^3 respectivement. De même pour les configurations d^{10} , d^9 et d^8 , une seule configuration électronique est possible. Par exemple, d^8 a pour configuration en champ octaédrique : $t_{2g}^6 e_g^2$.

Mais pour les configurations électroniques d^4 , d^5 , d^6 et d^7 , deux configurations électroniques en champ octaédrique sont possibles. Dans la première, le niveau t_{2g} est peuplé aussi complètement que possible. La deuxième configuration obéit à la règle de Hund. L'état à spin faible ne peut exister que si l'énergie de sa configuration électronique E_{tot}^{LS} est inférieure à l'énergie E_{tot}^{HS} de l'état spin fort imposé par la règle de Hund, soit

$$\begin{aligned}\Delta E &= E_{tot}^{HS} - E_{tot}^{LS} \\ &= -0.4\Delta_0 + P - (-2.4\Delta_0 + 3P) \\ &= 2\Delta_0 - 2P > 0.\end{aligned}\tag{1.9}$$

Ainsi le complexe est dans un état de spin faible (LS) si la valeur de séparation Δ_0 est supérieure à l'énergie d'appariement P des électrons. En revanche, si Δ_0 est inférieure à P , le complexe est dans un état de spin fort. A un champ cristallin faible, correspond un état à spin fort et réciproquement.

Dans le cas des complexes tétraédriques, le champ tétraédrique est nettement plus faible que le champ octaédrique [$\Delta_{\text{tétra}} = (4/9)\Delta_0$]. Les complexes sont donc essentiellement à haut spin.

1.2.4 Propriétés magnétiques

La distinction expérimentale entre les complexes à spin fort et les complexes à spin faible est fondée sur la détermination des propriétés magnétiques. Les complexes possédant un ou plusieurs électrons non appariés sont dits paramagnétiques ; ils sont attirés par un champ magnétique. Les complexes ayant tous leurs électrons appariés sont dits diamagnétique ; ils sont repoussés par un champ magnétique. Pour déterminer si un complexe possède l'une ou l'autre de ces propriétés, une mesure de susceptibilité peut-être effectuée avec la balance de Gouy. Le moment magnétique s'exprime par le nombre effectif n_{eff} de magnétons de Bohr μ_B donné par $n_{eff} = (n(n+2))^{1/2}$. n_{eff} constitue la grandeur physique caractéristique du nombre n d'électrons célibataires d'une sous couche $3d$. Le moment magnétique de

spin seul μ , d'un complexe ayant n électrons célibataires, est donc donné par :

$$\mu = (n(n+2))^{1/2} \mu_B \quad (1.10)$$

avec $\mu_B = eh/(2\pi m_e) = 9,274 \times 10^{-24}$ J.T⁻¹ (T : Tesla)

Par exemple, le moment magnétique du complexe [FeF₆][−], mesuré en solution, vaut $\sim 6\mu_B$. Cette valeur est en accord avec le moment magnétique attendu ($\sqrt{5 \times 7}\mu_B \sim 6\mu_B$) pour un complexe à haut spin à 5 électrons non appariés. De plus, le ligand fluor se situe dans la partie gauche de la série spectrochimique confirmant un complexe HS avec une petite valeur Δ_0 de 13900 cm^{−1}. Un autre complexe de fer, [Fe(CN)₆]^{3−}, est à spin faible. Son moment magnétique vaut 1,8 μ_B et Δ_0 vaut environ 30000 cm^{−1}. Ces valeurs sont également en accord avec la série spectrochimique dans laquelle CN[−] se situe à droite.

1.2.5 Effet Jahn-Teller

Un accroissement de la stabilisation d'énergie lié à une déformation spontanée de la molécule porte le nom d'effet Jahn-Teller. L'hypothèse utilisée jusqu'ici, selon laquelle les atomes et les ions libres présentent une symétrie sphérique, n'est pas conforme à la réalité. En fait, cette hypothèse est valable seulement lorsque tous les électrons du cortège électronique parviennent soit à occuper identiquement un sous-niveau donné, soit à le saturer complètement. En champ octaédrique, ceci implique une occupation de 50% ou 100% des niveaux t_{2g} et e_g. Par contre toute configuration, comme d¹, d², d⁴, d⁸, d⁹ et d¹⁰, se caractérise par une déformation structurale telle qu'un aplatissement ou une élongation de l'octaèdre. Les perturbations les plus importantes apparaissent avec les états d⁴, comme l'ion Cr²⁺ et d⁹, comme l'ion Cu²⁺.

1.2.6 Limites de cette théorie

La théorie du champ cristallin (CFT) est purement électrostatique. Il est donc impossible de l'adapter à des ligands non chargés, comme le monoxyde d'azote ou l'éthylénediamine.

Pour pallier cette lacune, le modèle AOM (dérivé de la théorie des orbitales moléculaires) interprète la levée de dégénérence des orbitales *d* en terme d'interactions de liaisons covalentes faibles σ et π avec les orbitales des ligands. Ceci a l'avantage d'être plus proche du langage et de la conception de l'interaction atomique des chimistes.

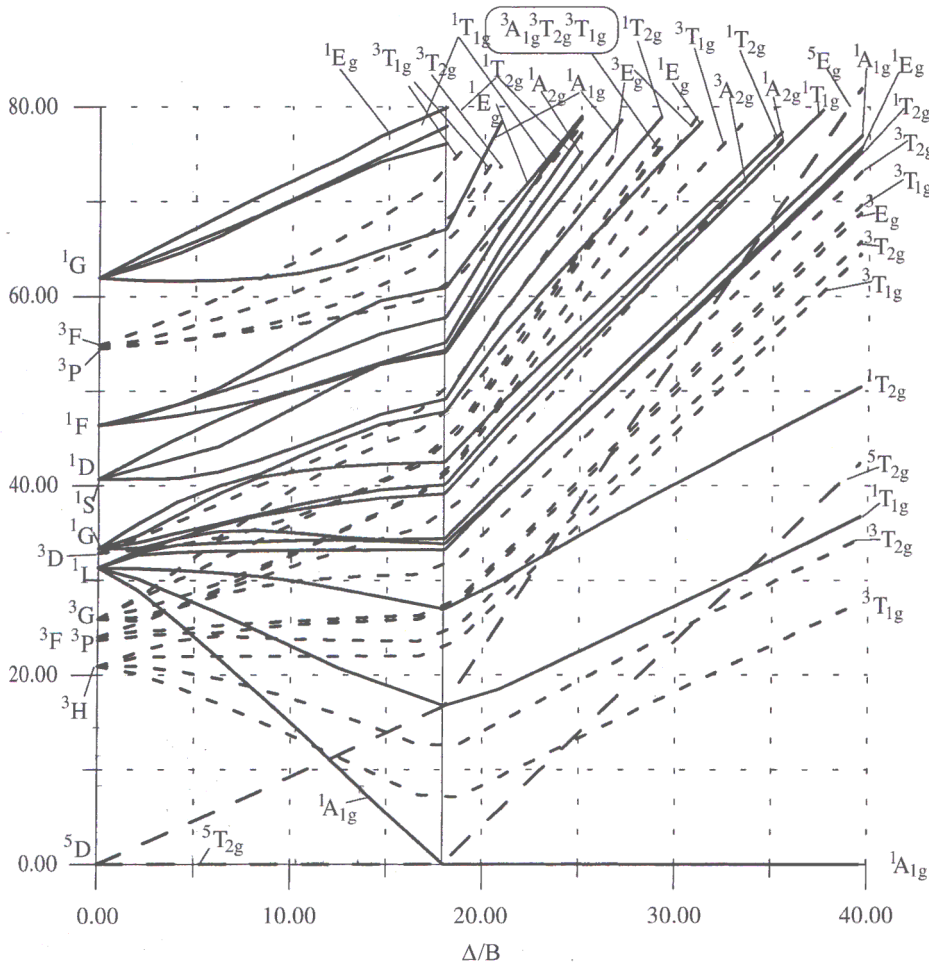


FIG. 1.2: Diagramme de Tanabe-Sugano pour une configuration d^6 avec $B = 1080 \text{ cm}^{-1}$ et $C/B = 4.42$. (Tiré de [4] page 139.)

Cependant, dans ces deux modèles (CFT et AOM), la répulsion interélectronique n'est pas prise en compte.

1.2.6.1 Paramètres de Racah et diagramme de Tanabe-Sugano

Il est possible de développer une théorie de la répulsion électronique dans une configuration d^n donnée afin d'obtenir l'énergie d'un état par rapport à l'état fondamental. Cette énergie est fonction de deux paramètres : les paramètres de Racah B et C . Les résultats sont présentés sous forme de diagramme de Tanabe-Sugano dans lesquels les niveaux d'énergie d'un système d^n sont représentés sur l'axe des ordonnées et la force du champ de ligand Δ_0 sur l'axe des abscisses (cf. figure 1.2). Souvent, les valeurs E et Δ_0 sont ramenées sur le paramètre de Racah permettant une généralisation des diagrammes. Ainsi, un même diagramme peut-être utilisé

indépendamment de la valeur B d'un complexe. Les 2 paramètres B et C sont nécessaires pour décrire la répulsion interélectronique d'un système d^n . Le rapport C/B doit donc être donné pour chaque diagramme.

1.2.6.2 Estimations des paramètres principaux

La différence d'énergie entre les deux états HS et LS, $\Delta E_{HL}^{\text{vert}}$, peut donc être déterminée à l'aide du diagramme de Tanabe-Sugano pour une configuration d^6 . L'estimation de Δ_0 peut se faire à l'aide de valeurs tabulées f et g dépendant respectivement des ligands et de l'atome central ([4] p.218-219). Nous avons

$$\Delta_0 = fg \times 10^3 \text{ cm}^{-1}. \quad (1.11)$$

Dans le cas des complexes $[\text{Fe}(\text{H}_2\text{O})_6]^{2+}$ et $[\text{Fe}(\text{NH}_3)_6]^{2+}$, les valeurs tabulées f et g sont reportées dans le tableau 1.1 et nous obtenons alors les estimations pour Δ_0 et $\Delta E_{HL}^{\text{vert}}$ reportées dans le tableau 1.2.

Métal	g	Ligand	f
Fe^{2+}	10.0 cm^{-1}	$6\text{H}_2\text{O}$	1.00 cm^{-1}
		6NH_3	1.25 cm^{-1}

TAB. 1.1: Paramètres empiriques pour estimer Δ_0 (tiré de [4] p.218-219).

Complexes	Δ_0	$\Delta E_{HL}^{\text{vert}}$
$[\text{Fe}(\text{H}_2\text{O})_6]^{2+}$	$10\ 000 \text{ cm}^{-1}$	$15\ 500 \text{ cm}^{-1}$
$[\text{Fe}(\text{NH}_3)_6]^{2+}$	$12\ 500 \text{ cm}^{-1}$	$9\ 200 \text{ cm}^{-1}$

TAB. 1.2: Estimations de Δ_0 et $\Delta E_{HL}^{\text{vert}}$ pour les complexes $[\text{Fe}(\text{H}_2\text{O})_6]^{2+}$ et $[\text{Fe}(\text{NH}_3)_6]^{2+}$

1.3 Le phénomène de transition de spin

1.3.1 Un brin d'histoire

La notion de transition de spin a été introduite après un certain nombre d'expériences qui sont apparues, dans un premier temps, comme surprenantes. C'est en 1931 que Cambi [5] met en évidence pour la première fois un comportement magnétique "anormal" lors de son étude d'une série de composés du Fe(III) à base de

ligand dithiocarbamate. Par la suite, en 1956, la notion d'équilibre de spin est évoquée dans un composé de ferrihémoglobine hydroxyde [6]. Mais ce n'est qu'en 1959 que l'équilibre de spin de certains complexes tétracoordinés du Ni(II) est justifié par la faiblesse de l'écart énergétique entre les niveaux singulet et triplet [7]. Balhausen et Liehr prédisent même que cette conversion de spin est susceptible d'être induite thermiquement par peuplement de Boltzmann de l'état triplet. Cette conversion thermique est vérifiée en 1961 sur un composé à base de cobalt, le $[\text{Co}(\text{PdAdH})_2]\text{I}_2$, par un suivi du moment magnétique en fonction de la température [8]. En 1964, Baker et Bobonich mettent en évidence la première transition de spin de l'ion Fe(II) à l'état solide sur le composé $[\text{Fe}(\text{phen})_2(\text{NCS})_2]$ [9]. Cette même année, la notion de transition de spin (spin-crossover) est introduite par Ewald *et al.* [10]. Les auteurs proposent un changement d'état de spin lorsque l'énergie du champ de ligand est de grandeur comparable à l'énergie moyenne d'appariement des électrons dans les orbitales *d*. Depuis, cette vision n'a pratiquement pas évolué. De nombreux articles et revues ont été consacrés au phénomène de transition de spin. Celui-ci est connu pour les ions Fe(III) [11], Cr(II) [12], Mn(II) [13], Co(II) [14], Mn(III) [15] et Co(III) [16], sans oublier l'ion Fe(II), le plus largement étudié, et sur lequel nous allons focaliser notre étude.

L'observation d'une transition de spin n'est possible que si le champ de ligand est intermédiaire entre un champ fort et un champ faible. Une telle zone intermédiaire est, en réalité, très étroite [17]. Ceci explique le petit nombre de composés à transition de spin en comparaison avec l'ensemble des complexes de coordination existants. Par ailleurs, ce domaine énergétique étroit permet de comprendre qu'une faible modification de la nature du composé peut entraîner une modification importante du comportement magnétique.

1.3.2 Comment induire une transition de spin ?

Différentes perturbations extérieures sont connues pour influencer l'état de spin d'un ion métallique, telles qu'une modification de la température (T), de la pression (P), du champ magnétique (H) ou de la lumière ($h\nu$).

1.3.2.1 Transition de spin induite par la température

La température est historiquement le premier et le plus utilisé des moyens d'induction d'une transition de spin. Elle sert le plus souvent de référence pour les autres moyens d'induction de la transition de spin. A l'échelle moléculaire, ce sont Ewald *et al.* [10] qui ont introduit la notion de population thermique de type Boltzmann

des états de spin. Ces auteurs ont calculé les courbes d'évolution énergétique des différents niveaux électroniques en fonction de la distance métal-ligand. A l'échelle macroscopique, la transition de spin est décrite selon les lois de la thermodynamique. Le changement d'état de spin correspond à un équilibre physique entre deux espèces LS et HS régi par la variation d'enthalpie libre

$$\Delta G = G_{HS} - G_{LS} = \Delta H - T\Delta S \quad (1.12)$$

où ΔH et ΔS sont respectivement les variations d'enthalpie et d'entropie.

La variation d'enthalpie, ΔH , est décomposée en plusieurs contributions électroniques

$$\Delta H = H_{HS} - H_{LS} = \Delta H_{el} + \Delta H_{vib(intra)} + \Delta H_{vib(inter)}. \quad (1.13)$$

La contribution électronique ΔH_{el} a été estimée à $\sim 1000 \text{ cm}^{-1}$, la contribution vibrationnelle intramoléculaire $\Delta H_{vib(intra)}$ à $\sim 100 \text{ cm}^{-1}$ et la contribution vibrationnelle intermoléculaire $\Delta H_{vib(inter)}$ à $\sim 10 \text{ cm}^{-1}$ [18]. Ainsi en première approximation, la variation d'enthalpie peut être directement reliée à la contribution électronique ΔH_{el} . Elle est positive lors du passage LS \rightarrow HS.

La variation d'entropie est décomposée en deux contributions, d'une part électronique ΔS_{el} et d'autre part vibrationnelle ΔS_{vib} .

La variation d'entropie d'origine électronique est la somme des contributions tenant compte, respectivement, des changements de spin ΔS_{el}^{spin} et de moment orbital ΔS_{el}^{orb} . Ces deux contributions s'expriment simplement par le rapport des dégénérescences des états respectifs :

$$\Delta S_{el}^{spin} = R \left[\ln \left(\frac{(2S+1)_{HS}}{(2S+1)_{LS}} \right) \right] \quad (1.14)$$

$$\Delta S_{el}^{orb} = R \left[\ln \left(\frac{(2L+1)_{HS}}{(2L+1)_{LS}} \right) \right] \quad (1.15)$$

où $2L+1$ peut prendre les valeurs 1, 2, 3 respectivement pour les termes A et B , E ou T . La transition LS \rightarrow HS (état singulet ${}^1A_{1g}$ \rightarrow état quintuplet ${}^5T_{2g}$) implique donc :

$$\Delta S_{el}^{spin} = R \ln 5 = 13.38 \text{ J.K}^{-1}.\text{mol}^{-1} \quad \text{et} \quad \Delta S_{el}^{orb} = R \ln 3 = 9.13 \text{ J.K}^{-1}.\text{mol}^{-1} \quad (1.16)$$

En symétrie octaédrique parfaite, les deux contributions doivent être prises en compte. En revanche, dans la plupart des cas, la symétrie autour du Fe(II) est beaucoup plus basse, la dégénérescence orbitalaire est alors levée et ΔS_{el}^{orb} est négligée.

La variation d'entropie d'origine vibrationnelle est la somme de deux contribu-

tions tenant compte respectivement des changements de vibrations intramoléculaires et intermoléculaires. De nombreuses études calorimétriques ont été réalisées sur des complexes du Fe(II) et ont révélé des variations d'entropie variant de 48 à 86 J.mol⁻¹.K⁻¹ [19]. Ces valeurs sont nettement supérieures à celles attendues pour un changement d'état de spin seul ($\Delta S_{el} = 13,38 \text{ J.mol}^{-1}.\text{K}^{-1}$). En 1974, Sorai et Seki ont montré le rôle prépondérant de l'entropie de vibration par des études calorimétriques et de spectroscopie infrarouge des composés [Fe(phen)₂(NCX)₂] (avec X = S, Se) [20]. Environ 50 % de l'entropie vibrationnelle a été attribuée aux vibrations d'elongation Fe-ligand et aux vibrations de déformation N-Fe-N. En revanche, la contribution des vibrations intermoléculaires a été considérée comme négligeable [20].

Comme ΔH et ΔS sont du même signe, il existe une température d'équilibre $T_{1/2}$ où les enthalpies libres des phases LS et HS sont égales, c'est-à-dire $\Delta G = 0$, définissant $T_{1/2} = \Delta H / \Delta S$. A cette température $T_{1/2}$, autant de molécules se trouvent dans l'état LS et dans l'état HS. En-dessous de $T_{1/2}$, ΔH est supérieure à $T\Delta S$ ($\Delta G > 0$), le facteur enthalpique domine et l'état LS est le plus stable. Au contraire, au-dessus de $T_{1/2}$, ΔH est inférieure à $T\Delta S$ ($\Delta G < 0$), le facteur entropique domine et l'état HS est le plus stable. L'accroissement de la température favorise l'état HS en raison d'un gain d'entropie lors du passage de l'état LS à l'état HS. La transition de spin thermo-induite est donc un processus moléculaire gouverné par l'entropie [20, 21].

Jusqu'en 1964, les transitions de spin de l'ion Fe(II) observées en phases liquide et solide étaient graduelles. On parlait alors de conversion de spin. Dans certains cas, la conversion était incomplète : il restait un résidu HS à basse température ou LS à haute température. Ceci était bien compris par la théorie d'Ewald tenant compte d'une population thermique des états de spin [10]. C'est en 1964 que la première transition de spin abrupte est décrite en phase solide. Les auteurs observent pour le composé [Fe(phen)₂(NCS)₂] une variation extrêmement rapide et abrupte du moment magnétique en fonction de la température [9]. En 1967, König et Madajka [17] confirme la présence d'une transition de spin thermique dans ce composé. À cette époque, cette transition de spin était problématique car non-modélisable par un peuplement de type Boltzmann. Au fil des années, divers modèles ont été développés afin de rendre compte d'un tel comportement. En 1976, König et Ritter rapportent le premier effet d'hystéresis pour un composé à transition de spin, [Fe(4,7-(CH₃)₂-phen)₂(NCS)₂] [22]. Aujourd'hui, de nombreux composés sont connus pour présenter des hystéresis allant de 2-3 K à 90 K de largeur [23]. La première transition de spin en deux étapes a été observée en 1982 [24].

1.3.2.2 Transition de spin induite par la pression

Si une transition de spin est induite par la pression alors l'état de moindre volume est favorisé. Le volume de l'état HS étant plus grand que celui de l'état LS, l'application d'une pression permet au moins de stabiliser l'état LS et peut induire la transition HS → LS. Les premiers travaux rapportés sur ce sujet sont ceux de Drickamer en 1971 [25, 26]. D'autres articles font état de recherches sur la transition de spin induite par la pression [25, 26, 27, 28, 29, 30, 31, 32]. Les études sont généralement réalisées sur des composés présentant une transition de spin thermique. Suivant le pression appliquée, l'évolution de la transition de spin thermique varie ; plus la pression est importante, plus l'état LS est favorisé et la transition de spin thermique déplacée vers les hautes températures.

1.3.2.3 Transition de spin induite par un champ magnétique

Si une transition de spin est induite par un champ magnétique alors l'état le plus magnétique est favorisé. Dans le cas du Fer(II), l'état HS est paramagnétique et l'état LS est diamagnétique. L'application d'un champ magnétique va donc favoriser l'état HS et donc la transition LS → HS. En 1982, Sasaki et Kambara [33] ont réalisé une étude théorique sur la perturbation engendrée par un champ magnétique statique fort (100 Tesla). Cette théorie, basée sur un effet Jahn-Teller coopératif, n'a pas été confirmée par des expériences, mais reste la première à faire référence à l'action d'un champ magnétique. En 1983, Spiering *et al.* [34] réalisent des expériences en champ statique (5,5 Tesla) sur un composé de référence, le $[\text{Fe}(\text{phen})_2(\text{NCS})_2]$ et montrent un déplacement de la transition LS → HS vers les basses températures de 0,11 K. Ils modélisent ce comportement et estiment alors ce déplacement en température à 0,1 K. Celui-ci est bien sûr fonction de l'intensité du champ appliqué. En 1991, Lejay *et al.* appliquent un champ de 22 T sur un composé du Co(III) et observent un déplacement de 0,6 K [35]. Plus récemment, 32 T ont été appliqués sur le $[\text{Fe}(\text{phen})_2(\text{NCS})_2]$, à l'aide d'un champ magnétique pulsé [36]. En se plaçant au pied de la transition de spin du composé, l'application d'un pulse a permis d'accroître la proportion d'état HS. Ce phénomène a été observé tout au long de la branche ascendante LS → HS. Un modèle basé sur le champ moyen a été proposé.

1.3.2.4 Transition de spin induite par la lumière

Induire une transition de spin par l'action de la lumière est plus complexe. Pour y parvenir, les deux principaux moyens sont d'agir soit sur le ligand (LD-LISC) (pour l'anglais *Ligand-Driven Light-Induced Spin Change*), soit directement

sur le métal (LIESST), à l'aide de rayonnements UV-Visible. Notons également l'effet SOXIESST [37] (pour l'anglais *Soft X-ray Induced Excited Spin-State Trapping*) permettant d'agir sur le métal pour passer de l'état LS à l'état HS par un rayonnement X "doux". Enfin, l'effet NIESST (pour l'anglais *Nuclear Decay-Induced Excited Spin-State Trapping*) est analogue à l'effet LIESST, mais la source lumineuse excitatrice est ici "interne". Cette source provient de la désintégration radioactive d'atomes de ^{57}Co , présents dans le matériau, en ^{57}Fe [38, 39].

L'effet LD-LISC La découverte du processus LD-LISC est attribuée à Zarembowitch [40]. Le principe est basé sur une perturbation photochimique du ligand modifiant le champ de ligand [41].

Les premières expériences rapportées sur l'effet LD-LISC ont été réalisées à partir du composé $[\text{Fe}(\text{stpy})_4(\text{NCS})_2]$ (avec stpy = 4-styrylpyridine). La modification photochimique utilisée est l'isomérisation cis-trans du ligand [42]. Le composé $[\text{Fe}(\text{trans-stpy})_4(\text{NCS})_2]$ présente une transition de spin centrée autour de 108 K alors que le composé $[\text{Fe}(\text{cis-stpy})_4(\text{NCS})_2]$ reste HS sur toute la gamme de température 10-300 K. Cette différence de propriété magnétique a été attribuée à un champ de ligand plus fort dans le cas du ligand *trans* que dans le cas du ligand *cis*. Depuis cette expérience, divers travaux ont été réalisés afin d'accroître la température de photocommutation. Finalement, en 1999 Boillot *et al.* rapportent le premier effet LD-LISC à température ambiante [43].

L'effet LIESST Le principe de ce processus photochimique consiste à agir sur les bandes d'absorption du centre métallique par irradiation lumineuse. Nous détaillerons cet effet dans la section 1.4.

1.3.3 Rôle des interactions intermoléculaires

En phase solide, le réseau cristallin et les interactions entre les molécules du réseau jouent un rôle important sur les propriétés macroscopiques du système. De nombreux modèles ont ainsi vu le jour dans le but de déterminer l'origine de ces interactions et de les quantifier. Les deux principaux sont l'approche moléculaire et l'approche macroscopique. Dans le cas des modèles dits "moléculaires", les interactions entre molécules perturbent le système moléculaire de base et la thermodynamique statistique permet de corrélérer les paramètres microscopiques avec les expériences. Les modèles dits "macroscopiques" utilisent les lois de la thermodynamique classique et ne tiennent pas compte de la structure intrinsèque de la molécule.

1.3.3.1 Approche moléculaire

Le premier modèle historiquement publié introduisant la notion d'interaction intermoléculaire est celui de Wajnflasz en 1970 [44]. L'approche moléculaire de ce modèle représente chaque centre métallique par un système à quatre niveaux (deux états de spin et deux rayons ioniques). L'interaction est introduite à l'aide d'un hamiltonien d'Ising et la résolution du problème est faite dans l'approximation du champ moyen. Ce modèle est le premier à prédire des transitions de spin discontinues pour un paramètre d'interaction J supérieur à $k_B T_{1/2}$ (où $T_{1/2}$ est la température de transition de spin thermique). L'objectif principal d'une telle approche est la détermination de la fonction de partition Z permettant de remonter aux données macroscopiques.

1.3.3.2 Approche macroscopique

Le principal modèle macroscopique rendant compte des interactions intermoléculaires est celui de Slichter et Drickamer développé en 1972 [26]. Il est basé sur la théorie des solutions régulières en supposant une répartition aléatoire des molécules dans le matériau. L'état de spin de chacune des molécules est indépendant de celui des molécules voisines. Les auteurs prévoient, suivant la valeur d'un terme d'interaction Γ , des transitions de spin discontinues mais également la présence d'une hystérésis. Cette prévision sera confirmée expérimentalement en 1976 [22]. Une explication de l'origine de la coopérativité est celle proposée par Onishi et Sugano en 1981 [45] et Spiering *et al.* [46]. Les auteurs considèrent que les ions sont susceptibles de transiter comme des sphères dures (isotropes) insérées dans un milieu élastique. En effet, la transition de spin s'accompagne d'un changement de volume. Un champ de contrainte est alors induit et se propage à l'ensemble du réseau *via* son élasticité. Le terme d'interaction s'écrit alors comme un développement en puissance de la fraction de molécule dans l'état HS γ_{HS} : $\Delta\gamma_{HS} - \Gamma\gamma_{HS}^2$. Par la suite, le modèle de Spiering a traité les systèmes dilués (avec x le taux de molécules susceptibles de transiter). Dans cette approche, il utilise un réseau de référence (constitué le plus souvent de zinc) ne subissant pas de transition de spin. Les termes d'interactions Γ et Δ s'écrivent alors :

$$\Gamma = x \frac{1}{2} B \frac{\gamma_0 - 1}{\gamma_0} \frac{(V_{HS} - V_{LS})^2}{V_C} \quad (1.17)$$

$$\Delta = 2\Gamma \frac{V_M - V_{LS}}{V_{HS} - V_{LS}}. \quad (1.18)$$

B représente le module de compressibilité isotherme du matériau et rend compte de ses capacités à se déformer. γ_0 (constante d'Eshelby) est fonction des coefficients de Poisson permettant de quantifier les déformations du réseau. V_C est le volume par molécule (volume de la maille divisé par le nombre de molécules dans la maille). V_M est le volume de l'ion métallique de dilution.

Lorsque l'élément de dilution est le Zinc(II), le rayon ionique est très proche de celui du Fer(II) dans l'état HS et le rapport Δ/Γ est égal à 2. Si l'élément de dilution est le Nickel(II), le rayon ionique est intermédiaire entre celui du Fer(II) HS et du Fer(II) LS et le rapport Δ/Γ est égal à 1.

Ce modèle repose sur le principe d'élasticité et réagit donc à une contrainte extérieure telle que la pression. Dans le cas des composés à transition de spin, cette contrainte est interne au système puisque la variation de pression est induite par le changement de volume pendant la transition. Or, comme cela a été vu précédemment, la pression favorise l'état LS. Cette pression interne dépend du réseau de référence. Plus l'ion métallique formant le réseau d'accueil aura un petit volume, plus la pression interne sera importante et favorisera l'état LS. La dilution permet donc d'induire une certaine "pression chimique" à l'intérieur même du composé.

D'autre part, d'après l'équation 1.18 plus la différence de volume entre l'état HS et l'état LS est grande, plus la coopérativité sera importante. A l'inverse, plus le milieu est compressible (B grand), plus la coopérativité sera faible.

1.4 Le phénomène LIESST

Historiquement, l'effet LIESST (*Light-Induced Excited Spin-State Trapping*) a été décrit en phase solide. Cependant, un certain nombre d'études antérieures décrivent des effets photo-induits en phase liquide.

1.4.1 En phase liquide

Les premières études remontent à celles de Beattie en 1973. En réalité, il ne s'agissait pas réellement d'une excitation par irradiation lumineuse dans le domaine spectral du complexe à transition de spin, mais de techniques de chauffage rapide (25 ns) par irradiation laser ou par des variations rapides de pression (quelques ns) créées par onde acoustique (ultrasons). L'équilibre $\text{HS} \leftrightarrow \text{LS}$ était modifié et le retour à l'état initial en fonction du temps après photo-perturbation était enregistré pour différentes températures initiales. De telles études ont ainsi permis de déterminer la dynamique de l'équilibre $\text{HS} \leftrightarrow \text{LS}$.

McGarvey [47] fût le premier en 1982 à rapporter une expérience attribuable aujourd’hui à l’effet LIESST. Cet auteur a montré qu’une irradiation laser pulsée dans la bande de transfert de charge métal-ligand MLCT (pour l’anglais *Metal Ligand Charge Transfer*) de certains complexes du Fe(II) à transition de spin, induisait la population d’un état HS. Ce phénomène a été expliqué par un passage intersystème entre la transition électronique MLCT de l’état LS et l’état HS.

1.4.2 En phase solide

La première étude en phase solide remonte aux travaux de Decurtins *et al.* en 1984. Ces auteurs ont rapporté que l’irradiation à 530 nm de cristaux de $[\text{Fe}(\text{ptz})_6](\text{BF}_4)_2$, ($\text{ptz}=1\text{-propyltetrazole}$), dans l’état LS à basse température (20 K) permettait la population d’un état excité à durée de vie supérieure à 10^6 s (~ 116 jours). Par la suite, cet état métastable a été attribué à l’état HS ${}^5\text{T}_2$ [48, 49]. En 1986, Hauser a démontré que ce processus était réversible (reverse-LIESST ou LIESST inverse) [50]. Ainsi l’état HS piégé par effet LIESST pouvait être converti en état LS par une irradiation dans le proche infra-rouge. Le mécanisme proposé, illustré sur la figure 1.3, fait intervenir deux passages intersystèmes successifs, comme l’avait suggéré McGarvey [47]. L’irradiation dans la bande d’absorption de l’état LS peuple les niveaux excités ${}^1\text{T}_1$ (ou ${}^1\text{T}_2$). Le système se relaxe alors de manière non radiative vers un état intermédiaire triplet, ${}^3\text{T}_1$ (ou ${}^3\text{T}_2$), puis de cet état intermédiaire vers l’état métastable HS, ${}^5\text{T}_2$. Le retour de l’état HS vers l’état LS peut s’effectuer, soit par relaxation non-radiative ${}^5\text{T}_2 \rightarrow {}^1\text{A}_1$, soit par irradiation dans la bande d’absorption de l’état HS (${}^5\text{T}_2 \rightarrow {}^5\text{E}$). Dans ce dernier cas, le recouvrement spectral entre la transition ${}^5\text{T}_2 \rightarrow {}^5\text{E}$ et les transitions ${}^1\text{A}_1 \rightarrow {}^3\text{T}_1$ et ${}^1\text{A}_1 \rightarrow {}^3\text{T}_2$ de faibles intensités à 980 et 670 nm, conduit à un taux de conversion de 0,9. L’existence de l’état triplet intermédiaire a été démontré par la conversion directe LS \rightarrow HS à 980 nm [51]. Dans le cas du $[\text{Fe}(\text{ptz})_6](\text{BF}_4)_2$, les rendements quantiques des passages intersystèmes ont été déterminés [51]. Les rendements quantiques de la première étape de l’effet LIESST ${}^1\text{A}_1 \rightarrow {}^3\text{T}_1$ et de l’effet LIESST inverse ${}^5\text{T}_2 \rightarrow {}^3\text{T}_1$ sont proches de l’unité et les constantes de vitesse sont estimées supérieures à 10^{10} s^{-1} . Cette étude montre aussi une dépendance linéaire du rendement quantique de photoexcitation en fonction de la fraction HS. La durée de vie de l’état ${}^3\text{T}_1$ est très courte puisque même à l’échelle de la nanoseconde aucune absorption transitoire n’a été détectée [53]. Hauser a estimé qu’à 20 K, le rapport d’embranchement de l’état ${}^3\text{T}_1$ vers l’état fondamental, ${}^1\text{A}_1$, et vers l’état métastable, ${}^5\text{T}_2$, était de 1 pour 4 [51].

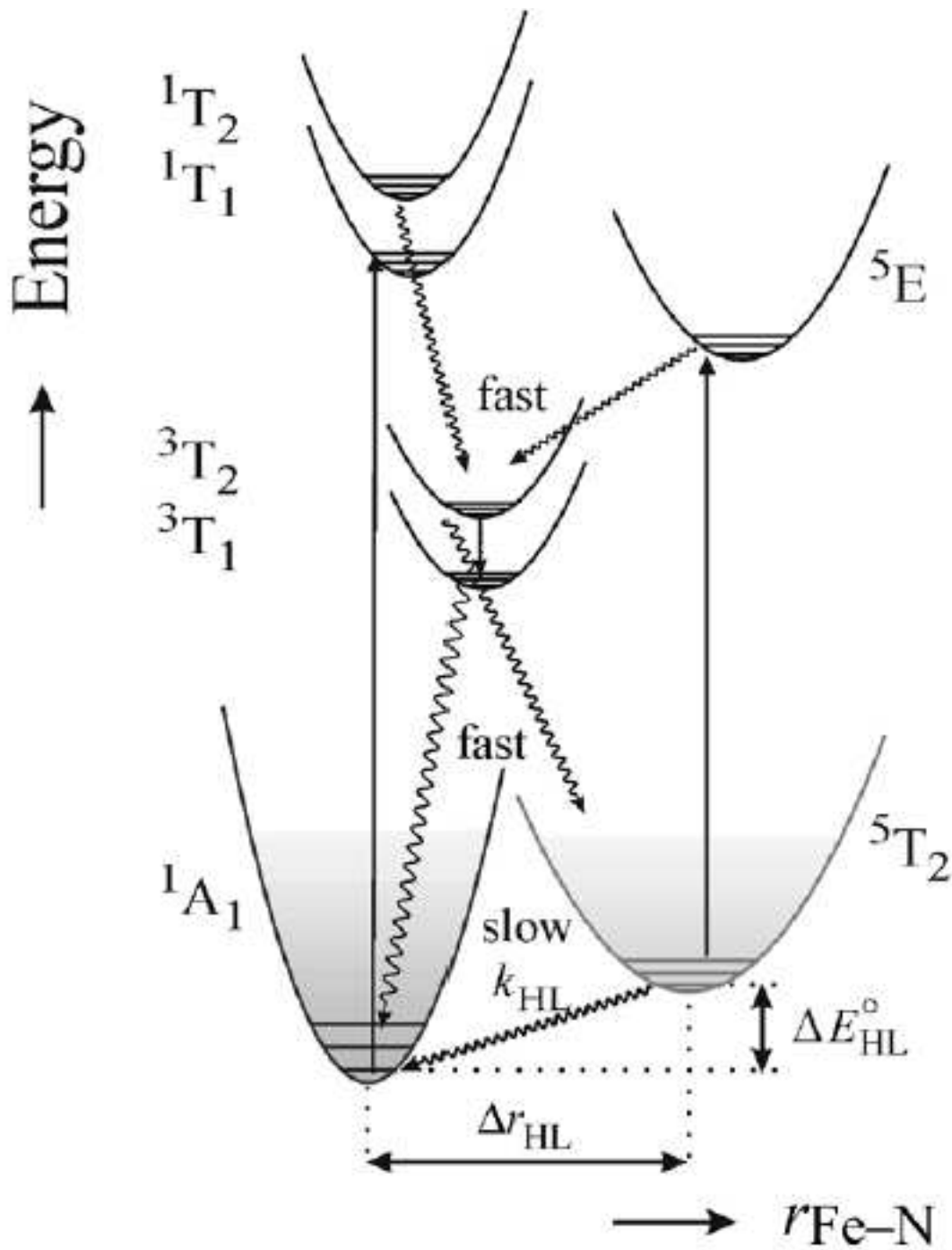


FIG. 1.3: Diagramme schématique proposé pour les effets LIESST et reverse-LIESST. Les flèches rectilignes représentent les excitations électroniques et les flèches ondulées symbolisent les processus de relaxation non-émissifs (tiré de la Ref [52]).

1.4.2.1 Le retour à l'état fondamental : la relaxation HS → LS

Hauser [50, 54, 55, 56, 57, 58, 59] et Hendrickson [53] ont étudié le processus de recombinaison HS → LS. Ils ont déterminés les constantes de vitesse de relaxation, k_{HL} , en fonction de la température, pour divers composés mixtes $[Fe_xM_{1-x}]$ ($x < 0.1$) purs ou dilués en matrice polymère. Les auteurs ont observé à basse température une forte déviation de la loi classique d'Arrhenius attribuée à la présence de l'effet tunnel. En réalité, c'est en 1980 que Buhks *et al.* [60] ont introduit la notion de processus multiphonon non-adiabatique entre états de spin différents. Cette approche théorique prévoyait une relaxation HS → LS indépendante de la température pour $T < 50$ K et un processus activé thermiquement pour les hautes températures [61, 62].

La théorie multiphonon non-adiabatique est basée sur un couplage vibrationnel fort entre les deux états de spin. L'énergie électronique de l'état initial est transformée en énergie vibrationnelle, lors du passage non-adiabatique et non-radiatif à l'état final. Dans l'approche SCC (pour l'anglais *Single Configurational Coordinate*) où la distance Fe-ligand est prise comme coordonnée de réaction, chaque état de spin est représenté par un puits de potentiel harmonique. Ces puits sont séparés en énergie par ΔE_{LH}^0 (figure 1.3) et représentent les limites classiques de la vibration de la liaison Fe-ligand. Les vibrations de ces liaisons, Fe_{LS}-ligand et Fe_{HS}-ligand, sont quantifiées en niveaux vibrationnels, dont la population dépend de la température. La probabilité de présence du système dans un état vibrationnel est décrite par une fonction d'onde. ΔE_{LH}^0 représente la différence d'énergie entre le premier niveau vibrationnel de l'état LS et celui de l'état HS. Le processus de relaxation est fortement dépendant du recouvrement des fonctions d'onde des états HS et LS. Aux basses températures, ces recouvrements se situent en marge des puits de potentiel et la probabilité de couplage est très faible. On parle alors de région à "effet tunnel" et les durées de vie sont souvent très longues. Aux hautes températures, les niveaux vibrationnels d'énergies supérieurs sont peuplés. Le recouvrement des fonctions d'onde entre les deux états est favorisé. Cette région peut alors être perçue comme une somme d'effets tunnel. La constante de relaxation dépend de la thermalisation des niveaux de vibration et des couplages électroniques entre les deux états de spin.

La relaxation HS → LS dépend du facteur de Huang-Rhys, S , qui est une mesure du déplacement horizontal entre les puits de potentiel des états HS et LS (rélié à la variation moyenne Δr_{HL}), et du facteur d'énergie réduite p ($p = \Delta E_{LH}^0 / \hbar\omega$). Si la fréquence de vibration de la liaison Fe-ligand, $\hbar\omega$, est supposée constante dans les deux états, p est alors une mesure du déplacement vertical entre les puits de potentiel des états HS et LS. Hauser a proposé pour les composés FeN₆ d'utiliser les données suivantes [50] : $\Delta Q = \sqrt{6}\Delta r_{HL} \sim 0,5$ Å, constante de force $f = 2.10^5$ dyn.cm⁻¹

et $\hbar\omega \sim 250 \text{ cm}^{-1}$. Soit un facteur S compris entre 40 et 50. Hauser a montré l'influence directe des termes p et S sur la vitesse de relaxation $k_{HL}(T)$ [54]. Un accroissement de p et/ou une diminution de S accélèrent la relaxation HS → LS à basse température.

La modification du facteur S affecte directement l'elongation de la liaison Fe-ligand, c'est-à-dire le déplacement vertical entre les deux puits de potentiel LS et HS. Ainsi, plus S est grand, plus la distance entre les deux puits est grande et plus les processus de recombinaison HS → LS sont lents. Enfin, en 1991, Hauser a proposé de relier directement p à $T_{1/2}$ [61]. Il a montré expérimentalement que les composés avec $T_{1/2} < 100 \text{ K}$ avaient une valeur de p inférieure à 1 tandis que les composés LS possédaient un facteur p supérieur à 10. Cette dépendance a donné naissance à la loi dite en "énergie inverse". Plus $T_{1/2}$ est élevée, plus la relaxation HS → LS est rapide.

1.4.2.2 Cas des systèmes peu coopératifs

Dans les systèmes dilués, c'est-à-dire peu coopératifs, les cinétiques de relaxation en fonction du temps et à température constante, sont généralement reproduites par des déclins monoexponentiels

$$\gamma_{HS} = \exp(-k_{HL}(T)t) \quad \text{avec} \quad k_{HL}(T) = k_{HL}(T \rightarrow \infty)e^{(-E_a/k_b T)}. \quad (1.19)$$

Cependant, dans certains cas, les cinétiques de relaxation ne suivent pas totalement une évolution exponentielle. Hauser [63] a proposé d'analyser cette évolution comme une distribution des vitesses de relaxation $k_{HL}(T)$, liée à une répartition des énergies d'activation. À une température T , $k_{HL}(T)$ peut être obtenue en utilisant une distribution Gaussienne des énergies d'activation centrée à E_0 avec un écart type σ .

1.4.2.3 Cas des systèmes coopératifs

L'influence des interactions intermoléculaires au sein du réseau cristallin sur la transition de spin thermique a été décrite dans la partie 1.3.3. L'effet de la coopérativité est également très important sur le processus de relaxation HS → LS. Lors de l'étude de composés dilués, $[\text{Fe}_x\text{Zn}_{1-x}(\text{ptz})_6](\text{BF}_4)_2$, Hauser a montré que cette relaxation dépendait de la valeur de la concentration x [50, 54]. Lorsque les ions Fe(II) sont très dilués ($x < 0.2$), les effets coopératifs sont faibles. Les processus de relaxation résultent d'un équilibre de spin et le traitement de type exponentiel est alors satisfaisant.

Pour les composés concentrés ($0.2 \leq x \leq 1$), le rôle des effets coopératifs est,

par contre, primordial. Les cinétiques de relaxation s'éloignent très fortement d'une loi exponentielle. Aux temps courts, la relaxation est très lente puis s'accélère aux temps longs. Il se produit un phénomène "d'autoaccélération" de la cinétique. Dans le cas des composés à transition de spin, Hauser a mis en évidence cet effet d'autoaccélération était directement relié à une modification de l'énergie d'activation en fonction de la fraction LS et du taux de dilution. Une telle variation a été expliquée sur la base du modèle d'élasticité de Spiering [46]. Les ions Zn(II), de volume très proche de celui de l'ion Fe(II) HS, exercent une pression interne favorisant l'état HS. Ainsi, les relaxations sont d'autant plus rapides que le taux de Fe(II) est important. L'accélération atteint son maximum pour le système pur.

Afin de confirmer cette variation d'énergie d'activation en fonction de la fraction LS, les spectres d'absorption UV-Visible ont été enregistrés pendant le processus de relaxation. Hauser a pu ainsi observer un déplacement de la bande ${}^1\text{A}_1 \rightarrow {}^1\text{T}_1$ à mesure que la fraction LS augmentait [50, 55]. Cette évolution a été interprétée comme un déplacement vertical et horizontal des puits de potentiel correspondant aux états HS et LS. Une analyse détaillée a montré que le déplacement vertical des puits de potentiel est responsable de la déviation à la cinétique du premier ordre. Au cours de la relaxation, la différence d'énergie au point zéro $\Delta E_{HL}^0 = E_{HS}^0 - E_{LS}^0$ augmente linéairement avec γ_{HS} , ΔE_{HL}^0 étant directement relié à l'énergie d'activation. Ce phénomène explique l'effet d'autoaccélération lorsque γ_{HS} décroît.

Cet effet de pression interne associé à la dilution d'un ion Fe(II) dans une matrice hôte a été, par la suite, confirmé par des études de pression externe. Jeftić et Hauser [57] ont ainsi rapporté que le système $[\text{Fe}_x\text{Zn}_{1-x}(\text{ptz})_6](\text{BF}_4)_2$ (avec $x=0.1$) soumis à une pression extérieure de 1 kbar, présentait par rapport au système initial, un processus de relaxation HS \rightarrow LS accéléré d'un ordre de grandeur ainsi qu'un déplacement de la bande d'absorption.

1.5 Conclusion

De cet ensemble de rappels, nous voudrions dégager quelques points utiles pour la compréhension de la suite de ce manuscrit. Ainsi, même si le comportement d'une assemblée de molécules en phase solide est fortement dépendant de la nature des interactions intermoléculaires, le phénomène de transition de spin est de nature essentiellement intramoléculaires.

L'origine de la coopérativité est le plus souvent attribuée à des interactions de type élastique. Différents stimuli externes peuvent être utilisés pour induire le phénomène de transition de spin. Parmi eux, l'utilisation d'une perturbation optique est

particulièrement intéressante. Dans ce chapitre, nous avons rapporté les deux effets photomagnétiques connus, les effets LD-LISC et LIEST. Les mécanismes mis en jeu au cours de l'excitation et de la relaxation ont été particulièrement décrits dans le cas de l'effet LIEST. Hauser a montré que le seul processus relativement lent était la relaxation $^5T_2 \rightarrow ^1A_1$. D'un point de vue électronique, ce processus correspond à un double passage intersystème et cette transition est fortement interdite. D'un point de vue structural, le passage HS \rightarrow LS est accompagné d'une forte modification de la liaison Fe-Ligand. Le processus de recombinaison est donc fortement dépendant de la différence de longueur de liaison associée à la conversion de spin et à la facilité de propagation de l'information au sein du réseau cristallin. Dans le cas du $[Fe(ptz)_6](BF_4)_2$, la durée de vie de l'état HS photo-induit est quasiment infinie ($>10^6$ s) à 20 K. Ainsi, Hauser a montré que $k_{HL}(T \rightarrow \infty)$ est de l'ordre de $10^6\text{-}10^8$ s $^{-1}$ quels que soient les composés. La constante de relaxation à basse température, $k_{HL}(T \rightarrow 0)$, varie de douze ordres de grandeur : de 10 $^{-6}$ s $^{-1}$ pour des composés présentant une transition de spin à 10 6 s $^{-1}$ pour ceux restant LS sur toute la gamme de température étudiée.

Bibliographie

- [1] F.A. Cotton, G. Wilkinson, C.A. Murillo et M. Bochmann, *Advanced Inorganic Chemistry, 6th Edition*, (Wiley-Interscience, 1999).
- [2] S.F.A. Kettle, *Physico-chimie inorganique*, (De Boeck université, 1999).
- [3] H. Bethe, Ann. Phys. **3**, 133 (1929).
- [4] B.N. Figgis and M.A. Hitchman, *Ligand Field Theory and Its Applications*, (Wiley-VCH, New York, 2000).
- [5] L. Cambi et A. Cagnasso, Atti. Accad. Naz. Lincei **13**, 809 (1931).
- [6] J.S. Griffith, Proc. Roy. Soc. **23**, 23 (1956).
- [7] C.J. Ballhausen et A.D. Liehr, J. Am. Chem. Soc. **81**, 538 (1959).
- [8] R.C. Stoufer, D.H. Bush et W.B. Hardley, J. Am. Chem. Soc. **83**, 3732 (1961).
- [9] (a) W.A. Baker et H.M. Bobonich, Inorg. Chem. **3**, 1184 (1964);
(b) H.A. Goodwin, Coord. Chem. Rev. **18**, 293 (1976).
- [10] A.H. Ewald, R.L. Martin, I.G. Ross et A.H. White, Proc. Roy. Soc. A. **280**, 235 (1964).
- [11] S. Schenker, A. Hauser et R.M. Dyson, Inorg. Chem. **35**, 4676 (1996).

- [12] M. Sorai, Y. Yumoto, D.M. Halepoto et L.F. Larkworthy, *J. Phys. Chem. Solids* **54**, 421 (1993).
- [13] D. Cozak et F. Gauvin, *Organometallics* **6**, 1912 (1987).
- [14] K. Heinze, G. Huttner, L. Zsolnai et P. Schober, *Inorg. Chem.* **36**, 5457 (1997).
- [15] L. Kaustov, M.E. Tal, A.I. Shames et Z. Gross, *Inorg. Chem.* **36**, 3503, (1997).
- [16] W. Kläui, W. Eberspach et P. Gütlich, *Inorg. Chem.* **26**, 3977, (1987).
- [17] E. König et K. Madeja, *Inorg. Chem.* **6**, 48. (1967).
- [18] L.F. Lindoy et S.E. Livingstone, *Coord. Chem. Rev.* **2**, 173 (1967).
- [19] E. König, G. Ritter et S.K. Kulshreshtha, *Chem. Rev.* **85**, 219 (1985).
- [20] M. Sorai et S. Seki, *J. Phys. Soc. Japan.* **33**, 575 (1972).
- [21] M. Sorai et S. Seki, *J. Phys. Chem. Solids* **35**, 555 (1974).
- [22] E. König et G. Ritter, *Sol. State Comm.* **18**, 279 (1976).
- [23] M. Sorai, J. Ensling, K.M. Hasselbach et P. Gütlich, *Chem. Phys.* **20**, 197 (1977).
- [24] H. Köppen, E.W. Müller, C.P. Köhler, H. Spiering, E. Meissner, P. Gütlich, *Chem. Phys. Lett.* **91**, 348 (1982).
- [25] C.B. Bargeron, M. Avinor et H.G. Drickamer, *Inorg. Chem.* **10**, 1338 (1971).
- [26] C.P. Slichter, H.G. Drickamer, *J. Chem. Phys.* **56**, 2142 (1972).
- [27] G.J. Long, B.B. Hutchinson, *Inorg. Chem.* **26**, 608 (1987).
- [28] V. Ksenofontov, G. Levchenko, H. Spiering, P. Gütlich, J.-F. Létard, Y. Bouhedja et O. Kahn, *Chem. Phys. Lett.* **294**, 545 (1998).
- [29] Y. Garcia, P.J. van Koningsbruggen, R. Lapouyade, L. Fournès, L. Rabardel, O. Kahn, V. Ksenofontov, G. Levchenko et P. Gütlich, *Chem. Mater.* **10**, 2426 (1998).
- [30] Y. Garcia, V. Ksenofontov, G. Levchenko, G. Schmitt et P. Gütlich, *J. Phys. Chem. B* **104**, 5046 (2000).
- [31] P. Guionneau, C. Brigouleix, Y. Barrans, A.E. Goeta, J.-F. Létard, J.A.K. Howard, J. Gaultier et D. Chasseau, *C. R. Acad. Sci. Paris / Chimie* **4**, 161 (2001).
- [32] P. Gütlich, A.B. Gaspar, V. Ksenofontov et Y. Garcia, *J. Phys. C* **16**, 1087 (2004).
- [33] N. Sasaki et T. Kambara, *J. Phys. C : Solid State Phys.* **1**, 1035 (1982).

- [34] Y. Qi, E.W. Müller, H. Spiering et P. Gütlich, *Chem. Phys. Lett.* **101**, 503 (1983).
- [35] J. Lejay, A.G.M. Jansen, P. Wyder, *Phys. Rev. B* **43**, 8196 (1991).
- [36] A. Bousseksou, N. Negre, M. Goiran, L. Salmon, J.-P. Tuchagues, M.-L. Boillot, K. Boukheddaden et F. Varret, *Eur. Phys. J. B* **13**, 451 (2000).
- [37] D. Collison, C.D. Garner, C.M. Mc Grath, J.F.W. Mosselmans, M.D. Roper, J.M.W. Seddon, E. Sinn et N.A. Toung, *J. Chem. Soc. Dalton Trans.* **4371**, 40 (1997).
- [38] P. Gütlich, A. Hauser, and H. Spiering, *Angew. Chem. Int. Ed. Engl.* **33**, 2024 (1994).
- [39] P. Gütlich, *Mol. Cryst. Liq. Cryst.* **305**, 17 (1997).
- [40] J. Zarembowitch et C. Roux, *Brevet Français* 9205928, 1992.
- [41] (a) J. Zarembowitch, C. Roux, M.-L. Boillot, R. Claude, J.-P. Itie, A. Polian et M. Bolte, *Mol. Cryst. Liq. Cryst.* **234**, 247 (1993);
(b) M.-L. Boillot, A. Sour, P. Delhaès, C. Mingotaud, H. Soyer, *Coord. Chem. Rev.* **190**, 47 (1999).
- [42] C. Roux, J. Zarembowitch, B. Gallois, T. Granier, and R. Claude, *Inorg. Chem.* **33**, 2273 (1994).
- [43] M.-L. Boillot, S. Chantraine, J. Zarembowitch, J.-Y. Lallemand et J. Prunet, *New J. Chem.* **179** (1999).
- [44] J. Wajnflasz et R. Pick, *J. Phys. Status Solidi* **40**, 537 (1970).
- [45] S. Ohnishi et S. Sugano, *J. Phys. C : Solid State Phys.* **14**, 39 (1981).
- [46] (a) H. Spiering, E. Meissner, H. Köppen, E.W. Müller et P. Gütlich, *J. Chem. Phys.* **68**, 65 (1982);
(b) N. Willenbacher et H. Spiering, *J. Phys. C : Solid State Phys.* **21**, 1423 (1988);
(c) H. Spiering et N. Willenbacher, *J. Phys. : Condensed Matter* **1**, 10089 (1989).
- [47] J.J. McGarvey et I. Lawthers, *J. Chem. Soc., Chem. Comm.* 906 (1982).
- [48] S. Decurtins, P. Gütlich, C.P. Köhler, H. Spiering, and A. Hauser, *Chem. Phys. Lett.* **105**, 1 (1984).
- [49] S. Decurtins, P. Gütlich, K.M. Hasselbach, and H. Spiering, *Inorg. Chem.* **24**, 2174 (1985).
- [50] A. Hauser, P. Gütlich et H. Spiering, *Inorg. Chem.* **25**, 4245 (1986).
- [51] A. Hauser, *J. Chem. Phys.* **94**, 2741 (1991).

- [52] P. Gütlich, Y. Garcia et H.A. Goodwin, Chem. Soc. Rev. **29**, 419 (2000).
- [53] C.L. Xie et D.N. Hendrickson, J. Am. Chem. Soc. **109**, 6981 (1987).
- [54] A. Hauser, A. Vef et P. Adler, J. Chem. Phys. **95**, 8710 (1991).
- [55] A. Hauser, Chem. Phys. Lett. **192**, 65 (1992).
- [56] A. Hauser, Comments Inorg. Chem. **17**, 17 (1995).
- [57] J. Jeftić et A. Hauser, Chem. Phys. Lett. **248**, 458 (1996).
- [58] J. Jeftić, H. Romstedt et A. Hauser, J. Phys. Chem. Solids **57**, 1743 (1996).
- [59] A. Hauser, Chem. Phys. Lett. **173**, 507 (1990).
- [60] E. Buhks, G. Navon, M. Bixon, and J. Jortner, J. Am. Chem. Soc. **102**, 2918 (1980).
- [61] A. Hauser, Coord. Chem. Rev. **111**, 275(1991).
- [62] A. Hauser, J. Jeftić, H. Romstedt, R. Hinek et H. Spiering, Coord. Chem. Rev. **190-192**, 471 (1999).
- [63] A. Hauser, J. Adler, and P. Gütlich, Chem. Phys. Lett. **152**, 468 (1988).

Chapitre 2

Aspects Théoriques

La différence d'énergie et la différence de distance Métal-Ligand, ΔE_{HL} et Δr_{HL} respectivement, sont deux quantités importantes pour décrire le phénomène LIESST. Dans cette partie, nous allons voir différentes méthodes nous permettant de calculer ces deux quantités. Les géométries d'équilibres, et donc Δr_{HL} , sont trouvées en minimisant l'énergie moléculaire.

2.1 Les méthodes *ab initio*

Au XVII^{ème} siècle, Isaac Newton formule la mécanique classique dont les lois régissent le déplacement des objets macroscopiques. Au début du XX^{ème} siècle, les physiciens découvrent que les lois de la mécanique classique ne décrivent pas correctement le comportement de très petites particules comme les électrons, les noyaux d'atomes et les molécules. En fait, leur comportement est régit par les lois de la mécanique quantique.

Les propriétés de systèmes atomiques et moléculaires sont prédits par des calculs de dynamique moléculaire, des calculs de mécanique statistique et par des calculs de structures électroniques. Ces derniers utilisent des approximations et des transformations mathématiques pour résoudre les équations fondamentales de la mécanique quantique décrites dans la partie suivante.

2.1.1 L'équation de Schrödinger

L'équation de Schrödinger décrit la fonction d'onde d'une particule :

$$\left(\frac{-\hbar^2}{2m} \nabla^2 + V(\mathbf{r}, t) \right) \Psi(\mathbf{r}, t) = i\hbar \frac{\partial \Psi(\mathbf{r}, t)}{\partial t} \quad (2.1)$$

avec Ψ la fonction d'onde de la particule, m sa masse, h la constante de Planck ($\hbar = h/2\pi$) et V le potentiel dans laquelle la particule se déplace. Dans le cas de plusieurs particules, comme dans une molécule, Ψ sera fonction des coordonnées de ces particules ainsi que du temps t .

La résolution de l'équation de Schrödinger permet d'obtenir l'énergie d'un système mais aussi beaucoup d'autres propriétés. Plusieurs fonctions d'ondes sont solutions de cette équation et correspondent à différents états du système.

Si V ne dépend pas du temps, l'équation de Schrödinger peut-être simplifiée en utilisant une technique mathématique nommée séparation de variables. Dans le cas d'une seule particule, la fonction d'onde peut s'écrire comme un produit d'une fonction d'espace et d'une fonction de temps :

$$\Psi(\mathbf{r}, t) = \Psi(\mathbf{r})\tau(t) . \quad (2.2)$$

En remplaçant cette écriture dans l'équation 2.1, deux équations sont obtenues. L'une dépend uniquement du temps et l'autre, uniquement de la position des particules. Dans le cas de notre étude, cette séparation de variables est valide. Nous allons donc nous focaliser sur la résolution de la très familière équation de Schrödinger indépendante du temps (donnée pour une seule particule) :

$$\hat{H}\Psi(\mathbf{r}) = E\Psi(\mathbf{r}) , \quad (2.3)$$

où E est l'énergie de la particule et \hat{H} l'opérateur Hamiltonien. Les différentes solutions de l'équation 2.3 correspondent à différents états stationnaires de la particule. Celui pour lequel l'énergie est la plus petite est appelé l'*état fondamental*. L'équation 2.3 correspond à la description non relativiste d'un système. Elle ne donne donc pas une description précise pour les particules se déplaçant à des vitesses proches de celle de la lumière comme les électrons de cœur des gros atomes (plus gros que le Brome).

2.1.1.1 Hamiltonien moléculaire

Dans le cas d'un système moléculaire, Ψ dépend des positions des électrons et des noyaux dans la molécule, désignées respectivement par \mathbf{r} et \mathbf{R} . Pour parler d'une particule en particulier, nous utiliserons les indices i et j pour les électrons et A et B pour les noyaux. La fonction d'onde

$$\psi(\boldsymbol{\tau}_1, \boldsymbol{\tau}_2, \dots, \boldsymbol{\tau}_i, \dots, \boldsymbol{\tau}_n, \mathbf{R}_1, \mathbf{R}_2, \dots, \mathbf{R}_A, \dots, \mathbf{R}_N) \quad (2.4)$$

est celle d'un système à n électrons et N noyaux. Elle dépend des $4n$ coordonnées spatiales \mathbf{r}_i et de spin σ_i ($\boldsymbol{\tau}_i = (\mathbf{r}_i, \sigma_i)$) des électrons ainsi que des $3N$ coordonnées spatiales des noyaux.

L'opérateur Hamiltonien est composé d'un terme d'énergie cinétique et d'un terme d'énergie potentielle,

$$\hat{H} = \hat{T} + \hat{V}. \quad (2.5)$$

Le terme d'énergie cinétique est la sommation de l'opérateur ∇^2 sur toutes les particules de la molécule,

$$\hat{T} = -\frac{\hbar^2}{2} \left(\underbrace{\sum_i^n \frac{1}{m_i} \nabla_i^2}_{\hat{T}_e} + \underbrace{\sum_A^N \frac{1}{m_A} \nabla_A^2}_{\hat{T}_N} \right), \quad (2.6)$$

avec \hat{T}_e , le terme d'énergie cinétique associé aux électrons et \hat{T}_N , le terme d'énergie cinétique associé aux noyaux.

Le terme d'énergie potentielle est composé de la répulsion Coulombienne entre chaque paire de particules chargées,

$$\hat{V} = \underbrace{-\frac{1}{4\pi\epsilon_0} \sum_i^n \sum_A^N \left(\frac{Z_A e^2}{r_{iA}} \right)}_{\hat{V}_{eN}} + \underbrace{\frac{1}{4\pi\epsilon_0} \sum_i^n \sum_{j < i}^n \left(\frac{e^2}{r_{ij}} \right)}_{\hat{V}_{ee}} + \underbrace{\frac{1}{4\pi\epsilon_0} \sum_A^N \sum_{B < A}^N \left(\frac{Z_A Z_B e^2}{r_{AB}} \right)}_{\hat{V}_{NN}}, \quad (2.7)$$

avec \hat{V}_{eN} , \hat{V}_{ee} et \hat{V}_{NN} les termes d'attraction électrons-noyaux, répulsion électrons électrons et répulsion noyaux-noyaux respectivement. Ici, $r_{iA} = |\mathbf{r}_i - \mathbf{R}_A|$ est la distance entre le $i^{\text{ème}}$ électron et le $A^{\text{ème}}$ noyau, $r_{ij} = |\mathbf{r}_i - \mathbf{r}_j|$ la distance entre le $i^{\text{ème}}$ et le $j^{\text{ème}}$ électron, et $r_{AB} = |\mathbf{R}_A - \mathbf{R}_B|$ la distance entre le $A^{\text{ème}}$ et le $B^{\text{ème}}$ électron.

2.1.1.2 Unités atomiques

Afin de simplifier l'écriture des équations, il est possible d'utiliser les unités atomiques qui permettent d'exprimer les quantités physiques comme des multiples ou des combinaisons de constantes fondamentales. Leur définition et leur relation avec les unités du Système International (SI) sont résumées dans le tableau 2.1. Dans la suite de ce manuscrit, toutes les équations seront écrites avec ces unités.

Quantité	Unités atomiques	Valeur en unité SI	Symbole
masse	masse de l'électron au repos	9.1094×10^{-31} kg	m_e
charge	charge élémentaire	1.6022×10^{-19} C	e
action	constante de Planck/ 2π	1.0546×10^{-34} J.s	\hbar
longueur	$4\pi\epsilon_0/m_e e^2$	5.2918×10^{-11} m	a_0
énergie	$\hbar^2/m_e a_0^2$	4.3597×10^{-18} J	E_h

TAB. 2.1: Unités atomiques.

L'Hamiltonien de notre système s'écrit en unités atomiques,

$$\hat{H} = - \sum_i^n \sum_A^N \frac{Z_A}{r_{iA}} + \sum_i^n \sum_{j < i}^n \frac{1}{r_{ij}} + \sum_A^N \sum_{B < A}^N \frac{Z_A Z_B}{r_{AB}} - \sum_i^n \frac{1}{2} \nabla_i^2 - \sum_A^N \frac{1}{2m_A} \nabla_A^2 . \quad (2.8)$$

2.1.1.3 L'approximation Born-Oppenheimer

Il est possible de simplifier l'équation de Schrödinger en considérant la grande différence de masse entre les électrons et les noyaux. Dans le cas de l'atome d'hydrogène, son noyau, le plus léger, est environ 1800 fois plus lourd que l'électron. Il est alors considéré que les noyaux se déplacent très lentement par rapport aux électrons. En première approximation, les électrons s'adaptent ainsi instantanément aux déplacements des noyaux. En d'autres termes, les noyaux apparaissent immobiles aux électrons. Il s'agit de l'approximation Born-Oppenheimer [1]. Si les noyaux sont immobiles, leurs énergies cinétiques sont nulles. L'interaction noyaux-noyaux devient une constante et la fonction d'onde ne dépend plus que paramétriquement des coordonnées des noyaux. Nous devons alors simplement résoudre

$$\hat{H}_{el} \Psi_{el} = E_{el} \Psi_{el} \quad (2.9)$$

avec

$$\hat{H}_{el} = - \sum_i^n \frac{1}{2} \nabla_i^2 - \sum_i^n \sum_A^N \frac{Z_A}{r_{iA}} + \sum_i^n \sum_{j < i}^n \frac{1}{r_{ij}} = \hat{T}_e + \hat{V}_{eN} + \hat{V}_{ee} \quad (2.10)$$

$$= \sum_i^n h(i) - \sum_i^n \sum_A^N \frac{Z_A}{r_{iA}} \quad (2.11)$$

et l'énergie totale du système est alors donnée par

$$E_{tot} = E_{el} + E_{noy} , \quad (2.12)$$

où E_{noy} est l'énergie correspondant à l'opérateur \hat{V}_{NN} .

Dans l'approximation Born-Oppenheimer, l'énergie totale E_{tot} , fonction des coordonnées des noyaux, définit une surface d'énergie potentielle. Le mouvement des noyaux sur cette surface définit les différents chemins de réactions. Sur cette surface, les points stationnaires sont les plus intéressants. Les points de selles d'ordre 1 définissent les états de transition et les minima définissent les géométries d'équilibres.

À partir de maintenant, nous nous attacherons donc à ne résoudre que la partie électronique de l'équation de Schrödinger (Eq. 2.9).

2.1.1.4 Quelques propriétés de la fonction d'onde

La fonction d'onde n'est pas une observable et n'a donc pas d'interprétation physique. En revanche, son module au carré, nommé densité de probabilité,

$$|\Psi(\tau_1, \tau_2, \dots, \tau_n)|^2 d\tau_1 d\tau_2 \dots d\tau_n \quad (2.13)$$

est une observable et représente la probabilité de trouver les électrons $1, 2, \dots, n$ dans l'élément de volume $d\tau_1 d\tau_2 \dots d\tau_n$.

D'autre part, la probabilité de trouver ces n électrons dans tout l'espace doit être de l'unité puisque les électrons sont forcément "quelque part". Nous avons donc,

$$\iint \dots \int |\Psi(\tau_1, \tau_2, \dots, \tau_n)|^2 d\tau_1 d\tau_2 \dots d\tau_n = 1. \quad (2.14)$$

Une fonction d'onde satisfaisant à l'équation 2.14 est dite normalisée. Seul ce type de fonction d'onde sera utilisée par la suite.

La densité électronique, grandeur très importante, est la probabilité de trouver n'importe lequel des n électrons à l'intérieur de l'élément de volume $d\mathbf{r}_1$ avec un spin quelconque, alors que les $n - 1$ autres électrons ont des spins et des positions quelconques dans l'état Ψ

$$\rho(\mathbf{r}_1) = n \iint \dots \int |\Psi(\tau_1, \tau_2, \dots, \tau_n)|^2 d\sigma_1 d\tau_2 \dots d\tau_n. \quad (2.15)$$

Les électrons étant des fermions (particules de spin demi-entier), Ψ doit être antisymétrique c'est-à-dire que la fonction d'onde doit changer de signe lors de l'échange des coordonnées de 2 électrons,

$$\Psi(\tau_1, \tau_2, \dots, \tau_i, \dots, \tau_j, \dots, \tau_n) = -\Psi(\tau_1, \tau_2, \dots, \tau_j, \dots, \tau_i, \dots, \tau_n). \quad (2.16)$$

Une conséquence de l'équation 2.16 est le principe d'exclusion de Pauli pour lequel

deux électrons ne peuvent pas se trouver dans la même spin orbitale.

2.1.2 L'approximation Hartree-Fock

Cette approximation est très importante car elle est à la base de presque toutes les méthodes *ab initio* (basées sur la fonction d'onde). Il n'existe de solutions exactes à l'équation 2.9 que pour des systèmes triviaux comme l'atome d'hydrogène ou les atomes hydrogénoides. Ceci est lié à la complexité intrinsèque du problème à N -corps. Cependant, quelques hypothèses simplificatrices et quelques astuces mathématiques permettent de trouver une solution approchée.

2.1.2.1 Les Orbitales Moléculaires

La première approximation découle de l'interprétation de $|\Psi|^2$ comme une densité de probabilité de trouver les électrons dans le système. La théorie des orbitales moléculaires (OM) décompose Ψ comme une combinaison d'orbitales moléculaires ψ_1, ψ_2, \dots . Pour remplir les conditions sur Ψ établies précédemment, nous choisissons les orbitales moléculaires orthogonales et normalisées telles que

$$\iiint \psi_i^*(\boldsymbol{\tau}) \psi_j(\boldsymbol{\tau}) dx dy dz d\sigma = \int \psi_i^* \psi_j d\boldsymbol{\tau} = \delta_{ij}. \quad (2.17)$$

La manière la plus simple pour construire Ψ à partir de ces orbitales moléculaires est d'en faire le produit de *Hartree*,

$$\Psi(\boldsymbol{\tau}) = \psi_1(\boldsymbol{\tau}_1) \psi_2(\boldsymbol{\tau}_2) \dots \psi_n(\boldsymbol{\tau}_n). \quad (2.18)$$

Cependant, une telle fonction n'est pas antisymétrique puisque l'échange de 2 coordonnées (qui est équivalent à échanger les orbitales de 2 électrons) ne change pas le signe de la fonction d'onde.

La plus simple fonction antisymétrique, combinaison d'orbitales moléculaires, est un déterminant de Slater

$$\Psi(\boldsymbol{\tau}) = \frac{1}{\sqrt{n!}} \begin{vmatrix} \psi_1(\boldsymbol{\tau}_1) & \psi_2(\boldsymbol{\tau}_1) & \dots & \psi_n(\boldsymbol{\tau}_1) \\ \psi_1(\boldsymbol{\tau}_2) & \psi_2(\boldsymbol{\tau}_2) & \dots & \psi_n(\boldsymbol{\tau}_2) \\ \vdots & \vdots & \ddots & \vdots \\ \psi_1(\boldsymbol{\tau}_n) & \psi_2(\boldsymbol{\tau}_n) & \dots & \psi_n(\boldsymbol{\tau}_n) \end{vmatrix}. \quad (2.19)$$

Chaque ligne du déterminant est formée par toutes les assignations possibles de l'électrons i dans toutes les combinaisons de spin orbitales. Echanger deux électrons

correspond à permuter deux lignes et donc à changer le signe du déterminant. Le préfacteur est nécessaire pour respecter les conditions de normalisations (cf. eq. 2.14).

Cette écriture de la fonction d'onde n'est pas seulement une astuce mathématique pour former une fonction antisymétrique. La mécanique quantique considère que la position de l'électron n'est pas déterministe mais consiste plutôt en une densité de probabilité. L'électron peut donc se situer à n'importe quel endroit. Le déterminant de Slater crée donc toutes les possibilités de mettre tous les électrons dans toutes les orbitales pour former la fonction d'onde.

2.1.2.2 Les orbitales

Jusqu'à présent, nous avons travaillé dans la représentation des spin-orbitales. Il est possible de factoriser les spin-orbitales dans une partie spatiale, ψ_i^σ , et une partie de spin, σ . L'ensemble,

$$\{\psi_1(\boldsymbol{\tau}), \psi_2(\boldsymbol{\tau}), \dots, \psi_n(\boldsymbol{\tau})\} , \quad (2.20)$$

est remplacé par,

$$\{ \phi_1^\alpha(\mathbf{r})\alpha, \phi_2^\alpha(\mathbf{r})\alpha, \dots, \phi_{n_\alpha}^\alpha(\mathbf{r})\alpha, \\ \phi_1^\beta(\mathbf{r})\beta, \phi_2^\beta(\mathbf{r})\beta, \dots, \phi_{n_\beta}^\beta(\mathbf{r})\beta \} , \quad (2.21)$$

avec

$$n_\alpha + n_\beta = n . \quad (2.22)$$

En général,

$$\phi_1^\alpha(\mathbf{r}) \neq \phi_1^\beta(\mathbf{r}) . \quad (2.23)$$

Dans ce cas, la méthode Hartree-Fock est dite non-restreinte (UHF [2, 3] pour l'anglais *Unrestricted Hartree-Fock*). En revanche, nous trouvons très souvent pour les systèmes à couche fermée,

$$\phi_i^\alpha(\mathbf{r}) = \phi_i^\beta(\mathbf{r}) = \phi_i(\mathbf{r}) \quad (2.24)$$

($n_\alpha = n_\beta = n/2$). Lorsque cette condition est imposée, la méthode Hartree-Fock est dite restreinte (RHF [4] pour l'anglais *Restricted Hartree-Fock*).

Par souci de généralité, les équations seront écrites de préférence dans le formalisme spin non-restreint même si le formalisme spin restreint est celui trouvé habituellement dans les textes d'introduction à la chimie quantique.

2.1.2.3 Les fonctions de bases

L'approximation suivante exprime les orbitales moléculaires comme une combinaison linéaire de fonctions à un électron connues sous le nom de *fonctions de bases*. En principe, tous types de fonctions (exponentielles, gaussiennes, ondes planes,...) peuvent être utilisées. Ces fonctions sont généralement centrées sur le noyau et ont une certaine ressemblance avec les orbitales atomiques. Elles sont conventionnellement appelées *orbitales atomiques*, bien qu'elles ne soient pas solution du problème atomique. Cette décomposition porte le nom de LCAO pour l'anglais *Linear Combination of Atomic Orbitals*. Chaque orbitale moléculaire est définie par

$$\phi_i^\sigma(\mathbf{r}) = \sum_{\mu=1}^N \chi_\mu(\mathbf{r}) c_{\mu i}^\sigma \quad (2.25)$$

où $c_{\mu i}^\sigma$ sont les coefficients d'expansion des OM, χ_μ sont les fonctions de bases normalisées. Les indices romains sont utilisés pour les fonctions d'orbitales moléculaire et les indices grecs pour les fonctions de bases. Les fonctions gaussiennes (primitives) ont la forme

$$g(\alpha, \mathbf{r}) = cx^n y^m z^l e^{-\alpha r^2} \quad (2.26)$$

où α est une constante déterminant la taille (extension radiale) de la fonction. Dans une fonction gaussienne, $e^{-\alpha r^2}$ est multiplié par des puissances de x , y et z , ainsi que par une constante de normalisation c . Nous avons donc

$$\int g^2(\mathbf{r}) d\mathbf{r} = 1. \quad (2.27)$$

Voici quelques fonctions gaussiennes représentatives (s , p_y et d_{xy}) :

$$g_s(\alpha, \mathbf{r}) = \left(\frac{2\alpha}{\pi} \right)^{\frac{3}{4}} e^{-\alpha r^2} \quad (2.28)$$

$$g_y(\alpha, \mathbf{r}) = \left(\frac{128\alpha^5}{\pi^3} \right)^{\frac{1}{4}} y e^{-\alpha r^2} \quad (2.29)$$

$$g_{xy}(\alpha, \mathbf{r}) = \left(\frac{2048\alpha^7}{\pi^3} \right)^{\frac{1}{4}} xy e^{-\alpha r^2} \quad (2.30)$$

Des combinaisons linéaires de *primitives gaussiennes* comme les fonctions précédentes sont utilisées pour former les fonctions de bases. Les fonctions *gaussiennes*

contractées ont la forme suivante

$$\chi_\mu(\mathbf{r}) = \sum_p g_p(\mathbf{r}) d_{p\mu} \quad (2.31)$$

où les coefficients $d_{p\mu}$ sont constants dans une base donnée.

Nous pouvons donc écrire les orbitales moléculaires comme suit

$$\phi_i^\sigma(\mathbf{r}) = \sum_\mu \chi_\mu(\mathbf{r}) c_{\mu i}^\sigma = \sum_\mu \left(\sum_p g_p(\mathbf{r}) d_{p\mu} \right) c_{\mu i}^\sigma. \quad (2.32)$$

2.1.2.4 Le principe variationnel

Le problème est maintenant de résoudre l'équation de Schrödinger électronique pour l'ensemble des coefficients d'orbitale moléculaire $c_{\mu i}^\sigma$. La méthode Hartree-Fock utilise le principe variationnel permettant d'affirmer que pour l'état fondamental, la valeur de l'énergie associée à n'importe quelle fonction antisymétrique normalisée Ψ_{essai} , sera toujours supérieure à l'énergie associée à la fonction d'onde exacte Ψ_0

$$E(\Psi_{essai}) \geq E(\Psi_0). \quad (2.33)$$

Pour un système non dégénéré, l'égalité n'est obtenue que lorsque Ψ_{essai} est identique à Ψ_0 . L'énergie de la fonction d'onde exacte peut servir de borne limite inférieure à l'énergie calculée pour n'importe quelle autre fonction d'onde antisymétrique normalisée. Le problème est donc de trouver l'ensemble des coefficients $c_{\mu i}^\sigma$ minimisant l'énergie de la fonction d'onde d'essai.

2.1.2.5 Les équations de Roothaan-Hall

Le principe variationnel mène aux équations suivantes décrivant les coefficients d'orbitales moléculaires $c_{\mu i}^\sigma$ dérivés par Roothaan et Hall [4] :

$$\sum_{\nu=1}^N (F_{\mu\nu}^\sigma - \epsilon_i S_{\mu\nu}) c_{\nu i}^\sigma = 0 \quad \text{avec } \mu = 1, 2, \dots, N \quad (2.34)$$

où $F_{\mu\nu}^\sigma$ est défini par

$$F_{\mu\nu}^\sigma = \int \chi_\mu^*(\mathbf{r}_1) \hat{f}_\sigma(\mathbf{r}_1) \chi_\nu(\mathbf{r}_1) d\mathbf{r}_1 \quad (2.35)$$

avec \hat{f}_σ défini par

$$\hat{f}_\sigma = \hat{h} + \hat{V}_{eff}^\sigma = \hat{h} + \hat{J} - \hat{K}^\sigma. \quad (2.36)$$

Le terme \hat{V}_{eff} dans l'équation 2.36 représente le potentiel moyen dans lequel se déplace chaque électron. Il est constitué d'une somme d'opérateurs de Coulomb,

$$\hat{J}\phi_i^\sigma(\mathbf{r}_1) = \sum_{j\tau} n_{j\tau} \int \frac{|\phi_j^\tau(\mathbf{r}_2)|^2}{r_{12}} d\mathbf{r}_2 \phi_i^\sigma(\mathbf{r}_1) \quad (2.37)$$

$$= \int \frac{\rho(\mathbf{r}_2)}{r_{12}} d\mathbf{r}_2 \phi_i^\sigma(\mathbf{r}_1), \quad (2.38)$$

et d'échange,

$$\hat{K}^\tau \phi_i^\sigma(\mathbf{r}_1) = \sum_j n_{j\tau} \phi_j^\tau(\mathbf{r}_1) \int \frac{[\phi_j^\tau(\mathbf{r}_2)]^* \phi_i^\sigma(\mathbf{r}_2)}{r_{12}} d\mathbf{r}_2 \quad (2.39)$$

$$= \delta_{\sigma,\tau} \int \frac{\gamma_\tau(\mathbf{r}_1, \mathbf{r}_2) \phi_i^\sigma(\mathbf{r}_2)}{r_{12}} d\mathbf{r}_2. \quad (2.40)$$

Dans l'équation 2.37, la densité de charge est présente,

$$\rho_\tau(\mathbf{r}) = \sum_j h_{j\tau} \phi_j^\tau(\mathbf{r}), \quad (2.41)$$

$$\rho(\mathbf{r}) = \rho_\alpha(\mathbf{r}) + \rho_\beta(\mathbf{r}), \quad (2.42)$$

et les nombres d'occupation $n_{j\tau}$ sont égaux à 0 ou 1 si l'orbitale est respectivement occupée ou vacante. Dans l'équation 2.38, \hat{J} représente le potentiel lié à la distribution de charge moyenne des électrons. L'opérateur d'échange n'a pas d'interprétation physique mais peut-être écrit dans une forme semblable à celle de l'opérateur de Coulomb en utilisant la matrice de la densité,

$$\gamma_\sigma(\mathbf{r}, \mathbf{r}') = \sum_i n_{i\sigma} \psi_i^\sigma(\mathbf{r}) [\psi_i^\sigma(\mathbf{r}')]^*, \quad (2.43)$$

$$\gamma(\mathbf{r}, \mathbf{r}') = \gamma_\alpha(\mathbf{r}, \mathbf{r}') + \gamma_\beta(\mathbf{r}, \mathbf{r}'). \quad (2.44)$$

La densité est donnée par la diagonale de la matrice de la densité,

$$\rho_\sigma(\mathbf{r}) = \gamma_\sigma(\mathbf{r}, \mathbf{r}), \quad (2.45)$$

$$\rho(\mathbf{r}) = \gamma(\mathbf{r}, \mathbf{r}). \quad (2.46)$$

L'opérateur d'échange est présent car les particules élémentaires, comme les électrons, ne sont pas discernables. Cependant, une partie importante de l'opérateur d'échange est une correction de l'erreur d'auto-interaction présent dans le terme de Coulomb.

L'équation 2.34 peut s'écrire sous forme matricielle,

$$\underline{\underline{F}}^\sigma \underline{\underline{C}}^\sigma = \underline{\underline{S}} \underline{\underline{C}}^\sigma \underline{\underline{\epsilon}}^\sigma \quad (2.47)$$

où chaque élément est une matrice. $\underline{\underline{\epsilon}}^\sigma$ est la matrice diagonale des énergies orbitales de spin σ , chacun de ses éléments ϵ_i^σ est l'énergie orbitalaire d'un électron de l'orbitale moléculaire ϕ_i^σ . $\underline{\underline{F}}^\sigma$ est la *matrice de Fock* représentant l'effet moyen du champ créé par tous les électrons sur chaque orbitale. Pour un système à couche fermée, nous avons

$$F_{\mu\nu}^\sigma = H_{\mu\nu}^{\text{coeur}} + \sum_{\mu'\nu'} P_{\mu'\nu'}(\mu\nu|\mu'\nu') - \sum_{\mu'\nu'} P_{\mu'\nu'}^\sigma(\mu\nu'|\mu'\nu') , \quad (2.48)$$

où $H_{\mu\nu}^{\text{coeur}} = \langle \mu | \hat{h} | \nu \rangle$ est une autre matrice représentant l'énergie d'un électron dans le champ des noyaux et P est une autre représentation de la *matrice de la densité* définie par

$$P_{\mu\nu}^\sigma = \sum_i c_{\mu i}^\sigma n_{i\sigma} (c_{\mu i}^\sigma)^* , \quad (2.49)$$

$$P_{\mu\nu} = P_{\mu\nu}^\alpha + P_{\mu\nu}^\beta , \quad (2.50)$$

d'où

$$\gamma_\sigma(\mathbf{r}, \mathbf{r}') = \sum_{\mu\nu} \chi_\mu(\mathbf{r}) P_{\mu\nu}^\sigma \chi_\nu^*(\mathbf{r}') . \quad (2.51)$$

La matrice S est la *matrice de recouvrement* représentant le recouvrement entre chaque orbitale.

La matrice de Fock, la matrice de la densité et les orbitales dépendent des coefficients des orbitales moléculaires. L'équation 2.47 n'est donc pas linéaire et doit être résolue de manière itérative à l'aide de la procédure nommée champ auto-cohérent (SCF pour l'anglais *Self-Consistent Field*). Lorsque cette procédure converge, l'énergie est à son minimum et les orbitales génèrent un champ qui produit les mêmes orbitales d'où le nom de la méthode. Les solutions produisent un ensemble d'orbitales soit occupées, notées ψ_i, ψ_j, \dots , soit virtuelles, notées ψ_a, ψ_b, \dots . Le nombre total d'orbitales est égal au nombre de fonctions de bases utilisées.

La stratégie utilisée par la méthode SCF conventionnelle est la suivante :

1. Evaluation des intégrales
2. Construction de la fonction d'essai pour les coefficients d'orbitales moléculaire
3. Construction de la matrice de la densité
4. Construction de la matrice de Fock

5. Résolution des équations de Roothan-Hall pour déterminer les nouveaux coefficients d'orbitales moléculaires
6. Construction de la nouvelle matrice de la densité. Si elle est suffisamment proche de la matrice de la densité précédente, le calcul est convergé. Sinon, l'étape 4 et les suivantes doivent être recommencées.

Dans l'équation 2.48, le terme $(\mu\nu|\lambda\sigma)$ représente les intégrales bi-électroniques de répulsion électronique ERI (pour l'anglais *Electronic Repulsion Integral*) définies par

$$(\mu\nu|\lambda\sigma) = \iint \chi_\mu^*(\mathbf{r}_1)\chi_\nu(\mathbf{r}_1) \frac{1}{r_{12}} \chi_\lambda^*(\mathbf{r}_2)\chi_\sigma(\mathbf{r}_2) d\mathbf{r}_1 d\mathbf{r}_2 . \quad (2.52)$$

En raison de leur grand nombre, l'évaluation et la manipulation de ces intégrales sont les principaux problèmes des calculs HF. Il existe des techniques comme la résolution de l'identité afin d'éviter leur évaluation.

Dans la méthode Hartree-Fock (HF), les électrons sont considérés comme indépendants les uns des autres et se déplaçant chacun dans un potentiel moyen créé par l'ensemble des noyaux et des autres électrons. Il n'y a donc pas d'interaction instantanée électron-électron. D'autres méthodes, appelées méthode post-Hartree-Fock, tentent de remédier à ce problème de manque de corrélation.

2.1.2.6 La corrélation électronique

Une fonction d'onde représentée par un seul déterminant de Slater ne sera jamais égale à la fonction d'onde exacte. Ceci signifie que E_{HF} doit nécessairement être plus grande que l'énergie exacte de l'état fondamental. La différence entre ces deux énergies est appellée l'énergie de corrélation définie par

$$E_{corr} = E_0 - E_{HF} < 0 . \quad (2.53)$$

E_{corr} est une mesure de l'erreur introduite par l'approximation HF et elle est principalement liée à la répulsion pratiquement instantanée des électrons non inclue dans le potentiel effectif HF, \hat{V}_{eff} . Dans ce schéma et de manière imagée, les électrons se retrouvent trop souvent proches les uns des autres car l'interaction électrostatique n'est traitée que par des termes moyennés. Le terme de répulsion inter-électronique est donc trop grand et l'énergie E_{HF} est plus grande que l'énergie exacte E_0 . Cette partie de l'énergie de corrélation est reliée au terme $1/r_{12}$ contrôlant la répulsion inter-électronique dans l'Hamiltonien. Cette quantité est d'autant plus grande que la distance r_{12} entre les électrons 1 et 2 est petite. Le terme de *corrélation dynamique* est alors employé car il est lié aux mouvements des électrons. Par opposition,

le terme de *corrélation statique (ou non-dynamique)* est relié à l'existence de déterminants de Slater, dégénérés (ou presque) en énergie. Dans ce cas, l'approximation mono-déterminantale n'est pas appropriée pour la description de la fonction d'onde. Cela se produit lors de la séparation dans l'espace d'une paire d'électrons intervenant au cours d'un processus dissociatif entre deux atomes. Un exemple typique est la dissociation de l'hydrogène moléculaire, H_2 .

2.1.3 Les méthodes Post-Hartree-Fock

Il existe un grand nombre de solutions nommées solutions *post-Hartree-Fock* permettant de remédier au problème de non-prise en compte de l'énergie de corrélation dans le cadre de l'approximation HF. Elles se partagent essentiellement en deux catégories : les méthodes perturbatives et les méthodes multi-configurationnelles. La solution la plus économique est la théorie perturbative de Møller-Plesset au second ordre (MP2). Celles d'ordres supérieurs (MP3, MP4,...) sont aussi utilisées mais elles requièrent beaucoup plus de ressources informatiques. Le coût informatique de la méthode MP2 augmente formellement avec la cinquième puissance de la taille du système alors que celui de la méthode MP4 augmente avec la septième. Ceci est à comparer avec la quatrième puissance pour la méthode HF. De plus, il n'est pas possible d'affirmer que les résultats sont améliorés avec l'augmentation de l'ordre de la perturbation. Parmi les méthodes multi-configurationnelles, nous ne citerons que les méthodes d'interaction de configurations (CI pour l'anglais *Configuration Interaction*) et MCSCF (pour l'anglais *Multi-Configuration Self-Consistent Field*).

2.1.3.1 La théorie des perturbations à plusieurs corps

Les méthodes des perturbations sont utilisées lorsque le problème à résoudre est (exactement ou approximativement) le même qu'un problème déjà résolu. La solution du nouveau problème doit donc être assez proche de la solution du problème déjà résolu. Ce processus est décrit mathématiquement par un Hamiltonien en deux parties : un Hamiltonien de référence \hat{H}_0 et une perturbation $\lambda\hat{V}$. Pour appliquer cette méthode, la perturbation $\lambda\hat{V}$ doit être petite devant \hat{H}_0 . En mécanique quantique, les méthodes perturbatives peuvent être utilisées pour ajouter des corrections à des solutions utilisant l'approximation des particules indépendantes. Le cadre théorique est alors appelé théorie des perturbations à plusieurs corps (MBPT pour l'anglais *Many-Body Perturbation Theory*).

Nous avons donc

$$\hat{H} = \hat{H}_0 + \lambda\hat{V} \quad (2.54)$$

et

$$H_0 \Psi_I^0 = E_I^0 \Psi_I^0 \text{ avec } I = 0, 1, 2, \dots, \infty \quad (2.55)$$

sont les solutions, choisies orthonormales ou non, de l'opérateur Hamiltonien non perturbé pour une base complète. λ est un paramètre déterminant la taille de la perturbation. L'équation de Schrödinger perturbée est

$$\hat{H} \Psi_i = E_i \Psi_i . \quad (2.56)$$

Si $\lambda = 0$, nous avons $\hat{H} = \hat{H}_0$, $\Psi_i = \Psi_i^0$ et $E_i = E_i^0$. Quand la perturbation augmente de zéro jusqu'à une valeur finie, la nouvelle énergie et la nouvelle fonction d'onde doivent changer continûment. Celles-ci peuvent être écrites comme des développements en série de Taylor en puissance du paramètre de perturbation λ ,

$$E_i = \lambda^0 E_i^{(0)} + \lambda^1 E_i^{(1)} + \lambda^2 E_i^{(2)} + \lambda^3 E_i^{(3)} + \dots \quad (2.57)$$

$$\Psi_i = \lambda^0 \Psi_i^{(0)} + \lambda^1 \Psi_i^{(1)} + \lambda^2 \Psi_i^{(2)} + \lambda^3 \Psi_i^{(3)} + \dots \quad (2.58)$$

Pour simplifier les dérivations de ces équations, la condition de normalisation intermédiaire est introduite

$$\langle \Psi_i^{(0)} | \Psi_i \rangle = 1 . \quad (2.59)$$

En reportant les expressions 2.58 dans l'équation 2.56 et en les développant, nous obtenons une série de relations représentant successivement des ordres de perturbations plus élevés :

$$\lambda^0 : (\hat{H}_0 - E_i^{(0)}) \Psi_i^{(0)} = 0 \quad (2.60)$$

$$\lambda^1 : (\hat{H}_0 - E_i^{(0)}) \Psi_i^{(1)} = (E_i^{(1)} - \hat{V}) \Psi_i^{(0)}$$

$$\lambda^2 : (\hat{H}_0 - E_i^{(0)}) \Psi_i^{(2)} = (E_i^{(1)} - \hat{V}) \Psi_i^{(1)} + E^2 \Psi_i^{(0)} .$$

La théorie des perturbations Møller-Plesset. Jusqu'ici, seule la théorie générale des perturbations a été présentée. Dans le cas particulier de la méthode Møller-Plesset, \hat{H}_0 est défini comme la somme des opérateurs de Fock mono-électroniques :

$$\hat{H}_0 = \sum_i^n \hat{f}(i) . \quad (2.61)$$

Les différentes corrections de l'énergie sont obtenues à partir du système d'équations 2.60. A partir de la première équation, la correction à l'ordre zéro est obtenue :

$$E_i^{(0)} = \frac{\langle \Psi_i^{(0)} | \hat{H}_0 | \Psi_i^{(0)} \rangle}{\langle \Psi_i^{(0)} | \Psi_i^{(0)} \rangle} . \quad (2.62)$$

Etant donnée la définition de H_0 , l'énergie corrigée à l'ordre zéro correspond à la somme des énergies orbitalaires :

$$E_i^{(0)} = \sum_{i\sigma} n_{i\sigma} \epsilon_i^\sigma . \quad (2.63)$$

A partir de la deuxième équation du système 2.60, la correction à l'ordre un est obtenue :

$$E_i^{(1)} = \frac{\langle \Psi_i^{(0)} | \hat{V} | \Psi_i^{(0)} \rangle}{\langle \Psi_i^{(0)} | \Psi_i^{(0)} \rangle} . \quad (2.64)$$

L'énergie totale obtenue au premier ordre est la somme $E_i^{(0)} + E_i^{(1)}$ correspondant à l'énergie Hartree-Fock E^{HF} .

La correction au deuxième ordre est obtenue à partir de la troisième équation du système 2.60 :

$$E_i^{(2)} = \sum_{j \neq i} \frac{|\langle \Psi_i^{(0)} | \hat{V} | \Psi_j^{(0)} \rangle|^2}{E_i^{(0)} - E_j^{(0)}} \quad (2.65)$$

L'énergie totale corrigée à l'ordre deux est donc la somme $E_i^{(2)} + E^{HF}$. Elle est donnée par

$$\begin{aligned} E^{(2)} &= \sum_{i\sigma} n_i^\sigma h_{ii} + \frac{1}{2} \sum_{i\sigma j\tau} n_i^\sigma (ii|jj) n_j^\tau - \frac{1}{2} \sum_{ij\sigma} n_i^\sigma (ij|ji) n_j^\sigma \\ &+ \sum_{i\sigma} n_i^\sigma n_j^\tau (1 - n_a^\mu) (1 - n_b^\nu) \frac{(ia|jb)(ai|bj)\delta_{\mu\sigma}\delta_{\tau\nu} - (ia|jb)(aj|bi)\delta_{\mu\sigma}\delta_{\tau\nu}}{\epsilon_i^\sigma + \epsilon_j^\tau - \epsilon_a^\mu - \epsilon_b^\nu} \end{aligned} \quad (2.66)$$

Les indices i et j concernent les orbitales occupées et les indices a et b correspondent aux orbitales virtuelles dans Ψ_{HF} . Suivant la définition de $E_i^{(2)}$, l'énergie totale ainsi calculée sera toujours inférieure à l'énergie HF.

La méthode s'arrêtant au deuxième ordre est notée MP2 mais il est possible de prendre en compte des corrections perturbatives d'ordre supérieur aboutissant au formalisme Møller-Plesset d'ordre 3, 4, 5, ... (MP3, MP4, MP5, ...). Ces méthodes MP n prennent uniquement en compte la corrélation dynamique. Une description multi-configurationnelle est nécessaire afin d'inclure la corrélation statique.

2.1.3.2 Les méthodes multi-configurationnelles

La méthode HF détermine la meilleure fonction d'onde mono-déterminantale (pour une base donnée). Afin d'améliorer le résultat HF, une fonction d'onde contenant plusieurs déterminants de Slater est utilisée. Comme la solution HF donne souvent $\sim 99\%$ de la bonne réponse pour les molécules à couche fermée dans leur géométrie d'équilibre, les méthodes multi-configurationnelles utilisent la fonction d'onde HF comme point de départ. La forme générale de la fonction d'onde multi-déterminantale peut-être écrite comme suit

$$\Psi = a_0 \Psi_{HF} + \sum_{I \neq 0} a_I \Psi_I \quad (2.67)$$

avec a_0 généralement proche de 1. Les méthodes multiconfigurationnelles diffèrent dans la manière de calculer les coefficients en face des autres déterminants, a_0 étant déterminé par les conditions de normalisation.

2.1.3.3 Interaction de Configuration

La méthode d'Interaction de Configuration (CI pour l'anglais *Configuration Interaction*) est certainement la plus facile à comprendre. Elle est basée sur le principe variationnel. La fonction d'onde d'essai est écrite comme une combinaison linéaire de déterminants dont les coefficients sont obtenus en minimisant l'énergie.

$$\Psi_{CI} = a_0 \Psi_{HF} + \sum_{ia} a_i^a \Psi_i^a + \sum_{ijab} a_{ij}^{ab} \Psi_{ij}^{ab} + \dots \quad (2.68)$$

$$= a_0 \Psi_{HF} + \sum_S a_S \Psi_S + \sum_D a_D \Psi_D + \dots \quad (2.69)$$

où Ψ_{HF} est le déterminant HF, Ψ_i^a et Ψ_{ij}^{ab} sont respectivement les déterminants excités simples et doubles. Les électrons des orbitales occupées i et j sont excités dans les orbitales non occupées a et b . Ce type de calcul est appelé *full CI* et, dans la limite d'une base complète, *complete CI*. Les OM utilisées pour construire les déterminants de Slater excités proviennent d'un calcul HF et sont gardées fixes. Le principal problème de ces calculs est l'augmentation factorielle du nombre de déterminants avec la taille de la base. Dans le cas de la molécule d'eau, nous obtenons $\sim 30 \times 10^6$ déterminants avec une base 6-31G(d) et $\sim 106 \times 10^9$ avec la base 6-311G(2d,2p). Ce type de calcul est donc limité à de petites molécules et à des calculs de références.

Un moyen de réduire la taille de ce calcul est de tronquer les excitations en ne prenant en compte que les Doubles, ou les excitations Simples et Doubles condui-

sant respectivement à des calculs CID (*Configuration Interaction Doubles*) et CISD (*Configuration Interaction Singles and Doubles*). La description du système peut-être améliorée en incluant les excitations triples, quadruples, ... menant ainsi aux calculs CISDT, CISDTQ, L'inclusion de ces dernières excitations augmente considérablement le coût du calcul. Le calcul CISD augmente formellement en N^6 alors que CISDT en N^8 et CISDTQ en N^{10} . Ces 2 derniers calculs ne seront donc appliquer qu'à de petites molécules. Si la troncation est utilisée, la méthode n'est plus *size consistent* (cf. annexe 3).

2.1.3.4 Complete Active Space Self-Consistent Field

La méthode *Multi-Configuration Self-Consistent Field* (MCSCF) peut-être considérée comme une interaction de configuration dans laquelle les coefficients en face des déterminants, mais aussi les OM, sont optimisés par le principe variationnel. L'application de ces méthodes est possible seulement si le nombre de déterminants utilisés est restreint. Le choix des déterminants à prendre en compte doit être réfléchi et repose sur une bonne connaissance de la structure électronique du système étudié.

La méthode MCSCF la plus utilisée est la méthode *Complete Active Space Self-Consistent Field* (CASSCF) notée plus généralement CASSCF[n,m] où n électrons sont distribués de toutes les manières possibles parmi m orbitales. La sélection des configurations est effectuée en partitionnant les OM, issues d'un calcul HF, en orbitales *actives* et *inactives*. Les orbitales actives seront généralement les plus hautes occupées (HOMO pour l'anglais *Highest Occupied Molecular Orbital*) et les plus basses vacantes (LUMO pour l'anglais *Lowest Unoccupied Molecular Orbital*). Les orbitales inactives ont soit 2 électrons, soit 0, elles sont donc toujours doublement occupées ou vides. Un *full CI* est réalisé dans toutes les orbitales actives. En fonction du problème et du coût informatique, le choix des OM devant être incluses dans l'espace actif doit être fait *à la main*.

L'expansion factorielle *full CI*, dans l'espace actif, restreint le nombre d'orbitales et d'électrons qui peuvent être traités par la méthode CASSCF à 12-14 électrons/orbitales. Bien sélectionner les orbitales "importantes" à corréler devient alors primordial.

La méthode CASSCF va au-delà de la méthode de champ moyen HF en tenant compte des interactions exactes entre un nombre restreint d'électrons (les électrons actifs) soumis au champ moyen créé par tous les autres électrons.

2.1.3.5 Calcul perturbationel des effets dynamiques : CASPT2

La méthode *2ndorder CAS* (CASPT2) [5, 6] est une méthode perturbative de deuxième ordre multiconfigurationnelle. Elle permet de récupérer la partie de la corrélation dynamique liée aux mono et di-exitations sur le CAS.

Cette méthode est contractée, le rapport entre les coefficients des déterminants composant la fonction d'onde d'ordre zéro de type CAS n'est pas modifié par la perturbation. Pour inclure les effets dynamiques, des configurations dont le coefficient est déterminé perturbativement à l'ordre deux sont additionnées à la fonction d'onde d'ordre zéro,

$$|\Psi_{\text{CASPT2}}\rangle = \frac{1}{N} \left(|\Psi_{\text{CAS}}\rangle + \sum_{I \in SD} c_I |\Phi_I\rangle \right), \quad (2.70)$$

où $|\Psi_{\text{CASPT2}}\rangle$ est la fonction d'onde issue du calcul CASPT2, $|\Psi_{\text{CAS}}\rangle$ la fonction d'onde d'ordre zéro issue d'un calcul CASSCF, Φ_I est un déterminant mono ou diexcité par rapport aux déterminants du CAS, c_I son coefficient évalué perturbativement, I parcourt toutes les mono et di-exitations. N assure la normalisation de $|\Psi_{\text{CASPT2}}\rangle$.

L'importance fondamentale du choix de l'espace actif est ainsi mis en évidence. Il doit contenir les principaux effets physiques présents dans le système étudié. Mais les effets dynamiques ne doivent pas modifier profondément les rapports entre les coefficients des différentes configurations composant les états calculés.

2.2 La théorie de la fonctionnelle de la densité

En théorie, tel que cela a été vu précédemment, il est possible de déterminer toutes les propriétés électroniques d'un système en résolvant l'équation de Schrödinger. En pratique, les moyens informatiques (mémoire, temps de calcul, ...) imposent une limite et seuls des systèmes contenant un petit nombre d'électrons peuvent être traités par le biais des méthodes *ab initio* basées sur la fonction d'onde. Ne serait-il pas possible de remplacer la fonction d'onde, *gros objet mathématique*, par quelque chose de beaucoup plus simple : la densité électronique ?

2.2.1 Les théorèmes de Hohenberg-Kohn

Les théorèmes d'Hohenberg-Kohn¹ [7] impliquent l'existence d'une fonctionnelle² de la densité électronique F_{HK} permettant de calculer l'énergie de l'état fondamental d'un système à N électrons. Cette fonctionnelle, pourtant connue (dans sa forme

Levy-Lieb), n'est pas utilisable sous cette forme. Différentes approches sont utilisées afin de l'approximer. La méthode la plus usitée est sans doute celle de Kohn-Sham [8] dans laquelle seule la contribution dominante de certaines composantes de F_{HK} sont calculées exactement.

2.2.1.1 Le premier théorème de Hohenberg-Kohn

Ce théorème montre que la densité électronique $\rho(\mathbf{r})$ est la seule fonction nécessaire pour obtenir toutes les propriétés électroniques d'un système quelconque. Dans les méthodes *ab initio*, la fonction d'onde Ψ tenait le même rôle. Citons ce théorème [7] :

“The external potential $V_{ext}(\mathbf{r})$ is (to within a constant) a unique functional of $\rho(\mathbf{r})$; since in turn $V_{ext}(\mathbf{r})$ fixes the Hamiltonian H we see that the full many particle ground state is a unique functional of $\rho(\mathbf{r})$.”

Sa démonstration est très simple et repose sur une démonstration par l'absurde. Supposons que deux potentiels $V_{ext}(\mathbf{r})$ et $V'_{ext}(\mathbf{r})$, qui diffèrent par plus d'une constante, correspondent à la même densité électronique $\rho_0(\mathbf{r})$. A ces deux potentiels sont associés deux Hamiltoniens \hat{H} et \hat{H}' tels que

$$\hat{H} = \hat{T} + \hat{V}_{ee} + \hat{V}_{ext} \neq \hat{T} + \hat{V}_{ee} + \hat{V}'_{ext} = \hat{H}' \quad (2.71)$$

où \hat{T} est l'énergie cinétique et \hat{V}_{ee} est le terme de répulsion électron-électron. \hat{H} et \hat{H}' sont associés à deux états fondamentaux, Ψ_0 et Ψ'_0 avec des énergies E_0 et E'_0 . Cependant, ces deux états possèdent la même densité électronique $\rho_0(\mathbf{r})$ (par hypothèse). Le principe variationnel peut-être appliqué en utilisant Ψ'_0 comme fonction d'onde d'essai pour \hat{H} ,

$$E_0 = \langle \Psi_0 | \hat{H} | \Psi_0 \rangle < \langle \Psi'_0 | \hat{H} | \Psi'_0 \rangle . \quad (2.72)$$

Puisque \hat{H} et \hat{H}' diffèrent seulement par leur potentiel externe, il est possible d'écrire

$$E_0 < \langle \Psi'_0 | \hat{H}' | \Psi'_0 \rangle + \langle \Psi'_0 | \hat{H} - \hat{H}' | \Psi'_0 \rangle \quad (2.73)$$

correspondant à

$$E_0 < E'_0 + \int \rho_0(\mathbf{r})(V_{ext}(\mathbf{r}) - V'_{ext}(\mathbf{r})) d\mathbf{r} . \quad (2.74)$$

¹Une version valable pour un système non dégénéré est présenté ici. Pour un système dégénéré, se référer au livre de Dreizler et Gross [9]

²La définition d'une fonctionnelle est donnée en annexe 4.

Maintenant, si Ψ_0 est utilisée comme fonction d'onde d'essai pour \hat{H}' nous obtenons

$$E'_0 < E_0 + \int \rho_0(\mathbf{r})(V'_{ext}(\mathbf{r}) - V_{ext}(\mathbf{r})) d\mathbf{r}. \quad (2.75)$$

En additionnant 2.74 et 2.75, nous obtenons la contradiction suivante

$$E_0 + E'_0 < E'_0 + E_0 \quad (2.76)$$

prouvant la validité du premier théorème d'Hohenberg-Kohn. Le potentiel externe V_{ext} est déterminé par la densité électronique $\rho_0(\mathbf{r})$ (à une constante additive près). De plus, puisque V_{ext} définit l'Hamiltonien, les propriétés de l'état fondamental sont complètement déterminées par sa densité.

En d'autres mots, l'énergie de l'état fondamental E_0 est une fonctionnelle de la densité électronique de l'état fondamental $\rho_0(\mathbf{r})$. Elle s'exprime par

$$E_0[\rho_0] = T[\rho_0] + E_{ee}[\rho_0] + E_{ext}[\rho_0] \quad (2.77)$$

où $T[\rho_0]$ est la fonctionnelle d'énergie cinétique, $E_{ee}[\rho_0]$ est la fonctionnelle d'énergie d'interaction électron-électron. $E_{ext}[\rho_0]$ est la fonctionnelle d'énergie potentielle externe qui, en cas d'absence de perturbation externe, est réduite à l'énergie d'attraction Coulombienne noyau-électron

$$E_{Ne}[\rho_0] = \int V_{Ne}(\mathbf{r})\rho_0(\mathbf{r}) d\mathbf{r} \quad (2.78)$$

où $V_{Ne}(\mathbf{r})$ est définie par l'équation 2.7. $T[\rho_0]$ et $E_{ee}[\rho_0]$ définissent une fonctionnelle connue sous le nom de la "fonctionnelle d'Hohenberg et Kohn" $F_{HK}[\rho_0]$ définie par

$$F_{HK}[\rho_0] = T[\rho_0] + E_{ee}[\rho_0] \quad (2.79)$$

valable pour n'importe quel nombre d'électrons et dans n'importe quel potentiel externe. Une forme explicite de $T[\rho_0]$ et $E_{ee}[\rho_0]$ n'est pas connue dans une forme applicable. Cependant, en isolant la composante classique de la répulsion Coulombienne électron-électron du terme $E_{ee}[\rho_0]$, il est possible de réécrire l'équation 2.79 comme

$$F_{HK}[\rho_0] = T[\rho_0] + \iint \frac{\rho_0(\mathbf{r}_1)\rho_0(\mathbf{r}_2)}{r_{12}} d\mathbf{r}_1 d\mathbf{r}_2 + E_{non-cl}[\rho_0]. \quad (2.80)$$

$E_{non-cl}[\rho_0]$ contient toutes les contributions non-classiques de l'interaction électron-électron comme la correction de *self-interaction*, l'échange et la corrélation.

La fonctionnelle d'Hohenberg et Kohn joue un rôle très important en DFT. En effet, si une forme explicite de $T[\rho_0]$ et $E_{non-cl}[\rho_0]$ était connue, l'énergie de l'état fondamental de n'importe quel système serait déterminée en insérant la densité électronique fondamentale $\rho_0(r)$ dans la fonctionnelle d'énergie

$$E[\rho_0] = \int V_{Ne}(\mathbf{r})\rho_0(\mathbf{r}) d\mathbf{r} + F_{HK}[\rho_0]. \quad (2.81)$$

Nous savons que la densité électronique de l'état fondamental est suffisante pour obtenir toutes les propriétés de cet état mais comment savoir si une densité quelconque est celle de l'état fondamental ? Ceci est l'objet du deuxième théorème de Hohenberg et Kohn.

2.2.1.2 Le deuxième théorème de Hohenberg-Kohn

Ce théorème montre que la fonctionnelle d'énergie $E[\rho]$ est minimum quand une densité électronique quelconque $\rho(\mathbf{r})$ correspond à la densité électronique de l'état fondamental $\rho_0(\mathbf{r})$. La démonstration repose sur le principe variationnel. Dans le premier théorème, à une densité électronique $\rho'(\mathbf{r})$ correspond un potentiel externe $V'_{ext}(\mathbf{r})$ et donc

$$\rho'(\mathbf{r}) \Rightarrow V'_{ext}(\mathbf{r}) \Rightarrow \hat{H}' \Rightarrow \Psi'. \quad (2.82)$$

Ψ' peut être utilisé comme fonction d'onde d'essai pour l'Hamiltonien \hat{H} généré par le vrai potentiel externe $V_{ext}(\mathbf{r})$,

$$\langle \Psi' | \hat{H} | \Psi' \rangle = T[\rho'] + V_{ee}[\rho'] + \int \rho'(\mathbf{r}) V_{ext}(\mathbf{r}) d\mathbf{r} = E[\rho']. \quad (2.83)$$

$E[\rho']$ représente une borne supérieure de l'énergie exacte de l'état fondamental,

$$E[\rho'] \geq E_0[\rho_0] = \langle \Psi_0 | \hat{H} | \Psi_0 \rangle \quad (2.84)$$

ce qui démontre le théorème.

Le premier théorème de Hohenberg et Kohn prouve l'existence d'une correspondance bi-univoque entre la densité électronique de l'état fondamental $\rho_0(\mathbf{r})$ et le potentiel externe $V_{ext}(\mathbf{r})$ et donc entre $\rho_0(\mathbf{r})$ et la fonction d'onde de l'état fondamental Ψ_0 . Le second théorème démontre que l'énergie de l'état fondamental E_0 est une fonctionnelle de la densité électronique $\rho(\mathbf{r})$ et qu'elle atteint une valeur minimale quand $\rho(\mathbf{r}) = \rho_0(\mathbf{r})$. $\rho_0(\mathbf{r})$ peut donc être obtenue par un schéma variationnel.

La densité de l'état fondamental peut être facilement déterminée à partir de la fonction d'onde de l'état fondamental (cf. 2.15) mais la réciproque n'est pas vraie.

En fait, pour la même densité électronique, une infinité de fonctions d'ondes différentes peuvent être obtenues. La méthode pour chercher la fonction d'onde de l'état fondamental parmi toutes celles possibles est la recherche avec contrainte de Lévy.

2.2.1.3 La recherche avec contrainte de Levy

L'adaptation du principe variationnel,

$$E_0 = \min_{\Psi \rightarrow N} \langle \Psi | \hat{T} + \hat{V}_{ee} + \hat{V}_{Ne} | \Psi \rangle \quad (2.85)$$

à la DFT, a été faite par Levy, Lieb et Perdew [10, 11, 12, 13]. Cette recherche s'effectue en deux étapes. Dans un premier temps, la densité électronique $\check{\rho}(\mathbf{r})$ est choisie et une recherche du minimum d'énergie est réalisée sur toutes les fonctions d'ondes $\check{\Psi}$ donnant $\check{\rho}(\mathbf{r})$ par minimisation

$$\check{E}_{min}[\check{\rho}] = \min_{\check{\Psi} \rightarrow \check{\rho}} \langle \check{\Psi} | \hat{T} + \hat{V}_{ee} + \hat{V}_{Ne} | \check{\Psi} \rangle. \quad (2.86)$$

Dans un deuxième temps, la recherche est étendue à toutes les densités électroniques $\rho_0(r)$ s'intégrant au nombre d'électrons du système, *i.e.* à toutes les densités électronique N-représentables¹

$$E_0 = \min_{\rho \rightarrow N} \left[\min_{\Psi \rightarrow \rho} \langle \Psi | \hat{T} + \hat{V}_{ee} + \hat{V}_{Ne} | \Psi \rangle \right]. \quad (2.87)$$

Puisque le potentiel externe est défini par la densité électronique, il peut être exclu de la première étape de la recherche,

$$E_0 = \min_{\rho \rightarrow N} \left[\min_{\Psi \rightarrow \rho} \langle \Psi | \hat{T} + \hat{V}_{ee} | \Psi \rangle + \int \rho(\mathbf{r}) V_{Ne}(\mathbf{r}) d\mathbf{r} \right]. \quad (2.88)$$

Par analogie avec l'équation 2.79, nous pouvons définir une fonctionnelle universelle du type

$$F[\rho] = \min_{\Psi \rightarrow \rho} \langle \Psi | \hat{T} + \hat{V}_{ee} | \Psi \rangle \quad (2.89)$$

correspondant à la fonctionnelle de Hohenberg et Kohn seulement lorsque la densité électronique ρ correspond à la densité électronique ρ_0 . En terme de fonctionnelle universelle $F[\rho]$, l'équation 2.88 devient

$$E_0 = \min_{\rho \rightarrow N} \left[F[\rho] + \int \rho(\mathbf{r}) V_{Ne}(\mathbf{r}) d\mathbf{r} \right] \quad (2.90)$$

¹Harriman [14] a montré que toute densité non-négative et s'intégrant à N est N-représentable.

qui est l'équivalent du principe variationnel.

2.2.1.4 L'approche Kohn-Sham

Kohn et Sham [8] ont proposé une approche indirecte permettant de calculer exactement une grande partie de la fonctionnelle d'énergie cinétique $T[\rho]$. Leur stratégie est basée sur l'idée qu'un système à N électrons peut-être décrit par une équation exacte pour un système de N électrons non-interagissants. Cette équation à un-électron est connue sous le nom d'équation de "Kohn-Sham" (KS),

$$\left[-\frac{1}{2} \nabla^2 + V_{eff}(\sigma) \right] \psi_i(\mathbf{r}, \sigma) = \epsilon_i \psi_i(\mathbf{r}, \sigma) \quad (2.91)$$

où les ψ_i sont les plus bas états propres, avec les valeurs propres ϵ_i correspondantes. Ils forment la fonction d'onde de l'état fondamental $|\Psi\rangle = (N!)^{-1/2} |\psi_1 \psi_2 \dots \psi_N\rangle$ et sont appelés les orbitales KS. Ces orbitales sont déterminées à la condition que la fonction d'onde correspondante Ψ donne, par minimisation, la densité exacte de l'état fondamental d'un système à N particules en interaction

$$\rho_0(\mathbf{r}) = \sum_i^N \sum_{\sigma} |\psi_i(\mathbf{r}, \sigma)|^2. \quad (2.92)$$

Pour parvenir à cet objectif, le potentiel à un-électron V_{eff} est construit par

$$V_{eff}(\sigma) = V_{ext}(\mathbf{r}) + \int \frac{\rho(\mathbf{r}_2)}{r_{12}} d\mathbf{r} + V_{xc}(\sigma) \quad (2.93)$$

où le potentiel externe V_{ext} contient l'attraction noyau-électron et les interactions avec les autres champs externes. La grande innovation de l'approche KS est l'introduction du terme V_{xc} appelé le potentiel d'échange-corrélation défini par

$$V_{xc}(\sigma) = \frac{\partial(T[\rho] - T_S[\rho])}{\partial \rho(\sigma)} + \frac{\partial(E_{ee}[\rho] - J[\rho])}{\partial \rho(\sigma)} = \frac{\partial T_C[\rho]}{\partial \rho(\sigma)} + \frac{\partial E_{non-cl}[\rho]}{\partial \rho(\sigma)}. \quad (2.94)$$

V_{xc} contient la contribution à la corrélation de l'énergie cinétique $T_C[\rho]$ qui provient du traitement du système interagissant dans le système non-interagissant. De plus, V_{xc} contient aussi la partie non-classique de l'énergie d'interaction électron-électron dans le terme $E_{non-cl}[\rho]$.

L'avantage de l'approche KS réside dans la séparation de l'énergie cinétique en

deux parties. La contribution la plus importante est

$$T_S[\rho] = \sum_i^N \langle \psi_i | -\frac{1}{2} \nabla_i^2 | \psi_i \rangle \quad (2.95)$$

qui est exacte pour un système à N électrons non-interagissant. L'expression exacte de la contribution de l'énergie cinétique à E_{xc} , $T_C[\rho]$, est inconnue. Cependant, $T_C[\rho]$ ne représente qu'une petite fraction de l'énergie cinétique totale [15, 16].

Les équations 2.91, 2.93 et 2.94 indiquent que la méthode KS est formellement exacte puisque aucune approximation n'a été faite. Donc, si une expression exacte de $V_{xc}[\rho]$ était connue, l'approche KS donnerait la densité exacte et l'énergie exacte.

2.2.2 Les différentes classes de fonctionnelles

Le problème de la méthode KS est qu'une forme exacte et utilisable de la fonctionnelle d'échange-corrélation $E_{xc}[\rho]$ n'est toujours pas connue à ce jour. De plus, aucune méthode permettant une amélioration systématique des approximations proposées pour $E_{xc}[\rho]$ n'est connue.

Généralement, la recherche de la meilleure fonctionnelle est sujette à deux contraintes principales. D'une part, elle doit donner des résultats en accord avec l'expérience. Pour ce faire, Pople *et al.* ont développé une procédure de validation nommée test "Gaussian- n " ($n=1, 2$ ou 3) [17, 18, 19, 20]. D'autre part, elle doit être en accord avec les caractéristiques physiques et mathématiques du trou d'échange-corrélation $h_{xc}(\mathbf{r}_1, \mathbf{r}_2)$.

2.2.2.1 Le trou d'échange-corrélation

La densité de paire $\rho_2(\mathbf{r}_1, \mathbf{r}_2)$ représente la probabilité de trouver deux électrons avec des spins σ_1 et σ_2 quelconque dans les deux éléments de volume $d\mathbf{r}_1$ et $d\mathbf{r}_2$,

$$\rho_2(\mathbf{r}_1, \mathbf{r}_2) = \frac{N(N-1)}{2} \int \dots \int |\Psi(\boldsymbol{\tau}_1, \boldsymbol{\tau}_2, \dots, \boldsymbol{\tau}_N)|^2 d\sigma_1 d\sigma_2 d\boldsymbol{\tau}_3 d\boldsymbol{\tau}_4 \dots d\boldsymbol{\tau}_N . \quad (2.96)$$

Pour des fermions chargés, comme les électrons, la probabilité de trouver un des deux électrons est grandement dépendante de la position de l'autre. Leurs mouvements sont donc corrélés. La nature des fermions empêche deux électrons de même spin de s'approcher. Les électrons étant des particules chargées, ils se repoussent à cause de la répulsion Coulombienne. Le premier type d'interaction est connu sous le nom de corrélation d'échange ou de Fermi et le deuxième, sous le nom de corrélation de Coulomb. L'effet de ces deux types de corrélation peut s'exprimer à l'aide de la

densité de paire par

$$\rho_2(\mathbf{r}_1, \mathbf{r}_2) = \frac{1}{2}\rho(\mathbf{r}_1)\rho(\mathbf{r}_2)[1 + f(\mathbf{r}_1, \mathbf{r}_2)] \quad (2.97)$$

où $f(\mathbf{r}_1, \mathbf{r}_2)$ est la fonction de corrélation de paire tenant compte de la corrélation de Fermi et de Coulomb dans l'interaction entre deux électrons. Quand $f(\mathbf{r}_1, \mathbf{r}_2)$ est égal à 0, l'équation 2.97 représente le mouvement non-corréle de deux électrons.

La fonction de corrélation de paire $f(\mathbf{r}_1, \mathbf{r}_2)$ satisfait à la relation fondamentale

$$\int \rho(\mathbf{r}_2)f(\mathbf{r}_1, \mathbf{r}_2) d\mathbf{r}_2 = -1 \quad (2.98)$$

nommée *règle de somme*. L'interprétation de cette règle devient plus claire avec

$$h_{xc}(\mathbf{r}_1, \mathbf{r}_2) = \rho(\mathbf{r}_2)f(\mathbf{r}_1, \mathbf{r}_2) \quad (2.99)$$

représentant le *trou d'échange-corrélation*. Le terme *trou* représente la diminution de la densité électronique en \mathbf{r}_2 liée aux interactions électron-électron non-classiques. Lorsque nous exprimons l'équation 2.98 en terme de trou d'échange-corrélation,

$$\int h_{xc}(\mathbf{r}_1, \mathbf{r}_2) d\mathbf{r}_2 = -1 \quad (2.100)$$

nous comprenons que le trou d'échange-corrélation s'intègre exactement à moins un électron. La règle de somme n'est qu'une caractéristique physique de la fonction de trou qui devrait être satisfaite par les fonctionnelles d'échange-corrélation approchées.

Le principe de Pauli ne permet pas à deux électrons de même spin d'être au même endroit donc le trou d'échange (ou trou de Fermi) doit s'intégrer à -1 électron

$$\int h_x(\mathbf{r}_1, \mathbf{r}_2) d\mathbf{r}_2 = -1. \quad (2.101)$$

Par conséquent, le trou de corrélation (ou trou de Coulomb) s'intègre à 0

$$\int h_c(\mathbf{r}_1, \mathbf{r}_2) d\mathbf{r}_2 = 0 \quad (2.102)$$

et sa forme est déterminée par l'interaction Coulombienne $1/r_{12}$. Il présente donc un point de rebroussement (pour l'anglais *cusp*) en \mathbf{r}_1 et il est négatif à proximité de \mathbf{r}_1 mais, en accord avec l'équation 2.102, il est positif partout ailleurs.

2.2.2.2 La connection adiabatique

D'après l'équation 2.94, le potentiel d'échange-corrélation n'est pas seulement composé du potentiel d'interaction électron-électron non-classique V_{non-cl} , mais aussi d'une contribution provenant de la différence entre l'énergie cinétique du système interagissant $T[\rho]$ et l'énergie cinétique KS du système non-interagissant $T_S[\rho]$. Afin de déterminer la meilleure approximation possible de la fonctionnelle d'échange-corrélation exacte, la contribution de l'énergie cinétique doit être incluse. Le trou d'échange-corrélation, h_{xc} , ne contient aucune information sur l'énergie cinétique, celle-ci n'étant pas une quantité reliée à la densité de paire.

Un moyen simple de prendre en compte la contribution de l'énergie cinétique et les composantes non-classique de l'interaction électron-électron est celui donné par la *connection adiabatique* [21, 22, 23, 24]. La fonctionnelle d'échange-corrélation peut être écrite comme

$$E_{xc}[\rho] = (T[\rho] - T_S[\rho]) + (E_{ee}[\rho] - J[\rho]) . \quad (2.103)$$

Par analogie avec le concept thermodynamique d'un processus adiabatique, il est possible de concevoir un passage continu du système fictif non-interagissant au système réel interagissant en gardant la densité fixe grâce à un potentiel externe V_λ et à l'aide d'un paramètre λ de force de couplage variant de 0 à 1,

$$F_\lambda[\rho] = \min_{\Psi \rightarrow \rho} \langle \Psi | \hat{T} + \lambda \hat{V}_{ee} | \Psi \rangle . \quad (2.104)$$

Quand $\lambda = 1$, l'équation 2.104 représente le système réel interagissant,

$$F_1[\rho] = T[\rho] + E_{ee}[\rho] , \quad (2.105)$$

lorsque $\lambda = 0$, elle représente le système fictif non-interagissant,

$$F_0[\rho] = T_S[\rho] . \quad (2.106)$$

D'après les équations 2.103, 2.104 et 2.105, nous pouvons définir,

$$E_{xc}[\rho] = \int_0^1 \frac{\partial F_\lambda[\rho]}{\partial \lambda} + \frac{\partial V_\lambda}{\partial \lambda} d\lambda - J[\rho] . \quad (2.107)$$

De l'équation 2.104, nous avons,

$$\frac{\partial F_\lambda[\rho]}{\partial \lambda} = \min_{\Psi \rightarrow \rho} \langle \Psi | \hat{V}_{ee} | \Psi \rangle . \quad (2.108)$$

Nous pouvons alors écrire l'équation 2.107 en terme de densité de paire,

$$E_{xc}[\rho] = \iint \frac{\bar{\rho}_2(\mathbf{r}_1, \mathbf{r}_2)}{r_{12}} d\mathbf{r}_1 d\mathbf{r}_2 - J[\rho] \quad (2.109)$$

où $\bar{\rho}_2(\mathbf{r}_1, \mathbf{r}_2)$ est la densité de paire moyennée de la force de couplage.

$$\bar{\rho}(\mathbf{r}_1, \mathbf{r}_2) = \int_0^1 \rho_2(\mathbf{r}_1, \mathbf{r}_2) d\lambda. \quad (2.110)$$

A l'aide des équations 2.97 et 2.99, $E_{xc}[\rho]$ peut s'écrire

$$E_{xc}[\rho] = \frac{1}{2} \iint \frac{\rho(\mathbf{r}_1) \bar{h}_{xc}(\mathbf{r}_1, \mathbf{r}_2)}{r_{12}} dr_1 dr_2 \quad (2.111)$$

où $\bar{h}_{xc}(\mathbf{r}_1, \mathbf{r}_2)$ est la moyenne sphérique du trou d'échange-corrélation

$$\bar{h}_{xc}(\mathbf{r}_1, \mathbf{r}_2) = \int_0^1 h_{xc}(\mathbf{r}_1, \mathbf{r}_2) d\lambda. \quad (2.112)$$

2.2.2.3 L'approximation locale de la densité

Afin d'obtenir une bonne approximation pour la fonctionnelle d'échange-corrélation, E_{xc} , celle-ci doit reproduire au mieux les caractéristiques physiques de la moyenne sphérique du trou d'échange-corrélation \bar{h}_{xc} plutôt que du trou lui-même h_{xc} . Ceci est l'explication des "bons" résultats de l'approximation locale de la densité (LDA pour l'anglais *Local Density Approximation*) ou l'approximation locale de la densité de spin (LSDA pour l'anglais *Local Spin-Density Approximation*), pour le cas couche ouverte. Elle est à la base de toutes les fonctionnelles d'échange-corrélation moderne. Elle est définie par

$$\begin{aligned} E_{xc}^{LDA}[\rho] &= \int \rho(\mathbf{r}) \epsilon_{xc}(\rho(\mathbf{r})) d\mathbf{r} \\ E_{xc}^{LSDA}[\rho_\alpha, \rho_\beta] &= \int \rho(\mathbf{r}) \epsilon_{xc}(\rho_\alpha(\mathbf{r}), \rho_\beta(\mathbf{r})) d\mathbf{r}. \end{aligned} \quad (2.113)$$

C'est la fonctionnelle pour laquelle une forme exacte est presque connue. L'approximation de $E_{xc}[\rho]$ est basée sur le modèle du gaz d'électron uniforme, où le terme $\epsilon_{xc}(\rho(\mathbf{r}))$ est l'énergie d'échange-corrélation par particule du gaz d'électron uniforme de densité $\rho(\mathbf{r})$. $\epsilon_{xc}(\rho(\mathbf{r}))$ peut-être considéré comme la somme d'une contribution d'échange et de corrélation

$$\epsilon_{xc}(\rho(\mathbf{r})) = \epsilon_x(\rho(\mathbf{r})) + \epsilon_c(\rho(\mathbf{r})). \quad (2.114)$$

Le terme d'échange, communément appelé “échange de Dirac” (symbolisé par S car cette expression fut reprise par Slater) est connu exactement

$$\epsilon_x^S(\rho(\mathbf{r})) = -\frac{3}{4} \left(\frac{3\rho(\mathbf{r})}{\pi} \right)^{\frac{1}{3}}. \quad (2.115)$$

La partie corrélation $\epsilon_c(\rho(\mathbf{r}))$ ne peut être exprimée de manière exacte. L'approximation de ce terme établie par Vosko, Wilk et Nussair (VWN) [25] a obtenu le plus de succès. Elle est basée sur une interpolation de résultats de calculs Monte-Carlo quantique très précis sur le gaz uniforme d'électrons réalisé par Ceperley et Alder [26]¹.

L'idée de base de la LDA est qu'il est possible d'estimer l'énergie d'échange-corrélation d'un système inhomogène en utilisant, sur des portions infinitésimales, les résultats d'un gaz homogène d'électrons de densité égale à la densité locale du système inhomogène. Cette approximation est raisonnable pour un système où la densité varie lentement mais son application aux atomes et molécules n'est justifié que par le succès de ses applications numériques. En effet, le résultat du test G2 (calcul d'énergies d'atomisation de 50 petites molécules comportant exclusivement des éléments de la série principale) donne une déviation moyenne de $+36 \text{ kcal.mol}^{-1}$ [28] par rapport au données expérimentales. Ceci représente une grande amélioration par rapport aux résultats HF qui produisent une erreur de $-78 \text{ kcal.mol}^{-1}$. Cependant, ces résultats sont encore loin de la précision chimique : 1 kcal.mol^{-1} .

2.2.2.4 L'approximation du gradient généralisé

La plus grande source d'erreur dans la LDA vient de l'énergie d'échange souvent sous-estimée de 10 à 15 %. L'énergie de corrélation est souvent sur-estimée d'environ 200% [9] mais, en valeur absolue, sa contribution à l'énergie totale est plus petite. Ces deux erreurs ont tendance à s'annuler. Pour améliorer la précision des calculs DFT, nous avons besoin de meilleures approximations pour la fonctionnelle d'échange-corrélation. Certains ont pensé à définir une fonctionnelle de la densité et ses dérivées dans le but de prendre en compte l'inhomogénéité du système. Dans un premier temps, la LDA fut traitée comme le premier terme d'un développement en série de Taylor,

$$E_{xc}^{GEA}[\rho] = \int \epsilon_{xc}^{GEA}(\rho(\mathbf{r}))\rho(\mathbf{r}) d\mathbf{r} + \int C_{xc}(\rho(\mathbf{r})) \frac{|\nabla \rho(\mathbf{r})|}{\rho^{4/3}(\mathbf{r})} d\mathbf{r} + \dots. \quad (2.116)$$

¹En réalité, il existe une autre approximation, donnée dans le même article de Vosko, Wilk et Nussair, reposant sur la RPA (pour l'anglais *Random Phase Approximation*) qui n'est utilisée que dans la fonctionnelle hybride B3LYP [27] (cf. paragraphe 2.2.2.6)

Cette forme de fonctionnelle est l'approximation du développement du gradient (GEA pour l'anglais *Gradient Expansion Approximation*). Malheureusement, ceci donne de plus mauvais résultats que la LDA. En effet, le trou d'échange-corrélation ne satisfait plus les conditions qui assuraient à la LDA un certain sens physique. Par exemple, les règles de sommes ne donnent plus 1 et 0 pour l'échange et la corrélation.

Afin de corriger ces problèmes, la fonctionnelle 4.42 a été modifiée pour la forcer à respecter les principales conditions aux limites. Nous obtenons alors l'approximation du gradient généralisé (GGA pour l'anglais *Generalized Gradient Approximation*), à l'origine du succès de la DFT,

$$E_{xc}^{GGA}[\rho; \nabla\rho] = \int \epsilon_{xc}^{GGA}(\rho(\mathbf{r}), \nabla\rho(\mathbf{r})) d\mathbf{r}. \quad (2.117)$$

Souvent, les contributions pour l'échange et la corrélation sont développées séparément,

$$E_{xc}^{GGA}(\rho, \nabla\rho) = E_x^{GGA}(\rho, \nabla\rho) + E_c^{GGA}(\rho, \nabla\rho). \quad (2.118)$$

Le majeur problème de la LDA provenant de l'échange, une attention particulière fut portée sur le développement de la partie d'échange,

$$E_x^{GGA}(\rho, \nabla\rho) = E_x^{LDA} - \int F(s(\mathbf{r}))\rho^{4/3}(\mathbf{r}) d\mathbf{r} \quad (2.119)$$

où F est une fonction du gradient de densité réduit (sans dimension),

$$s(\mathbf{r}) = \frac{|\vec{\nabla}\rho(\mathbf{r})|}{\rho^{4/3}(\mathbf{r})}. \quad (2.120)$$

Nous citerons les fonctions de Becke(B88) [29], celle de Perdew (PW86) [30] et celle de Handy et Cohen (OPTX) [31].

B88 La fonctionnelle d'échange B88 est basée sur une analyse dimensionnelle et sur un comportement asymptotique correct de la densité d'énergie d'échange,

$$F^{B88}(s) = \frac{\beta s^2}{1 + 6\beta s \sinh^{-1}(s)} \quad \text{avec } \beta = 0.0042 \text{ u.a..} \quad (2.121)$$

β est un paramètre empirique déterminé par une analyse des moindre-carrés des énergies d'échange des six atomes de gaz rares (de He à Rn).

La fonctionnelle de Perdew et Wang (PW91) [32] provient d'une modification de cette fonctionnelle pour qu'elle satisfasse à certaines conditions de mise à l'échelle.

PW86 Cette fonctionnelle est basée sur une analyse de l’expansion du gradient du trou d’échange-corrélation autour de sa forme LSDA,

$$F^{PW86}(s) = \left[1 + 1.296 \left(\frac{s}{p} \right)^2 + 14 \left(\frac{s}{p} \right)^4 + 0.2 \left(\frac{s}{p} \right)^6 \right]^{1/15} \quad \text{avec } p = (24\pi^2)^{1/3}. \quad (2.122)$$

La fonctionnelle de Perdew, Burke et Ernzerhof (PBE) [33] est une modification de cette fonctionnelle. Il est intéressant de remarquer que ni PW86, ni PBE ne contiennent de paramètres empiriques.

OPTX Cette fonctionnelle est une amélioration de la fonctionnelle d’échange de Becke [34] dans laquelle les auteurs ont non seulement optimisé le facteur d’amélioration F (pour l’anglais *enhancement factor*) mais aussi le coefficient d’échange de Dirac dans la partie LDA obtenant ainsi

$$E_x^{GGA}(\rho, \nabla\rho) = 1.05151 \times E_x^{LDA} - \int F^{OPTX}(s(\mathbf{r})) \rho^{4/3}(\mathbf{r}) d\mathbf{r} \quad (2.123)$$

avec

$$F^{OPTX}(s) = 1.43169 \left(\frac{\gamma s^2}{1 + \gamma s^2} \right)^2 \quad \text{avec } \gamma = 0.006 \text{ u.a..} \quad (2.124)$$

Les trois coefficients ont été obtenus en reproduisant l’énergie Hartree-Fock de l’état fondamental des 18 premiers atomes (H-Ar).

Les fonctionnelles de corrélation Les fonctionnelles de corrélation ont des formes analytiques beaucoup plus compliquées qui ne peuvent être comprises à l’aide de raisonnements physiques simples. Il s’agit surtout d’expressions satisfaisant à des propriétés mathématiques connues. Nous pouvons citer les fonctionnelles de Lee, Yang et Parr (LYP) [35], de Perdew (P86) [36] (contrepartie de la fonctionnelle d’échange PW86) et celle de Perdew et Wang (PW91) [32].

Les fonctionnelles d’échange-corrélation GGA représentent une amélioration très importante des LDA. La principale raison est la modification de la partie échange. Dans la détermination des énergies d’atomisation du test G2, l’utilisation de la fonctionnelle d’échange B88 combinée à la fonctionnelle de corrélation VWN diminue la déviation moyenne de 36 kcal.mol⁻¹ pour SVWN à 5 kcal.mol⁻¹ pour B88VWN [28].

2.2.2.5 Les fonctionnelles meta-GGA

Dans le but d’améliorer les performances des GGA, les fonctionnelles d’échange-corrélation meta-GGA (mGGA) prennent en compte la densité d’énergie cinétique

des orbitales KS,

$$\tau = \frac{1}{2} \sum_i^{occ} |\nabla \psi_i|^2 \quad (2.125)$$

en plus de la dépendance sur le gradient de la densité déjà inclu dans les GGA.

Le terme d'échange E_x^{mGGA} peut s'écrire

$$E_x^{mGGA} = -\frac{3}{4} \left(\frac{3}{4}\right)^{1/3} \int f(\rho, \nabla \rho, \tau) \rho^{4/3}(\mathbf{r}) d\mathbf{r}. \quad (2.126)$$

La dépendance sur le Laplacien de la densité améliore beaucoup la précision de ces fonctionnelles. La fonctionnelle VSXC [37] donne de très bons résultats pour la description de liaisons hydrogènes mais ne décrit pas correctement l'angle de torsion des molécules contenant des systèmes π -conjugués [38].

Cependant, la dépendance sur la densité d'énergie cinétique pose des problèmes d'implémentation de ces fonctionnelles dans un schéma auto-cohérent pour le potentiel d'échange-corrélation qui rend la procédure SCF plus consomatrice de temps.

D'autre part, la précision chimique n'a pas encore été atteinte et la principale partie à améliorer est l'échange. Pourquoi utiliser une fonctionnelle d'échange approchée alors que nous savons calculer l'échange exactement ?

2.2.2.6 Les fonctionnelles hybrides

Il nous suffirait de remplacer l'échange LDA ou GGA par

$$E_x^{HF} = -\frac{1}{2} \sum_{i,j} \iint \psi_i^*(\mathbf{r}_1) \psi_j^*(\mathbf{r}_1) \frac{1}{r_{12}} \psi_i^*(\mathbf{r}_2) \psi_j^*(\mathbf{r}_2) d\mathbf{r}_1 d\mathbf{r}_2 \quad (2.127)$$

en remplaçant les spin-orbitales HF ψ_i par les spin orbitales KS. L'échange exact, E_x^{KS} est alors obtenu. Les fonctionnelles approchées sont utilisées uniquement pour la corrélation. Les résultats sont très décevants car le caractère non-local de l'échange exact, permettant de reproduire les caractéristiques locales du trou d'échange-corrélation, a été oublié.

Un compromis serait d'inclure seulement une fraction d'échange exact [39, 40]. Cette idée trouve sa justification théorique avec la connection adiabatique (cf. paragraphe 2.2.2.2). Nous pouvons exprimer $E_{xc}[\rho]$ par,

$$E_{xc}[\rho] = \int_0^1 E_{non-cl}^\lambda[\rho] d\lambda \quad (2.128)$$

où λ est le paramètre de couplage. Pour $\lambda = 1$, le système électronique est inter-

agissant à cause du terme Coulombien V_{ee} . Pour $\lambda = 0$, l'interaction est inexisteante donc les électrons sont traités comme des fermions non-chargés, le terme d'échange exact est alors inclu.

En première approximation, E_{non-cl}^λ peut s'écrire comme une fonction linéaire du paramètre λ . Une solution simple est donnée par,

$$E_{xc}^{HH}[\rho] = \frac{1}{2}E_x^{KS}[\rho] + \frac{1}{2}E_{xc}^{LDA}[\rho]. \quad (2.129)$$

Cette approche est connue sous le nom de *half-and-half* (HH) [39]. Ses performances dans le test G2 sont comparables à celles d'une fonctionnelle GGA. De meilleurs résultats peuvent être obtenus en donnant plus de flexibilité par l'introduction de 3 paramètres d'ajustement,

$$E_{xc}^{B3PW91} = (1 - a_0)E_{xc}^{LSDA} + a_0 E_x^{KS} + a_x E_x^{B88} + a_c E_c^{PW91}, \\ \text{avec } a_0 = 0.20 \quad a_x = 0.72 \quad a_c = 0.81. \quad (2.130)$$

a_0 , a_x et a_c sont des coefficients semi-empiriques ajustés aux données expérimentales par une analyse des moindres carrés sur 56 énergies d'atomisation, 42 potentiels d'ionisation, 8 affinités protoniques et les énergies atomiques des 10 atomes des deux premières rangées du tableau périodique (test G1).

Cette fonctionnelle, nommée B3PW91 [40], réduit encore la déviation moyenne sur le test G2 jusqu'à une erreur proche de la précision chimique.

Une erreur plus petite est obtenue par la fonctionnelle B3LYP [27]. Elle est identique à B3PW91 mis à part qu'elle utilise la fonctionnelle de corrélation LYP au lieu de PW91.

L'utilisation de paramètres ajustables a permis le développement de variantes de cette dernière fonctionnelle en modifiant la proportion d'échange exact. 5% pour des calculs de déplacement chimique en RMN [41], 15% pour le calcul de différence d'énergie dans des complexes de Fer(II) [42], et jusqu'à 30% pour le calcul d'énergie d'excitation [43].

L'utilisation de 25% d'échange exact a été proposé par Perdew, Burke et Ernzerhof sur la base d'une estimation *ab initio* qui conduit à la fonctionnelle sans paramètre semi-empirique PBE0 [44],

$$E_{xc}^{PBE0} = E_{xc}^{PBE} + 0.25(E_x^{KS} - E_x^{PBE}). \quad (2.131)$$

Cette fonctionnelle donne de très bons résultats pour diverses propriétés [44, 45, 46].

2.2.2.7 Les fonctionnelles très paramétrées

Pour améliorer les fonctionnelles d'échange-corrélation, il est possible d'utiliser les densités et les énergies totales provenant de calculs *ab initio*, de calculer les potentiels d'échange-corrélation correspondants et ensuite de construire des fonctionnelles paramétrées basées sur une analyse des moindres carrés des résultats. Handy *et al.* [47] proposent de faire l'analyse des moindres carrés sur l'énergie totale, sur le potentiel et sur le terme représentant l'influence de la discontinuité dans la dérivée de la fonctionnelle d'échange-corrélation aux nombres entiers d'électrons. Contrairement à une régression faite sur une seule propriété, beaucoup plus de physique est ainsi incorporée dans la fonctionnelle.

2.2.2.8 Autres fonctionnelles

Il existe d'autres fonctionnelles comme le potentiel effectif optimisé (OEP pour l'anglais *Optimized Effective Potential*). Nous n'avons pas utilisé ce type de fonctionnelle dans notre étude donc nous n'allons pas les décrire ici.

2.3 Conclusion

A travers ces rappels théoriques, nous avons montré les avantages et les inconvénients des méthodes *ab initio* et DFT. La première étant très précises mais réservé à des petites molécules. Au contraire, la DFT peut-être appliquée à des molécules beaucoup plus grosses en gardant une certaine précision au prix d'une calibration comme les tests *Gn* ou d'une étude, comme celle présentée dans ce manuscrit, cherchant les limites d'application de la DFT.

Bibliographie

- [1] M. Born et J.R. Oppenheimer, Ann. Phys. **84**, 457 (1927).
- [2] (a) G. Berthier, Séance C. R. Acad. Sc. Paris **238**, 91 (1954);
(b) G. Berthier, J. Chem. Phys. **51**, 363 (1954).
- [3] J.A. Pople et R.K. Nesbet, J. Chem. Phys. **22**, 571 (1954).
- [4] C.C.J. Roothaan, Rev. Mod. Phys. **23**, 69 (1951).
- [5] K. Andersson, P.-Å. Malmqvist, B.O. Roos, A.J. Sadlej and K. Wolinski, J. Phys. Chem. **94**, 5483 (1990).
- [6] K. Andersson, P.-Å. Malmqvist and B.O. Roos, J. Phys. Chem. **96**, 1218 (1992).

- [7] P. Hohenberg et W. Kohn, Phys. Rev. **136**, B864 (1964).
- [8] W. Kohn and L.J. Sham, Phys. Rev. **140**, A1133 (1965).
- [9] R.M. Dreizler and E.K.U. Gross, *Density Functional Theory An Application to the Quantum Many-Body Problem*, (Springer-Verlag, 1990).
- [10] M. Levy, Proc. Natl. Acad. Sci. USA **76**, 6062 (1979).
- [11] M. Levy, Phys. Rev. A **26**, 1200 (1982).
- [12] E.H. Lieb, Int. J. Quantum Chem. **24**, 243 (1983).
- [13] J.P. Perdew et M. Levy, Phys. Rev. B **31** 6264 (1985).
- [14] J.E. Harriman, Phys. Rev. A **24**, 680 (1980).
- [15] C.-O. Almbladh et A.C. Pedroza, Phys. Rev. A **29**, 2322 (1984).
- [16] A. Savin, H. Stoll et H. Preuss, Theor. Chim. Acta **70**, 407 (1986).
- [17] J.A. Pople, M. Head-Gordon, D.J. Fox, K. Raghavachari and L.A. Curtiss, J. Chem. Phys. **90**, 5622 (1989).
- [18] L.A. Curtiss, C. Jones, G.W. Trucks, K. Raghavachari and J.A. Pople, J. Chem. Phys. **93**, 2537 (1990).
- [19] L.A. Curtiss, K. Raghavachari, G.W. Trucks and J.A. Pople, J. Chem. Phys. **94**, 7221 (1991).
- [20] L.A. Curtiss, K. Raghavachari, P.C. Redfern, V. Rassolov and J.A. Pople, J. Chem. Phys. **109**, 7764 (1998).
- [21] J. Harris and R.O. Jones, J. Phys. F **4**, 1170 (1974).
- [22] O. Gunnarson and B.I. Lundqvist, Phys. Rev. B **13**, 4274-4298 (1976).
- [23] D.C. Langreth et J.P. Perdew, Phys. Rev. B **15**, 2884 (1977).
- [24] R.A. Harris, J. Chem. Phys. **81**, 2403 (1984).
- [25] S.H. Vosko, L. Wilk, and M. Nusair, Can. J. Phys. **58** (1980) 1200.
- [26] D.M. Ceperley et B.J. Alder, Phys. Rev. Lett. **45**, 566 (1980).
- [27] (a) A.D. Becke, J. Chem. Phys. **98**, 5648 (1993) ;
(b) C. Lee, W. Yang, and R.G. Parr, Phys. Rev. B **37**, 785 (1988) ;
(c) S.H. Vosko, L. Wilk, and M. Nusair, Can. J. Phys. **58** 1200 (1980) ;
(d) P.J. Stevens, J.F. Devlin, C.F. Chabalowski et M.J. Frish, J. Phys. Chem. **98**, 11623 (1994).
- [28] B.G. Johnson, P.M.W. Gill et J.A. Pople, J. Chem. Phys. **98**, 5612 (1993).
- [29] A.D. Becke, Phys. Rev. A **38**, 3098 (1988).
- [30] J.P. Perdew et Y. Wang, Phys. Rev. B **33**, 8800 (1986).

- [31] N.C. Handy et A.J. Cohen, Mol. Phys. **99**, 403 (2001).
- [32] J.P. Perdew, K. Burke and Y. Wang, Phys. Rev. B **54**, 16533 (1996).
- [33] J.P. Perdew, K. Burke, and M. Ernzerhof, Phys. Rev. Lett. **77**, 3865 (1996) ; Erratum : Phys. Rev. Lett. **78**, 1386 (1997).
- [34] A.D. Becke, J. Chem. Phys. **84**, 4524 (1986).
- [35] C. Lee, W. Yang, and R.G. Parr, Phys. Rev. B **37**, 785 (1988).
- [36] J.P. Perdew, Phys. Rev. B **33**, 8822 (1986).
- [37] T.V. Voorhis and G.E. Scuseria, J. Chem. Phys. **109**, 400 (1998).
- [38] J.C. Sacho-García et J. Cornil, J. Chem. Phys. **121**, 3096 (2004).
- [39] A.D. Becke, J. Chem. Phys. **98**, 1372 (1993).
- [40] A.D. Becke, J. Chem. Phys. **98**, 5648 (1993).
- [41] P. J. Xilson, R. D. Amos, and N. C. Handy, Chem. Phys. Lett. **312**, 475 (1999).
- [42] M. Reiher, O. Salomon, and B.A. Hess, Theor. Chem. Acc. **107**, 48 (2001).
- [43] U. Salzner, J.B. Lagowski, P.G. Pickup, and R.A. Poirier, J. Phys. Chem. A **102**, 2572 (1998).
- [44] C. Adamo and V. Barone, J. Chem. Phys. **110**, 6158 (1999).
- [45] C. Adamo, G.E. Scuseria et V. Barone, J. Chem. Phys. **111**, 2889 (1999).
- [46] C. Adamo, M. Cossi, G. Scalmani et V. Barone, Chem. Phys. Lett. **307**, 265 (1999).
- [47] F.A. Hamprecht, A.J. Cohen, D.J. Tozer and N.C. Handy, J. Chem. Phys. **109**, 6264 (1998).

Chapitre 3

Étude des complexes $[\text{Fe}(\text{H}_2\text{O})_6]^{2+}$ et $[\text{Fe}(\text{NH}_3)_6]^{2+}$

Deux articles sont présentés dans ce chapitre,

1. Antony Fouqueau, Sébastien Mer, Mark E. Casida, Latévi Max Lawson Daku, Andreas Hauser, Tsonka Mineva et Frank Neese,
J. Chem. Phys. **120**, 9473 (2004).

Comparison of Density Functionals for Energy and Structural Differences Between the High $[^5T_{2g} : (t_{2g})^4(e_g)^2]$ and Low $[^1A_{1g} : (t_{2g})^6(e_g)^0]$ Spin States of the Hexaquoferrrous Cation, $[\text{Fe}(\text{H}_2\text{O})_6]^{2+}$.

2. Antony Fouqueau, Mark E. Casida, Latévi Max Lawson Daku, Andreas Hauser et Frank Neese,
J. Chem. Phys. accepté.

Comparison of Density Functionals for Energy and Structural Differences Between the High $[^5T_{2g} : (t_{2g})^4(e_g)^2]$ and Low $[^1A_{1g} : (t_{2g})^6(e_g)^0]$ Spin States of Iron(II) Coordination Compounds : II. More Functionals and the Hexaminoferrous Cation, $[\text{Fe}(\text{NH}_3)_6]^{2+}$.

La plupart des études sur les complexes de Fer(II), présentant le phénomène de transition de spin, ont porté sur des complexes de grandes tailles [1, 2, 3, 4, 5, 6]. Le choix des fonctionnelles était basé sur des comparaisons avec des données expérimentales. Afin de s'affranchir des effets d'environnement de la phase condensée, des effets de température (et donc d'entropie), et autres complications (énergie vibrationnelle de point zéro, effets relativistes), nous avons décidé de comparer nos résultats avec ceux de calculs *ab initio*. Pour ce faire, nous avons choisi d'étudier des petits complexes modèles de Fer(II) : les complexes hexaaqua fer(II), $[\text{Fe}(\text{H}_2\text{O})_6]^{2+}$ et hexaamine fer(II), $[\text{Fe}(\text{NH}_3)_6]^{2+}$. Nous devions alors nous intéresser à la qualité de

nos calculs *ab initio*. Ces derniers sont à la limite de ce qui est actuellement réalisable avec cette approche. Dans les paragraphes suivants, je vais décrire ma contribution à ce travail collectif et je vais présenter les principaux résultats.

Ce domaine d'études étant nouveau pour l'équipe, j'ai dû l'étudier à l'aide de calculs DFT et CASPT2 sur le complexe $[Fe(H_2O)_6]^{2+}$. Les premiers calculs furent très difficiles à converger. Au départ, les calculs DFT avec le logiciel GAUSSIAN étaient loin d'être triviaux pour ce type de molécules. En effet, rien ne pouvait garantir que le résultat obtenu correspondait à la solution de plus basse énergie. Parfois, un même calcul (même fichier d'entrée, même révision de GAUSSIAN) réalisé sur deux machines différentes donnait deux résultats différents. Ces problèmes étaient liés à la grande densité d'états pour cette molécule. Pour les éviter, j'ai développé une méthodologie permettant d'être relativement sûr de mes résultats. Elle consistait à faire des calculs HF puis DFT avec différentes fonctionnelles en utilisant le fichier de redémarrage du premier calcul et ainsi de suite, jusqu'à autocohérence. Par la suite, mes résultats ont pu être vérifiés en utilisant l'algorithme ODA [7, 8, 9] (pour l'anglais *Optimal Damping Algorithm*). Cet algorithme relâche la contrainte d'occupation entière des spin-orbitales pendant le cycle SCF. Cependant, lorsque le cycle SCF est convergé, l'occupation est de nouveau entière. Cet algorithme permet alors une convergence plus sûre et plus rapide en comparaison avec l'algorithme DIIS standard. L'algorithme ODA est maintenant utilisé par défaut dans GAUSSIAN 03.

D'autre part, cette étude a permis de mettre en évidence le problème d'énergie d'appariement de spin en DFT. Ce problème est d'autant plus important lorsque des états de spin différents comme les états quintuplet $^5T_{2g}$ et singulet $^1A_{1g}$ de nos complexes modèles sont étudiés.

Au niveau géométrique, mis à part la fonctionnelle LDA, toutes les fonctionnelles donnent des résultats en bon accord avec les résultats *ab initio* et les données expérimentales. La LDA a tendance à surlier et donne donc des liaisons trop courtes. Les GGA améliorent ce comportement et donnent toutes des résultats très similaires avec une préférence pour la fonctionnelle RPBE qui donne des liaisons plus longues et en meilleur accord avec les calculs *ab initio*.

Au niveau énergétique, mon travail a montré que même les méthodes *ab initio* telle que la méthode CASPT2 nécessitent une correction empirique afin de décrire correctement la différence d'énergie HS-LS nous intéressant. Cette correction empirique est basée sur le fait que l'erreur sur l'énergie d'excitation $^5D \rightarrow ^1I$ au niveau atomique (Fe^{2+}) serait la même qu'au niveau moléculaire. Nous avons estimé cette erreur à environ 3000 cm^{-1} . J'ai alors obtenu des résultats cohérents avec les calculs *ab initio* SORCI ne nécessitant pas cette correction. En utilisant la méthode de

sommation MSM [10](pour l'anglais *Multiplet Sum Method*), les calculs DFT au niveau atomique donnent des résultats en bon accord avec la valeur attendue. Aucune correction empirique ne sera alors appliquée à nos résultats DFT.

Au niveau moléculaire, l'approximation LDA sous-estime largement cette différence d'énergie. Les approximations GGA améliorent ce résultat mais la sous-estimation reste néanmoins trop importante et peut même mener à une mauvaise prédiction de l'état fondamental. Une exception est la fonctionnelle RPBE qui donne des résultats en bon accord avec les fonctionnelles hybrides B3LYP et PBE0, ainsi qu'avec les fonctionnelles très paramétrées VSXC et HCTH.

Les fonctionnelles permettant la meilleure description de nos petits complexes sont donc les fonctionnelles PBE0 (hybride), VSXC (meta-GGA) et RPBE (GGA).

Bibliographie

- [1] H. Paulsen, L. Duelund, H. Winkler, H. Toftlund, and A.X. Trautwein, Inorg. Chem. **40**, 2201 (2001).
 - [2] M. Reiher, O. Salomon, and B.A. Hess, Theor. Chem. Acc. **107**, 48 (2001).
 - [3] H. Paulsen, H. Grünsteudel, W. Meyer-Klaucke, M. Gerdan, H.F. Grünsteudel, A.I. Chumakov, R. Rüffer, H. Winkler, H. Toftlund, and A.X. Trautwein, Eur. Phys. J. B **23**, 463 (2001).
 - [4] O. Salomon, M. Reiher, and B.A. Hess, J. Chem. Phys. **117**, 4729 (2002).
 - [5] M. Reiher, Inorg. Chem. **41**, 6928 (2002).
 - [6] G. Baranović, Chem. Phys. Lett. **269**, 668 (2003).
 - [7] E. Cancès, J. Chem. Phys. **114**, 10616 (2001).
 - [8] K.N. Kudin, G.E. Scuseria, and E. Cancès, J. Chem. Phys. **116**, 8255 (2002).
 - [9] E. Cancès, K.N. Kudin, G.E. Scuseria et G. Turinici, J. Chem. Phys **118**, 5364 (2003).
 - [10] T. Mineva, A. Goursot, and C. Daul, Chem. Phys. Lett. **350**, 147 (2001).
- 3.1 Comparison of Density Functionals for Energy and Structural Differences Between the High [$^5T_{2g} : (t_{2g})^4(e_g)^2$] and Low [$^1A_{1g} : (t_{2g})^6(e_g)^0$] Spin States of the Hexaquoferrrous Cation, $[\text{Fe}(\text{H}_2\text{O})_6]^{2+}$**

Comparison of Density Functionals for Energy and Structural Differences Between the High [$^5T_{2g}$: $(t_{2g})^4(e_g)^2$] and Low [$^1A_{1g}$: $(t_{2g})^6(e_g)^0$] Spin States of the Hexaquoferrrous Cation, $[Fe(H_2O)_6]^{2+}$

Antony Fouqueau, Sébastien Mer, Mark E. Casida¹

Institut de Chimie Moléculaire de Grenoble (ICMG, FR-2607),
Laboratoire d'Études Dynamiques et Structurales de la Sélectivité (LÉDSS, UMR
5616), Équipe de Chimie Théorique (LÉDSS-ECT),
Université Joseph Fourier (Grenoble I), F38041 Grenoble, FRANCE

Latévi Max Lawson Daku, Andreas Hauser

Département de Chimie Physique, Université de Genève,
30 quai Ernest-Ansermet, CH-1211 Genève 4, SWITZERLAND

Tsonka Mineva

Institute of Catalysis, Bulgarian Academy of Sciences, 1113 Sofia, BULGARIA

Frank Neese

Max Planck Institut für Bioanorganische Chemie,
Stiftstrasse 34-36, Mülheim an der Ruhr 45470, GERMANY

¹Mark.Casida@ujf-grenoble.fr

Abstract

A comparison of density-functionals is made for the calculation of energy and geometry differences for the high [$^5T_{2g}$: (t_{2g}) 4 (e_g) 2] and low [$^1A_{1g}$: (t_{2g}) 6 (e_g) 0] spin states of the hexaquoferrrous cation, $[Fe(H_2O)_6]^{2+}$. Since very little experimental results are available (except for crystal structures involving the cation in its high spin state), the primary comparison is with our own complete active space self-consistent field (CASSCF), second-order perturbation theory-corrected complete active space self-consistent field (CASPT2) and spectroscopy oriented configuration interaction (SORCI) calculations. We find that generalized gradient approximations (GGAs) and the B3LYP hybrid functional provide geometries in good agreement with experiment and with our CASSCF calculations provided sufficiently extended basis sets are used (i.e. polarization functions on the iron and polarization and diffuse functions on the water molecules). In contrast, CASPT2 calculations of the low spin - high spin energy difference, $\Delta E_{LH} = E_{LS} - E_{HS}$, appear to be significantly overestimated due to basis set limitations in the sense that the energy difference of the atomic asymptotes ($^5D \rightarrow ^1I$ excitation of Fe^{2+}) are overestimated by about 3 000 cm^{-1} . An empirical shift of the molecular ΔE_{LH} based upon atomic calculations provides a best estimate of 12 000 - 13 000 cm^{-1} . Our unshifted SORCI result is 13 300 cm^{-1} , consistant with previous comparisons between SORCI and experimental excitation energies which suggest that no such empirical shift is needed in conjunction with this method. In contrast, after estimation of incomplete basis set effects, GGAs with one exception underestimate this value by 3 000 - 4 000 cm^{-1} while the B3LYP functional underestimates it by only about 1 000 cm^{-1} . The exception is the GGA functional RPBE which appears to perform as well as or better than the B3LYP functional for the properties studied here. In order to obtain a best estimate of the molecular ΔE_{LH} within the context of DFT calculations we have also performed atomic excitation energy calculations using the multiplet sum method. These atomic DFT calculations suggest that no empirical correction is needed for the DFT calculations.

I Introduction

A well-known feature of d^6 Tanabe-Sugano ligand field theory (LFT) diagrams for octahedral complexes is the reversal of the ordering of the low-spin 1A and high-spin 5T in the spin-crossover region of ligand field strength [31]. For compounds in this region, spin-crossover may be either thermally- or optically-induced [3], leading to

possible applications in storage and display devices [3, 4, 5]. We are particularly interested in the phenomenon of light-induced excited spin-state trapping (LIESST) in octahedral iron II compounds, which involves the optical interconversion of the high-spin (HS) $^5T_{2g}$ and low-spin (LS) 1A_g electronic states. While this can be understood at a qualitative level using LFT [31, 3], it is also known that the e_g orbitals, populated in going from the LS to the HS state, are antibonding, so that bonds are longer in the HS than in the LS state. This change in geometry results in a change of ligand field which is difficult to take into account quantitatively in simple LFT. Hence theoretical treatments which go beyond LFT are needed for a detailed treatment of spin-crossover and LIESST in particular. In this article we examine the performance of various density-functionals for describing the HS and LS geometries and energetics of the hexaquoferrrous cation, $[Fe(H_2O)_6]^{2+}$. Since water is a weak-field ligand, hexaquoferrrous cation is quite far from the interesting spin-crossover region. However, it is interesting as a “textbook example” of an octahedral ferrous compound and provides a useful preliminary for future studies of octahedral ferrous compounds which do exhibit LIESST.

To our knowledge, there has been only a few previous applications of DFT to spin-crossover in octahedral ferrous compounds [4, 5, 8, 6, 7, 11]. Those aspects of these studies which are pertinent to an investigation of functionals will be reviewed in the next section. Suffice it to say that they all involve calculations on molecules which are too large to allow comparison against detailed *ab initio* calculations. As such we do not yet have a general calibration on a variety of simple octahedral ferrous compounds on which to draw firm conclusions as to what quality of HS and LS geometries and energies should be expected in general from a given level of density-functional approximation. By examining a far simpler compound, namely $[Fe(H_2O)_6]^{2+}$, where detailed *ab initio* calculations can be performed, we hope to be able to begin to provide the necessary background data for a general assessment of functionals.

It should probably be pointed out that the issue of whether density functionals should be assessed by comparison against experimental data or against the results of *ab initio* calculations is not entirely clear. Although it might seem that the most direct comparison of results from gas-phase zero-temperature DFT calculations should be with the results of gas-phase zero-temperature *ab initio* calculations, rather than with the condensed-phase finite-temperature experimental data which is typically available for the compounds of interest here, calculations of 3d transition metal complexes are far from trivial, primarily because of the large amount of electron correlation created by the pseudo degeneracy of the 4s and 3d orbitals. Often the best

ab initio treatments seem to require empirical corrections to give “best estimates” in order to approach an accuracy better than 5 kcal/mol ($1\ 750\ \text{cm}^{-1}$) [49, 50]. This is an immense error when compared with the HS-LS energy difference of $100\ \text{cm}^{-1}$ typical in compounds exhibiting the LIESST phenomenon, and places a distinct limitation on how well we can expect to be able to assess density-functionals for describing this phenomenon. Nevertheless *ab initio* and DFT calculations remain our most reliable theoretical models for the overall behavior of these compounds and, when used with suitable care and consciousness of the limitations inherent in these models, should provide an important complement to LFT. It is our objective to establish just what type of care is needed and where lie the numerical limitations of the theory. The *ab initio* methods used here are well-established and can now be said to be fairly well understood. We find that the principle limitation *ab initio* methods is to underestimate dynamic correlation, leading to an overestimate of the differences between the LS and HS states, leading to similar results from the different *ab initio* methods we have considered. Note however that the difference dedicated configuration interaction method is an exception to this rule since it is deliberately designed to give a balanced cancellation of errors between the ground and excited state. [40, 15] The difference dedicated configuration interaction philosophy was also used in the design of the recently developed spectroscopy oriented configuration interaction (SORCI) procedure [38]. This method is an efficient multireference variation/perturbation approach which focuses on the calculation of energy differences between several states of possibly different multiplicity within an individually selecting configuration interaction strategy. As far as DFT is concerned, it seems fair to say that the behavior of different density functionals seems to be less well understood, particularly when it comes to specific types of applications such as the spin transitions which interest us. For this reason, and because most LIESST compounds are simply too large to treat adequately with traditional *ab initio* methods, our emphasis will be on determining the limitations of present day density functionals. In this way, we hope to foresee and avoid carrying out expensive calculations whose “theoretical error bars” are too big to address the questions being asked.

In this context, we also note a study somewhat similar to our own but for $[\text{Fe}(\text{H}_2\text{O})_6]^{3+}$ [17]. Harris, Loew, and Kormornicki found that DFT, with a suitably chosen functional, could compete with *ab initio* theory and that semiempirical ZINDO excitation energies *obtained at DFT optimized geometries* were in excellent agreement with experiment.

Our paper is divided into the following sections. Some of the issues which distinguish different functionals of interest for applications to spin-crossover ferrous

compounds are reviewed in the next section. The technical details of our calculations are given in Sec. IV. In Sec. V, we give our results. We consider first optimized geometries, followed by a comparison of HS and LS complex energies. This comparison of energies also involves the atomic limit, i.e. at the Fe^{2+} atom 5D ground and 1I excited states, not only because of the spectroscopic importance of knowing the separated complex limit of our potential energy surfaces but also because very detailed experimental data is available for the atom which might be used as an additional criterium for assessing density functionals. The multiplet sum method used to estimate DFT excitation energies is briefly discussed in the Appendix. Sec. VI summarizes.

II Density Functionals

Since our objective is the evaluation of density functionals for spin-crossover compounds, it is necessary to say a few words about the functionals which were considered in this paper. More general background information about density-functional theory (DFT) may be found in Refs. [18, 14, 20].

Most modern DFT calculations are carried out in a modified Kohn-Sham formalism [11] where the total electronic energy is written (in hartree atomic units) as,

$$E = \sum_{i\sigma} n_{i\sigma} \langle \psi_{i\sigma} | \hat{h}_{\text{core}} | \psi_{i\sigma} \rangle + \frac{1}{2} \iint \frac{\rho(\mathbf{r})\rho(\mathbf{r}')}{|\mathbf{r} - \mathbf{r}'|} d\mathbf{r}' + E_{xc}[\rho_\uparrow, \rho_\downarrow], \quad (3.1)$$

where $n_{i\sigma}$ is the occupation number of the Kohn-Sham orbital $\psi_{i\sigma}$, \hat{h}_{core} is the usual core hamiltonian, and the spin up, spin down, and total charge densities are given by,

$$\begin{aligned} \rho_\sigma(\mathbf{r}) &= \sum_i n_{i\sigma} |\psi_{i\sigma}(\mathbf{r})|^2 \\ \rho(\mathbf{r}) &= \rho_\uparrow(\mathbf{r}) + \rho_\downarrow(\mathbf{r}). \end{aligned} \quad (3.2)$$

The exchange-correlation energy is often written in terms of the exchange-correlation energy density per particle,

$$E_{xc}[\rho_\uparrow, \rho_\downarrow] = \int \rho(\mathbf{r}) \epsilon_{xc}[\rho_\uparrow, \rho_\downarrow](\mathbf{r}) d\mathbf{r}. \quad (3.3)$$

The local density approximation (LDA) [11] consists of the assumption that

$$\epsilon_{xc}^{\text{LDA}}[\rho_\uparrow, \rho_\downarrow](\mathbf{r}) = \epsilon_{xc}^{\text{HEG}}(\rho_\uparrow(\mathbf{r}), \rho_\downarrow(\mathbf{r})), \quad (3.4)$$

where the universality of the exchange-correlation functional is used to justify the use of ϵ_{xc} for the homogeneous electron gas (HEG). Calculations reported in this paper use the Vosko-Wilk-Nusair parameterisation for the LDA correlation energy [13] (the VWN5, *not* the VWN, option in GAUSSIAN), except where we have used the exchange-only variant of the LDA known X α . The full (exchange + correlation) LDA works remarkably well for the calculation of molecular ionization potentials, equilibrium geometries, and vibrational frequencies. It does this by underestimating exchange by about 14% and overestimating correlation by a factor of about 2.5 in such a way that the two errors tend to cancel (Ref. [14] pg. 231.) One might think that an approximation which underestimates exchange by more than 10% would lead to serious errors in describing parallel spin (i.e. Fermi) correlation. In particular it is often reasoned that the lower energy state of two states differing only in their number of unpaired electrons is always that with more parallel spin electrons since Fermi correlation keeps the parallel-spin electron pairs spacially separated, thereby reducing the electron repulsion energy. Thus an error in the DFT description of exchange may be expected to lead to an underestimation of the splitting between these states of different spin multiplicity (in cases where the HS state is lower in energy than the LS state.)

An important drawback of the LDA is that it tends to overbind molecules. This drawback was corrected by the discovery of generalized gradient approximations (GGAs), which incorporate the gradient of the charge density in order to improve the description of the exchange-correlation energy in the “boundary region” at the outer edges of atoms and where molecular binding occurs [23]. The general formula is particularly simple for the exchange part,

$$\epsilon_x^{\text{GGA}}[\rho_\uparrow, \rho_\downarrow](\mathbf{r}) = \sum_{\sigma} \epsilon_x^{\text{HEG}}(\rho_\sigma(\mathbf{r}))(1 + F(\rho_\sigma(\mathbf{r}), x_\sigma(\mathbf{r}))), \quad (3.5)$$

where the enhancement factor F depends upon the reduced gradient,

$$x_\sigma(\mathbf{r}) = \frac{|\vec{\nabla} \rho_\sigma(\mathbf{r})|}{\rho^{4/3}(\mathbf{r})}. \quad (3.6)$$

An example in the present work is Becke’s 1988 exchange-only GGA (B) [17]. Expressions for correlation GGAs are complicated, among other things, by a different spin dependence. We have used both Perdew’s 1986 correlation GGA (P86) [77] and the GGA correlation functional of Lee, Yang, and Parr (LYP) [18]. The combination B + P86 is referred to as BP86 while the combination B + LYP is referred to as BLYP. More modern GGAs have been developed without separating exchange and

correlation. We have used the 1991 exchange-correlation GGA of Perdew and Wang (PW91) [27], the 1997 exchange-correlation GGA of Perdew, Burke, and Ernzerhof (PBE) [28], as well as the revised PBE (RPBE) of Hammer, Hansen, and Nørskov [79]. These latter GGAs have been carefully designed to satisfy as many as possible of the known conditions which should be satisfied by the exact exchange-correlation functional. It is natural to expect that GGA exchange is also underestimated with respect to the true exchange since GGA exchange is dominated by its LDA component. Thus GGAs might also be expected to give artificially small splitting energies between states of different spin multiplicities.

By 1993, GGAs seemed to have reached the limit of what they could do for thermochemistry. In order to go beyond this limit, Becke [19] introduced the idea of a hybrid functional by using the adiabatic connection formalism of Harris and Jones [20] in which the electron repulsion, $\lambda \hat{v}_{ee}$ for $\lambda = 1$, is gradually turned on in the presence of a compensating potential, $\hat{w}_\lambda[\rho_\uparrow, \rho_\downarrow]$, which keeps the density fixed. For any given value of λ ,

$$\left(\hat{h}_{KS} + \lambda \hat{v}_{ee} + \hat{w}_\lambda[\rho_\uparrow, \rho_\downarrow] \right) \Psi_\lambda = E_\lambda \Psi_\lambda . \quad (3.7)$$

At $\lambda = 0$, there is no electron repulsion, so we have Kohn-Sham's fictitious system of noninteracting electrons whose wave function, $\Psi_{\lambda=0}$, is a single determinant. At $\lambda = 1$, we have the fully interacting real system. This way of adiabatically connecting the Kohn-Sham and real system allows us to write that

$$E_{xc} = \int_0^1 E_{xc}^\lambda d\lambda . \quad (3.8)$$

The single determinant nature of $\Psi_{\lambda=0}$ tells us that

$$E_{xc}^{\lambda=0} = E_x . \quad (3.9)$$

Perdew, Ernzerhof, and Burke [23] have suggested the *ansatz* that

$$E_{xc}^\lambda = E_{xc}^{\lambda=1} + (1 - \lambda)^{n-1} (E_x^{\lambda=0} - E_x^{\lambda=1}) , \quad (3.10)$$

where $n = 4$ is chosen on the basis of fourth order Møller-Plesset perturbation theory. This then leads to

$$E_{xc} = E_{xc}^{\lambda=1} + \frac{1}{4} (E_x^{\lambda=0} - E_x^{\lambda=1}) . \quad (3.11)$$

If we then reason (as did Becke [19]) that $E_x^{\lambda=0}$ should be well approximated by Hartree-Fock exchange, E_x^{HF} , while GGAs should best describe $E_x^{\lambda=1}$ and $E_{xc}^{\lambda=1}$, we

arrive at hybrid functionals with the formula,

$$E_{xc}^{\text{hybrid}} = E_{xc}^{\text{GGA}} + \frac{1}{4} (E_x^{\text{HF}} - E_x^{\text{GGA}}) . \quad (3.12)$$

In practice, the best known hybrid functional, and the one we use here is the B3LYP functional [33] defined by,

$$E_{xc} = (1 - a_0)E_x^{X\alpha} + a_0E_x^{\text{HF}} + a_xE_x^B + a_cE_c^{\text{LYP}} + (1 - a_c)E_c^{\text{VWN}} , \quad (3.13)$$

where $a_0 = 0.20$, $a_x = 0.72$, and $a_c = 0.81$. In agreement with the ideas of Perdew, Ernzerhof, and Burke [23], $a_0 \approx 1/4$ and $a_x \approx 3/4$.

One might expect the estimate of Fermi correlation to be improved in going from GGAs to hybrid functionals because of the inclusion of some Hartree-Fock exchange, thus increasing and so improving the splitting between states of different spin multiplicities. In fact Paulsen *et al* [4] have examined the ability of the BLYP and PW91 generalized gradient functionals and the B3LYP hybrid functional to predict the spin-crossover transition temperature of substituted and unsubstituted di[*tris*-(1-pyrazolyl)methane] ferrous cation, $[\text{Fe(tpm)}_2]^{2+}$. They noticed that the B3LYP significantly stabilized the HS state, making it lower in energy than the LS state, contrary to what is observed experimentally. Interestingly the same preference for a low multiplicity ground state seen in nature for this compound was also found with the GGAs. At about the same time Hess, Reiher, and Salomon [5] confirmed that the B3LYP functional stabilizes the HS state with respect to the LS state more than do GGA functionals in an examination of the ability of various density functionals to predict the experimentally observed HS-LS splitting in the Fe(II) spin-crossover complexes with sulfur-containing ligands of around 30 atoms. They found that the GGA BP86 (but also the GGA PBE and the hybrid PBE0) very much underestimated the HS-LS energy difference but that the hybrid functional B3LYP gave much more reasonable values. This then lead them to propose [5, 6, 7] the B3LYP* functional which differs from the B3LYP functional only in that the amount of HF exchange is reduced ($a_0 = 0.15$) to give a better fit of calculated and experimental HS-LS energy differences. The B3LYP* functional was further tested in Ref. [6], in particular for the HS-LS splittings in metallocenes and in bis(benzene) metal complexes of the first transition metal period, and found to be a dramatic improvement over the B3LYP functional alone for the calculation of HS-LS energy differences, without important changes in the prediction of other proper properties. This behavior has been further confirmed by Reiher in a study of the spin-crossover compound $\text{Fe}(\text{phen})_2(\text{NCS})_2$ using the GGAs BP86 and BLYP and

the hybrid functionals B3LYP and B3LYP* [7].

While reparameterizing the B3LYP functional is certainly an appealing simple approach to the problem it does have a few drawbacks. First of all, it would be nice to have a universal functional good for all properties. It is much easier to reparameterize a functional for one property and a limited class of compounds than to obtain a functional which will work for all properties and all compounds. Reiher [7] points out that the B3LYP* functional is not necessarily optimal for the calculation of other properties than the HS-LS energy difference and in particular is not recommended for the calculation of vibrational energies. Furthermore he recommends the BP86 functional for the calculation of the transition temperature in spin-crossover complexes because of a subtle cancelation of errors between the vibrational and electronic contributions to the overall energy difference. (In particular, BP86 *harmonic* frequencies agree better with experimental frequencies *which include anharmonic effects* than do B3LYP *harmonic* frequencies. [34] Thus there is a useful error in the BP86 frequencies which does not seem to be shared with those generated with the B3LYP functional.) This preference for a GGA over a hybrid functional for the calculation of HS-LS energy differences *which include vibrational effects* is also seen in the work of Paulsen *et al* [4] who obtained best agreement with experiment by using the PW91 functional. Most recently Baranović [11] has examined the theoretical prediction of the equilibria of the HS and LS Fe(II) spin-crossover complexes $Fe(1,10\text{-phenanthroline})_2(NCS)_2$, $[Fe(2\text{-picolylamine})_3]^{2+}$, $[Fe(\text{bis}(1,4,7\text{-triazacyclononane})_2]^{2+}$ with the BP86 functional and has found excellent agreement with experiment after the introduction of appropriate scaling parameters.

In fact, even the very arguments upon which is based the B3LYP* functional could be called into question. For example, Levine in his popular textbook points out that the traditional explanation of Hund's rule (given above) turns out to be wrong in most cases (though the conclusion is correct) and that the actual reason has more to do with the indirect reduction of electron-nucleus screening by Pauli repulsion ([16] pp. 328-329). Furthermore the quality of DFT calculations of $i \rightarrow a$ singlet ($i \uparrow i \downarrow$) - triplet ($i \uparrow a \uparrow$) excitation energies for organic molecules is well-established and GGAs give quite reasonable values. Could the situation actually be more complicated than it first appears? Koch and Holthausen ([20] pp. 173 - 176) have reviewed different functionals for the calculation of the energy difference between the lowest lying singlet and triplet states of carbenes and related species. This is a case where HF calculations fail rather badly because the singlet state

is strongly dominated by two nearly degenerate determinants. Hybrid functionals (B3LYP, B3P86, and B3PW91 in the particular case of methylene) do better but are still rather far from experiment as are some GGAs (BP86 and BPW91 for methylene). On the other hand, it is only the GGA functionals BVWN and BLYP which come within 1 kcal/mol of the experimental value of the $^1A_1 - ^3B_1$ energy gap in methylene. The authors' conclusion is that in this case, "pure density functionals are usually to be preferred over hybrid ones." Of course, this is a case where it could be argued that the BVWN and BLYP functionals give too high an energy for the singlet state because they do not take static correlation properly into account and give too high an energy for the triplet state for the reasons already mentioned. Thus the errors compensate. Nevertheless it may be taken as a warning that the arguments in favor of hybrid functionals over GGAs for calculating the relative energies of different spin states, while compelling from a heuristic point of view, are certainly not always easy to generalize. In fact, it has not yet been established that a GGA will never do as well as a hybrid functional for this property. In the remainder of this paper we compare the BP86, PW91, PBE, RPBE, BLYP, and B3LYP functionals against high-quality *ab initio* calculations and experiment for the characterisation of the LS and HS states of the hexaquio ferrous cation.

III Computational Details

A *Ab Initio* Calculations

Our choice of *ab initio* methods has been at least partially the result of attempting to seek the best compromise between the competing needs to use extensive basis sets and to include an accurate description of electron correlation. After some experimentation, we chose to focus on carrying out the best possible complete active space self-consistent field (CASSCF) with second-order perturbative correction (CASPT2) within the means at our disposal. The CASPT2 method has been compared with time-dependent density-functional theory and other *ab initio* methods by Chantal Daniel in a recent review [36] concerning what type of accuracy is now achievable for excitations in transition metal coordination compounds. The CASPT2 method is certainly one of the methods of choice. Estimates of its accuracy vary but typical errors are on the order of a few tenths of an eV (i.e. a few thousand cm⁻¹) [37]. This is also typical of what can be achieved with other *ab initio* methods [36] and is typical of what *ab initio* theory can provide for assessing density-functionals. After completing our CASPT2 study, we decided to also include results from the recently developed

spectroscopy oriented configuration interaction (SORCI) method[38]. This method has some features in common with the CASPT2 method, such as the combination of perturbation theory and multireference methods, but differs markedly in other ways, such as its accent on the calculation of energy differences and its ability to go beyond the limit of about 14 active orbitals frequently found in CASSCF/CASPT2 to as many as 40 or 50 active orbitals. Thus the SOCI method offers an interesting “second opinion” for comparison with our CASPT2 work.

1 Programs and Basis Sets

Our *ab initio* calculations were carried out with three different programs. The program GAUSSIAN was used to carry out spin-restricted Roothaan-Hartree-Fock (i.e. SCF) calculations (as well as some second-order Møller-Plesset calculations which we did not find interesting enough to report here). Our CASSCF and CASPT2 calculations were carried out with the program MOLCAS [42]. Spin-restricted Roothaan-Hartree-Fock (SCF) calculations were also carried out with MOLCAS. Our SOCI calculations were carried out with the ORCA program [39]. All of these programs use basis sets consisting of Gaussian-type orbitals, so that the same basis could (and frequently was) used in calculations using different programs. At the same time, the need for a more or less sophisticated basis set differs from method to method as does the amount of computer resources needed to perform a calculation with a given basis set. The basis sets used in our calculations are summarized in Table 3.12. They will be described in more detail below, in the context of the various methods used.

2 CASSCF and CASPT2 Calculations

The orbital basis sets used in our MOLCAS calculations were of 6-31G* and 6-31G** quality [43, 44]. For the atom, we also used the larger ANO-S basis set [42]. In the CASSCF and CASPT2 calculations, we have employed two different active spaces namely CAS1 and CAS2. In the CAS1, the 6 *d* electrons were distributed among the 5 *d* orbitals (i.e. CASSCF[6,5] and CASPT2[6,5]). As illustrated in Fig. 3.1, some of the 3*d* orbital density mixes with *p*-type orbitals on the ligand oxygens. It has been found important to include all of this 3*d* density in the CASSCF by expanding the active space to include not only the HOMO and LUMO orbitals but also the lowest three and highest two orbitals in the [6,5] calculations to make a [12,10] calculation (i.e. CASSCF[12,10] and CASPT2[12,10]). The strategy of adding this second *d* shell has been named the “3*d* double shell effect”[45, 46, 47]. It allows a better description of the large radial correlation effects due to the interaction between the 3*d* electrons. Automatic structure optimization and frequency calculations (to confirm minima)

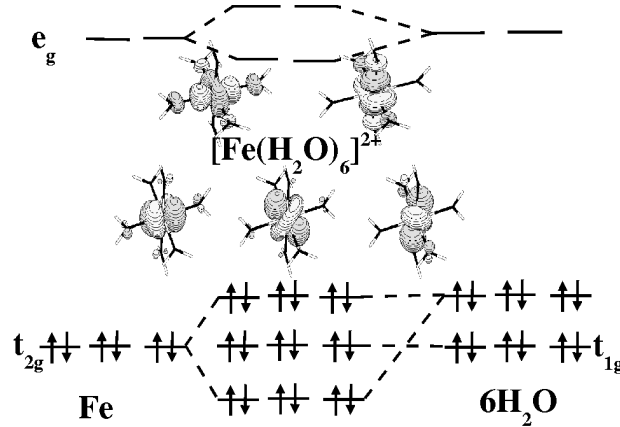


FIGURE 3.1: Correlation diagram for the highest-lying occupied and lowest-lying unoccupied molecular orbitals found in our DFT singlet calculations (not to scale). Also shown are pictures of the highest occupied molecular orbitals (HOMOs) and lowest unoccupied molecular orbitals (LUMOs) showing the d - π bonding nature of the former and the antibonding nature of the latter. Note that e_g Fe(II) orbitals correlate with e_g $6\text{H}_2\text{O}$ orbitals, t_{2g} Fe(II) orbitals correlate with t_{2g} $6\text{H}_2\text{O}$ orbitals, but that there is an absence of t_{1g} Fe(II) orbitals to correlate with the $6\text{H}_2\text{O}$ orbitals of the same symmetry representation.

were carried out at the CASSCF level. This was not possible at the CASPT2 level where only single point calculations were performed. In addition the lowest thirty orbitals were frozen in the molecular CASPT2 calculation.

3 SORCI Calculations

In addition to the CASPT2 calculations we have used the recently developed spectroscopy oriented configuration interaction (SORCI) procedure [38] as implemented in the ORCA package [39]. The orbital basis set used in our SORCI calculations (basis set F in Table 3.12) consists of Wachters basis set for Fe [53] supplemented with appropriate f functions [54], Ahlrichs TZVP basis set for O [52], and Ahlrichs TZV basis set for H [52]. As explained in detail in Ref. [38], the SORCI method is an individually selecting variation/perturbation approach which combines multi-configurational second-order Møller-Plesset perturbation theory with the difference dedicated configuration concept of Malrieu, Caballol and co-workers[40, 15]. The method introduces three cutoffs to achieve applicability to molecules with up to ~ 50 atoms or ~ 700 basis functions. The cutoffs control the reduction of the reference space (T_{pre} chosen to be 10^{-5}), the size of the variational space (T_{Sel} chosen to be 10^{-6} E_h), and the size of the approximate average natural orbital (AANO)

basis (T_{nat} chosen to be 10^{-4}). The calculations were carried out at the B3LYP optimized geometries. The orbitals came from a spin-averaged Hartree-Fock (SAHF) calculation according to Zerner[49, 57]. In the SAHF method, one obtains orbitals that are optimized for the average of all states of a given multiplicity that can be formed within a configuration of n electrons in m orbitals. In the present case, the SAHF was done for six electrons in the five iron 3d-based molecular orbitals. This procedure avoids any pitfalls of converging to low lying excited states and is thought to be an ideal starting point for the following correlated calculations. The initial reference space for the SORCI calculations was CAS(6,5). Since the SORCI method is designed to provide energy differences at fixed geometry, an estimate of the change in total energy in going from the high-spin ($S = 2$) to the low-spin ($S = 0$) geometry must be provided in order to obtain the adiabatic excitation energy. This number was estimated from DDCI3 (difference dedicated configuration interaction calculations with choice 3 of screening procedure [15, 38]) calculations at the optimized singlet and quintet geometries respectively and employed the estimate proposed by Caballol and coworkers for the effect of the inactive double excitations [51]. The correction amounts to 807 cm^{-1} which was added to the vertical quintet-singlet excitation energy calculated at the singlet optimized geometry.

4 SCF Convergence

At the SCF level, in both our Hartree-Fock and DFT calculations, convergence to the wrong electronic state was frequently encountered. This problem was overcome by a series of calculations using restart files for different size basis sets. Correct convergence for the LS electronic state was further confirmed by Eric Cancès who was able to reproduce our result with his more robust fractional occupation convergence algorithm [72].

B DFT Calculations

The DFT calculations reported here were carried out with GAUSSIAN [71] and with ADF [70]. These programs differ in several respects, making comparisons between them ideal for distinguishing numerical artifacts and algorithmic features from differences due to the choice of functional. Among the algorithmic differences, the most important is certainly that GAUSSIAN uses basis sets of Gaussian-type orbitals (GTOs) while ADF uses Slater-type orbital (STO) basis sets. These two types of basis sets behave rather differently and it is difficult to say *a priori* which GTO and STO basis sets should be of comparable quality. The basis sets used in this study

are summarized in Table 3.12. In order to be thorough and to verify convergence with respect to the quality of the different basis sets, calculations were carried out with basis sets A, A', B, B', C, D, and E. However we have opted to present only results for basis sets A', C, and E as these are adequate for illustrating the main points of our discussion. We were unable to converge our ADF calculations for the HS state with the LDA and the C" basis set.

TABLE 3.1: Summary of basis sets used in this work.

Name	Basis Sets			Size
	Fe	O	H	
Contracted Gaussian-Type Orbitals				
A	DZVP	DZVP	DZVP	132
A'	6-31G*	6-31G*	6-31G*	142
D	6-31G*	6-31G*	6-31G**	178
F	(8s6p4d2f) Wachters	TZVP Ahlrichs	TZV Ahlrichs	182
B	DZVP CS	6-31G**++	6-31G**	192
C	TZVP Ahlrichs	TZVP Ahlrichs	TZVP Ahlrichs	219
E	6-31G*	6-311G**++	6-311G**++	250
B'	6-31G*	6-311G++(3df,3pd)	6-311G**	340
Slater-Type Orbitals				
C"	TZ2P	TZ2P	TZ2P	379

1 Atomic DFT Calculations

Our *ab initio* calculations use wave functions which belong to correct space and spin representations, which sometimes requires a linear combination of several Slater determinants. In contrast, DFT is based on calculations with single Slater determinants, making the DFT treatment of atomic multiplet states conceptually different in nature than in the *ab initio* calculations. The DFT calculations for the atomic limit [${}^5D-{}^1I$ splitting of $\text{Fe}^{2+}(d^6)$] reported here have been carried out using the “multiplet sum method” (MSM) [55, 56, 57, 58]. In particular, we have followed the MSM procedure for d^n (s^2d^n) atomic multiplets given in Ref. [58]. The basic idea of the MSM is described in the Appendix. The MSM calculations reported here were carried out using the ADF program.

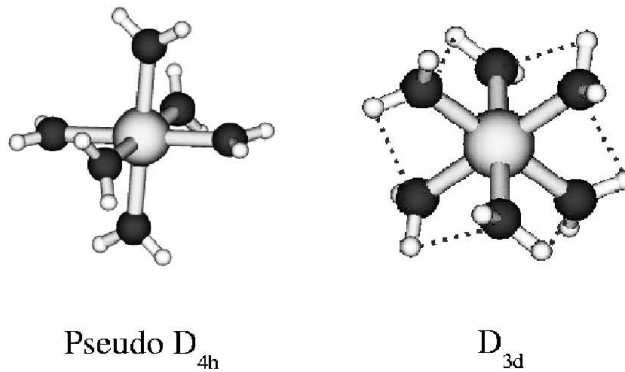
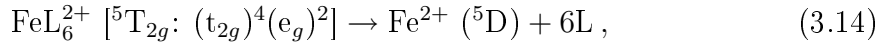


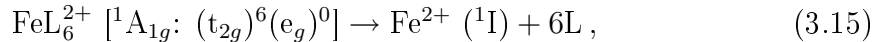
FIGURE 3.2: The two pseudosymmetries found for $[Fe(H_2O)_6]^{2+}$ in our calculations. Arrows have been added to the D_{4h} structure to indicate a Jahn-Teller distortion. Dotted lines have been added to the D_{3d} structure to indicate the presence of weak H-bonding interactions. The distortion of the D_{3d} structure has been exaggerated for clarity.

IV Results

This section presents a critical analysis of our *ab initio* and DFT results for the high-spin (HS) and low-spin (LS) states of the hexaquoferrrous cation, $[Fe(H_2O)_6]^{2+}$. A qualitative understanding of these two states can be obtained from simple ligand-field theory (LFT) considerations, assuming a complex with O_h symmetry. Since water is a low field ligand, the pair repulsion energy is expected to be more important than is the ligand splitting energy. The ground state is thus expected to be the HS state,



while the LS state,



is expected to lie at considerably higher energy. (L stands for water.) In fact, while the HS state is reasonably well characterized experimentally, almost nothing appears to be known about the LS state.

A Optimized Geometries

We now consider the geometrical structure of the free gas phase cation. Two main types of geometries have been found and these are shown schematically in Fig. 3.2. Our results for the HS state are summarized in Tables 3.2 and 3.3.

TABLE 3.2: ${}^5T_{2g}$ $[Fe(H_2O)_6]^{2+}$ bond lengths. Our notation is based upon the idea of a pseudo D_{4h} structure since, neglecting the hydrogens, since this is what we find in our best calculations. Footnotes indicate geometries which, neglecting the hydrogens, are better described as D_{3d} and give the OFeO C_{3v} angle.

Method	${}^5T_{2g}$ $[Fe(H_2O)_6]^{2+}$	
	Equatorial R(Fe-O) (Å)	Axial R(Fe-O) (Å)
MOLCAS		
CASSCF(12,10)	2.194	2.171
GAUSSIAN		
Xα/A ^a	2.070	2.070
SVWN/A ^a	2.056(2)	2.051
BP86/A'	2.134(8)	2.101
BP86/C	2.165(0)	2.130
BP86/E	2.154(6)	2.126
BLYP/C	2.190(4)	2.152
BLYP/E	2.180(2)	2.138
PW91/C	2.160(5)	2.124
PW91/E	2.150(6)	2.112
B3LYP/C	2.174(6)	2.143
B3LYP/E	2.166(1)	2.131
ADF		
BP86/C"	2.158(4)	2.120
PW91/C"	2.155(5)	2.118
PBE/C"	2.160(0)	2.122
RPBE/C"	2.201(0)	2.160

^a D_{3d} with a OFeO C_{3v} angle of 101(1) $^\circ$.

1 Ab Initio: HS results

As expected, the CASSCF results are dominated by a single determinant (coefficient=0.990) indicating a lack of strong static correlation contributions and that the independent particle model is a reasonable zero-order starting point for qualitative discussions (note however that dynamic correlation is important at a quantitative level and might eventually also lead to changes in the qualitative picture.) According to the simple LFT model [Eq. (3.14)], this electronic state is degenerate in O_h symmetry. We should therefore expect a Jahn-Teller distortion. This distortion appears in the *ab initio* results as a shortening of the two axial Fe-O bonds relative to the four equatorial Fe-O bonds. At the same time, the D_{4h} symmetry complex (neglecting hydrogens) is broken by a slight inclination (1.7°) of the O-Fe-O axis with respect to perpendicularity with the equatorial plane of the molecule. This inclination allows a slight reduction of the O-H distance between a hydrogen of each

TABLE 3.3: $^5T_{2g}$ $[Fe(H_2O)_6]^{2+}$ bond angles. Our notation is based upon the idea of a pseudo D_{4h} structure since, neglecting the hydrogens, since this is what we find in our best calculations. Footnotes indicate geometries which, neglecting the hydrogens, are better described as D_{3d} and give the OFeO C_{3v} angle. The abbreviation NA appears in the table for these entries to indicate that the D_{4h} angles are “not applicable.”

Method	$^5T_{2g}$ $[Fe(H_2O)_6]^{2+}$	
	$\angle OFeO'$	Dihedral OFeO'H
MOLCAS		
CASSCF(12,10)	91.9	11.4
GAUSSIAN		
X α /A' ^a	NA	NA
SVWN/A' ^a	NA	NA
BP86/A'	90.8	15.5
BP86/C	90.7	15.2
BP86/E	90.9	18.3
BLYP/C	91.0	14.7
BLYP/E	90.9	17.4
PW91/C	90.7	15.1
PW91/E	91.0	17.7
B3LYP/C	91.0	14.1
B3LYP/E	91.3	15.7
ADF		
BP86/C"	90.6	16.1
PW91/C"	90.6	15.8
PBE/C"	90.7	15.9
RPBE/C"	90.6	15.0

^a D_{3d} with a OFeO C_{3v} angle of 101(1) $^\circ$.

axial water and an oxygen of each of two opposing equatorial waters. The hydrogen atoms of the other two equatorial waters compensate by rotating about 11.4 $^\circ$ out of the equatorial plane.

2 DFT: HS Results

Geometries optimized using the LDA functional have six almost equal Fe-O bond lengths in a D_{3d} -type distortion. In both the exchange-only (X_α) and exchange-correlation (SVWN) cases, these bond lengths are significantly shorter than the *ab initio* values. A comparison between the X_α and SVWN geometries shows that including correlation shortens bond lengths. However the LDA bond lengths are too short compared with the *ab initio* results. Including gradient corrections via the BP86 functional increases the bond lengths as compared to the LDA. Augmenting

the quality of the basis sets, leads to further bond length increases and tidies up the geometry so that it is no longer a D_{3d} type structure, but is now the same D_{4h} pseudosymmetry as the CASSCF results but with a smaller inclination of the equatorial waters and a larger angle of rotation out of the plane.

As might be expected, we were unable to find any experimental structural data for the free gas phase cation, but a large amount of solution and crystallographic data exists for this cation in conjunction with various anions. This data has been collected in Table 3.4. The observed bond lengths are in the range 2.07-2.19 Å in agreement with both the *ab initio* and DFT calculations with GGA and hybrid functionals. Apparently, depending upon the salt considered, either the axial waters have moved *out* and the equatorial waters have moved *in* ($\text{FeSO}_4 \cdot 7\text{H}_2\text{O}$) or the the axial waters have moved *in* and the equatorial waters have moved *out* [$\text{Fe}(\text{NH}_4)_2(\text{SO}_4)_2 \cdot 6\text{H}_2\text{O}$] in agreement with the results of both the *ab initio* and the DFT calculations. Given the very small difference (~ 0.04 Å between the calculated equatorial and axial Fe-O bond lengths, we conclude from the results of the *ab initio* and DFT calculations that the Jahn-Teller effect is rather weak. Consequently the more pronounced differences in the Fe-O bond lengths seen in the experimental geometries in Table 3.4 should be interpreted as indicating that crystal packing effects are strong and dominate the much weaker Jahn-Teller effect.

3 LS: *Ab Initio* and DFT results

Our results for the LS state are summarized in Table 3.5. According to the simple LFT model [Eq. (3.15)], this electronic state is nondegenerate in the O_h symmetry and no Jahn-Teller distortion is expected. This is what is found in our *ab initio* calculations. The bonds are distinctly shorter in the LS state than in the HS state, consistant with the idea that the e_g orbital occupied in the HS state is antibonding in nature. The DFT calculations also show a single Fe-O bond length, but show a slight distortion to the pseudo D_{3d} structure, apparently because this allows energetically favorable H-bonding interactions (see Fig. 3.2). It should be emphasized, however, that this apparent H-bonding interaction is highly unlikely to be real and gradually disappears as the calculations become more realistic. Adding electron correlation at the local level ($\text{X}\alpha \rightarrow \text{SVWN}$) reduces this distortion. Both gradient corrections and extending the basis set initially enhances the distortion and then, with the largest basis set (E), brings the structure back to O_h symmetry. However it is worth emphasizing that the distortion of the D_{3d} from the O_h structure is almost always relatively small as emphasized by the superposition of the BP86/B' HS and LS structures shown in Fig. 3.3. The comparison between the geometries of HS and LS

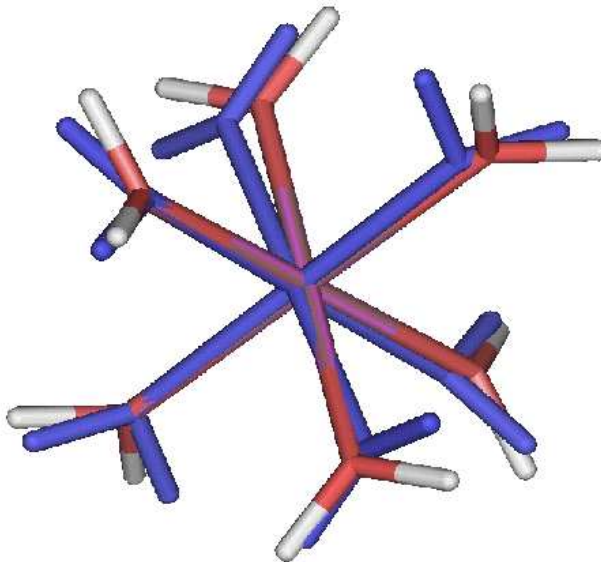


FIGURE 3.3: Superposition of the HS (single color) and LS (multicolor) $[Fe(H_2O)_6]^{2+}$ minima found at the BP86/B' level of calculation.

states shows that, on average, the Fe-O bond lengths are ~ 0.15 Å longer in the HS state. This difference, $\Delta R_{HL} = R_{HS} - R_{LS}$, takes here a value which is slightly less than the value of ~ 0.2 Å expected for spin-crossover compounds with a $[FeN_6]$ coordination sphere [59]. This difference may be attributed to the π -backbonding effects which takes place in spin-crossover $[FeN_6]$ compounds (for which a common feature is the use of π -ligands) and are responsible for their t_{2g} orbitals being more bonding than in the case of the hexaquoferric cation.

B Energetics

The HS-LS energy difference is a far more sensitive test of the quality of a density-functional than is the structure.

1 Atomic Limit

We first consider the atomic limit. Results are collected in Table 3.7.

A few remarks are in order regarding the “experimental” $^5D \rightarrow ^1I$ Fe^{2+} excitation energy. The number given in Table 3.7 is derived from the observation that the experimental transition energies given in the National Institute of Science and Technology (NIST) Atomic Spectra Database are well described by the Russell-Saunders

coupling scheme and the formula

$$E_{\text{SO}}(^{2S+1}L_J) = \frac{1}{2}A[J(J+1) - L(L+1) - S(S+1)] \quad (3.16)$$

for the spin-orbit energy, where A depends on L and S , but not on J (see for example, p. 336 of Ref. [16]). Since

$$\frac{\sum_{J=|L-S|}^{L+S} (2J+1) E_{\text{SO}}(^{2S+1}L_J)}{\sum_{J=|L-S|}^{L+S} (2J+1)} = 0, \quad (3.17)$$

we remove spin-orbit coupling from the experimental multiplet energies by a simple degeneracy-weighted average,

$$\bar{E}(^{2S+1}L) = \frac{\sum_{J=|L-S|}^{L+S} (2J+1) E(^{2S+1}L_J)}{\sum_{J=|L-S|}^{L+S} (2J+1)}. \quad (3.18)$$

This analysis shows the magnitude of spin-orbit coupling ($A \approx 100 \text{ cm}^{-1}$) and provides the experimentally-derived [$\bar{E}(^1I) - \bar{E}(^5D)$] spin-orbit-free excitation energy in Table 3.7. Had we instead used the observation that,

$$E_{\text{SO}}(^5D_3) = 0, \quad (3.19)$$

the resultant spin-orbit-free 5D energy would only differ from the degeneracy-weighted multiplet energy average by about 23 cm^{-1} .

The best available *ab initio* calculation over estimates the excitation energy by about 1800 cm^{-1} . To keep this in perspective, 350 cm^{-1} (1 kcal/mole or ‘‘chemical accuracy’’) is an often cited, but difficult to achieve, objective for quantum chemical methods, while 1749 cm^{-1} (5 kcal/mole) is more typical of what can be obtained from the best *ab initio* and DFT methods. In this case, the error is on the high end of what is expected, but reasonable. However this is only with the relatively large ANO-S basis set, which is too large to apply in *ab initio* calculations on the full complex. This is why atomic information is used to empirically correct the molecular HS-LS energy difference [48], particularly when basis set saturation becomes impossible.

The DFT results reported in the Table 3.7 were calculating using the multiplet-sum method already described in Sec. IV. This method has not been used in any of our molecular calculations, but is needed in the atomic case because of the essential multideterminantal nature of the atomic multiplets. The multiplet-sum method is not a formally exact method but is known to provide useful first-order estimates of excitation energies. As we have seen, the $^5D \rightarrow ^1I$ transition in Fe^{2+} poses problems

for high quality *ab initio* methods. Our expectations regarding the quality of first-order DFT estimates of this quantity should be moderate at best. Nevertheless the results in Table 3.7 show that the multiplet sum method implemented in the ADF program gives excellent results. With the best basis (TZ2P) the LDA (VWN) gives an excitation energy which is only 368 cm^{-1} too low compared to experiment. Similar or smaller errors are found with GGA functionals and the same basis set: 173 cm^{-1} for the BP86, 511 cm^{-1} for the PW91, 352 cm^{-1} for the PBE, and 118 cm^{-1} for the RPBE functionals. Thus there appears to be no justification in DFT for an atom-based empirical correction for the molecular HS-LS energy difference.

2 Molecular Energy Differences

Calculated HS-LS energy differences for the hexaquo complex are shown in Table 3.6 for the molecular case. The importance of electron correlation is immediately seen in the case of the *ab initio* calculations. Inclusion of higher levels of correlation decreases the HS-LS energy difference, indicating that electron correlation is more important for the higher-lying(LS) than for the lower-lying(HS) state. Our CASSCF[6,5] results are in good agreement with those previously reported by Åkeson, Pettersson, Sandström and Wahlgren [48]. However, increasing the active space to include the 3d double shell effect further decreases the HS-LS energy difference. Our CASPT2[12,10] calculation (which includes the 3d double shell effect) are in good agreement with the CI energy difference reported by Åkeson *et al.*, who noted that a better estimate of the true HS-LS energy difference might be obtained by using the difference between calculated and atomic excitation energies to correct the molecular HS-LS energy difference,

$$\Delta E_{LH}^{shifted} = \Delta E_{LH}^{direct} + (\Delta E_{atom}^{expt} - \Delta E_{atom}^{calc}) . \quad (3.20)$$

This shift makes sense if part of the molecular error is inherited from the error in the asymptotic energies of the dissociated complex ($Fe^{2+}\text{ }^5D$ or $^1I + 6 H_2O$ ground state energies). This shift further lowers the best *ab initio* values for the HS-LS energy difference by about $3\ 000\text{ cm}^{-1}$ to give a best estimate of the true HS-LS energy difference in the range

$$12\ 000\text{ cm}^{-1} < \Delta E_{LH}^{\text{best}} < 13\ 000\text{ cm}^{-1} . \quad (3.21)$$

At the singlet optimized geometry, the SORCI calculations provide a $^1A_{1g}$ vertical excitation energy of $12\ 553\text{ cm}^{-1}$. Accounting for the geometric relaxation which stabilizes the quintet state by another 807 cm^{-1} , we arrive at an adiabatic excitation

of

$$\Delta E_{LH}^{direct} = 13\ 300\ \text{cm}^{-1} \quad (3.22)$$

without any empirical shift. This number is in pleasing agreement with the best estimate from the CASPT2 calculations. It is rationalized by the generally good success of the SORCI method for $d - d$ spectra [61] which accounts for the high-order effects of the most strongly perturbing configuration state functions in the outer space. We therefore believe the uncorrected SORCI HS-LS energy difference.

Adding correlation(SVWN) to exchange only ($X\alpha$) LDA calculations also results in a decrease in the value of the HS-LS energy difference. The amount of the decrease is comparable to that seen at the *ab initio* level (about $10\ 000\ \text{cm}^{-1}$), but the final LDA value of about $3\ 000\ \text{cm}^{-1}$ is far too small. This is certainly in line with the idea that the LDA underestimates Fermi correlation and so gives too low a quintet energy relative to the singlet energy.

Going to Generalized Gradient Approximations (GGAs) increases the value of the HS-LS energy difference by about $3\ 000\ \text{cm}^{-1}$ and improving the basis set leads to another increase of about $3\ 000\ \text{cm}^{-1}$. The final result varies between about $7\ 500$ and $9\ 500\ \text{cm}^{-1}$ which, while in significantly better agreement with our best estimate of the true HS-LS energy difference than is the LDA value, is still too low by a few thousand wave numbers. An exception is the RPBE functional which gives a HS-LS energy difference of about $12\ 000\ \text{cm}^{-1}$, in remarkable agreement with the *ab initio* best estimate.

The hybrid functional, B3LYP, gives a HS-LS energy difference of about $11\ 500\ \text{cm}^{-1}$, similar to the RPBE value but not as close to the *ab initio* best estimate. It certainly would be interesting to see how the multiplet-sum method would work for energies excitation with the B3LYP functional, however we were not able to perform multiplet-sum atomic calculations with this functional due to the software limitations.

Since we have the HS-LS energy difference for both the B3LYP and BLYP functionals and the HS-LS energy difference is to a good approximation linear in the a_0 exchange-mixing parameter, we can also estimate the value of the HS-LS energy difference with the B3LYP* functional: $8\ 500\ \text{cm}^{-1}$ with basis A, $9\ 700\ \text{cm}^{-1}$ with basis B, $10\ 689\ \text{cm}^{-1}$ with basis C, $10\ 800\ \text{cm}^{-1}$ with basis D, and $11\ 100\ \text{cm}^{-1}$ with basis E. In this case the B3LYP* functional appears to correct the B3LYP HS-LS energy difference in the wrong direction compared to the *ab initio* best estimate. However it should be kept in mind that the RPBE, B3LYP, and B3LYP* results are all very close to our *ab initio* best estimates for the HS-LS energy difference.

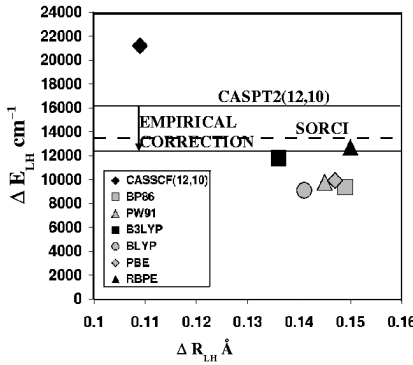


FIGURE 3.4: Comparison of *ab initio* and DFT best estimates for bond length and energy differences between the high and low spin states of $[Fe(H_2O)_6]^{2+}$. Results of atomic calculations have been used to empirically correct our CASPT2(12,10) energy difference for an insufficiently large basis set. DFT results are for GAUSSIAN calculations with the E basis set and ADF calculations with the fictitious “E” basis set. (PW91 results shown only for the GAUSSIAN calculations.) In particular, ADF results with the C" basis set have been empirically scaled in order to estimate what they would be with the better E basis set. See text for further details.

C Comparison of STO and GTO-Based DFT Calculations

As mentioned in Sec. IV, it is difficult to say *a priori* which GTO and STO basis sets should be of comparable quality. This is especially true because GTO and STO basis sets have qualitative differences that can lead to systematic errors which cancel when taking differences. However, as shown in Table 3.8 we can say *a posteriori* that ADF calculations with the C" basis set (TZ2P) give energies and geometries similar to those obtained in GAUSSIAN calculations with the C basis set (Ahlrichs TZVP) for DFT calculations with the BP86 and PW91 functionals. In retrospect this seems reasonable since the two basis sets have roughly the same degree of flexibility. Note however that we have more confidence in results obtained with the E basis set since the E basis set is more flexible than is the C basis set. In order to be able to compare results obtained with functionals available only in ADF with the results of functionals only available in GAUSSIAN, the ADF C" results have been scaled to make the “E” basis set results in Table 3.8. Results with the E and “E” basis sets have been used to prepare Figure 3.4 which provides a nice summary of the principle results of this paper.

V Conclusion

It is now possible to carry out rigorous *ab initio* and density-functional theory (DFT) calculations on transition metal complexes and, while the former tend to be limited to simpler complexes, the latter can be applied to molecules of practical interest. Neither method is expected to replace ligand field theory (LFT) anytime in the near future. Indeed LFT provides an excellent starting point for beginning to understand the electronic properties of transition metal complexes and can even provide better numerical values than either *ab initio* or DFT when properly parameterized for specific properties of interest. However LFT has important limitations, especially when considering changes in geometry and the consequent changes in ligand field strengths, and this is where the more rigorous models are expected to make important contributions. These aspects play a crucial role in understanding the light-induced excited-state spin trapping (LIESST) phenomenon in Fe(II) compounds, and so we may expect *ab initio* and especially (because of the size of the molecules involved) DFT to make an important contribution to modeling LIESST. Unfortunately relatively little is known about the intrinsic applicability of these more rigorous models to Fe(II) coordination complexes. This paper presents a first study concerning the accuracy and choice of density-functionals in the context of the simple “textbook” complex, $[Fe(H_2O)_6]^{2+}$. Little experimental data is available for these complexes, though X-ray crystal structures are available for compounds containing the high-spin cation. However we have compensated for this by performing *ab initio* calculations at the CASPT2 and SOCI levels with reasonably extensive basis sets.

It should be noted that the CASPT2 calculations are far from being a “black box” because of the question of how to choose the active space in the multiconfigurational calculations. In principle this is one of the reasons that DFT is often preferred over *ab initio* methods for treating transition metal complexes. However we have found that this is somewhat countered by the tendency of DFT to converge to the incorrect electronic state unless great care is taken to analyse results for possible excited states and treat them accordingly. This is certainly one reason why some workers prefer multiconfigurational calculations to DFT calculations for these compounds. However multiconfigurational calculations soon become unmanageable as the compounds become large (at least if the active space is also increased) and so we have concentrated on developing tricks to help guarantee convergence of DFT to the right electronic state. Our most useful tool has turned out to be the clever use of sequences of restart files to guide our calculations, combined with careful examination of the molecular orbitals. Ultimately, however, we think that the algorithm of Eric Cancès will be helpful in mitigating this problem [72].

Both our *ab initio* and DFT optimized geometries are consistant with the available experimental data. More importantly (given the relative lack of detailed experimental data), our DFT geometries are found to be consistent with our *ab initio* geometries provided functionals are used which go beyond the local level and large basis sets are used. Of course, our objective here has been to test functionals by focusing on details, but it should be kept in mind that smaller basis sets may be adequate for many practical applications.

The low spin - high spin energy difference, ΔE_{LH} , is a far greater challenge for theory. Here there is no available experimental data for $[Fe(H_2O)_6]^{2+}$ but there is for the atom. Our CASPT2 calculations are consistant with previous *ab initio* work [62] indicating that there is a systematic over estimation of the difference of the atomic asymptotes of about $3\ 000\ \text{cm}^{-1}$. When this correction is added to our molecular calculations, we obtain a best estimate of the ΔE_{LH} in the range of about $12\ 000 - 13\ 000\ \text{cm}^{-1}$. The SOCI method gives the same best estimate of ΔE_{LH} *without the need for a semiempirical correction*. In striking contrast, the values of ΔE_{LH} obtained from DFT show wide variations depending upon the class of functional, with about $3\ 000\ \text{cm}^{-1}$ with the local functional, about $8\ 000 - 10\ 000\ \text{cm}^{-1}$ for better basis sets and generalized gradient approximations (GGAs) other than the RPBE functional, and about $12\ 000\ \text{cm}^{-1}$ for the B3LYP hybrid and RPBE GGA functionals. An estimate of what ΔE_{LH} would be for the B3LYP* functional suggests that this is one case where reducing the exact exchange contribution to the B3LYP functional may not be a good idea, although one should be hesitant about over interpreting this conclusion since it is based on an *ab initio* best estimate which itself is not entirely certain.

It is important to realize that, while the B3LYP and RPBE values of ΔE_{LH} looks very good compared with the best estimate available from *ab initio* calculations, all DFT results very much underestimate the *uncorrected* ΔE_{LH} *ab initio* value of about $16\ 000 - 17\ 000\ \text{cm}^{-1}$. That is, it is not enough to examine DFT for the molecule, we must also look at the atomic asymptotes. We were able to do this for local and GGA functionals using the multiplet-sum method (though not for the B3LYP functional for technical reasons.) The results of the multiplet-sum method suggest that no empirical correction is necessary for DFT as was the case for the *ab initio* calculations.

These results are consistant with the idea that the B3LYP and RPBE functionals are the most reliable for our intended application of the various functionals tried. Of course, the present work is a study of only a few aspects of a single molecule, though it is a detailed study. We intend to extend this study in the near future to other

aspects of this Fe(II) complex and to other small Fe(II) complexes, providing what we hope will be an excellent data bank for determining the strengths and limitations of DFT for studies of general Fe(II) complexes.

Acknowledgments

This study was carried out in the context of the *groupe de recherche en Commutateurs Optiques Moléculaires à l'Etat Solide* (COMES). AF would like to thank the French *Ministère d'Education* for a *Bourse de Mobilité*. MEC and AF would like to thank Pierre Vatton and Denis Charapoff for technical support of the LEDSS and *Centre d'Expérimentation pour le Calcul Intensif en Chimie* (CECIC) computers used for many of the calculations reported here and would also like to acknowledge supercomputer time at the *Institut du Développement et des Ressources en Informatique Scientifique* (IDRIS) in the context of IDRIS project number 021576. AH and LMD acknowledge supercomputer time at the *Centro Svizzero di Calcolo Scientifico* (CSCS) in the framework of the CSCS project entitled “Photophysics and Photochemistry of Transition Metal Compounds: Theoretical Approaches.” FN acknowledges financial support from the Deutsche Forschungsgemeinschaft in the framework of the priority program “Molecular Magnetism.” Dr. Eric Cancès of the *Centre d'Enseignement et de Recherche en Mathématiques, Informatique, et Calcul Scientifique* (CERMICS) at the *Ecole National des Ponts et Chaussées* is thanked for his calculations confirming our SCF energies. Drs. Emilia Sicilia and Nino Russo of the Department of Chemistry at the Università della Calabria (Cozenza, Italy) are thanked for providing us with their optimized basis set (designated as DZVP CS in this article.) We would also like to thank Trond Saue, John Perdew, Markus Reiher, Jeremy Harvey, and an unknown referee for useful discussions concerning and/or comments on our work.

Bibliography

- [1] B.N. Figgis and M.A. Hitchman, *Ligand Field Theory and Its Applications*, (Wiley-VCH, New York, 2000).
- [2] P. Gütlich, A. Hauser, and H. Spiering, Angew. Chem. Int. Ed. Engl. **33**, 2024 (1994).
- [3] J.A. Real, E. Andrés, M.C. Muñoz, M. Julve, T. Granier, A. Bousseksou, and F. Varret, Science **268**, 265 (1995).

- [4] W.W. Gibbs, Scientific American **August 1995**, 31 (1995).
- [5] Y. Ogawa, S. Koshihara, K. Koshino, T. Ogawa, C. Urano,k and H. Takagi, Phys. Rev. Lett. **84**, 3181 (2000).
- [6] H. Paulsen, L. Duelund, H. Winkler, H. Toftlund, and A.X. Trautwein, Inorg. Chem. **40**, 2201 (2001).
- [7] M. Reiher, O. Salomon, and B.A. Hess, Theor. Chem. Acc. **107**, 48 (2001).
- [8] H. Paulsen, H. Grünsteudel, W. Meyer-Klaucke, M. Gerdan, H.F. Grünsteudel, A.I. Chumakov, R. Rüffer, H. Winkler, H. Toftlund, and A.X. Trautwein, Eur. Phys. J. B **23**, 463 (2001).
- [9] O. Salomon, M. Reiher, and B.A. Hess, J. Chem. Phys. **117**, 4729 (2002).
- [10] M. Reiher, Inorg. Chem. **41**, 6928 (2002).
- [11] G. Baranović, Chem. Phys. Lett. **269**, 668 (2003).
- [12] C.W. Bauschlicher Jr., in *Modern Electronic Structure theory, Part II* edited by D.R. Yarkong (World Scientific, Singapore, 1995).
- [13] P.E.M. Siegbahn, Adv. Chem. Phys. **93**, 333 (1996).
- [14] J. Miralles, J.P. Daudey, and R. Caballol, Chem. Phys. Lett. **198**, 555 (1992).
- [15] J. Miralles, O. Castell, R. Caballol, and J.-P. Malrieu, Chem. Phys. **172**, 33 (1993).
- [16] F. Neese, J. Chem. Phys. *in press*.
“A spectroscopy oriented configuration interaction procedure”
- [17] D. Harris, G.H. Loew, and A. Kormornicki, J. Phys. Chem. A, 3959 (1997).
- [18] R.G. Parr and W. Yang, *Density-Functional Theory of Atoms and Molecules* (Oxford University Press: New York, 1989).
- [19] R.M. Dreizler and E.K.U. Gross, *Density Functional Theory, An Approach to the Quantum Many-Body Problem* (Springer-Verlag: New York, Springer-Verlag, 1990).
- [20] W. Koch and M.C. Holthausen, *A Chemist's Guide to Density Functional Theory* (Wiley-VCH: New York, 2000).

- [21] W. Kohn and L.J. Sham, Phys. Rev. **140**, A1133 (1965).
- [22] S.H. Vosko, L. Wilk, and M. Nusair, Can. J. Phys. **58**, 1200 (1980).
- [23] D.C. Langreth and J.P. Perdew, Phys. Rev. B **21**, 5469 (1980).
- [24] A.D. Becke, Phys. Rev. A **38**, 3098 (1988).
- [25] J.P. Perdew, Phys. Rev. B **33**, 8822 (1986).
- [26] C. Lee, W. Yang, and R.G. Parr, Phys. Rev. B **37**, 785 (1988).
- [27] J.P. Perdew, J.A. Chevary, S.H. Vosko, K.A. Jackson, M.R. Pederson, D.J. Singh, and C. Fiolhais, Phys. Rev. B **46**, 6671 (1992); Erratum, Phys. Rev. B **48**, 4978 (1993).
J.P. Perdew, K. Burke, and Y. Wang, Phys. Rev. B **54**, 16533 (1996); Erratum, Phys. Rev. B **57**, 14999 (1998).
- [28] J.P. Perdew, K. Burke, and M. Ernzerhof, Phys. Rev. Lett. **77**, 3865 (1996); Erratum: Phys. Rev. Lett. **78**, 1386 (1997).
- [29] B. Hammer, L.B. Hansen, and J. Nørskov, Phys. Rev. B. **59**, 7413 (1999).
- [30] A.D. Becke, J. Chem. Phys. **98**, 1372 (1993).
- [31] J. Harris and R.O. Jones, J. Phys. F **4**, 1170 (1974).
- [32] J.P. Perdew, M. Ernzerhof, and K. Burke, J. Chem. Phys. **105**, 9982 (1996).
- [33] Gaussian, Inc. NEWS, v. 5, (Wallingford, Connecticut 06492, summer 1994).
- [34] J. Neugebauer and B.A. Hess, J. Chem. Phys. **118** 7215 (2003).
- [35] I.N. Levine, *Quantum Chemistry, Fifth Edition* (Prentice Hall: Upper Saddle River, New Jersey 07458, 2000).
- [36] C. Daniel, Coord. Chem. Rev. **238-239**, 143 (2003).
- [37] B.R. Roos, in *New Challenges in Computational Quantum Chemistry*, edited by R. Broer, P.J.C. Aerts, and P.S. Bagus (published by the Department of Chemical Physics and Material Science Centre, University of Groningen: Groningen, The Netherlands, 1994), p. 12.

- [38] MOLCAS Version 5. K. Andersson, M. Barysz, A. Bernhardsson, M.R.A. Blomberg, D. L. Cooper, T. Fleig, M.P. Fülscher, C. de Graaf, B.A. Hess, G. Karlstörm, R. Lindh, P.-Å. Malmqvist, P. Neogrády, J. Olsen, B.O. Roos, A.J. Sadlej, M. Schütz, B. Schimmelpfennig, L. Seijo, L. Serrano-Andrés, P.E.M. Siegbahn, J. Stårling, T. Thorsteinsson, V. Veryazov, and P.-O. Widmark, Lund University, Sweden (2000).
- [39] F. Neese, *ORCA—an Ab Initio, Density-Functional and Semiempirical Program Package, Version 2.2, revision 74, March 2003* (Max Planck Institut für Bioanorganische Chemie, Mülheim, 2003).
- [40] P.C. Hariharan and J.A. Pople, *Theor. Chim. Acta* **28**, 213 (1973).
- [41] V. Rassolov, J.A. Pople, M. Ratner and T.L. Windus, *J. Chem. Phys.* **109**, 1223 (1998).
- [42] R. Pou-Amerigo, M. Merchan, I. Nebot-Gil, P.O. Widmark and B. Roos, *Theor. Chim. Acta*, **92**, 149 (1995)
- [43] C. Froese-Fischer, *J. Phys. B* **10** 1241, (1977).
- [44] T.H. Dunning Jr, B.H. Botch and J.F. Harrisson, *J. Chem. Phys.* **72**, 3419 (1980).
- [45] B.H. Botch, T.H. Dunning Jr and J.F. Harrisson, *J. Chem. Phys.* **75**, 3466 (1981).
- [46] A.J.H. Wachters, *J. Chem. Phys.* **52**, 1033 (1970).
- [47] C.W. Bauschlicher jr., S.R. Langhoff, and L.A. Barnes, *J. Chem. Phys.* **91**, 2399 (1989).
- [48] A. Schäfer, C. Huber, and R. Ahlrichs, *J. Chem. Phys.* **100**, 5829 (1994).
- [49] M.C. Zerner, *Int. J. Quant. Chem.* **35**, 567 (1989).
- [50] K.K. Stavrev and M.C. Zerner, *Int. J. Quantum Chem.* **65**, 877 (1997).
- [51] O. Castell, V.M. Garcia, C. Bo, and R. Caballol, *J. Comp. Chem.* **17**, 42 (1996).
- [52] E. Cancès, *J. Chem. Phys.* **114**, 10616 (2001).

- [53] M.J. Frisch, G.W. Trucks, H.B. Schlegel, G.E. Scuseria, M.A. Robb, J.R. Cheeseman, V.G. Zakrzewski, J.A. Montgomery, R.E. Stratmann, J.C. Burant, S. Dapprich, J.M. Millam, A.D. Daniels, K.N. Dudin, M.C. Strain, O. Farkas, J. Tomasi, V. Barone, M. Cossi, R. Cammi, B. Mennucci, C. Pomelli, C. Adamo, S. Clifford, J. Ochterski, G.A. Petersson, P.Y. Ayala, Q. Cui, K. Morokuma, D.K. Malick, A.D. Rabuck, K. Raghavachari, J.B. Foresman, J. Gomperts, R.L. Martin, D.J. Fox, T. Keith, M.A. Al-Laham, C.Y. Peng, A. Nanayakkara, C. Gonzalez, M. Challacombe, P.M.W. Gill, B.G. Johnson, W. Chen, M.W. Wong, J.L. Andres, M. Head-Gordon, E.S. Replogle, and J.A. Pople, GAUSSIAN 98, Revision A.7, Gaussian Inc., Pittsburgh, PA, 1998.
- [54] AMSTERDAM DENSITY FUNCTIONAL Program, Theoretical Chemistry, Vrije Universiteit, Amsterdam, the Netherlands, <http://www.scm.com>
- .
- [55] T. Ziegler, A. Rauk, and E.J. Baerends, *Theor. Chim. Acta* **43**, 261 (1977).
- [56] C. Daul, *Int. J. Quant. Chem.* **52**, 867 (1994).
- [57] C.A. Daul, K.G. Doclo, and A.C. Stückel, in *Recent Advances in Density Functional Methods, Part II*, edited by D.P. Chong (World Scientific, Singapore, 1997) p. 61.
- [58] T. Mineva, A. Goursot, and C. Daul, *Chem. Phys. Lett.* **350**, 147 (2001).
- [59] A. Hauser, in *Topics in Current Chemistry*, P. Gütlich editor (Springer-Verlag : Heidelberg, *in press*).
- [60] R. Åkesson, L.G.M. Pettersson, M. Sandström, and U. Wahlgren, *J. Am. Chem. Soc.* **116**, 8691 (1994).
- [61] F. Neese and G. Olbrich, *manuscript in preparation*.
- [62] R. Åkesson, L.G.M. Pettersson, M. Sandström, and U. Wahlgren, *J. Am. Chem. Soc.* **116**, 8713 (1994).
- [63] Y. Marcus, *Chem. Rev.* **88**, 1475 (1988).
- [64] T.K. Sham, J.B. Hastings, and M.L. Perlman, *J. Am. Chem. Soc.* **102**, 5904 (1980).
- [65] Hamilton, *Acta Cryst.* **15**, 353 (1962).

- [66] W.H. Baur, *Acta Cryst.* **17**, 1167 (1964).
- [67] H. Montgomery, R.V. Chastain, J.J. Natt, A.M. Witkowska, and E. Lingafelter, *Acta Cryst.* **22**, 775 (1967).
- [68] J. Do, X. Wang, and A.J. Jacobson, *J. Solid State Chem.* **143**, 77 (1999).

VI Appendix : Multiplet Sum Method

The basic idea of the multiplet sum method (MSM) is that DFT should provide a good description of states which are well-described by single-determinantal wave functions. Then, since it is well-known that atomic multiplet energies can often be expressed to first-order as weighted linear combinations of the energies corresponding to single-determinant states, it suffices to find appropriate linear combinations, taking care to eliminate integrals which should be equivalent by symmetry. In the present case, the energy of the atomic multiplet states is expressed as a linear combination of only three nonredundant single determinant energies, namely as

$$E[{}^5D] = -2.1000E[\Phi_1] + 0.4333E[\Phi_2] + 2.6667E[\Phi_3] \quad (3.23)$$

$$E[{}^1I] = -0.3000E[\Phi_1] + 0.6333E[\Phi_2] + 0.6667E[\Phi_3], \quad (3.24)$$

where

$$\Phi_1 = |\bar{d}_{x^2-y^2}d_{x^2-y^2}d_{z^2}\bar{d}_{z^2}\bar{d}_{xz}d_{xz}| \quad (3.25)$$

$$\Phi_2 = |d_{yz}\bar{d}_{yz}\bar{d}_{x^2-y^2}d_{x^2-y^2}\bar{d}_{xz}d_{xz}| \quad (3.26)$$

$$\Phi_3 = |\bar{d}_{xy}\bar{d}_{yz}\bar{d}_{x^2-y^2}d_{x^2-y^2}\bar{d}_{xz}d_{xz}|, \quad (3.27)$$

and overbars indicate spin β orbitals.

TABLE 3.4: Experimental $[Fe(H_2O)_6]^{2+}$ geometries. Bond distances in Å, bond angles in degrees.

$[Fe(H_2O)_6]^{2+}$			
R(FeO)	R(OH)	$\angle HOH$	$\angle OFeO'$
Fe(II) salts in solution ^a			
2.114			
	Fe(II) salts in solution ^b		
2.095			
	Fe(II) salts in solution ^c		
2.12			
	Fe(II) salts in crystal ^d		
2.13			
	$FeSiF_6 \cdot 6H_2O^e$		
2.146	0.924	111.9	91.4
	0.920		88.6
	$FeSO_4 \cdot 7H_2O^f$		
2.068			90.5
2.144			92.9
2.136			94.0
	$FeSO_4 \cdot 7H_2O^g$		
2.096			90.5
2.109			91.0
2.188			92.4
	$Fe(NH_4)_2(SO_4)_2 \cdot 6H_2O^h$		
2.156			89.3
2.136			90.9
2.086			91.2
	$[TMA]_2[Fe(H_2O)_6]Mo_8O_{26}^i$		
2.11			
2.10			

^a Average values from different X-ray and EXAFS studies [63].

^b From EXAFS data [64].

^c From X-ray data [64].

^d Average value originating from different X-ray studies [64].

^e Neutron scattering crystal data [65]. The two angles correspond to the two different angles of a D_{3d} structure.

^f Melanterite, parameters from site 1 in the crystal which was found to have two different D_{2h} sites [66]. An OH bond distance of 0.97 Å and an HOH angle of 109.5° was assumed by the author.

^g Melanterite, parameters from site 2 in the crystal which was found to have two different D_{2h} sites [66]. An OH bond distance of 0.97 Å and an HOH angle of 109.5° was assumed by the author.

^h Ammonium Tutton salt. [67].

ⁱ X-ray crystal data [68]. The $[Fe(OH_2)_6]^{2+}$ octahedron is stretched along the three-fold axis. Two slightly different OH distances are reported for the water molecules. Authors indicate that all reported values, except bond angles, have been corrected for thermal motion.

TABLE 3.5: ${}^1A_{1g}$ $[Fe(H_2O)_6]^{2+}$ geometry. A D_{3d} geometry has been assumed, neglecting hydrogens. The OFeO angle given is between oxygens related by the C_{3v} symmetry operation. The complex geometry becomes O_h when this angle is 90° .

Method	${}^1A_{1g}$ $[Fe(H_2O)_6]^{2+}$	
	R(Fe-O) (Å)	\angle O-Fe-O (°)
MOLCAS		
CASSCF(12,10)	2.077	90.0
GAUSSIAN		
Xα/A'	1.917	96.9(1)
SVWN/A'	1.912	98.7(1)
BP86/A'	1.985	96.2(2)
BP86/C	2.018	94.5
BP86/E	1.996	90.0
BLYP/C	2.045	93.7
BLYP/E	2.025	90.0
PW91/A'	1.980	95.5(1)
PW91/C	2.014	94.5
PW91/E	1.992	90.0
B3LYP/A'	2.010	96.2(2)
B3LYP/C	2.032	90.0
B3LYP/E	2.018	90.0
ADF		
BP86/C"	2.010	94.3
PW91/C"	2.007	94.3
PBE/C"	2.011	94.4
RPBE/C"	2.048	94.2

TABLE 3.6: $[Fe(H_2O)_6]^{2+}$ LS-HS energy differences as calculated directly and after shifting the asymptotes of the dissociation curves to match the known experimental atomic $Fe^{2+} \ ^5D \rightarrow ^1I$ energy difference.

Method	LS-HS Energy Differences (cm^{-1})	
	Direct	Shifted ^a
SCF ^b	27 500.	
CASSCF ^b	23 200.	
CI ^b	17 100.	13 700.
CASSCF(6,5)/D	23 125.	
CASSCF(12,10)/D	21 180.	17 892.
CASPT2(6,5)/D	21 610.	
CASPT2(12,10)/D	16 185.	12 347.
SOCI	13 360.	
GAUSSIAN		
X α /A'	11 273.	
SVWN/A'	2 745.	
BP86/A'	9 069.	
BP86/C	8 505.	
BP86/E	9 374.	
BLYP/C	8 388.	
BLYP/E	9 084.	
PW91/C	8 959.	
PW91/E	9 761.	
B3LYP/C	11 456.	
B3LYP/E	11 783.	
ADF		
BP86/C"	8 696.	
PW91/C"	8 225.	
PBE/C"	9 056.	
RPBE/C"	11 844.	

^a CI atomic correction from Ref. [48]. Other atomic corrections calculated from data in Table 3.7.

^b Ref. [48].

TABLE 3.7: Comparison of atomic excitation energies.

Method	Fe ²⁺ Excitation Energy: $^5D \rightarrow ^1I$	
	Energy (cm ⁻¹)	Energy (eV)
Expt. ^a	29 897.3	3.70
<i>ab initio</i>		
CI ^b	33 800.	4.19
CASSCF(6,10)/6-31G*	33 185.	4.11
CASSCF(6,10)/ANO-S	32 850.	4.07
CASPT2(6,10)/6-31G*	33 735.	4.18
CASPT2(6,10)/ANO-S	32 130.	3.98
SORCI	33 200.	4.12
DFT ADF		
SVWN/TZ2P	29 988.	3.59
BP86/TZ2P	30 529.	3.79
PW91/TZ2P	29 845.	3.70
PBE/TZ2P	30 321.	3.76
RPBE/TZ2P	30 238.	3.75

^a $^5D \rightarrow ^1I$ transition from National Institute of Science and Technology (NIST) Atomic Spectra Database (http://physics.nist.gov/cgi-bin/AtData/main_asd). See text.

^b Ref. [48].

TABLE 3.8: Calculated bond length and energy differences between high and low state structures for selected basis sets and functionals. The results for basis set “E” were obtained by multiplying the ΔR_{HL} results for basis set C" by 1.08 and the ΔE_{LH} results for basis set C" by 1.07.

Method	$[Fe(H_2O)_6]^{2+}$	
	ΔR_{HL} (\AA) ^a	ΔE_{LH} (cm^{-1}) ^b
ADF		
BP86/C"	0.130	9255
PW91/C"	0.130	9250
PBE/C"	0.136	9256
RPBE/C"	0.139	11844
BP86/“E”	0.140	9903
PW91/“E”	0.140	9898
PBE/“E”	0.147	9904
RPBE/“E”	0.150	12673
GAUSSIAN		
BP86/C	0.135	8505
PW91/C	0.130	8959
BLYP/C	0.132	8632
B3LYP/C	0.132	11456
BP86/E	0.149	9374
PW91/E	0.145	9761
BLYP/E	0.141	9084
B3LYP/E	0.136	11783

^a $\Delta R_{HL} = R_{LS} - R_{HS}$ where R refers to the weighted average of the Fe-O bond distances (i.e. 4 times the equitorial Fe-O distance plus 2 times the axial Fe-O distance, and the whole quantity divided by 6.)

^b $\Delta E_{LH} = E_{LS} - E_{HS}$.

3-2 *Comparison of Density Functionals for Energy and Structural Differences Between the High- [$^5T_{2g} : (t_{2g})^4(e_g)^2$] and Low- [$^1A_{1g} : (t_{2g})^6(e_g)^0$] Spin States of Iron(II) Coordination Compounds : II. More Functionals and the Hexaminoferrous Cation, $[Fe(NH_3)_6]^{2+}$*

Comparison of Density Functionals for Energy and Structural Differences Between the High- [$^5T_{2g}$: $(t_{2g})^4(e_g)^2$] and Low- [$^1A_{1g}$: $(t_{2g})^6(e_g)^0$] Spin States of Iron(II) Coordination Compounds : II. More Functionals and the Hexaminoferrous Cation, $[Fe(NH_3)_6]^{2+}$

Antony Fouqueau, Mark E. Casida¹

Institut de Chimie Moléculaire de Grenoble (ICMG, FR-2607),
Équipe de Chimie Théorique, Laboratoire d'Études Dynamiques et Structurales de
la Sélectivité (LEDSS), UMR CNRS/UJF 5616
Université Joseph Fourier (Grenoble I), F38041 Grenoble, FRANCE

Latévi Max Lawson Daku, Andreas Hauser
Département de Chimie Physique, Université de Genève,
30 quai Ernest-Ansermet, CH-1211 Genève 4, SWITZERLAND

Frank Neese
Max Planck Institute für Bioanorganische Chemie,
Stiftstrasse 34-36, Mülheim an der Ruhr 45470, GERMANY

¹Mark.Casida@ujf-grenoble.fr

Abstract

The ability of different density functionals to describe the structural and energy differences between the high [$^5T_{2g}$: (t_{2g})⁴(e_g)²] and low [$^1A_{1g}$: (t_{2g})⁶(e_g)⁰] spin states of small octahedral ferrous compounds is studied. This work is an extension of our previous study of the hexaquoferrous cation, $[Fe(H_2O)_6]^{2+}$, [J. Chem. Phys. **120**, 9473 (2004)] to include a second compound - namely the hexaminoferrous cation, $[Fe(NH_3)_6]^{2+}$ - and several additional functionals. In particular, the present study includes the highly-parameterized generalized gradient approximations (GGAs) known as HCTH and the meta-GGA VSXC [which together we refer to as highly parameterized density functionals (HPDFs)], now readily available in the GAUSSIAN 03 program, as well as the hybrid functional PBE0. Since there are very few experimental results for these molecules with which to compare, comparison is made with best estimates obtained from second-order perturbation theory-corrected complete active space self-consistent field (CASPT2) calculations, with Spectroscopy ORiented Configuration Interaction (SORCI) calculations, and with Ligand Field Theory (LFT) estimations. While CASPT2 and SORCI are among the most reliable *ab initio* methods available for this type of problem, LFT embodies many decades of empirical experience. These three methods are found to give coherent results and provide best estimates of the adiabatic low-spin - high-spin energy difference, $\Delta E_{LH}^{\text{adia}}$, of 12 000 - 13 000 cm⁻¹ for $[Fe(H_2O)_6]^{2+}$ and 9 000 - 11 000 cm⁻¹ for $[Fe(NH_3)_6]^{2+}$. All functionals beyond the purely local approximation, produce reasonably good geometries, so long as adequate basis sets are used. In contrast, the energy splitting, $\Delta E_{LH}^{\text{adia}}$, is much more sensitive to the choice of functional. The local density approximation (LDA) severely over stabilizes the low-spin state with respect to the high-spin state. This "DFT Spin Pairing Energy Problem" persists, but is reduced, for traditional GGAs. In contrast the hybrid functional B3LYP underestimates $\Delta E_{LH}^{\text{adia}}$ by a few thousand wave numbers. The RPBE GGA of Hammer, Hansen, and Nørskov gives good results for $\Delta E_{LH}^{\text{adia}}$ as do the HPDFs, especially the VSXC functional. Surprisingly the HCTH functionals actually over correct the DFT Spin Pairing Energy Problem, destabilizing the low-spin state relative to the high-spin state. Best agreement is found for the hybrid functional PBE0.

I Introduction

The identification of the spin symmetry of the ground and low-lying excited states is important for the comprehension of chemical reactivity. However, many interesting

cases occur, especially among transition metal coordination compounds, where the competition between the splitting of nearly degenerate orbitals with the electron pairing energy makes the prediction of relative spin-state energetics difficult at best. Our own interest is in the spin crossover phenomenon in transition metal coordination complexes and its use in making molecular switches. A recent review of this area may be found in Ref. [1] while Refs. [2, 3] provide older reviews. The difficulty of carrying out high quality *ab initio* calculations for transition metal coordination compounds, combined with the desire to go beyond simple ligand field theory, has pushed several workers to make a detailed examination of density functional theory for the prediction of relative spin-state energetics [4, 5, 6, 7, 8, 9, 10]. Much of this work is described in a recent review of Harvey [9]. The focus has frequently been on the comparison of DFT calculations with experimental results for medium and large-sized compounds. So far, our own contribution to this area has been a detailed comparison of DFT calculations with ligand field and *ab initio* results for the relatively small “textbook example” of $[Fe(H_2O)_6]^{2+}$ [8]. Although experimental data is often only available indirectly for such small compounds through ligand field parameters, we believe that the ability to compare with the results of *ab initio* calculations, even if far from trivial, without having to worry about additional factors such as vibrational and environmental effects typically present in experimental data, provides a valuable complement to previous assessments of density functionals for larger compounds. In this paper, we extend our previous work to several new functionals which have only recently become widely available as well as to a second simple compound, $[Fe(NH_3)_6]^{2+}$, with a larger ligand field splitting than in $[Fe(H_2O)_6]^{2+}$.

Our paper is divided into the following sections. A review of the different functionals used in this study is given in the next section. Ligand field estimations are given in Sec. III. The technical details and the results of our *ab initio* reference calculations are given in Sec. IV. In Sec. V, we give our DFT results. We give first the computational details, then, we consider optimized geometries, and then, we give a comparison of HS and LS complex energies. Sec. VI summarizes.

II Density Functionals and the pairing energy problem

An important goal of this paper is the comparison of the relative ability of density functionals to treat different spin states. This may be termed the “DFT pairing energy problem”. Although this name is particularly appropriate when considering

applications to transition metal coordination complexes, the problem is of course a more general one. This section introduces the DFT pairing energy problem and provides a brief review of the different exchange-correlation (xc) functionals used in the present study.

Almost all applications of DFT are based on the Kohn-Sham formalism [11] and our work is no exception. It is now common practice to use the spin-density variant [12]. The different approximations considered here differ by the form of the exchange correlation energy, E_{xc} .

The traditional workhorse of DFT is the local density approximation (LDA), where the xc energy density at each point, \mathbf{r} , is approximated by the xc energy density of a homogeneous electron gas (HEG) whose densities, ρ_σ , are identical to the local densities, $\rho_\sigma(\mathbf{r})$. We have used the Vosko-Wilk-Nussair (VWN) parameterisation of the Ceperley-Alder quantum Monte-Carlo calculations [13] (This is the VWN5 option in GAUSSIAN 03, *not* the VWN option). The LDA works much better than might be expected given that molecular densities are not at all homogeneous. Part of the explanation is that the LDA works by error compensation: a small ($\sim 14\%$) underestimation of the exchange energy is compensated by a large ($\sim 250\%$) overestimation of the correlation energy [14]. This is often good enough for such properties as molecular geometries and vibrational frequencies [15].

In contrast, an accurate treatment of exchange effects would seem of critical importance when comparing energies of different spin states. According to a common textbook explanation of Hund's rule [16], exchange effects favor high-spin states by keeping parallel spin electrons separated, thereby minimizing electron repulsion. We have pointed out that this reasoning is heuristic, not rigorous [8]. Nevertheless it suggests that the underestimation of exchange in the LDA should lead to an artificial destabilization (stabilization) of high (low) spin states relative to low (high) spin states. This is the DFT pairing energy problem and it is by no means limited to just the LDA [8, 9].

A well-known problem of the LDA is that it seriously overestimates molecular bond energies. Early attempts at correcting the LDA by introducing gradient-correction terms were largely unsuccessful until the development of generalized gradient approximations (GGAs) in the 1980s. One of the most successful GGAs has been Becke's 1988 exchange-only GGA (B) which has the proper asymptotic limit for ϵ_{xc} [17]. It contains a single parameter whose value was obtained by fitting to the Hartree-Fock exchange energies of the noble gases. An example of a GGA correlation functional is that of Lee, Yang, and Parr (LYP) [18]. Acronyms for xc functionals obtained by combining exchange-only functionals and correlation-only

functionals are generated by simply concatenating the acronyms of the separate functionals (e.g. B + LYP → BLYP).

Further improvement was obtained in the 1990s by the use of hybrid functionals which consist of linear combinations of exact (i.e. Hartree-Fock) exchange and GGAs. The justification for such an approach was presented by Becke [19] using the adiabatic connection formalism of Harris and Jones [20]. Becke proposed the B3PW91 hybrid functional,

$$E_{xc} = E_{xc}^{LDA} + a_0(E_x^{HF} - E_x^{LDA}) + a_x E_x^{B88} + a_c E_c^{PW91}, \quad (3.28)$$

where a_0 , a_x , and a_c are semiempirical coefficients obtained by fitting to experimental data [21] (the “3” in B3PW91 refers to the presence of 3 semiempirical parameters). Becke’s parameters have been used without reoptimization, in the popular B3LYP functional [22]. More recently, and in keeping with their *ab initio* philosophy, Perdew, Burke, and Erznerhof provided an *ab initio* estimate of the hybrid mixing parameter[23]. This had been incorporated into the zero-parameter PBE functional (PBE0) [24].

Previous work applying DFT to spin-crossover and related problems made use of pre-1995 functionals. (An exception is Reiher’s work [5] which also mentions calculations with the PBE and PBE0 functional). All GGAs were found to suffer from the DFT spin pairing problem, although less so than does the LDA [4, 5, 6, 7]. In contrast the B3LYP functional appeared to over stabilize the HS state because of the presence of too much HF exchange. Depending on the functional, DFT frequently gave the wrong ground state spin symmetry in comparison with experiment. This suggested that a pragmatic solution to the problem would be to retune the a_0 mixing parameter in the B3LYP functional so as to minimize the DFT pairing energy problem. The result is the B3LYP* functional with 15 % HF exchange [5, 6, 7]. The same approach has been used before to reoptimize the B3LYP functional for other sensitive properties. The result is unfortunately property dependent, being 30 % HF exchange for excitation energies [25] and 5 % HF exchange for NMR chemical shifts [26]. So this is certainly not a universal solution. Another criticism of previous DFT work applied to spin-crossover systems is that the comparison has always been between calculated properties of gas phase molecules with experimental values obtained from condensed phase measurements. Environmental effects on spin-crossover can be huge since the high-spin/low-spin difference in the metal bond length is on the order of 0.2 Å. Dramatic changes in spin-crossover behavior in crystals have even been observed just by varying the intercalated solvent [27]. This is why we prefer in this and our previous work [8] to compare results from DFT with

the results of good *ab initio* calculations for gas phase molecules.

Much improved GGAs have become readily available since the previous work on spin-crossover. Furthermore there are drawbacks to Hartree-Fock exchange. It can be expensive to calculate compared to a pure GGA (depending upon the size of the system and skill of the programmer) and is known to give qualitatively incorrect results for systems, such as transition metal complexes, where there are a number of low-lying virtual orbitals. Highly-Parameterized Density Functionals (HPDFs) provide an alternative to hybrid functionals at the cost of a large number of parameters to optimize. In one approach to making a HPDF, Voorhis and Scuseria [28] developed a Taylor series-like density matrix expansion to obtain the so-called VSXC exchange-correlation functional [29] which has 21 parameters. It is in fact a meta-GGA, since it depends not only on the density and its gradients but also on the orbital-dependent local kinetic energy density, τ . In another approach, Hamprecht, Cohen, Tozer and Handy [30] developed a series of HPDFs whose 15 parameters were fit simultaneously to experimental data and to *ab initio* xc potentials. The resultant HCTH93, HCTH147, and HCTH407 are distinguished by the number of molecules (93, 147, or 407) in the parameter training set. The HPDFs often do as well as, if not better than, previous hybrid functionals. They are included in the present assessment of density functionals for application to spin-crossover systems. All the functionals used in this work are reported in Table 3.9.

TABLE 3.9: Summary of functionals used in the present study.

Functional	Year	Citation	Type
X α	1951	[64]	Local, exchange-only
LDA	1980 ^a	[11]	Local, exchange-correlation
P86	1986	[77]	GGA, correlation-only
B	1988	[17]	GGA, exchange-only
LYP	1988	[18]	GGA, correlation-only
PW91	1991	[78]	GGA, exchange-correlation
B3LYP	1994	[22]	hybrid, exchange-correlation
PBE	1996	[23]	GGA, exchange-correlation
RPBE	1998	[79]	GGA, exchange-correlation
HCTH93	1998	[30]	GGA, exchange-correlation
HCTH107	1998	[30]	GGA, exchange-correlation
HCTH407	1998	[30]	GGA, exchange-correlation
VSXC	1998	[29]	meta-GGA, exchange-correlation
PBE0	1999	[24]	hybrid, exchange-correlation
B3LYP*	2002	[5]	hybrid, exchange-correlation

^a VWN parameterization [13]

III Ligand Field Theory

High spin-low spin bond length differences,

$$\Delta r_{HL} = r_{HS} - r_{LS} , \quad (3.29)$$

may be estimated using a simple model described by Figgis and Hitchmann (ref. [31] p. 146). Although not used for this purpose by Figgis and Hitchmann, the model can also be used to estimate the adiabatic energy difference,

$$\Delta E_{LH}^{\text{adia}} = E_{LS}(r_{LS}) - E_{HS}(r_{HS}) . \quad (3.30)$$

This model is briefly reviewed here for application in the present combox.

We assume strictly octahedral $[FeL_6]^{2+}$ with Fe-L distance r_{LS} in their LS $[^1A_{1g}; (t_{2g})^6(e_g)^0]$ state and r_{HS} in their HS $[^5T_{2g}; (t_{2g})^4(e_g)^2]$ state. Of course, the HS state is electronically degenerate in O_h symmetry and so will Jahn-Teller distort, but we presume that the distortion is small enough to be neglected. Since H_2O and NH_3 are relatively weak ligands, the spin pairing energy exceeds the ligand field splitting,

$$\Delta = \epsilon(e_g) - \epsilon(t_{2g}) , \quad (3.31)$$

so that the ground state configuration is HS. The HS→LS excitation energy at fixed r is,

$$\Delta E_{LH}(r) = E_{LS}(r) - E_{HS}(r) = -m\Delta(r) + S , \quad (3.32)$$

where

$$m = 2 \quad (3.33)$$

is the number of electrons de-excited from the e_g to the t_{2g} orbitals and the spin pairing energy, S , is assumed independent of r . Thus the vertical excitation energy is (Fig. 3.5)

$$\Delta E_{LH}^{\text{vert}} = \Delta E_{LH}(r_{HS}) . \quad (3.34)$$

Two approximations allow us to express $\Delta E_{LH}^{\text{adia}}$ in terms of $\Delta E_{LH}^{\text{vert}}$. The first is the harmonic approximation for the breathing mode of the HS state,

$$E_{HS}(r) = E_{HS}(r_{HS}) + \frac{N}{2}k_{HS}(r_{HS} - r)^2 , \quad (3.35)$$

where k_{HS} is the breathing mode force constant and $N=6$ is just the number of ligands. The second approximation is for the geometry dependence of the ligand

field splitting. From various considerations (see ref. [31] pp. 39 and 69),

$$\Delta(r) = \Delta_{HS} \left(\frac{r}{r_{HS}} \right)^{-n}, \quad (3.36)$$

where typically $5 < n < 6$, with $n \approx 5$ being a reasonable choice. Expanding

$$\left(1 + \frac{r - r_{HS}}{r_{HS}} \right)^{-n} = 1 - n \frac{r - r_{HS}}{r_{HS}} + \frac{n(n+1)}{2} \left(\frac{r - r_{HS}}{r_{HS}} \right)^2 + \dots, \quad (3.37)$$

and truncating to linear order gives the expression actually used in the model, namely

$$\Delta(r) \approx \Delta_{HS} \left(1 + n \frac{r_{HS} - r}{r_{HS}} \right). \quad (3.38)$$

The two aforementioned approximations lead to

$$\begin{aligned} E_{LS}(r) - E_{HS}(r_{HS}) &= \Delta E_{LH}(r) + \frac{N}{2} k_{HS} (r_{HS} - r)^2 \\ &= -m\Delta(r) + S + \frac{N}{2} k_{HS} (r_{HS} - r)^2 \\ &= -m \left(1 + n \frac{r_{HS} - r}{r_{HS}} \right) \Delta_{HS} \\ &\quad + S + \frac{N}{2} k_{HS} (r_{HS} - r)^2 \end{aligned} \quad (3.39)$$

Minimizing with respect to r leads to

$$\Delta r_{HL} = \frac{nm}{N} \frac{\Delta_{HS}}{k_{HS} r_{HS}}. \quad (3.40)$$

This formula is known to work well in a number of cases (ref [31], Table 7.1, p. 147). For $r = r_{LS}$ in Eq. (3.39), we obtain the formula for the adiabatic excitation energy

$$\Delta E_{LH}^{\text{adia}} = \Delta E_{LH}^{\text{vert}} - \frac{N}{2} k_{HS} (\Delta r_{HL})^2. \quad (3.41)$$

Note that there is something clearly disturbing about this latter formula since it implies the same force constant for the LS state as for the HS state [see Eq. (3.39)]. This is a consequence of keeping no more than linear terms in the expansion of $\Delta(r)$. Keeping quadratic terms leads to unphysical result that $k_{LS} < k_{HS}$ and results in an even more serious degradation of calculated Δr_{HL} when compared with experiment.

These equations are practical and reasonably reliable. They are practical because geometric quantities such as k_{HS} and r_{HS} are measurable or (as we shall see) relatively easy to calculate. The ligand field splitting may be estimated as $\Delta(r_{HS}) = fg$

using tabulated data for f and g . The vertical excitation energy $\Delta E_{LH}^{\text{vert}}$ may be determined from the appropriate Tanabe-Sugano diagram and appropriate values of the Racah parameters B and C ¹. The reliability of the equations comes from decades of LFT experience [31]. The results are quantitatively quite useful but the presence of rough approximations at some steps emphasizes the desirability of a more rigorous model.

Input parameters and calculated Δr_{HL} and $\Delta E_{HL}^{\text{adia}}$ are given in Table 3.10 for the two molecules treated in this paper.

TABLE 3.10: Parameters entering into and results of the simple model described in the text. Experimental data and corresponding results are given in parentheses.

LFT parameters	
$[Fe(NH_3)_6]^{2+}$	$[Fe(H_2O)_6]^{2+}$
From LFT	
Δ_{HS}^a	$12\ 500\ \text{cm}^{-1}$
$\Delta E_{LH}^{\text{vert}} b$	$9\ 200\ \text{cm}^{-1}$
From DFT ^c	
ν_{HS}	$304\ \text{cm}^{-1}$
r_{HS}	$2.260\ \text{\AA}$
Results	
k_{HS}	$0.93 \times 10^5\ \text{dyn.cm}^{-1}$
Δr_{HL}	$1.26 \times 10^5\ (1.5 \times 10^5)\ \text{dyn.cm}^{-1}$
$\Delta E_{LH}^{\text{adia}}$	$0.198\ \text{\AA}$
	$5\ 000\ \text{cm}^{-1}$
	$0.126\ (0.11)\ \text{\AA}$
	$12\ 000\ (12\ 500)\ \text{cm}^{-1}$

^a $\Delta_{HS} = fg$ (f and g are tabulated, see e.g. [31]p.219).

^b From the d⁶ Tanabe-Sugano diagram and appropriate values of the Racah parameters B and C (see text).

^c These are averages quantities over several DFT results.

^d From reference [80].

^e Averaged over known structures.

¹Racah parameters: LFT estimations very much depend upon which Tanabe-Sugano diagram one takes. The one most often reproduced in the literatures sets $C/B = 4.8$ which according to Tanabe and Sugano is the correct ratio for Co(III). We use the ratio 4.41 which according to Tanabe and Sugano is more appropriate for Fe(II). This diagram is the one we can find in the book by Figgis and Hitchman [31]. Then, we have to choose the value to take for B : Figgis give $B = 1080\ \text{cm}^{-1}$ with $C/B = 4.42$, Tanabe-Sugano [32] give $B = 917\ \text{cm}^{-1}$ with $C/B = 4.41$, Griffith [33] gives $B = 1058\ \text{cm}^{-1}$ with $C/B = 3.69$, and Schäfer [34] gives $B = 897\ \text{cm}^{-1}$ with $C/B = 4.3$. Then, we have to reduce the value of B by an orbital reduction factor β . In order to stay consistent, we choose to take all values and Tanabe-Sugano diagram as given by Figgis and Hitchman.

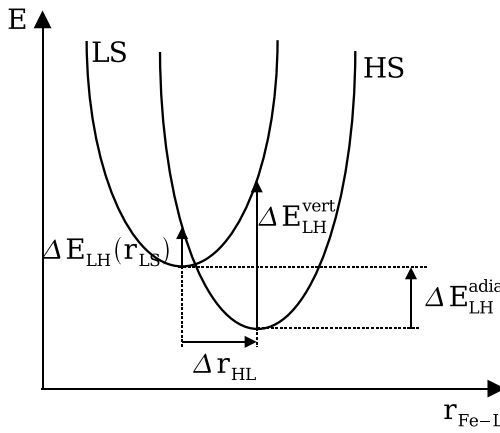


FIGURE 3.5: Representation of the potential wells for the quintet and singlet states with the different quantities cited in the text

IV *ab initio* reference calculations

Our objective is to assess the relative performance of different density functionals for calculation of the properties of small Fe(II) octahedral coordination complexes by direct comparison with zero-temperature gas phase non relativistic *ab initio* quantum chemistry calculations of the highest possible quality, in the sense that they are at the limit of what is currently computationally feasable. We have carried out such calculations using two different computational methods, namely (i) the well-established method of complete active space (CAS) [35] multiconfiguration self-consistent field (SCF) calculations with and without second-order perturbation theory (PT2) corrections [36, 37], and (ii) spectroscopy oriented configuration interaction (SORCI) [38] calculations based on the difference dedicated configuration interaction (DDCI) method of Malrieu and co-workers [39, 40]. There is an extensive experience with CASPT2 calculations and its strengths and limitations are now well-known [41]. In particular, as will be made clear below, the size of the CAS grows rapidly as new orbitals are included, so that only a limited number of orbitals may be included in the CAS. Furthermore the inclusion of dynamical correlation at the PT2 level is often insufficient for 3d transition metal complexes, partly because of practical difficulties using very large basis sets and partly because of the restriction to second order in the perturbation theory. The deficiencies are countered by the use of empirical ‘atomic corrections’. In principle, the DDCI approach used in the SORCI method allows the accurate calculation of differential dynamical correlation with a smaller number of configurations. The SORCI method is relatively new and so necessarily less well characterized, though all indications are that it works well.

A CASSCF and CASPT2 calculations

1 Computational details

Our CASSCF and CASPT2 calculations were carried out with the program MOLCAS [42]. The orbital basis sets used were of 6-31G** quality [43, 44]. This corresponds to basis D in paper I, which was the largest basis set (178 functions) for which we could perform CASPT2 calculations on the computers available to us. The choice of the active space was governed by the desire to include a maximum of orbitals in the CAS while keeping the calculations down to a practical size. In particular, we have accounted for the so-called “3d double shell effect” [45, 46, 47] which says that the inclusion in the CAS of all molecular orbitals containing significant metal 3d contributions is critical for describing the large radial correlation effects present in the type of complex being studied here. This means that the CASSCF performs a full CI calculation on 12 electrons distributed over 10 orbitals, denoted CASSCF(12,10) and CASPT2(12,10). See paper I for additional details regarding the choice of active space. Automatic structure optimization and frequency calculations (to confirm minima) were carried out at the CASSCF level. This was not possible at the CASPT2 level where only single point calculations were performed. As already, mentionned, although we have carried out CASSCF and CASPT2 calculations close to the limit of what we can do on the computers available to us, such calculations are known to require an empirical atomic correction for missing dynamical correlation [48, 8]. This correction which is described in greater detail in paper I, assumes that the missing correlation is primarily localized on the iron atom and so may be estimated by comparing CASPT2 calculations space and orbital basis set with known experimental excitation energies. The HS-LS energy difference is calculated as (paper I)

$$\Delta E_{LH}^{\text{shifted}} = \Delta E_{LH}^{\text{direct}} + (\Delta E_{\text{atom}}^{\text{expt}} - \Delta E_{\text{atom}}^{\text{calc}}) . \quad (3.42)$$

2 Results

The necessary *ab initio* calculations are far from trivial. An often cited objective for “chemical accuracy” is 1 kcal/mol (350 cm^{-1}), but errors of 5 kcal/mol (1750 cm^{-1}) are more typical in good *ab initio* calculations [49, 50]. Electron correlation is especially difficult to treat in compounds containing 3d transition metals such as Fe. In our earlier work [8], our best estimate of the true (i.e. Complete CI) value of $\Delta E_{LH}^{\text{adia}}$ for $[Fe(H_2O)_6]^{2+}$ were 12350 cm^{-1} , based upon a CASPT2 calculation with a 3000 cm^{-1} atom-based empirical shift [8] (labeled CASPT2corr) needed to in-

clude important dynamic correlation effects not present in the CASPT2 calculation, and 13 360 cm⁻¹, obtained by the SORCI method with its difference-dedicated CI philosophy [39, 40]. The same strategy applied to [Fe(NH₃)₆]²⁺ in the context of the present work gives 9 120 cm⁻¹ from CASPT2 with the atom-based empirical shift.

B SORCI calculations

1 Computational details

Spectroscopy oriented configuration interaction (SORCI) calculations were carried out with the ORCA package [51] at the B3LYP/TZVP optimized geometries. The SORCI method is a combination of several different many-body techniques. It is described in detail in Ref. [38]. We confine ourselves here to recalling some of the basic steps taken during the calculation and to defining the basis sets and thresholds that we used.

Two relatively extensive basis sets were used in the calculations. Basis C (312 functions) consists of the triple- ζ (TZV) basis of Schäfer *et al.* [52] augmented with one set of *p*-functions for H (5s1p contracted to 3s1p; 311/1) and two sets of *d*-functions for N (11s6p2d contracted to 5s3p2d; 62111/411/11) with polarization exponents taken from the TURBOMOLE library. [Basis sets were obtained from the ftp server of the quantum chemistry group at the University of Karlsruhe (Germany) under <ftp://ftp.chemie.uni-karlsruhe.de/pub/basen>]. The metal in Basis C is described by the Wachters basis [53] with two sets of *p*-type polarization functions and three *f*-sets contracted in a 2,1 fashion by Bauschlicher and co-workers [54] (14s11p6d3f contracted to 8s6p4d2f; 62111111/331211/3111/21). The second basis set (Basis D, 423 functions) is more extensive and features a second set of *p*-polarization functions on H and an additional *f*-set for N (TZVPP) basis. The metal is described by the recently developed quadruple- ζ [55] quality basis of the Ahlrichs group which already contains diffuse *p*- and *d*-sets and is augmented with three sets of *f*-polarization functions (QZVP, the *g*-function in the original QZVP basis was deleted; 24s18p10d3f contracted to 11s6p5d3f; 11,411111111/951111/61111/111). The fitting basis for the resolution of the identity (RI) approximation used in the ORCA correlation package where those developed for RI-MP2 by Weigend *et al.* [56] and in the case of the QZVP iron basis was taken from unpublished work in the TURBOMOLE library. For technical reasons *h*- and *i*-functions contained in this fit basis had to be deleted.

A simplified flow diagram of the SORCI algorithm is given in Fig. 3.6. The first step is to construct a set of occupied and virtual orbitals whose configurations define an initial reference space S_0 . This was done starting from spin-averaged Hartree-Fock

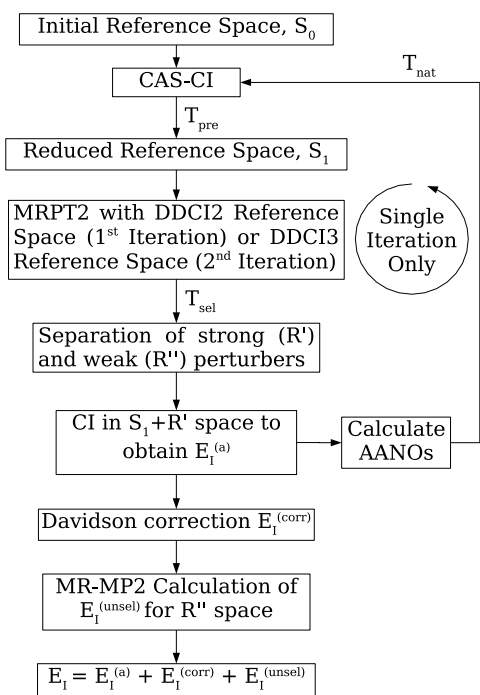


FIGURE 3.6: Diagram of the SORCI algorithm (based on Fig. 1 of Ref. [38]), showing the principle steps and the three thresholds, T_{pre} , T_{nat} and T_{sel} .

(SAHF) orbitals [57] with six electrons in the five iron d -based molecular orbitals. The virtual orbitals were improved by diagonalizing a $N-1$ electron Fock operator in the virtual space where the additional hole is smeared out over all occupied orbitals participating in the correlation calculation [58]. Since the core orbitals with energies less than -5 E _{h} (E _{h} =1 hartree) were frozen this amounts to the full valence space. No virtual orbitals were neglected in the correlation calculations.

In the next step the orbital space is partitioned into internal, active and external (virtual) MOs and a CAS-CI calculation is performed in the active space (in the present case, this is a CAS(6,5)). From this small CI the configurations with a weight exceeding the threshold value T_{pre} (10^{-4} in this study) are selected and the Hamiltonian is diagonalized again in the reduced reference space to give the zeroth order multiconfigurational many electron wavefunctions $|0\rangle$ and energies E_0 for each state of interest.

This is followed by second-order Møller-Plesset perturbation theory (MRPT2) within a restricted set of excited configurations, namely within a difference-dedicated configuration interaction (DDCI) set. The density corresponds to the zeroth order states used to define a spin-averaged Fock-type operator the diagonal elements of which are used to define orbital energies which are used in the diagonal definition of

the zeroth order Hamiltonian

$$\hat{H}_{0,\text{diag}} = \sum_p \epsilon_p \hat{a}_p^\dagger \hat{a}_p \quad (3.43)$$

(details are found in Refs. [59, 60]). The program proceeds by constructing the properly spin-coupled single- and double-excitations $|I\rangle$ relative to each individual reference configuration in $|0\rangle$. Configurations are sorted into the weakly and strongly interacting subspaces according to the diagonal second order energy estimate, *i.e.* configuration state functions (CSFs) with

$$|\langle 0 | \hat{H} | I \rangle|^2 \left(\langle I | \hat{H}_{0,\text{diag}} | I \rangle - \langle 0 | \hat{H}_{0,\text{diag}} | 0 \rangle \right)^{-1} \geq T_{\text{sel}} \quad (3.44)$$

are part of the strongly interacting subspace R' and the remaining CSFs are part of the weakly interacting subspace R'' (\hat{H} is the full Born-Oppenheimer Hamiltonian). The threshold T_{sel} was set as $10^{-6} E_h$ in this study. After the selection step, which is initially carried out in the difference-dedicated CI ‘2’ (DDCI2) subspace of the first-order interacting space (FOIS), the $R' + S_1$ space is diagonalized. This makes the method immune to intruder states and includes the electronic relaxation of the reference wavefunction in the dominant part of the “correlation field”.

The resulting CI first-order densities are averaged over all states of interest and the approximate average natural orbitals (AANOs) with significant occupations (according to a third threshold T_{nat} set to 10^{-5} in this study) are produced for the second step of the procedure. This second step is a selected DDCI3 calculation in the AANO basis.

The CI energies after this second step are corrected for higher than double excitations using the approximate multireference Davidson correction [61, 62], E_I^{corr} , and the energetic effect of the R'' space, E_I^{unsel} , is calculated with diagonal MR-MP2 theory as described above using the relaxed reference part of the final DDCI3 wavefunction.

2 Results

SORCI calculations were carried out for the B3LYP/TZVP HS and LS optimized structures with the two relatively extensive basis sets C and D. The larger basis set D leads to a further increase in transition energies by $\sim 1000 \text{ cm}^{-1}$ compared to the already rather flexible basis C (Table 3.11).

Since SORCI does not lend itself well to the calculation of adiabatic transition energies due to the neglect of inactive double excitations, some estimate of the relax-

TABLE 3.11: Vertical and Adiabatic transition energies calculated with the SORCI method for the $[Fe(NH_3)_6]^{2+}$ complex at the B3LYP/TZVP optimized HS and LS geometries

Basis	Vertical transition energies	
	$\Delta E_{LH}^{\text{vert}}(\text{HS})$	$\Delta E_{LH}^{\text{vert}}(\text{LS})$
C	16 635 cm ⁻¹	5 455 cm ⁻¹
D	17 780 cm ⁻¹	6 315 cm ⁻¹
Adiabatic transition energies		
Basis	$\Delta E_{LH}^{\text{adia}}(1)$	$\Delta E_{LH}^{\text{adia}}(2)$
C	10 247 cm ⁻¹	10 538 cm ⁻¹
D	11 293 cm ⁻¹	11 398 cm ⁻¹
$\Delta E_{LH}^{\text{adia}}(\text{SORCI})$		
	11 278 cm ⁻¹	13 277 cm ⁻¹

ation energy for each electronic state needs to be provided. At the B3LYP/TZVP level the relaxation energy for the HS state was found to be 6488 cm⁻¹ while that of the low spin state was calculated to be 5083 cm⁻¹. If these numbers are combined with the SORCI results for the vertical transition energy in order to arrive at an estimate of the adiabatic transition energy, two equivalent cycles (leading to estimates $\Delta E_{LH}^{\text{adia}}(1)$ and $\Delta E_{LH}^{\text{adia}}(2)$) can be conceived which would lead to identical results if all energies would be calculated with the same method and basis set:

$$\begin{aligned}\Delta E_{LH}^{\text{adia}}(1) &= \Delta E_{LH}^{\text{vert}}(\text{HS}) - \Delta E_{LH}^{\text{relax}}(\text{LS}) \\ \Delta E_{LH}^{\text{adia}}(2) &= \Delta E_{LH}^{\text{vert}}(\text{LS}) + \Delta E_{LH}^{\text{relax}}(\text{HS})\end{aligned}\quad (3.45)$$

Here $\Delta E_{LH}^{\text{vert}}(\text{HS})$ and $\Delta E_{LH}^{\text{vert}}(\text{LS})$ are the vertical transition energies at the optimized HS and LS geometries respectively and $\Delta E_{LH}^{\text{relax}}(\text{LS})$ and $\Delta E_{LH}^{\text{relax}}(\text{HS})$ are the relaxation energies for the low-spin and and high-spin states respectively. They are defined as the energy of the low-spin state at the high-spin geometry minus the energy of the low-spin state at the low-spin geometry and equivalently for the high-spin state. The results are summarized in Table 3.11. The entry $\Delta E_{LH}^{\text{adia}}(\text{SORCI})$ is the straightforward adiabatic energy from SORCI calculations which do not take any inactive double excitation into account and should therefore be viewed with caution.

In general, the results are pleasingly consistent in the sense that $\Delta E_{LH}^{\text{adia}}(1)$ and $\Delta E_{LH}^{\text{adia}}(2)$ differ only by ~ 200 cm⁻¹ which is within the uncertainty of the method. The results for Basis C and Basis D differ by ~ 1000 cm⁻¹ and we conclude that the best estimate of the adiabatic transition energy from SORCI is $\sim 11\,000$ cm⁻¹ which is in reasonable agreement with the empirically corrected CASPT2 calculations.

V Validation of Density Functionals

The quality of approximate density functionals for exchange-correlation (xc) energy has gradually improved since the introduction of the local density approximation by Kohn and Sham [11] (some would say, since the exchange functional of Dirac [63] and subsequent X α approximation [64]). This improvement seemed to have accelerated since the introduction of GGAs in the 1980s and of hybrid functionals in the 1990s. It is now *de rigueur* for the functionals to be tested against the popular G n ($n=1,2,3$) sets of comparison data [65, 66, 67, 68]. However this is a necessary, but not a sufficient, test of the general validity of an xc functional. The G n sets are notoriously weak in test data for compounds containing transition metals. The G n test sets also tend to be heavily weighted towards “normal” covalent-type bonding. Our interest is in the relative geometries and energetics of transition metals complexes in different spin states. In this section we present results extending our previous work [8] on $[\text{Fe}(\text{H}_2\text{O})_6]^{2+}$ to several new functionals and present results for $[\text{Fe}(\text{NH}_3)_6]^{2+}$, a compound not previously considered but which brings us (arguably) closer to the FeN₆ configuration often seen in Fe(II) spin-crossover compounds [3].

A Computational details

The DFT calculations reported here were carried out with GAUSSIAN [69], ORCA [51], and ADF [70]. These programs differ in several respects, among the algorithmic differences, the most important is certainly that GAUSSIAN and ORCA use basis sets of Gaussian-type orbitals (GTOs) while ADF uses Slater-type orbital (STO) basis sets. These two types of basis sets behave rather differently and it is difficult to say *a priori* which GTO and STO basis sets should be of comparable quality, though calculations carried out with identical functionals and the two types of basis sets permit a rough correspondence to be made. This was done in section IV.C of paper I where it was pointed out that the TZ2P STO basis gave results comparable to those obtained with a TZVP GTO basis set. The basis sets used in this study are summarized in Table 3.12.

At the SCF level, convergence to the wrong electronic state was less frequently encountered than in the previous study with the previous version of GAUSSIAN [71]. This problem has apparently been overcome by new convergence algorithms and in particular, the more robust fractional occupation convergence algorithm [72, 73].

TABLE 3.12: Summary of basis sets used in this work.

Name	Fe	Basis Sets		Size
		N	H	
Contracted Gaussian-Type Orbitals				
A	6-31G* ^a	6-31G* ^b	6-31G** ^b	208
B	TZVP Ahlrichs ^c	TZVP Ahlrichs ^c	TZVP Ahlrichs ^c	255
C	(8s6p4d2f) Wachters ^d	TZVP Ahlrichs ^{e,c}	TZVP Ahlrichs ^{e,c}	312
D	(11s6p5d3f) QZVP Ahlrichs ^f	TZVPP Ahlrichs ^{e,c}	TZVPP Ahlrichs ^{e,c}	423
Slater-Type Orbitals				
A"	DZ ^g	DZ ^g	DZ ^g	137
C"	TZ2P ⁺ ^g	TZ2P ^g	TZ2P ^g	457

^a Reference [44]^b Reference [43]^c Reference [81, 52]^d Reference [53, 54]^e Polarization exponents taken from TURBO MOLE library^f Reference [55]^g Taken from ADF library

B Optimized Geometries

We first consider the geometrical structures of the free gas phase cations. As remarked in our earlier work [8], available comparison data does not allow us to make fine distinction between $[Fe(H_2O)_6]^{2+}$ geometries optimized using different density functionals. This is partly because all functionals beyond the LDA level (except perhaps the RPBE functional) give relatively good geometries and partly because available experimental data is for crystals where cation structure is heavily influenced by (among other things) the nature of the counter ions. The same observation may be made for $[Fe(NH_3)_6]^{2+}$. We thus focus on identifying trends among geometries obtained using various functionals.

Both $[Fe(H_2O)_6]^{2+}$ and $[Fe(NH_3)_6]^{2+}$ are octahedral complexes. According to the simple LFT model, the HS electronic state is degenerate in O_h symmetry. We should therefore expect a Jahn-Teller distortion. As evidenced by our earlier work [8], this effect is small in $[Fe(H_2O)_6]^{2+}$. In $[Fe(NH_3)_6]^{2+}$, the axial Fe-N bonds are found to be only about 0.020 Å longer than the equitorial Fe-N bonds in calculations with our more complete basis sets (B or C"). A superposition of HS and LS geometries is shown in Fig. 3.7. Fig. 3 of Ref. [8] shows a superposition of HS and LS geometries for $[Fe(H_2O)_6]^{2+}$.

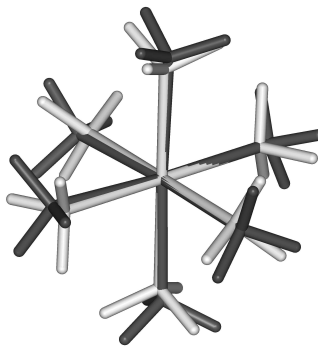


FIGURE 3.7: Superposition of the LS (light) and HS (dark) $[\text{Fe}(\text{NH}_3)_6]^{2+}$ geometries optimized at the PBE0/B level of calculation.

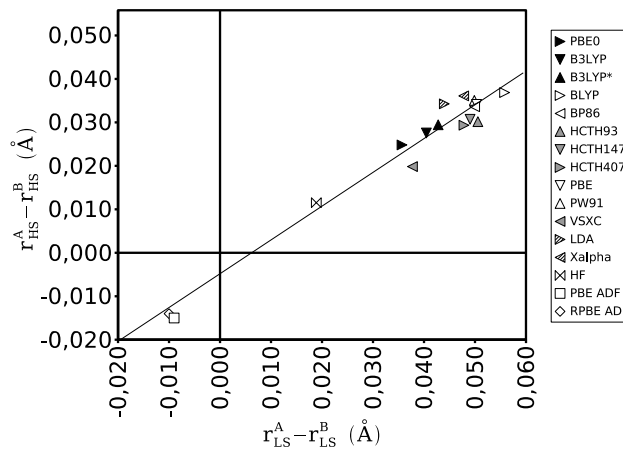


FIGURE 3.8: Comparison of metal-ligand bond length for the high- and low-spin states of $[\text{Fe}(\text{NH}_3)_6]^{2+}$ with the 2 basis sets A and B (with the 2 basis sets A'' and C'' for the ADF calculations)

Since the Jahn-Teller distortion is small, we will focus on average iron-ligand bond lengths. These bond lengths depend somewhat on the choice of basis set used for the calculation. Our $[\text{Fe}(\text{NH}_3)_6]^{2+}$ calculations were carried out with the 6-31G** basis set (A) and the more flexible TZVP basis set of Ahlrichs (B). Figure 3.8 shows that the bond length differences also depend upon the functional, with bond lengths being longer for basis set B than for basis set A. The inverse trend for basis A'' and C'' is observed for calculations with ADF but it must be kept in mind that these STO bases are not the same as the GTO bases. Basis set convergence for $[\text{Fe}(\text{H}_2\text{O})_6]^{2+}$ geometries has been discussed in our earlier work [8]. Most importantly, the value of Δr_{HL} (~ 0.20 Å) is relatively large compared to variations in r_{HS} (0.030 Å) and r_{LS} (0.050 Å) due to differences between the two basis sets.

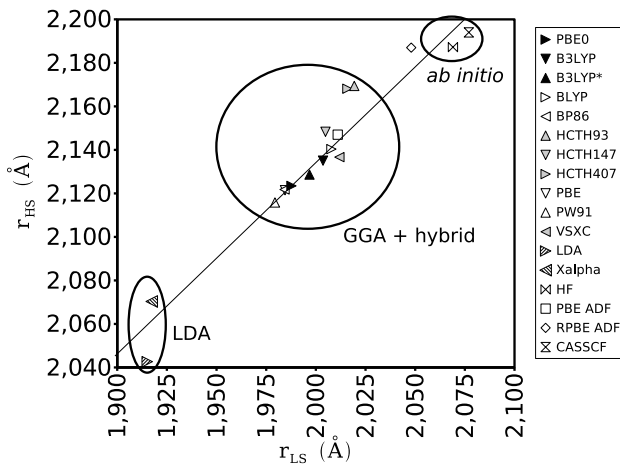


FIGURE 3.9: Comparison of metal-ligand bond length for the high- and low-spin states of $[Fe(H_2O)_6]^{2+}$ with the basis set B (with the basis set C'' for the ADF calculations)

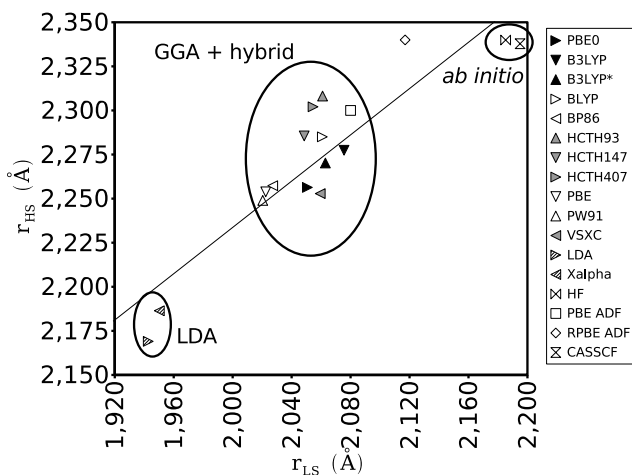


FIGURE 3.10: Comparison of metal-ligand bond length for the high- and low-spin states of $[Fe(NH_3)_6]^{2+}$ with the basis set B (with the basis set C'' for the ADF calculations)

Figures 3.9 and 3.10 summarize the various bond distances obtained for the HS and LS states of $[\text{Fe}(\text{H}_2\text{O})_6]^{2+}$ and $[\text{Fe}(\text{NH}_3)_6]^{2+}$ using various methods and basis sets. In the ideal case that Δr_{HL} is independent of the method used for the calculation,

$$r_{HS} = r_{LS} + \Delta r_{HL} . \quad (3.46)$$

This relationship is indeed found for $[\text{Fe}(\text{H}_2\text{O})_6]^{2+}$ to a remarkably good approximation (Fig. 3.9). A least squares fit gives

$$r_{HS} = 0.905 r_{LS} + 0.325 \text{ \AA} . \quad (3.47)$$

Figure 3.10 shows a less strong linear correlation between r_{HS} and r_{LS} for $[\text{Fe}(\text{NH}_3)_6]^{2+}$, with a least square fit result,

$$r_{HS} = 0.669 r_{LS} + 0.896 \text{ \AA} . \quad (3.48)$$

What is most important is that the overall ordering of points, corresponding to results with different functionals, is roughly the same for $[\text{Fe}(\text{H}_2\text{O})_6]^{2+}$ and for $[\text{Fe}(\text{NH}_3)_6]^{2+}$. The two local approximations (X α and LDA) give the shortest bond lengths (both HS and LS). The LDA is known to overbind : bonds tend to be too short. The GGAs correct this and lead generally to a lengthening of the bonds, as observed in the present results. One GGA stands out as giving markedly longer bonds and this is the RPBE functional. Within the cluster of points representing GGAs and hybrids other than the RPBE GGA, the ordering of bond length is very roughly : PW91, PBE, BP86, PBE0 < B3LYP*, B3LYP, BLYP < HCTH407, VSXC. The longest bond lengths are observed with the two *ab initio* methods (HF and CASSCF). These latter methods include little electron correlation (none in the case of HF and only a small amount of static correlation in the CASSCF case).

C Energetics

The HS-LS energy difference is a far more sensitive test of the quality of a density-functional than is the structure. As previously mentionned, although experimental data is available indirectly for small compounds such as $[\text{Fe}(\text{H}_2\text{O})_6]^{2+}$ and $[\text{Fe}(\text{NH}_3)_6]^{2+}$ through ligand field parameters, we believe that the ability to compare with the results of *ab initio* calculations provides a valuable complement to previous assessments of density functionals for larger compounds.

We thus expect the true value of $\Delta E_{LH}^{\text{adia}}$ for $[\text{Fe}(\text{NH}_3)_6]^{2+}$ to be in the range 9 000 - 11 000 cm⁻¹. These results are consistent with the results of the simple LFT

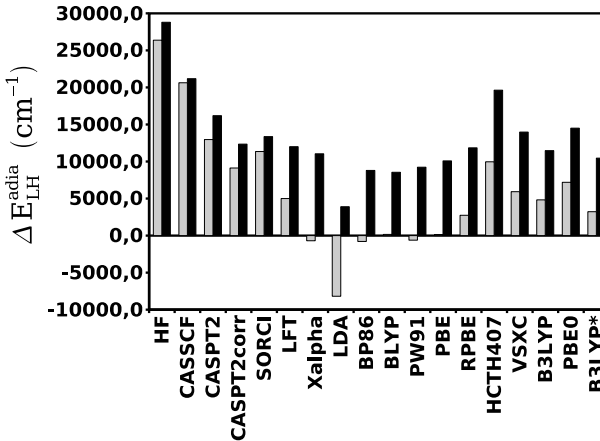


FIGURE 3.11: $\Delta E_{LH}^{\text{adia}}$ for $[Fe(H_2O)_6]^{2+}$ (dark bar) and $[Fe(NH_3)_6]^{2+}$ (light bar).

model of Figgis and Hitchmann which gives respectively $12\ 000\ \text{cm}^{-1}$ and $5\ 000\ \text{cm}^{-1}$ for $\Delta E_{LH}^{\text{adia}}$ for $[Fe(H_2O)_6]^{2+}$ and $[Fe(NH_3)_6]^{2+}$. Thus, in this case, both sophisticated *ab initio* calculations and simple empirically-based LFT calculations basically agree with each other.

Figure 3.11 and tables 3.13 and 3.14 summarizes the results of our DFT calculations of $\Delta E_{LH}^{\text{adia}}$ for $[Fe(H_2O)_6]^{2+}$ and $[Fe(NH_3)_6]^{2+}$. In this bar graph, *ab initio* results are grouped on the left hand side (LHS) followed by the LFT result, then come the results for local functionals, followed by GGAs, then HPDFs, and finally on the right-hand side (RHS) are hybrid functionals. For each functional the left (light) bar is for $[Fe(NH_3)_6]^{2+}$ and the right (dark) bar is for $[Fe(H_2O)_6]^{2+}$.

Let us focus first on trends among density functionals. It is remarkable that the $[Fe(NH_3)_6]^{2+}$ DFT bars in Fig. 3.11 very much resemble a rigid lowering of the $[Fe(H_2O)_6]^{2+}$ DFT bars in Fig. 3.11. That is, there appear to be definite molecule-independent trends in the values of $\Delta E_{LH}^{\text{adia}}$ calculated with different functionals. The trends for $\Delta E_{LH}^{\text{adia}}$ are roughly: LDA < Xα, BP86, BLYP, PW91, PBE < RPBE, VSXC, PBE0, B3LYP, B3LYP* < HCTH407. These are not the same trends observed for Δr_{HL} (LDA, Xα < PW91, PBE, BP86, PBE0 < B3LYP*, B3LYP, BLYP < HCTH407, VSXC).

Paulsen and Trautwein [10] have found in their calculations on larger spin-crossover compounds that good agreement with experimental (condensed phase) values of $\Delta E_{LH}^{\text{adia}}$ for several ligands could be obtained by a method-dependent, but ligand independent, shift which brings $\Delta E_{LH}^{\text{adia}}$ into agreement with the experimental values

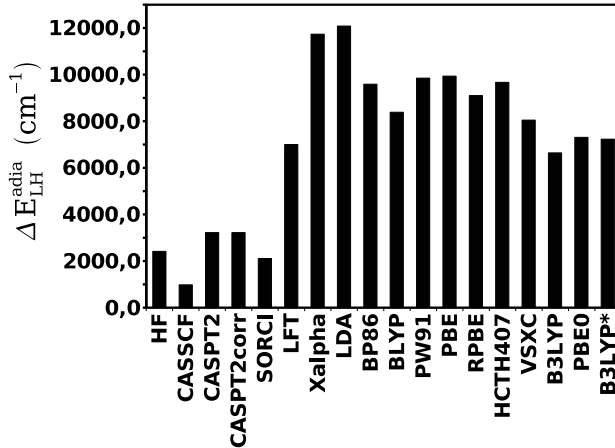


FIGURE 3.12: Difference of $\Delta E_{LH}^{\text{adia}}$ between $[\text{Fe}(\text{H}_2\text{O})_6]^{2+}$ and $[\text{Fe}(\text{NH}_3)_6]^{2+}$ with the basis set B

for a single choice of ligand. That is,

$$\Delta\Delta E_{LH}^{\text{adia}}(M) = \Delta E_{LH}^{\text{adia}}(L, M) - \Delta E_{LH}^{\text{adia}}(L, X) \quad (3.49)$$

where L represents the choice of ligand, M the computational method, and X the experimental result. It follows that

$$\begin{aligned} \Delta\Delta E_{LH}^{\text{adia}}(L, L') &= \Delta E_{LH}^{\text{adia}}(L, M) - \Delta E_{LH}^{\text{adia}}(L', M) \\ &= \Delta E_{LH}^{\text{adia}}(L, X) - \Delta E_{LH}^{\text{adia}}(L', X) \end{aligned} \quad (3.50)$$

should be roughly independent of the choice of computational method. Figure 3.12 shows that this is indeed roughly the case for different density functionals as long as we exclude the two local approximations. However, as opposed to the experience of Paulsen and Trautwein [10], we find that the constant is markedly different than that obtained from our *ab initio* and LFT calculations.

Unlike the case of Δr_{LH} where all of the DFT values were too close to each other and to best estimates of the true value, the different DFT values of $\Delta E_{LH}^{\text{adia}}$ differ significantly from our best estimates. We can thus try to assess which is the best functional for estimating this property.

The adiabatic HS-LS energy difference is overestimated at the HF level. Including electron correlation reduces the values, giving our best estimates (labeled

CASPT2corr and SORCI). These latter results are reproduced reasonably well by the LFT model. After that come our DFT results for the two molecules. The LDA seriously underestimates $\Delta E_{LH}^{\text{adia}}$, consistent with the DFT pairing-energy problem which overstabilizes low-spin states with respect to high-spin states. While this underestimation is less severe for traditional GGAs, it is still severe. The RPBE GGA is special in that it gives a larger value of $\Delta E_{LH}^{\text{adia}}$ than the GGAs on its LHS and gives a value of $\Delta E_{LH}^{\text{adia}}$ in reasonable agreement with our best estimate of the true value. The HPDFs on the RHS of the RPBE functional give even larger values of $\Delta E_{LH}^{\text{adia}}$, even exceeding in some cases our best estimate of the true value. The various hybrid functionals give values of which are more or less comparable to those of the HPDFs.

A closer examination (Fig. 3.11) suggests that the best functionals for $\Delta E_{LH}^{\text{adia}}$ are RPBE, HCTH407, VSXC, B3LYP, PBE0, and B3LYP*, with the best agreement with our best *ab initio* estimates obtained for the VSXC and PBE0 functionals. This is certainly what one might have hoped, namely that the quality of density-functionals is increasing with the time and effort spent on generating better functionals (albeit not necessarily monotonically nor without caveats [74]).

VI Conclusion

This paper is a continuation of our work [8] assessing density-functionals for their ability to properly predict changes in molecular geometries and energies associated with a change in spin. This work has been motivated in particular by our interest in iron(II) compounds because of their ability to exhibit spin-crossover phenomena making them interesting case studies for solid state molecular optical switches [3]. Molecular switches [75] are, of course, highly interesting because of the present international interest in developing nanotechnology. In particular spin-crossover phenomena in transition metal compounds is the subject of three recent volumes of the series *Topics in Current Chemistry* [1]. Nevertheless the ability of density-functionals to properly treat different spin states is by no means limited to material science as has been nicely emphasized in a recent review on chemical reactivity by Harvey [9].

Previous work aimed at assessing density-functionals for the treatment of spin-crossover phenomena focused on larger compounds and test data obtained from condensed matter experiments [4, 5, 6, 7, 10]. Although highly valuable, we feel that this work can be clouded by the difficulties of comparing gas phase computed values with condensed phase experimental values for compounds such as these where

TABLE 3.13: $[\text{Fe}(\text{NH}_3)_6]^{2+}$ and $[\text{Fe}(\text{H}_2\text{O})_6]^{2+}$ HS-LS energy differences

Method	HS-LS Energy Differences (cm^{-1})	
	$[\text{Fe}(\text{NH}_3)_6]^{2+}$	$[\text{Fe}(\text{H}_2\text{O})_6]^{2+}$
MOLCAS		^a
CASSCF(12,10)	20630/16792	21180/17892 ^b
CASPT2(12,10)	12963/ 9125	16185/12347 ^b
SORCI/C	10390 ^c	13360 ^b
SORCI/D	11250 ^c	
LFT	LFT	
	5000	12000
GAUSSIAN		
X α /A	-1238	11280 ^b
X α /B	-695	11040 ^b
VWN/A	-8817	3316 ^b
VWN/B	-8187	3896 ^b
BP86/A	-241	8985 ^b
BP86/B	-790	8798 ^b
BLYP/A	488	8564 ^b
BLYP/B	161	8548 ^b
PW91/A	-299	9271 ^b
PW91/B	-617	9232 ^b
PBE/A	581	10181 ^b
PBE/B	147	10081 ^b

environmental effects are known to be highly significant [3, 27]. That is why we have chosen to focus, in the first instance, upon small compounds such as $[\text{Fe}(\text{H}_2\text{O})_6]^{2+}$ and $[\text{Fe}(\text{NH}_3)_6]^{2+}$. The drawback of this approach is that very little experimental data is available for these compounds and so our primary comparison has been with the results of our own CASPT2 and SORCI calculations which we believe to be among the best in the literature for these compounds. In addition, it is interesting to note that they agree reasonably well with the results of a simple empirically-based LFT calculation.

In paper I [8], we reported our *ab initio* calculations for $[\text{Fe}(\text{H}_2\text{O})_6]^{2+}$ as well as calculations using the density functionals X α , LDA, BP86, BLYP, PW91, B3LYP, PBE, and RPBE. Previous work had pointed out the existence of what might be called the “density-functional theory pairing energy problem” where the LDA over-

stabilizes low-spin states relative to high-spin states (see Ref [8] for a thorough discussion). This problem is reduced but not eliminated by the GGAs BP86, BLYP, PW91, and PBE. We did however show that it is largely corrected for $[Fe(H_2O)_6]^{2+}$ by the RPBE and B3LYP functionals [8]. Since then other highly-parameterized density functionals (HPDFs) have become more widely available, making it interesting to extend the assessment of paper I to the HCTH family of functionals (HCTH93, HCTH147, and HCTH407), the VSXC functional, as well as the hybrid functional PBE0. In all, 13 functionals have now been evaluated for spin-state dependent changes in the geometry and total energy of $[Fe(H_2O)_6]^{2+}$. We also wanted to extend our study to at least one other molecule, which we have done here in the case of $[Fe(NH_3)_6]^{2+}$.

We find definite and distinct trends in the ability of different functionals to treat these complexes. All GGAs and hybrid functionals appear to do an acceptable job of treating changes in the geometries of these coordination complexes. Trends in Δr_{HL} are :

$$\Delta r_{HL} : \text{HCTH407, X}\alpha > \text{LDA, PW91, PBE, BP86, RPBE} > \text{BLYP, PBE0, B3LYP*, B3LYP} > \text{VSXC}$$

This is not the same trends observed in $\Delta E_{HL}^{\text{adia}}$:

$$\Delta E_{HL}^{\text{adia}} : \text{LDA} < \text{X}\alpha, \text{BP86, BLYP, PW91, PBE} < \text{B3LYP*, RPBE, VSXC, B3LYP, PBE0} < \text{HCTH407.}$$

Since our *ab initio* calculations provide best estimates of $\Delta E_{HL}^{\text{adia}}$, we are able to say with some confidence that the VSXC and PBE0 functionals (among functionals tested here) are the best functionals for calculating the adiabatic HS-LS energy difference in $[Fe(H_2O)_6]^{2+}$ and $[Fe(NH_3)_6]^{2+}$, though B3LYP, B3LYP*, RPBE, and HCTH407 are also quite good.

Although these results are encouraging, it may be useful to end on a note of caution. Since $[Fe(H_2O)_6]^{2+}$ and $[Fe(NH_3)_6]^{2+}$ are quite simple model compounds one should question their usefulness when trying to understand more complicated spin-crossover systems. Davidson and Antolovic [76] have suggested that dispersion forces are needed in the quantitative description of coordination bonding and DFT is commonly believed to severely underestimate dispersion forces. If dispersion forces are really needed for a quantitative description of coordination bonding, we may be getting “the right answer for the wrong reason,” in which case extrapolation to the case of true spin crossover complexes may or may not be possible. We are thus looking forward with some excitement to see what happens as we extend our

investigations to larger compounds which better reflect spin crossover chemistry. We are in the course of carrying out such tests.

Acknowledgments

This study was carried out in the context of the *groupe de recherche en Commutateurs Optiques Moléculaires à l'Etat Solide* (COMES), *groupe de recherche en Density Functional Theory* (DFT) and the working group COST D26/0013/02. A.F. would like to thank the French *Ministère d'Education* for a *Bourse de Mobilité*. M.E.C. and A.F. would like to thank Pierre Vatton, Denis Charapoff, Marie-Louise Dheu-Andries and Régis Gras for technical support of the LEDSS and *Centre d'Expérimentation pour le Calcul Intensif en Chimie* (CECIC) computers used for many of the calculations reported here and would also like to acknowledge supercomputer time at the *Institut du Développement et des Ressources en Informatique Scientifique* (IDRIS) in the context of IDRIS project number 021576. We would like to thank Carlo Adamo for helpful discussions. A.H. and L.M.L.D. acknowledge supercomputer time at the *Centro Svizzero di Calcolo Scientifico* (CSCS) in the framework of the CSCS project entitled “Photophysics and Photochemistry of Transition Metal Compounds : Theoretical Approaches”. F.N. thanks the Deutsche Forschungsgemeinschaft for financial support within the priority program 1137 “Molecular Magnetism”.

Bibliography

- [1] (a) Spin Crossover in Transition Metal Complexes I, Vol. 233 of the series Topics in Current Chemistry, edited by P. Gütlich and H.A. Goodwin (Springer, Berlin, 2004); (b) Spin Crossover in Transition Metal Complexes II, Vol. 234 of the series Topics in Current Chemistry, edited by P. Gütlich and H.A. Goodwin (Springer, Berlin, 2004); (c) Spin Crossover in Transition Metal Complexes III, Vol. 235 of the series Topics in Current Chemistry, edited by P. Gütlich and H.A. Goodwin (Springer, Berlin, 2004).
- [2] H.A. Goodwin, Coordination Chemistry Reviews **18**, 293 (1976).
- [3] P. Gütlich, A. Hauser, and H. Spiering, Angew. Chem. Int. Ed. Engl. **33**, 2024 (1994).
- [4] H. Paulsen, L. Duelund, H. Winkler, H. Toftlund, and A.X. Trautwein, Inorg. Chem. **40**, 2201 (2001).

- [5] M. Reiher, O. Salomon, and B.A. Hess, *Theor. Chem. Acc.* **107**, 48 (2001).
- [6] O. Salomon, M. Reiher, and B.A. Hess, *J. Chem. Phys.* **117**, 4729 (2002).
- [7] M. Reiher, *Inorg. Chem.* **41**, 6928 (2002).
- [8] A. Fouqueau, S. Mer, M.E. Casida, L.M. Lawson Daku, A. Hauser, T. Mineva, F. Neese, *J. Chem. Phys.* **120**, 9473 (2004).
- [9] J.N. Harvey, in *Principles and Applications of Density Functional Theory in Inorganic Chemistry I, Structure and Bonding* Vol. 112, edited by N. Kaltsoyannis and J.E. McGrady (Springer-Verlag, Heidelberg, 2004) p. 151.
- [10] H. Paulsen, and A.X. Trautwein, *J. Phys. Chem. Sol.* **65**, 793 (2004).
- [11] W. Kohn and L.J. Sham, *Phys. Rev.* **140**, A1133 (1965).
- [12] O. Gunnarson and B.I. Lundqvist, *Phys. Rev. B* **13**, 4274-4298 (1976).
- [13] S.H. Vosko, L. Wilk, and M. Nusair, *Can. J. Phys.* **58** (1980) 1200.
- [14] R.M. Dreizler and E.K.U. Gross, *Density Functional Theory An Application to the Quantum Many-Body Problem*, (Springer-Verlag, 1990).
- [15] J.K. Labanowski and J.W. Andzelm, *Density Functional Methods in Chemistry*, (Springer, New-York, 1991).
- [16] I.N. Levine, *Quantum chemistry, fifth edition*, (Prentice-Hall, Upper Saddle River, New Jersey 07458, 2000).
- [17] A.D. Becke, *Phys. Rev. A* **38**, 3098 (1988).
- [18] C. Lee, W. Yang, and R.G. Parr, *Phys. Rev. B* **37**, 785 (1988).
- [19] A.D. Becke, *J. Chem. Phys.* **98**, 1372 (1993).
- [20] J. Harris and R.O. Jones, *J. Phys. F* **4**, 1170 (1974).
- [21] A.D. Becke, *J. Chem. Phys.* **98**, 5648 (1993).
- [22] Gaussian, Incorporation NEWS, v. 5, (Wallingford, Connecticut 06492, summer 1994).
- [23] J.P. Perdew, M. Ernzerhof, and K. Burke, *J. Chem. Phys.* **105**, 9982 (1996).
- [24] C. Adamo and V. Barone, *J. Chem. Phys.* **110**, 6158 (1999).

- [25] U. Salzner, J.B. Lagowski, P.G. Pickup, and R.A. Poirier, *J. Phys. Chem. A* **102**, 2572 (1998).
- [26] P. J. Xilson, R. D. Amos, and N. C. Handy, *Chem. Phys. Lett.* **312**, 475 (1999).
- [27] M. Hosteller, K.W. Törnroos, D. Chernyshov, and H.B. Börgi, 21st European Cristallographic Meeting, Durban, South Africa, 24-29 August 2003, Abstract f4.m8.04, p. 88
- [28] T.V. Voorhis and G.E. Scuseria, *Mol. Phys.* **92**, 601 (1997).
- [29] T.V. Voorhis and G.E. Scuseria, *J. Chem. Phys.* **109**, 400 (1998).
- [30] F.A. Hamprecht, A.J. Cohen, D.J. Tozer and N.C. Handy, *J. Chem. Phys.* **109**, 6264 (1998).
- [31] B.N. Figgis and M.A. Hitchman, *Ligand Field Theory and Its Applications*, (Wiley-VCH, New York, 2000).
- [32] S. Sugano, Y Tanabe and H. Kamimura, *Multiplets of Transition-Metal Ions in Crystals* Vol. 33 of the series Pure and Applied Physics, edited by H.S.W. Massey and K.A. Brueckner (Academic Press, New York and London, 1970).
- [33] J.S. Griffith, *The Theory of Transition Metal Ions* (Cambridge University Press, 1961).
- [34] M. Brorson and C.E. Schäffer, *Inorg. Chem.* **27**, 2522 (1988).
- [35] B.O. Roos, P.R. Taylor and P.E.M. Siegbahn, *Chem. Phys.* **48**, 157 (1980).
- [36] K. Andersson, P.-Å. Malmqvist, B.O. Roos, A.J. Sadlej and K. Wolinski, *J. Phys. Chem.* **94**, 5483 (1990).
- [37] K. Andersson, P.-Å. Malmqvist and B.O. Roos, *J. Phys. Chem.* **96**, 1218 (1992).
- [38] F. Neese, *J. Chem. Phys.* **119**, 9428 (2003).
- [39] J. Miralles, O. Castell, R. Caballol and J.-P. Malrieu, *Chem. Phys.* **172**, 33 (1993).
- [40] J. Miralles, J.-P. Daudey and R. Caballol , *Chem. Phys. Lett.* **198**, 555 (1992).
- [41] B.O. Roos, K. Andersson, M.P. Fuelscher, P.-ÅMalmqvist, L.S. Andrés, K. Pierloot, and M. Manuela *Adv. Chem. Phys.* **93**, 219 (1996).

- [42] MOLCAS Version 5. K. Andersson, M. Barysz, A. Bernhardsson, M.R.A. Blomberg, D.L. Cooper, T. Fleig, M.P. Fülscher, C. de Graaf, B.A. Hess, G. Karlstörm, R. Lindh, P.-Å. Malmqvist, P. Neogrády, J. Olsen, B.O. Roos, A.J. Sadlej, M. Schütz, B. Schimmelpfennig, L. Seijo, L. Serrano-Andrés, P.E.M. Siegbahn, J. Stålring, T. Thorsteinsson, V. Veryazov, and P.-O. Widmark, Lund University, Sweden (2000).
- [43] P.C. Hariharan and J.A. Pople, *Theor. Chim. Acta* **28**, 213 (1973).
- [44] V. Rassolov, J.A. Pople, M. Ratner and T.L. Windus, *J. Chem. Phys.* **109**, 1223 (1998).
- [45] C. Froese-Fischer, *J. Phys. B* **10** 1241, (1977).
- [46] T.H. Dunning Jr, B.H. Botch and J.F. Harrisson, *J. Chem. Phys.* **72**, 3419 (1980).
- [47] B.H. Botch, T.H. Dunning Jr and J.F. Harrisson, *J. Chem. Phys.* **75**, 3466 (1981).
- [48] R. Åkesson, L.G.M. Pettersson, M. Sandström, and U. Wahlgren, *J. Am. Chem. Soc.* **116**, 8691 (1994).
- [49] C.W. Bauschlicher Jr., in *Modern Electronic Structure theory, Part II* edited by D.R. Yarkong (World Scientific, Singapore, 1995).
- [50] P.E.M. Siegbahn, *Adv. Chem. Phys.* **93**, 333 (1996).
- [51] F. Neese, Orca- an *ab initio*, density functional and Semiempirical Program Package. Version 2.4.16, Max-Planck Institut für Bioanorganische Chemie, Mülheim, Germany, 2004.
- [52] A. Schäfer, C. Huber, and R. Ahlrichs, *J. Chem. Phys.* **100**, 5829 (1994).
- [53] A.J.H. Wachters, *J. Chem. Phys.* **52**, 1033 (1970).
- [54] C.W. Bauschlicher jr., S.R. Langhoff, and L.A. Barnes, *J. Chem. Phys.* **91**, 2399 (1989).
- [55] F. Weigend,F. Furche, and R. Ahlrichs, *J. Chem. Phys.* **119**, 12753 (2003).
- [56] F. Weigend, A. Kohn, and C. Hattig, *J. Chem. Phys.* **116**, 3175 (2002).
- [57] K.K. Stavrev and M.C. Zerner, *Int. J. Quant. Chem.*, **65**, 877 (1997).

- [58] B.J. Mogensen and S. Rettrup, Int. J. Quant. Chem., **44**, 1045 (1992).
- [59] S. Grimme and M. Waletzke, Phys. Chem. Chem. Phys. **2**, 2075 (2000).
- [60] K. Andersson, Theor. Chim. Acta **91**, 31 (1995).
- [61] G. Hirsch, P.J. Bruna, S.D. Peyerimhoff and R.J. Buenker, Chem. Phys. Lett. **52** 442, (1977).
- [62] P.J. Bruna, S.D. Peyerimhoff and R.J. Buenker, Chem. Phys. Lett. **72**, 278 (1980).
- [63] P.A.M. Dirac, Proc. Cambridge Phil. Soc. **26**, 376 (1930).
- [64] J.C. Slater, Phys. Rev. **81**, 385 (1951).
- [65] J.A. Pople, M. Head-Gordon, D.J. Fox, K. Raghavachari and L.A. Curtiss, J. Chem. Phys. **90**, 5622 (1989).
- [66] L.A. Curtiss, C. Jones, G.W. Trucks, K. Raghavachari and J.A. Pople, J. Chem. Phys. **93**, 2537 (1990).
- [67] L.A. Curtiss, K. Raghavachari, G.W. Trucks and J.A. Pople, J. Chem. Phys. **94**, 7221 (1991).
- [68] L.A. Curtiss, K. Raghavachari, P.C. Redfern, V. Rassolov and J.A. Pople, J. Chem. Phys. **109**, 7764 (1998).
- [69] A.1, M. J. Frisch, G. W. Trucks, H. B. Schlegel, G. E. Scuseria, M. A. Robb, J. R. Cheeseman, J. A. Montgomery, Jr., T. Vreven, K. N. Kudin, J. C. Burant, J. M. Millam, S. S. Iyengar, J. Tomasi, V. Barone, B. Mennucci, M. Cossi, G. Scalmani, N. Rega, G. A. Petersson, H. Nakatsuji, M. Hada, M. Ehara, K. Toyota, R. Fukuda, J. Hasegawa, M. Ishida, T. Nakajima, Y. Honda, O. Kitao, H. Nakai, M. Klene, X. Li, J. E. Knox, H. P. Hratchian, J. B. Cross, C. Adamo, J. Jaramillo, R. Gomperts, R. E. Stratmann, O. Yazyev, A. J. Austin, R. Cammi, C. Pomelli, J. W. Ochterski, P. Y. Ayala, K. Morokuma, G. A. Voth, P. Salvador, J. J. Dannenberg, V. G. Zakrzewski, S. Dapprich, A. D. Daniels, M. C. Strain, O. Farkas, D. K. Malick, A. D. Rabuck, K. Raghavachari, J. B. Foresman, J. V. Ortiz, Q. Cui, A. G. Baboul, S. Clifford, J. Cioslowski, B. B. Stefanov, G. Liu, A. Liashenko, P. Piskorz, I. Komaromi, R. L. Martin, D. J. Fox, T. Keith, M. A. Al-Laham, C. Y. Peng, A. Nanayakkara, M. Challacombe, P. M. W. Gill, B. Johnson, W. Chen, M. W. Wong, C. Gonzalez, and J. A. Pople, Gaussian 03, Revision A.1, Gaussian, Inc., Pittsburgh PA, 2003.

- [70] AMSTERDAM DENSITY FUNCTIONAL Program, Theoretical Chemistry, Vrije Universiteit, Amsterdam, the Netherlands, <http://www.scm.com>
- [71] M.J. Frisch, G.W. Trucks, H.B. Schlegel, G.E. Scuseria, M.A. Robb, J.R. Cheeseman, V.G. Zakrzewski, J.A. Montgomery, R.E. Stratmann, J.C. Burant, S. Dapprich, J.M. Millam, A.D. Daniels, K.N. Dudin, M.C. Strain, O. Farkas, J. Tomasi, V. Barone, M. Cossi, R. Cammi, B. Mennucci, C. Pomelli, C. Adamo, S. Clifford, J. Ochterski, G.A. Petersson, P.Y. Ayala, Q. Cui, K. Morokuma, D.K. Malick, A.D. Rabuck, K. Raghavachari, J.B. Foresman, J. Gomperts, R.L. Martin, D.J. Fox, T. Keith, M.A. Al-Laham, C.Y. Peng, A. Nanayakkara, C. Gonzalez, M. Challacombe, P.M.W. Gill, B.G. Johnson, W. Chen, M.W. Wong, J.L. Andres, M. Head-Gordon, E.S. Replogle, and J.A. Pople, GAUSSIAN 98, Revision A.7, Gaussian Inc., Pittsburgh, PA, 1998.
- [72] E. Cancès, J. Chem. Phys. **114**, 10616 (2001).
- [73] K.N. Kudin, G.E. Scuseria, and E. Cancès, J. Chem. Phys. **116**, 8255 (2002).
- [74] R. Ahlrichs, F. Furche, and S. Grimme, Chem. Phys. Lett. **325**, 317 (2000).
- [75] B.L. Feringa, *Molecular Switches*, (Wiley-VCH, Weinheim, 2001).
- [76] D. Antolovic and E.R. Davidson, J. Chem. Phys. **88**, 4967 (1988).
- [77] J.P. Perdew, Phys. Rev. B **33**, 8822 (1986).
- [78] J.P. Perdew, K. Burke and Y. Wang, Phys. Rev. B **54**, 16533 (1996).
- [79] B. Hammer, L.B. Hansen and J.K. Nørskov, Phys. Rev. B **59**, 7413 (1999).
- [80] K. Nakamoto, *Infrared and Raman spectra of inorganic and coordination compounds*, (Wiley-Intersciences, New York, 1997).
- [81] A. Schäfer, H. Horn, and R. Ahlrichs, J. Chem. Phys. **97**, 2571 (1992).

TABLE 3.14: $[\text{Fe}(\text{NH}_3)_6]^{2+}$ and $[\text{Fe}(\text{H}_2\text{O})_6]^{2+}$ HS-LS energy differences

Method	HS-LS Energy Differences (cm^{-1})	
	$[\text{Fe}(\text{NH}_3)_6]^{2+}$	$[\text{Fe}(\text{H}_2\text{O})_6]^{2+}$
HCTH93/A	10299	19062
HCTH93/B	9430	18779
HCTH147/A	9344	18435
HCTH147/B	8576	18211
HCTH407/A	10682	19789
HCTH407/B	9962	19631
VSXC/A	6991	14860
VSXC/B	5928	13975
B3LYP*/A	3651	10519
B3LYP*/B	3226	10456
B3LYP/A	5260	11514 ^b
B3LYP/B	4978	11465 ^b
PBE0/A	7799	14676
PBE0/B	7195	14504
HF/A	25667	27627
HF/B	26381	28796
ADF		
PBE/A"	-498	
PBE/C"	-640	9056 ^b
RPBE/A"	2911	
RPBE/C"	2744	11844 ^b

^a The notation X/Y indicates with (Y) and without (X) the atomic corrections from [8].

^b Ref. [8].

^c Geometries relaxation energy obtained from B3LYP/TZVP calculations.

Chapitre 4

Étude des complexes $[\text{Fe}(\text{bpy})_3]^{2+}$ et $[\text{Fe}(\text{L})(\text{'NHS}_4)]$

Deux articles sont présentés dans ce chapitre,

1. Latévi Max Lawson Daku, Alfredo Vargas, Andreas Hauser, Antony Fouqueau et Mark Casida,

Chem. Phys. Chem. *soumis.*

Comparison of Density Functionals for Energy and Structural Differences Between the High [$^5T_{2g} : (t_{2g})^4(e_g)^2$] and Low [$^1A_{1g} : (t_{2g})_6(e_g)^0$] Spin States of Iron(II) Coordination Compounds : III. Density-Functional Study of the Low-Spin Iron(II) Tris(2,2'-bipyridine) Complex in Relation to the High-Spin \rightarrow Low-Spin Relaxation Dynamics

2. Georg Gutzenmüller, Nabil Berkaïne, Antony Fouqueau, Mark E. Casida et Markus Reiher,

J. Chem. Phys. *soumis.*

Comparison of Density Functionals for Energy and Structural Differences Between the High [$^5T_{2g} : (t_{2g})^4(e_g)^2$] and Low [$^1A_{1g} : (t_{2g})_6(e_g)^0$] Spin States of Iron(II) Coordination Compounds : IV. Comparison of Density-Functional and Experimental Results for the Ferrous Complexes $[\text{Fe}(\text{L})(\text{'NHS}_4)]$, where 'NHS₄' = 2,2'-Bis(2-mercaptophenylthio)diethylamine Dianion, and L = NH₃, N₂H₄, PMe₃, CO, and NO⁺.

Dans ces deux articles, nous avons comparé les résultats de calculs DFT avec l'expérience. Dans le cas du complexe *tris*(2,2'-bipyridine) fer(II), $[\text{Fe}(\text{bpy})_3]^{2+}$, nous nous sommes servi de nos résultats DFT pour confirmer une hypothèse expérimentale. Dans le cas des complexes $[\text{Fe}(\text{L})(\text{'NHS}_4)]$, nous avons directement comparé nos résultats DFT avec l'expérience en prenant en compte différentes contributions

thermodynamiques.

Pour le complexe $[Fe(bpy)_3]^{2+}$, mon travail a essentiellement consisté à réaliser les calculs avec les fonctionnelles hybrides B3LYP, B3LYP* et PBE0. Une estimation de la différence d'énergie de point zéro entre les états $^5T_{2g}$ et $^1A_{1g}$, ΔE_{HL}° , est de $2500 - 5000 \text{ cm}^{-1}$. Cette estimation est basée sur le modèle du processus multiphonon non-adiabatique proposé par Buhks [1](cf. annexe 1) dans lequel la différence de longueur de liaison métal-ligand, Δr_{HL} , est supposée égale à 0.2 \AA . Dans un premier temps, nous avons vérifié cette hypothèse grâce à des calculs DFT. Ceux-ci donnent de bonnes estimations géométriques tel que cela a été vu dans le chapitre précédent. Dans un deuxième temps, nous avons estimé ΔE_{HL}^{el} , défini par $\Delta E_{HL}^{el} = \Delta E_{HL}^\circ - \Delta E_{HL}^{vib}$. Nous obtenons alors une nouvelle estimation de $3500 - 6000 \text{ cm}^{-1}$. Nous pouvons alors nous en servir pour tester les différentes fonctionnelles.

Le meilleur accord est obtenu avec la fonctionnelle GGA RPBE et la fonctionnelle hybride B3LYP*. Les autres fonctionnelles GGA sur-estiment très largement cette valeur à cause d'une sous-estimation de l'échange alors que les autres fonctionnelles hybrides, B3LYP et PBE0, sous-estiment trop ΔE_{HL}^{el} . Il semble alors important de diminuer la proportion d'échange HF pour être en mesure de décrire correctement ce complexe.

Dans le cas des complexes $[Fe(L)('NHS_4')]$, j'ai co-encadré, avec Mark Casida, Nabil Berkaïne et Georg Gutzenmüller. Les effets de températures ont été pris en compte afin de comparer nos résultats avec les résultats expérimentaux. Nous n'avons pas comparé strictement des valeurs numériques car il n'y a pas de valeurs expérimentales de ΔG_{HL}^{el} pour ces complexes. Cependant, l'état fondamental de chaque complexe sera soit HS, soit LS, dépendant du ligands. Nous pourrons alors étudier la capacité de chaque fonctionnelle pour prédire le bon état fondamental. Indirectement, nous évaluons donc la capacité de chaque fonctionnelle à donner la bonne différence d'énergie.

Les meilleurs résultats sont obtenus avec la fonctionnelle GGA OLYP. Cette fonctionnelle, non testée auparavant, est la seule à prédire correctement l'état fondamental de tous les complexes étudiés en prenant en compte les corrections thermodynamiques. Les fonctionnelles hybrides ne décrivent pas correctement tous ces complexes. Pour pouvoir être capable de prédire le bon état fondamental, il apparaît de nouveau l'importance de diminuer la proportion d'échange à moins de 10 %.

Bibliographie

- [1] E. Buhks, G. Navon, M. Bixon, and J. Jortner, J. Am. Chem. Soc. **102**, 2918 (1980).

4-1 Comparison of density functionals for energy and structural differences between the high-[$^5T_{2g}(t_{2g}^4e_g^2)$] and low-[$^1A_{1g}(t_{2g}^6e_g^0)$] spin states of iron(II) coordination compounds : III. The low-spin iron(II)*tris*(2,2'-bipyridine) complex and assessment of density functionals through the comparison of calculated values and the experimental estimate of the high-spin/low-spin energy difference

**Comparison of density functionals for energy and structural differences between the high- [$^5T_{2g}(t_{2g}^4 e_g^2)$] and low- [$^1A_{1g}(t_{2g}^6 e_g^0)$] spin states of iron(II) coordination compounds:
III. The low-spin iron(II)tris(2,2'-bipyridine) complex and assessment of density functionals through the comparison of calculated values and the experimental estimate of the high-spin/low-spin energy difference**

Latévi Max Lawson Daku,^{*[a]} Alfredo Vargas,^[a] Andreas Hauser,^[a]
Antony Fouqueau,^[b] Mark E. Casida^[b]

[a] Dr. L. M. Lawson Daku, A. Vargas, Prof. A. Hauser

Département de Chimie physique, Université de Genève
30 quai Ernest-Ansermet, CH-1211 Genève 4, Switzerland
Fax: (+41) 22-379-6103
E-mail: max.lawson@chiphy.unige.ch

[b] A. Fouqueau, Prof. M. E. Casida

Institut de Chimie Moléculaire de Grenoble
Laboratoire d'Etudes Dynamiques et Structurales de la Sélectivité
Equipe de Chimie Théorique
Université Joseph Fourier (Grenoble I), F38041 Grenoble, France

Abstract

In the iron(II) low-spin complex $[\text{Fe}(\text{bpy})_3]^{2+}$, the zero-point energy difference between the $^5\text{T}_{2g}(t_{2g}^4 e_g^2)$ high-spin and the $^1\text{A}_{1g}(t_{2g}^6)$ low-spin state, $\Delta E_{\text{HL}}^\circ$, is estimated to lie in the range of 2500–5000 cm^{−1}. This estimate is based on the low-temperature dynamics of the high-spin→low-spin relaxation following the light-induced population of the high-spin state and on the assumption that the bond length difference between the two states Δr_{HL} is equal to the average value of ~ 0.2 Å as found experimentally for spin-crossover system. Calculations based on density functional theory (DFT) validate the structural assumption in so far as the low-spin state optimised geometries are found to be in very good agreement with the experimental X-ray structure of the complex and the predicted high-spin geometries are all very close to one another for a whole series of common GGA (PB86, PW91, PBE, RPBE) and hybrid (B3LYP, B3LYP*, PBE1PBE) functionals. This confirmation of the structural assumption underlying the estimation of $\Delta E_{\text{HL}}^\circ$ from experimental relaxation rate constants permits us to use this value to assess the ability of the density functionals for first principles calculation of the energy difference between the HS and the LS state. Since the different functionals give values from -1000 to 12000 cm^{−1}, the comparison of the calculated values with the experimental estimate thus provides a stringent criterion for the performance of a given functional. Based on this comparison the RPBE and B3LYP* functionals give the best agreement with experiment.

Keywords

Density functional calculations, iron(II)tris(2,2'-bipyridine) complex, time-resolved spectroscopy, high-spin→low-spin relaxation.

I Introduction

The electronic ground state of octahedral d⁶ iron(II) complexes is either the high-spin (HS) $^5\text{T}_{2g}(t_{2g}^4 e_g^2)$ state at low ligand-field strength or the low-spin (LS) $^1\text{A}_{1g}(t_{2g}^6 e_g^0)$ state at high ligand-field strength. Complexes with a LS ground state for which the HS state is sufficiently close in energy can exhibit the phenomenon of spin-crossover, that is, the entropy driven thermal transition from the LS state, populated at low temperatures, to the HS state, populated at higher temperatures [1, 2, 3]. For spin-crossover compounds, the zero-point energy difference between the two states

$\Delta E_{HL}^\circ = E_{HS}^\circ - E_{LS}^\circ$ is typically of the order of 100-1000 cm⁻¹. For iron(II) systems the associated entropy difference, being made up of an electronic and a vibrational contribution, is typically between 4 and 7 cm⁻¹K⁻¹ [4]. X-ray structures of iron(II) spin-crossover compounds in the LS and in the HS state, respectively, show that the spin transition is accompanied by a considerable elongation of the iron-ligand bond lengths. This is consistent with the promotion of two electrons from the essentially non-bonding t_{2g} orbitals to the anti-bonding e_g orbitals. Thus, for iron(II) spin-crossover complexes with a N₆ first coordination sphere, representing the vast majority of iron(II) spin-crossover complexes known to date, the change in Fe-N distance, $\Delta r_{HL} = r_{HS} - r_{LS}$, is found to be in the range of 0.16-0.22 Å [5, 6, 7, 8, 9, 10, 11]. The important lengthening of the iron-ligand bond and concomitant geometry changes give rise to a large increase of the molecular volume, $\Delta V_{HL} = V_{HS} - V_{LS}$. Experimentally this has been evidenced by a change of the crystal volume associated with the spin transition of 15-30 Å³ *per* molecular unit [8, 12, 13, 14]. Such a large difference of the molecular volume makes the spin-crossover phenomenon sensitive to external pressure as well as to variations in the second coordination sphere [15], and it is responsible for the cooperative effects often observed in neat spin-crossover compounds.

The spin transition can also be optically triggered by using laser excitation into metal-ligand charge transfer (MLCT) or *d-d* absorption bands to efficiently convert molecules from the LS state to the HS state. This discovery, made by McGarvey and Lawthers [16, 17] and used to study the HS→LS relaxation in solution, was followed by the observation of Decurtins *et al.* [18, 19] that at cryogenic temperatures, the HS→LS relaxation becomes so slow that iron(II) spin-crossover systems can be trapped quantitatively in the HS state, a phenomenon now known under the acronym of LIESST (light-induced excited spin state trapping). The mechanism for the light-induced LS→HS conversion is schematically shown in Figure 4.1. In a larger context LIESST is not restricted to spin-crossover compounds. It is likewise possible to achieve a light-induced population of the HS state in LS complexes such as the title complex $[Fe(bpy)_3]^{2+}$. Albeit, for these complexes the HS→LS relaxation is generally considerably faster than for spin-crossover complexes.

As described in more detail below, the HS→LS relaxation is a non-adiabatic process [21] with pure tunnelling below ~50 K and a thermally activated behaviour at elevated temperatures [22, 23], the most relevant parameters being Δr_{HL} and ΔE_{HL}° . Whereas for spin-crossover complexes these are directly accessible experimentally (the former from X-ray crystallography, the latter in the form of ΔH_{HL}° from the thermal transition curve extrapolated to $T \rightarrow 0$ [24, 25]), this is not the

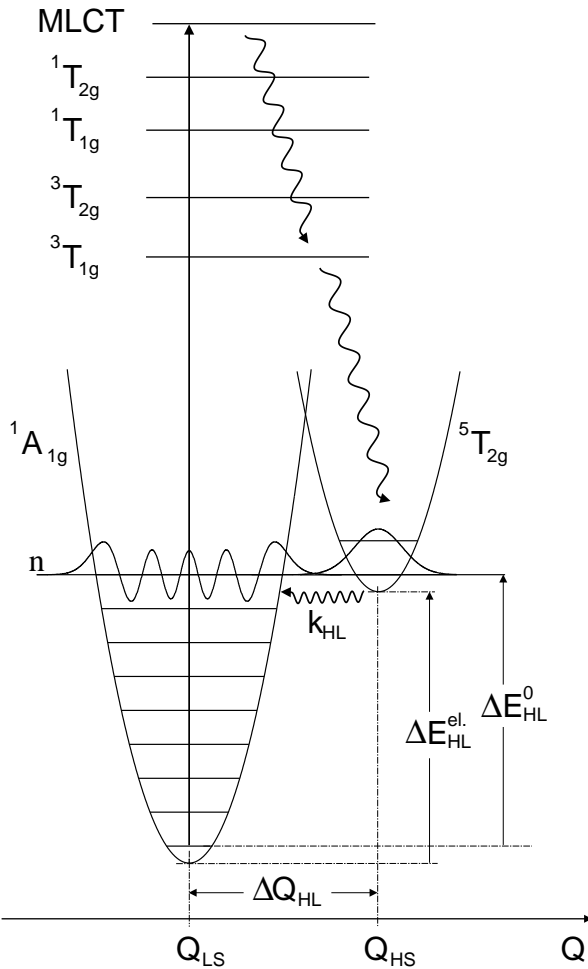


FIGURE 4.1: Configurational coordinate diagram along the totally symmetric breathing mode for an iron(II) complex with a LS $^1A_{1g}(t_{2g}^6)$ ground state. Only the potential wells of the ground state and the first excited state, namely the $^5T_{2g}(t_{2g}^4 e_g^2)$ HS state are explicitly shown, higher excited ligand-field and MLCT states are indicated schematically. The potential wells of the LS and HS states are plotted assuming equal vibrational frequencies, $\hbar\omega$, for the two states. Quantum efficiencies for the light-induced population of the HS state are generally close to unity [20].

case for LS complexes.

Although a description of the electronic structure of the complexes based on ligand-field theory (LFT) serves to rationalise qualitatively most of the observations on spin-crossover systems to date [26, 20], LFT does not provide numerical values of the geometric and energetic factors at the required level of accuracy. We aim to improve our understanding of the photophysical properties not only of iron(II) spin-crossover systems but for iron(II) complexes in general using quantum chemical methods. Such methods are expected to give a description of the complexes which complements and quantitatively goes beyond their characterisation based on LFT alone. They are indeed essential for LS complexes for which the direct experimental determination of the relevant parameters is not possible.

Generally the large number of atoms in the complexes of interest, including $[Fe(bpy)_3]^{2+}$, precludes the use of computationally demanding high-level *ab initio* (*i.e.*, wavefunction based) methods, in contrast to methods based on density functional theory (DFT) which can efficiently be applied to systems of such size. In two previous papers [27, 28], we compared the results of density-functional calculations with the results of high-level *ab initio* calculations for the description of the simple $[Fe(H_2O)_6]^{2+}$ and $[Fe(NH_3)_6]^{2+}$ complexes in the LS and HS states. In this paper, we extend our investigation of iron(II) complexes to the analysis of the low-temperature tunnelling process in the HS→LS relaxation dynamics for a LS complex. Specifically, we examine the extension of the relaxation model used for spin-crossover systems with the well established correlation between the low-temperature tunnelling rate constant and the thermal transition temperature as a measure for ΔE_{HL}° [20] to the LS complex $[Fe(bpy)_3]^{2+}$, and we relate the results to the relevant parameters as derived by density-functional calculations. The present study is addressed to both theoreticians as well as experimentalists. In order to make it tractable for both communities, we thus present the basic notions of DFT and the analysis of the HS→LS relaxation in some detail.

II The HS→LS relaxation and the zero-point energy difference

As mentioned above, HS→LS intersystem crossing may be observed for any iron(II) complex with a LS electronic ground state, that is, for iron(II) spin-crossover compounds but also for iron(II) LS compounds. However, because of the larger zero-point energy difference, the relaxation rates reported for the latter are considerably faster

than for spin-crossover compounds. Thus, whereas for spin-crossover compounds at cryogenic temperatures, relaxation rate constants, $k_{\text{HL}}(T \rightarrow 0)$, are typically between 10^{-6} s^{-1} to 10^{-1} s^{-1} , those for LS complexes are on the microsecond to sub-microsecond timescale. For the title complex $[\text{Fe}(\text{bpy})_3]^{2+}$ (Figure 4.2), for instance, they vary between $\sim 10^4 \text{ s}^{-1}$ and $\sim 10^8 \text{ s}^{-1}$, depending on the matrix in which the complex is embedded [29, 30, 31].

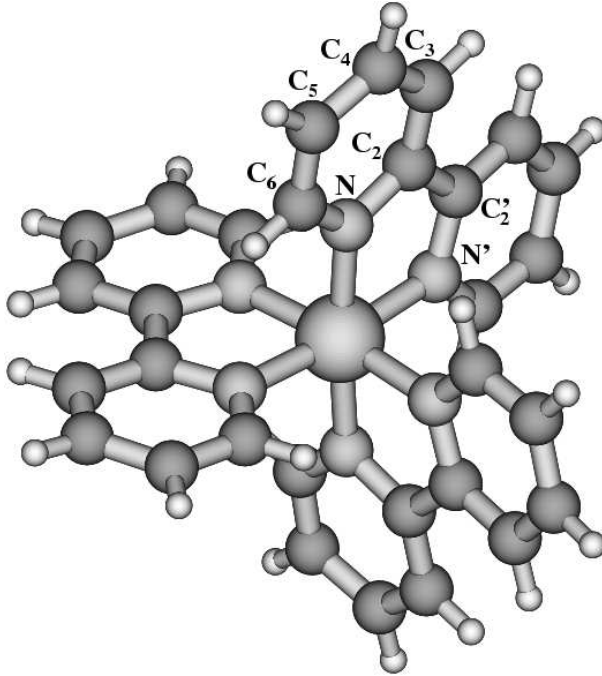


FIGURE 4.2: View of the X-ray structure [32] of $[\text{Fe}(\text{bpy})_3]^{2+}$ in the LS state: the complex possesses a D_3 site symmetry. The atom labelling used in the manuscript is indicated.

As proposed by Buhks *et al.* [21], the HS \rightarrow LS relaxation in spin-crossover compounds of first-row transition metal ions is basically a radiationless non-adiabatic multiphonon process occurring between two distinct zero-order spin states characterised by different nuclear configurations. Given that the metal-ligand bond is shown to undergo the largest structural changes, the reaction coordinate Q is naturally taken as the totally symmetric breathing mode. Figure 4.1 shows a cross section of the LS and HS potential energy surfaces along the Q coordinate. Harmonic potentials with equal force constants, f , and equal vibrational frequencies, $\hbar\omega$, are assumed for mathematical simplicity. Also, in this single configurational coordinate model, ΔQ_{HL} , the horizontal displacement of the two potential wells relative to each other is given by $\Delta Q_{\text{HL}} = \sqrt{6}\Delta r_{\text{HL}}$. The theory of non-adiabatic multiphonon relaxation, which is based on Fermi's Golden rule for non-radiative

processes, leads to the following expression for the low-temperature tunnelling rate constant (see Ref. [33] for details):

$$k_{HL}(T \rightarrow 0) = \frac{2\pi}{\hbar^2\omega} \beta_{HL}^2 |\langle \chi_n | \chi_0 \rangle|^2 \quad (4.1)$$

For iron(II) systems with $\Delta S = 2$ (S being the total electronic spin), the electronic coupling matrix element $\beta_{HL} = \langle \Phi_{LS} | \mathcal{H}_{SO} | \Phi_{HS} \rangle$ comes from second order spin orbit coupling and takes on a value of ~ 150 cm⁻¹ [21]. The reduced energy gap

$$n = \frac{\Delta E_{HL}^\circ}{\hbar\omega} \quad (4.2)$$

is a dimensionless measure for the vertical displacement of the potential wells of the initial HS and final LS states relative to each other. $|\langle \chi_n | \chi_0 \rangle|^2$ is the Franck-Condon factor, that is, the squared overlap of the wavefunction of the lowest vibrational level of the HS state, from which the low-temperature relaxation exclusively occurs, with the wavefunction of the n^{th} vibrational level of the LS state, as required by the principle of energy conservation. Inspection of Figure 4.1 shows the Franck-Condon factor to be a function of both ΔE_{HL}° as well as ΔQ_{HL} . In case of the harmonic approximation with equal force constants it can be expressed as

$$|\langle \chi_n | \chi_0 \rangle|^2 = \frac{\mathcal{S}^n e^{-\mathcal{S}}}{n!} \quad (4.3)$$

where

$$\mathcal{S} = \frac{(1/2)f\Delta Q_{HL}^2}{\hbar\omega}. \quad (4.4)$$

The quantity \mathcal{S} , the so-called Huang-Rhys factor, is a dimensionless measure of the horizontal displacement of the potential wells relative to each other. Using the model values of $\hbar\omega = 250$ cm⁻¹ for the average vibrational frequency of the active modes, $f = 2 \times 10^5$ dyn/cm for the corresponding force constant, and $\Delta Q_{HL} = \sqrt{6}\Delta r_{HL} = 0.5$ Å for the bond length difference expressed in terms of the totally symmetric stretch vibration, a value of \mathcal{S} of 40-50 can be estimated [33].

Figure 4.3 shows the low-temperature tunnelling rate constant on a logarithmic scale versus ΔE_{HL}° calculated according to equations (4.1)-(4.4), and using the above model values for the relevant parameters. Figure 4.3 includes the experimental points for a range of spin-crossover complexes from Ref. [20] (N.B: whereas in Ref. [20] the x -axis corresponds to the transition temperature $T_{1/2}$ for the thermal spin transition, the x -axis in Figure 4.3 corresponds to ΔE_{HL}° . The two are intimately related:

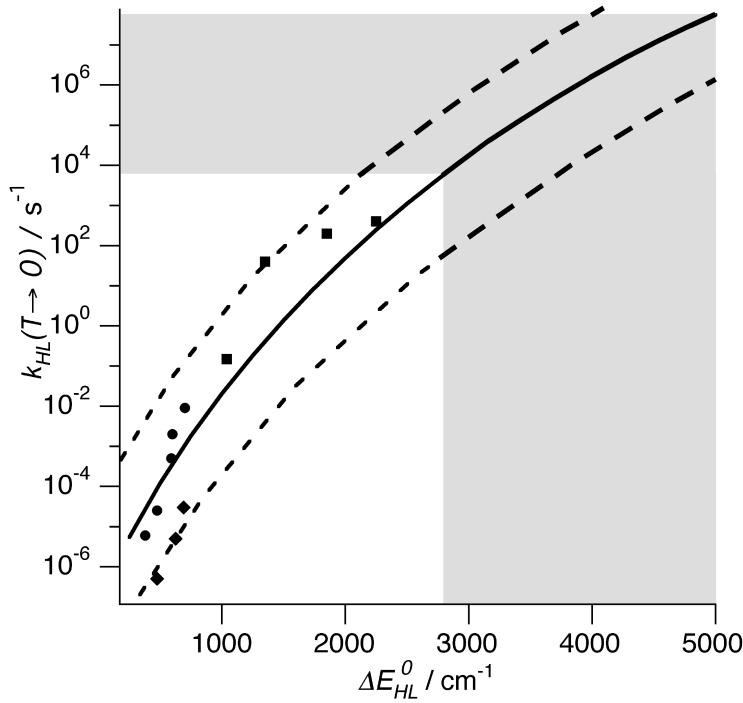


FIGURE 4.3: The low-temperature tunnelling rate constant, $k_{\text{HL}}(T \rightarrow 0)$, on a logarithmic scale as a function of $\Delta E_{\text{HL}}^{\circ}$. Theoretical curves were calculated using the model values as described in the text with an average value of $S = 45$ (solid line) and the limiting values 40 and 50 (dashed line). The lozenges, circles and squares represent experimental values for a series of spin-crossover compounds with a $[\text{FeN}_6]$ first coordination sphere according to Ref. [20]. The range of experimental values for the LS complex $[\text{Fe}(\text{bpy})_3]^{2+}$ doped into different crystalline host lattices [15] is also indicated (shaded area).

$\Delta E_{\text{HL}}^{\circ} \approx \Delta H_{\text{HL}}^{\circ} \approx T_{1/2} \Delta S_{\text{HL}}^{\circ}$, with an average value of $\Delta S_{\text{HL}}^{\circ} \approx 5 \text{ cm}^{-1}\text{K}^{-1}$. For a more detailed discussion on this point see Ref. [23]. In particular for compounds with quite high transition temperatures, this approximation is reasonable). The experimental points all lie within the range predicted for $S = 40-50$. Figure 4.3 also indicates the above mentioned range of low-temperature relaxation rate constants observed for the LS complex $[\text{Fe}(\text{bpy})_3]^{2+}$ doped into a series of inert crystalline host lattices. Assuming that for this complex, having the same $[\text{FeN}_6]$ coordination sphere as the spin-crossover compounds, the difference in bond length between the HS and the LS state is also $\sim 0.2 \text{ \AA}$, a value for $\Delta E_{\text{HL}}^{\circ}$ of between 2500 and 5000 cm^{-1} may thus be estimated. According to Ref. [26] such a value for $\Delta E_{\text{HL}}^{\circ}$ corresponds to a value of the ligand-field strength, $10Dq$, in the range of 22000-25000 cm^{-1} . To date, no reliable values for the ligand-field strength of $[\text{Fe}(\text{bpy})_3]^{2+}$ have been published as it is rather difficult to directly observe the ligand-field transitions in this complex

due to the low-lying MLCT band obscuring the ligand-field transitions. However, it confirms the tentative assignment of a shoulder on the low-energy side of the MLCT band to the $^1A_1 \rightarrow ^1T_1$ transition based on its CD spectrum [34].

The HS \rightarrow LS relaxation can be accelerated by external pressure. This is due to the work-term like expression $p\Delta V_{HL}$ giving an additional contribution to ΔE_{HL}° . External pressure is most effective in the low-temperature tunnelling region. For spin-crossover compounds the tunnelling rate constant is typically enhanced by one order of magnitude *per* kbar, for low-spin systems the enhancement is somewhat smaller. For the title complex $[Fe(bpy)_3]^{2+}$, an acceleration of a factor of two at 10 K has been reported [31]. At comparatively low pressure, the low-temperature tunnelling rate constant as a function of pressure can be expressed as

$$k_{HL}(T \rightarrow 0, p) = k_{HL}(T \rightarrow 0, p = 0) e^{\beta(T \rightarrow 0)p}, \quad (4.5)$$

where $k_{HL}(T \rightarrow 0, p = 0)$ is given by Eq. (4.1) while the acceleration factor at low temperature $\beta(T \rightarrow 0)$ is given by [35]

$$\beta(T \rightarrow 0) \approx \frac{\Delta V_{HL}}{\hbar\omega} \ln\left(\frac{S}{n}\right). \quad (4.6)$$

For spin-crossover compounds with $n \approx 1$ and a model value for the difference in molecular volume $\Delta V_{HL} \approx 25 \text{ \AA}^3$, $\beta(T \rightarrow 0)$ takes on a value of 2 kbar^{-1} in line with the observation of a one order of magnitude acceleration per kbar external pressure. According to the above estimate of ΔE_{HL}° , the reduced energy gap for $[Fe(bpy)_3]^{2+}$ is on the average around 15. With the experimental acceleration factor of $\beta = 0.69 \text{ kbar}^{-1}$, and assuming the same model values for S and $\hbar\omega$ as above, ΔV_{HL} for $[Fe(bpy)_3]^{2+}$ is estimated to be of the same order as for the spin-crossover systems.

III Theoretical framework

The fact that the structure of $[Fe(bpy)_3]^{2+}$ cannot be experimentally characterised in the HS state makes the theoretical validation of the working hypothesis, $\Delta r_{HL} \approx 0.2 \text{ \AA}$, of uttermost importance. The present study aims at validating this assumption by using a variety of density-functional methods to achieve an accurate description of the geometry of the complex in the LS and HS states, and also at probing the ability of these methods to provide reliable estimates of the energy difference. In

this section, we present an overview of the known performance of DFT methods with regard to the description of iron(II) complexes in the LS and HS states, which we precede by an outline of the density-functional formalism so as to introduce the necessary notions and notations. More general reviews of DFT may be found in Refs. [36, 37, 38].

A Outline of the density-functional formalism

Modern density-functional calculations are based on the Kohn-Sham (KS) formulation of spin-density functional theory [39, 40, 41, 42] wherein the ground-state energy of a N -electron system in an external potential $v(\mathbf{r})$ reads

$$E_v[\rho_\uparrow, \rho_\downarrow] = T_s[\rho_\uparrow, \rho_\downarrow] + \underbrace{\frac{1}{2} \int \int d\mathbf{r} d\mathbf{r}' \frac{\rho(\mathbf{r})\rho(\mathbf{r}')}{|\mathbf{r} - \mathbf{r}'|}}_{J[\rho]} + \int d\mathbf{r} \rho(\mathbf{r}) v(\mathbf{r}) + E_{xc}[\rho_\uparrow, \rho_\downarrow]. \quad (4.7)$$

$\rho_\uparrow(\mathbf{r})$ and $\rho_\downarrow(\mathbf{r})$ are the spin-up and spin-down densities, respectively. They sum to the charge density: $\rho(\mathbf{r}) = \rho_\uparrow(\mathbf{r}) + \rho_\downarrow(\mathbf{r})$, and integrate to the numbers of spin-up (N_\uparrow) and spin-down (N_\downarrow) electrons, with $N_\uparrow + N_\downarrow = N$. They determine the external potential and thus the system's Hamiltonian. Hence they determine the eigenstates, the energy spectrum and any other property O of the system; all of them being therefore functionals of the spin densities, denoted $O[\rho_\uparrow, \rho_\downarrow]$. $T_s[\rho_\uparrow, \rho_\downarrow]$ is the kinetic energy of the KS auxiliary noninteracting N -electron system which has the same spin-densities as the interacting system: it provides a very good estimate of the true kinetic energy $T[\rho_\uparrow, \rho_\downarrow]$ which is difficult to approximate by functionals which explicitly depend on the spin densities, and it is simple to evaluate. $J[\rho]$ is the Hartree self-interaction potential energy and the quantity $E_{xc}[\rho_\uparrow, \rho_\downarrow]$ thus defined by Eq. (4.7) is the exchange-correlation (XC) energy. It contains the residual part of the true kinetic energy: $T[\rho_\uparrow, \rho_\downarrow] - T_s[\rho_\uparrow, \rho_\downarrow]$, and the nonclassical part of the electronic interaction energy $V_{ee}[\rho_\uparrow, \rho_\downarrow]$ which is given by $U_{xc}[\rho_\uparrow, \rho_\downarrow] = V_{ee}[\rho_\uparrow, \rho_\downarrow] - J[\rho]$. For the noninteracting system, denoting the energy, the spinorbital and the occupation number of its i th σ -type ($\sigma = \uparrow, \downarrow$) single-particle level by $\varepsilon_{i\sigma}$, $\psi_{i\sigma}(\mathbf{r})$ and $f_{i\sigma}$, respectively, the ground state energy is obtained by filling the lowest lying N_\uparrow spin-up and lowest lying N_\downarrow spin-down levels as follows:

$$\begin{aligned} f_{i\sigma} &= 1, & \varepsilon_{i\sigma} &< \mu_\sigma; \\ 0 \leq f_{i\sigma} \leq 1, & & \varepsilon_{i\sigma} &= \mu_\sigma; \\ f_{i\sigma} &= 0, & \varepsilon_{i\sigma} &> \mu_\sigma; \end{aligned} \quad (4.8)$$

μ_σ is the energy of the highest occupied σ -type level whose occupation can be fractional if it is degenerate and partially occupied and, in this case, the noninteracting ground state can be degenerate. From the ground state of the noninteracting system one deduces that the ground-state spin-up and spin-down densities for both the interacting and noninteracting systems, are given by

$$\rho_\sigma(\mathbf{r}) = \sum_{i=1}^{\infty} f_{i\sigma} |\psi_{i\sigma}(\mathbf{r})|^2; \quad (4.9)$$

and that the noninteracting kinetic energy reads

$$T_s[\rho_\uparrow, \rho_\downarrow] = \sum_{\sigma=\uparrow,\downarrow} \sum_i f_{i\sigma} \int d\mathbf{r} \psi_{i\sigma}^*(\mathbf{r}) \left(-\frac{1}{2} \nabla^2 \right) \psi_{i\sigma}(\mathbf{r}). \quad (4.10)$$

The single-particle levels are obtained as solutions of the celebrated KS equations

$$\left(-\frac{1}{2} \nabla^2 + v(\mathbf{r}) + \int d\mathbf{r}' \frac{\rho(\mathbf{r}')}{|\mathbf{r} - \mathbf{r}'|} + v_{xc\sigma}[\rho_\uparrow, \rho_\downarrow](\mathbf{r}) \right) \psi_{i\sigma}(\mathbf{r}) = \varepsilon_{i\sigma} \psi_{i\sigma}(\mathbf{r}) \quad (4.11)$$

where the spin-dependant XC potential $v_{xc\sigma}(\mathbf{r})$ is the functional derivative

$$v_{xc\sigma}[\rho_\uparrow, \rho_\downarrow](\mathbf{r}) = \frac{\delta E_{xc}[\rho_\uparrow, \rho_\downarrow]}{\delta \rho_\sigma(\mathbf{r})} \Bigg|_{(\rho_\uparrow, \rho_\downarrow) = (\rho_\uparrow, \rho_\downarrow)}. \quad (4.12)$$

Because of the dependence of the potential felt by the single particles on the spin-densities, hence on the KS spinorbitals through Eq. (4.9), Eqs. (4.11) must be solved using a self-consistent field (SCF) approach. For spin-polarised systems, the XC potential will be different for spin-up and spin-down particles, and spin-up and spin-down orbitals will have different spatial extensions. Given that the analytical form of the XC energy functional is unknown, approximations are devised requiring that either the largest number of the mathematical properties of the true XC energy functional, or, at least, a few conditions known to be limiting for the evaluation of selected properties are satisfied.

For dealing with the XC energy functional, one distinguishes between the exchange and correlation contributions, noted $E_x[\rho_\uparrow, \rho_\downarrow]$ and $E_c[\rho_\uparrow, \rho_\downarrow]$, respectively, which both may be further expressed in terms of the exchange ($\epsilon_x[\rho_\uparrow, \rho_\downarrow](\mathbf{r})$) and correlation ($\epsilon_c[\rho_\uparrow, \rho_\downarrow](\mathbf{r})$) energies per particle

$$E_\kappa[\rho_\uparrow, \rho_\downarrow] = \int d\mathbf{r} \rho(\mathbf{r}) \epsilon_\kappa[\rho_\uparrow, \rho_\downarrow](\mathbf{r}), \quad (\kappa = x, c). \quad (4.13)$$

The exchange energy is defined as the nonclassical part of the expectation value of the electronic repulsion operator for the ground-state of the noninteracting system. This formulation is given by

$$E_x^{\text{KS}}[\rho_{\uparrow}, \rho_{\downarrow}] = -\frac{1}{2} \sum_{\sigma=\uparrow, \downarrow} \iint d\mathbf{r} d\mathbf{r}' \frac{|\sum_{i\sigma} f_{i\sigma} \psi_{i\sigma}(\mathbf{r}) \psi_{i\sigma}^*(\mathbf{r}')|^2}{|\mathbf{r} - \mathbf{r}'|} \quad (4.14)$$

$E_x^{\text{KS}}[\rho_{\uparrow}, \rho_{\downarrow}]$ takes on the same form as the Hartree-Fock (HF) exchange energy, thus reflecting the fact that the definition of the exchange energy follows naturally from the one of the HF exchange and similarly accounts for the Pauli exclusion principle which tends to keep electrons of alike spin apart. Nevertheless the two quantities are not equal because the KS and HF orbitals differ [43]. $E_x^{\text{KS}}[\rho_{\uparrow}, \rho_{\downarrow}]$ is an implicit functional of the spin densities because the KS spinorbitals also are functionals of the spin densities but their explicit dependence on $\rho_{\uparrow}(\mathbf{r})$ and $\rho_{\downarrow}(\mathbf{r})$ is unknown.

Several schemes allow to obtain approximate exchange and correlation energy functionals explicitly stated in terms of the spin densities. The oldest is the local density approximation (LDA) [40], wherein it is assumed on the basis of the universality of the XC energy functional that the exchange and correlation energies per particle of a system at a given point \mathbf{r} are those of a homogeneous electron gas, (HEG), whose constant spin densities are the ones of the investigated system at \mathbf{r} :

$$\epsilon_{\kappa}^{\text{LDA}}[\rho_{\uparrow}, \rho_{\downarrow}](\mathbf{r}) = \epsilon_{\kappa}^{\text{HEG}}(\rho_{\uparrow}(\mathbf{r}), \rho_{\downarrow}(\mathbf{r})), \quad (\kappa = x, c). \quad (4.15)$$

The HEG, (that is, an ideal electronic system made of a uniform electron cloud of given spin densities, $(\rho_{\uparrow}^{\circ}, \rho_{\downarrow}^{\circ})$, which evolves in a uniform positive background which compensates for the electronic charge), offers the advantage that the density-functional study of its ground state leads to an analytical expression for $\epsilon_x^{\text{HEG}}(\rho_{\uparrow}^{\circ}, \rho_{\downarrow}^{\circ})$ for which the LDA exchange energy can be written as

$$E_x^{\text{LDA}}[\rho_{\uparrow}, \rho_{\downarrow}] = 2^{1/3} C_x \sum_{\sigma=\uparrow, \downarrow} \int d\mathbf{r} \rho_{\sigma}^{4/3}(\mathbf{r}) \quad \text{with} \quad C_x = -\frac{3}{4} \left(\frac{3}{\pi} \right)^{1/3}; \quad (4.16)$$

and it leads to the parameterisations of $\epsilon_c^{\text{HEG}}(\rho_{\uparrow}^{\circ}, \rho_{\downarrow}^{\circ})$ based on the accurate results of the Quantum Monte Carlo calculations of Ceperley and Alder [44], the Vosko-Wilk-Nusair (VWN) parameterisation being the one most widely used [45]. The LDA is valid for slowly varying densities. For atomic, molecular and solid systems characterised by rapidly varying densities, the LDA underestimates the exchange energy by about 14% and overestimates the correlation energy by a factor of 2.5

approximatively; and quite often the two errors cancel [37, p. 231]. The LDA however tends to overestimate bond energies.

The generalised gradient approximation (GGA) remedies this deficiency by adding correction terms $\Delta E_\kappa[\rho_\uparrow, \rho_\downarrow]$, ($\kappa = x, c$), which depend on the gradients of the spin densities and which allow a better description of exchange and correlation, especially in the boundary region at the outer edges of atoms and where molecular binding occurs. The GGA XC functionals thus read:

$$\begin{aligned} E_{xc}^{\text{GGA}}[\rho_\uparrow, \rho_\downarrow] &= \underbrace{E_x^{\text{LDA}}[\rho_\uparrow, \rho_\downarrow] + \Delta E_x[\rho_\uparrow, \rho_\downarrow]}_{E_x^{\text{GGA}}[\rho_\uparrow, \rho_\downarrow]} + \underbrace{E_c^{\text{LDA}}[\rho_\uparrow, \rho_\downarrow] + \Delta E_c[\rho_\uparrow, \rho_\downarrow]}_{E_c^{\text{GGA}}[\rho_\uparrow, \rho_\downarrow]} \\ &= E_{xc}^{\text{LDA}}[\rho_\uparrow, \rho_\downarrow] + \Delta E_x[\rho_\uparrow, \rho_\downarrow] + \Delta E_c[\rho_\uparrow, \rho_\downarrow]. \end{aligned} \quad (4.17)$$

The GGA enhances exchange while turning off correlation. This reproduces the expected trend that exchange turns on and correlation turns off with respect to exchange with increasing spin density gradients [46, 47, 48, 49], but also with increasing charge density, or increasing spin polarisation measured locally by

$$\zeta(\mathbf{r}) = [\rho_\uparrow(\mathbf{r}) - \rho_\downarrow(\mathbf{r})] / \rho(\mathbf{r}). \quad (4.18)$$

In contrast to the LDA, the GGA is not related to a physically well-defined system. The GGA functionals are therefore not “uniquely” defined in the sense that they can be derived in different ways. Nevertheless, the exchange part of the GGA XC energy admits the general form

$$E_x^{\text{GGA}}[\rho_\uparrow, \rho_\downarrow] = 2^{1/3} C_x \sum_{\sigma=\uparrow, \downarrow} \int d\mathbf{r} \rho_\sigma^{4/3}(\mathbf{r}) F_x(2^{1/3} s_\sigma(\mathbf{r})), \quad (4.19)$$

where the enhancement factor F_x depends on the reduced gradients

$$s_\sigma(\mathbf{r}) = |\nabla \rho_\sigma(\mathbf{r})| / (2(3\pi^2)^{1/3} \rho_\sigma^{4/3}(\mathbf{r})), \quad (4.20)$$

and must give $F_x(0) = 1$ in order to reproduce the HEG results. The expressions of the GGA correlation energy functionals turn out to be far more complicated [36, 37, 38]. The GGA improves the LDA description of the equilibrium geometries in that it usually stretches bond lengths, and of the energetics. These improvements are one reason for the increased acceptance of DFT methods in Quantum Chemistry.

Further improvements were achieved with hybrid XC energy functionals which are characterised by the fact that they include a contribution of the exact-exchange

energy (Eq. (4.14)) as advocated for by Becke [50, 51] on the basis of the adiabatic connection formalism of Harris and Jones [52]. The adiabatic connection formalism relates a physical system with fully interacting electrons to its noninteracting KS counterpart through the equation

$$E_{xc}[\rho_\uparrow, \rho_\downarrow] = \int_0^1 d\lambda U_{xc}^\lambda[\rho_\uparrow, \rho_\downarrow], \quad (4.21)$$

where $U_{xc}^\lambda[\rho_\uparrow, \rho_\downarrow]$ is λ^{-1} times the XC potential energy of a system for which (i) the electronic repulsion interaction has been scaled by $\lambda \in [0, 1]$, and (ii) the external potential has been chosen to maintain the ground-state spin densities fixed at their values $\rho_\uparrow(\mathbf{r})$ and $\rho_\downarrow(\mathbf{r})$ for the physical $\lambda = 1$ system. In practice, Eq. (4.21) is solved by using an interpolation scheme for the integrand, knowing that $U_{xc}^{\lambda=0}[\rho_\uparrow, \rho_\downarrow]$ rigorously reduces to $E_x^{\text{KS}}[\rho_\uparrow, \rho_\downarrow]$, while approximate XC functionals $E_{xc}^{\text{approx.}}[\rho_\uparrow, \rho_\downarrow]$ can be used for $U_{xc}^{\lambda=1}[\rho_\uparrow, \rho_\downarrow]$. For instance, the simplest scheme [50] consists in using a linear interpolation that results in the so-called half-and-half hybrids of the form $\frac{1}{2}(E_x^{\text{KS}} + E_{xc}^{\text{approx.}})$. Still the exact λ -dependence of the interpolation function is a subject of on-going study [53, 54, 55].

GGA and hybrid functionals are routinely used in nowadays DFT applications. Because there is no systematic approach for improving their quality, their performance must be assessed by comparing the results to which they lead for some specific properties with accurate data that originate from experiments or *ab initio* calculations.

B DFT characterisation of LS and HS states of iron(II) complexes

Whereas LFT serves to explain qualitatively most of the physical properties of spin-crossover compounds, it cannot provide structural and energetic parameters at the required level of accuracy. Unfortunately, the large size of spin-crossover complexes prohibits the use of detailed *ab initio* calculations. In principle, DFT offers a feasible alternative, but to date none of the numerous DFT based methods has been acknowledged to constitute a fool proof approach to the problem of the description of spin-crossover compounds in their LS and HS states. Following Gunnarsson and Lundqvist [41], who extended the density-functional formalism for the ground state to the lowest lying state of each spatial and spin symmetry, advantage is taken of the fact that the LS and the HS states represent the lowest lying state for their

respective spin multiplicity. Using this so-called Δ SCF approach, distinct KS SCF calculations thus provide a structural and energetic characterisation of the complexes in both states. Whereas optimised LS and HS geometries satisfactorily compare with available experimental geometries, the DFT methods often fail to correctly describe the electronic contribution $\Delta E_{HL}^{\text{el}}$ to the zero-point energy difference. Thus, Paulsen *et al.* [56] noticed that, commonly used GGAs - namely, the BLYP functional which combines Becke's 1988 (B or B88) exchange GGA [57] and the Lee-Yang-Parr (LYP) correlation GGA [58], as well as the PW91 exchange-correlation GGA of Perdew and Wang [59, 60, 61, 62] - give the expected LS ground state for the investigated iron(II) spin-crossover complexes, but they tend to give too high $\Delta E_{HL}^{\text{el}}$ values. Baranović [63], using the BP86 GGA made of the B exchange and Perdew's 1986 (P86) correlation [64] parts, obtained similar results and proposed an empirical parameter to appropriately scale calculated $\Delta E_{HL}^{\text{el}}$ values.

In contrast Paulsen *et al.* [56] also showed that the HS state is stabilised with respect to the LS state and is falsely predicted to be the ground state if the B3LYP functional is used. This functional is the workhorse of the hybrid XC energy functionals. Omitting the explicit reference to the spin densities in the notation of the functionals, it reads [65]

$$E_{xc}^{\text{B3LYP}} = (1 - a_0)E_x^{\text{LDA}} + a_0E_x^{\text{KS}} + a_x\Delta E_x^{\text{B}} + (1 - a_c)E_c^{\text{VWN}} + a_cE_c^{\text{LYP}}, \quad (4.22)$$

where E_c^{VWN} is the VWN parameterisation corresponding to the random phase approximation (RPA) correlation energy [45]. ΔE_x^{B} stands for the nonlocal component (*i.e.*, gradient corrections) of the Becke's 1988 exchange GGA; and the coefficients $(a_0, a_x, a_c) = (0.20, 0.72, 0.81)$ are the ones determined by Becke [51], originally for the B3PW91 hybrid, by fitting to a data set of atomisation energies. Given the incorporation of an exact-exchange contribution in hybrid functionals, the B3LYP behaviour reported by Paulsen *et al.* [56] can be ascribed to the fact that such functionals inherit from the HF scheme the tendency towards over stabilising states of high spin multiplicity with respect to states of lower multiplicity.

The preference of the B3LYP for a high multiplicity ground state in iron(II) complexes was also observed by Reiher, Salomon and Hess [66] who evidenced a linear dependence of $\Delta E_{HL}^{\text{el}}$ on the amount a_0 of exact-exchange admixture in Eq. (4.22). They recommended a reduced a_0 value of 0.15 for which the resulting B3LYP* functional correctly predicts the ground state of a number of iron(II) complexes [66, 67]. Nevertheless, in the particular case of the spin-crossover $Fe(1,10\text{-phenanthroline})_2(NCS)_2$ complex, even the B3LYP* functional incorrectly gives the

HS state as the ground state [68]. As pointed out by Reiher, this suggests that the amount of exact exchange may be further reduced in the case of this complex. As previously mentioned, the question of the amount of exact exchange to include in hybrid functionals is a subject of on-going study [53, 54, 55], and although an improvement is often observed when exact exchange is admixed in density functional approximations, so far no sound reasons have been established as to why hybrid functionals should perform better than modern GGAs, especially with regard to estimating energy gaps between states of different spin multiplicities.

This ambiguous situation regarding the reliability of DFT methods for the study of spin-crossover and related systems, combined with the lack of a calibration of density functionals against accurate *ab initio* results for simpler iron(II) complexes, led us to perform a comparison of density functionals for energy and structural differences between the HS and LS states of the HS $[\text{Fe}(\text{H}_2\text{O})_6]^{2+}$ complex [27] (paper I of the series). We used the BP86, BLYP, PW91 GGAs, the recent exchange-correlation GGA of Perdew-Burke-Ernzerhof (PBE) [69, 70] and the revised PBE (RPBE) functional of Hammer, Hansen and Nørskov [71] as well as the B3LYP hybrid, and compared the DFT results with results obtained at the complete active space SCF (CASSCF), second-order perturbation theory-corrected CASSCF (CASPT2), and spectroscopy oriented configuration interaction (SORCI, [72]) levels. Whatever the theoretical method, the HS state was correctly reproduced as the ground state for this HS system, ($\Delta E_{\text{HL}}^{\text{el}} < 0$). A good agreement was achieved between the experimental geometries of the complex in its HS state and the ones obtained at the CASSCF and DFT levels. All theoretical methods consistently predicted quite similar geometries for the excited LS state. The situation was quite different with regard to the energetics. Comparison of the DFT molecular energy gaps with the best *ab initio* estimate revealed that the functionals, with the noticeable exception of the B3LYP and RPBE, systematically underestimate the stability of the HS state with respect to the LS state by giving too small $|\Delta E_{\text{HL}}^{\text{el}}|$ values. The B3LYP and RPBE functionals on the other hand were shown to be the most reliable of the functionals. Subsequently, the comparison was extended to the HS $[\text{Fe}(\text{NH}_3)_6]^{2+}$ complex and additional functionals [28] (paper II of the series), and the overall best agreement for the energetics of the two complexes was obtained for the PBE1PBE hybrid functional (also known as PBE0). This functional is of the parameter-free form

$$E_{xc}^{\text{hybrid}} = E_{xc}^{\text{GGA}} + a_0 (E_x^{\text{KS}} - E_x^{\text{GGA}}) \quad (4.23)$$

with $a_0 = 1/4$, proposed by Perdew, Ernzerhof and Burke [53, 54] and for which the

GGA contribution is given by the PBE functional [73, 74].

The present theoretical study of the LS $[Fe(bpy)_3]^{2+}$ complex, for which high quality *ab initio* calculations clearly are not manageable but for which experimental data are available, provides a further assessment of the performance of the density functionals. The following sections deal with the characterisation of the trigonal complex in the LS and HS states using the BP86, PW91, PBE, RPBE, B3LYP, and B3LYP* and PBE1PBE functionals.

IV Computational details

The Amsterdam Density Functional (ADF) [75] program package was used to carry out calculations with the BP86, PW91, PBE and RPBE GGAs. In order to probe the influence of the choice of the basis, two qualities of Slater-type orbital (STO) basis sets from the ADF basis set database were employed for the Fe, N, C and H atoms, namely, the double- ζ “DZ” and triple- ζ polarised “TZP” STO basis. Computations involving the B3LYP, B3LYP* and PBE1PBE hybrids were performed with the GAUSSIAN [76] program package, using for all atoms either the triple- ζ polarised Gaussian-type orbital (GTO) basis “TZVP” of Schäfer, Huber and Ahlrichs [77] or the 6-311+G** basis set [78, 79, 80, 81], which is a triple- ζ polarised GTO basis set with sets of diffuse functions on the Fe, N, and C atoms. For comparison purposes (see below), the GAUSSIAN package was also used to perform calculations with the PBE GGA. Fractional occupation numbers were used in the ADF calculations but are not allowed in the present implementation of GAUSSIAN (except as an intermediate step in the SCF convergence strategy [82]). For the LS state spin-restricted and for the HS state spin-unrestricted calculations where performed constraining M_S , the projection of the total electronic spin along a reference axis, to $M_S = 0$ and $M_S = +2$, respectively. In all cases, the symmetry for the $[Fe(bpy)_3]^{2+}$ complex was constrained to D_3 . Results were visualised using the MOLEKEL [83] and the MOLDEN [84] softwares.

V Results and Discussion

A LS and HS states

In carrying out the DFT calculations, we typically seek the lowest-lying state of each spatial and spin symmetry. According to LFT, the LS and HS states should

be the $^1\text{A}_{1g}(t_{2g}^6)$ and $^5\text{T}_{2g}(t_{2g}^4 e_g^2)$ states, respectively. These states do not appear directly as such in the DFT calculations because the $[\text{Fe}(\text{bpy})_3]^{2+}$ complex is not of O_h symmetry but of D_3 symmetry. In particular, this means that the $^5\text{T}_{2g}(t_{2g}^4 e_g^2)$ state actually splits into two states, one of ^5E symmetry and one of $^5\text{A}_1$ symmetry. In addition, there exists for complexes such as $[\text{Fe}(\text{bpy})_3]^{2+}$ a high density of states sometimes making the identification of the lowest-lying state of each spatial and spin symmetry difficult. For these reasons and to seek additional chemical insight, we performed a careful analysis of the resulting KS molecular orbitals (MOs) and orbital energy levels, thus verifying that the characterised electronic states indeed correspond to the ligand-field $^1\text{A}_{1g}(t_{2g}^6)$ and $^5\text{T}_{2g}(t_{2g}^4 e_g^2)$ states of interest.

The different DFT calculations performed for a given M_S value result in similar KS orbital energy levels, with an occupation of the orbital levels associated with each of the spin-up and spin-down electronic subsystems which follows Eq. (4.8). Thus, for $M_S = 0$, there is a full occupation of the lowest-lying orbital energy levels from which one readily deduces that the converged KS determinants characterise the lowest-lying electronic state of $^1\text{A}_1$ symmetry. That this state relates to the ligand-field $^1\text{A}_{1g}(t_{2g}^6)$ state is confirmed from calculated iron net charges and population analysis. The GAUSSIAN and ADF packages provide different schemes for analysing the SCF densities and evaluating the net atomic charges. In the case of the results obtained with ADF for the LS state, the values obtained for the iron atom from Mulliken population analysis are large whatever the theoretical level used, indicating that the molecular charge is as expected mainly on the iron atom. They are reported in Table 4.1 for the calculations performed at the PBE/TZP and RPBE/TZP levels. Results for the other functionals and basis sets are given in Table S1.

Table 4.1

That the molecular charge is mainly on the iron atom is also confirmed by the values reported in Table 4.1 (and Table S1) for the Voronoi net charge of the iron atom, that is the total nuclear and electronic charge in the Voronoi cell of the iron atom; the Voronoi cell of an atom being the region in space closer to its nucleus than to any other nucleus [85]. The Mulliken and Voronoi net charges indicate that about one half of the molecular charge is on the iron atom, the remaining half being shared by the three equivalent ligands. Natural population analysis [86, 87, 88] has been used in the case of the results obtained with the GAUSSIAN package. The results found for the LS state are summarised in Table 4.1 for the calculations done at the PBE/TZVP and B3LYP*/TZVP levels, and in Table S1 for the other calculations. In this case, the calculated natural net charge of the iron atom also indicates that the iron atom bears the main part of the molecular charge. Both the natural (GAUSSIAN)

and Mulliken (ADF) populations of the “effective” atomic orbitals (AOs) of the Fe atom, presented in Table 4.1 (and Table S1) per l -values, agree well with the $[Ar]3d^6$ configuration of the free Fe^{2+} ion. The deviations of the populations of the iron atom from their free ion values reflect the covalence of the metal-ligand bonds. From a MO viewpoint, the existence of chemical bonding between the metal and the ligands is seen in the composition of the “metallic” KS MOs which are no longer pure metal orbitals. These MOs with a $Fe(3d)$ main parentage which belong to the frontier MOs are represented in the energy level diagram of Figure 4.4, for the PBE/TZP calculation. Thus, the “metallic” frontier levels are the highest-occupied $25a_1$ and

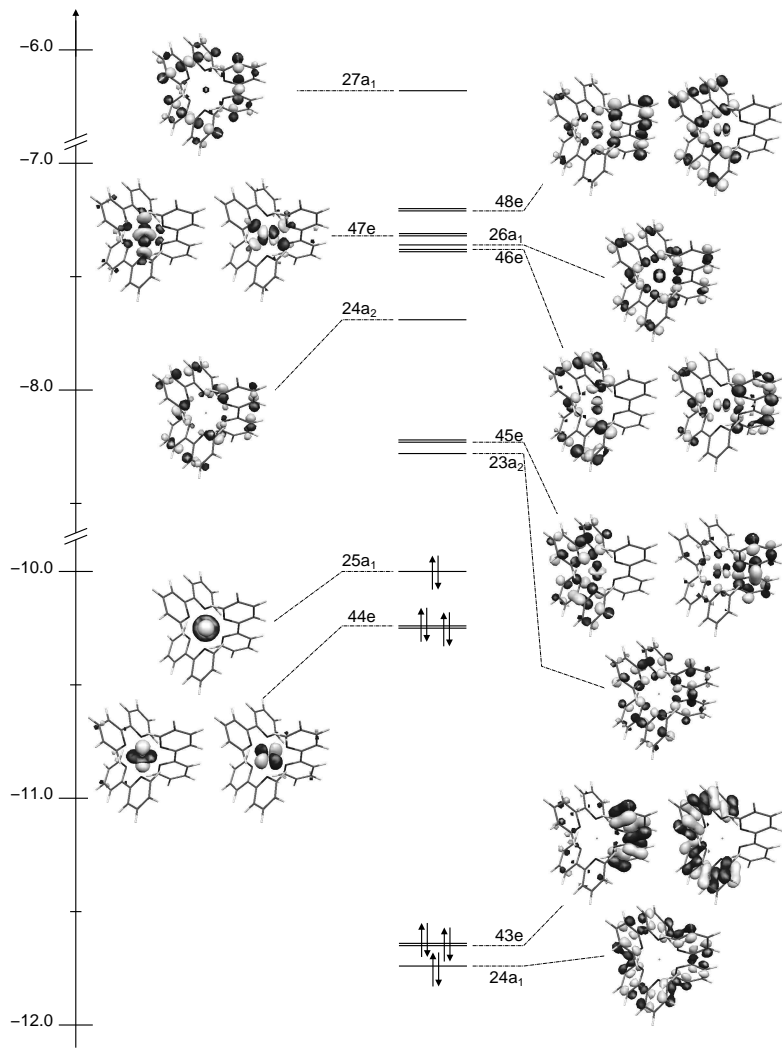


FIGURE 4.4: Frontier KS MOs of $[Fe(bpy)_3]^{2+}$ in the 1A_1 state (PBE/TZP results; eigenvalues in eV).

44e levels and the virtual 47e level. Other virtual levels of e or a_1 symmetry can exhibit small but noticeable “metallic” contributions as a result of the complex orbital

interactions of σ and π types occurring in $[\text{Fe}(\text{bpy})_3]^{2+}$. The unoccupied “metallic” level results from σ -type orbital interactions and is anti-bonding. It contains a significant admixture of ligand contribution in contrast to the $25a_1$ and $44e$ levels which are mainly non-bonding and remain “metallic” in nature. It can thus be concluded that the highest-occupied levels originate from the trigonal splitting of the octahedral $\text{Fe}(t_{2g})$ level whereas the virtual “metallic” level comes from the anti-bonding octahedral $\text{Fe}(e_g)$ level. Hence their occupation also confirms that the characterised singlet state corresponds to the ligand-field $^1\text{A}_{1g}(t_{2g}^6)$ state.

Some properties of $[\text{Fe}(\text{bpy})_3]^{2+}$ in the characterised $^1\text{A}_1$ state can be deduced directly from the diagram of the frontier MOs of Figure 4.4. Thus, given that the KS eigenvalue differences correspond to the zero-order energy excitation energies [89, 90, 91, 92], the absorption spectrum can theoretically be depicted as follows: the Franck-Condon transitions of lowest energies are metal-to-ligand charge transfer (MLCT) transitions originating from the $25a_1$ and $44e$ levels; they are followed, higher in energy, by other MLCT transitions which may mask the $d-d$ transitions ($25a_1, 44e \rightarrow 47e$) of weaker intensity, and by ligand-centred $\pi \rightarrow \pi^*$ transitions (*e.g.*, $24a_1, 43e \rightarrow 23a_2$). This sketch exactly corresponds to the schematic description of the experimental UV/VIS absorption spectrum of the $[\text{Fe}(\text{bpy})_3]^{2+}$ complex in its grounds state. Moreover, the first ionisation energy of a molecule being given by its highest-occupied KS orbital energy level [93, 94, 95], here the “metallic” $25a_1$ level, the ionisation of the complex affects mainly the metal atom, as observed for $[\text{Fe}(\text{bpy})_3]^{2+}$ in its ground state upon a one-electron oxidation.

The characterisation of the complex in the HS state proved to be trickier than the one of the LS state as the two possible HS states, namely the $^5\text{A}_1$ and ^5E states which result from the trigonal splitting of the octahedral $^5\text{T}_{2g}$ state, had to be accounted for. Within D_3 symmetry the two states were found to be nearly degenerate. The near-degeneracy of the $^5\text{A}_1$ and ^5E is due to the fact that passing from one state to the other corresponds mainly to a charge redistribution within the non-bonding KS orbital levels of $\text{Fe}(t_{2g})$ parentage which hardly affects the metal-ligand bond (see below for a more detailed discussion). In the following the two trigonal components of the HS state are discussed in more detail. Due to the difference in the way they handle degenerate states, GAUSSIAN was restricted to the $^5\text{A}_1$ component, whereas ADF allowed the characterisation of both the $^5\text{A}_1$ as well as the ^5E trigonal components of the HS $^5\text{T}_{2g}$ state.

For the HS ^5E state, ADF gave similar electronic structures for all functionals and irrespective of the quality of the basis set. This is illustrated by the diagram of the frontier KS orbital levels of Figure 4.5, which has been constructed from

the PBE/TZP results. For clarity, only the frontier MOs with significant metallic character

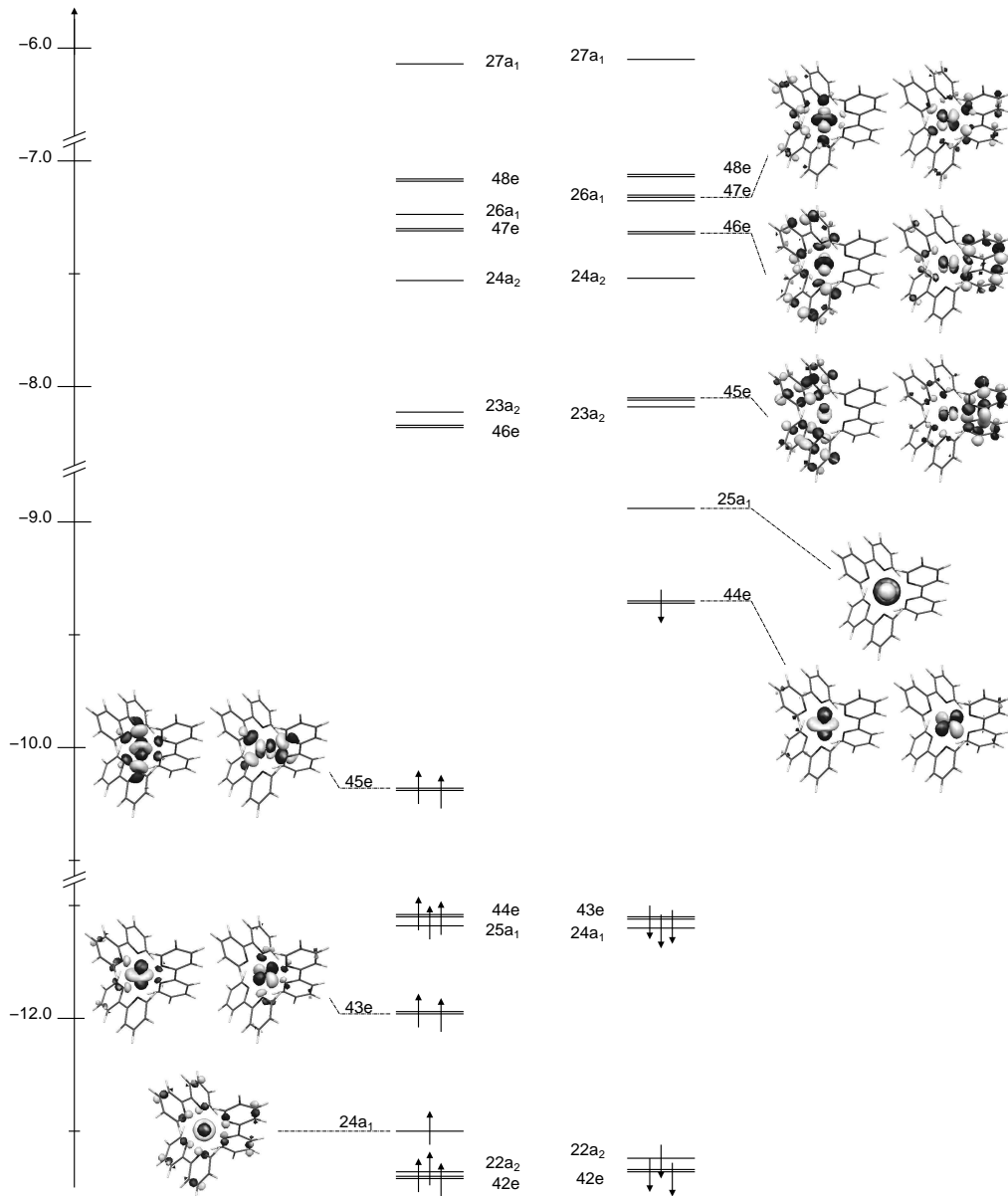


FIGURE 4.5: Frontier KS MOs of $[Fe(bpy)_3]^{2+}$ in the 5E state: for clarity, MOs with noticeable metallic character only are represented (PBE/TZP results; eigenvalues in eV).

character are drawn and the spin-up and spin-down orbital levels are represented separately. The orbital picture is obfuscated by the use of unrestricted calculations since different energies and orbitals are obtained for related spin-up and spin-down single-particle levels. The spin-down orbital levels of Figure 4.5 remain similar in their energy ordering and in the shapes of their orbitals to the ones reported for the LS case. In particular, the $44e$ and $25a_1$ spin-down-orbital levels are also non-

bonding and of octahedral Fe(t_{2g}) parentage, while the $47e$ spin-down-orbital level results from anti-bonding σ -type metal-ligand interactions and is of octahedral Fe(e_g) parentage. The $24a_1$, $43e$ and $45e$ spin-up-orbital levels are the only spin-up frontier levels with a significant metallic character, the $24a_1$, $43e$ levels being of Fe(t_{2g}) parentage and the $45e$ level of Fe(e_g) parentage. They possess more ligand contributions than their spin-down counterparts do, and their energies and ordering also differ from the ones of their spin-down counterparts, accentuating thus the difference between the spin-up and spin-down orbital levels. When considering the occupation of the KS levels, it appears that the characterised electronic state is obtained from the LS state by a two-electron excitation with spin-flip within the subset of the metallic frontier orbital levels of the LS state: using the notation of Figure 4.4, this $d-d$ excitation corresponds to the promotion of two electrons from the $25a_1$ and $44e$ spin-down KS levels of octahedral Fe(t_{2g}) parentage into the $47e$ spin-up level of Fe(e_g) parentage. Finally, from the orbital degeneracy due to the occupation of the highest spin-down orbital level of e symmetry by a single electron (Figure 4.5), it can be concluded that the characterised electronic state is the $M_S = +2$ sublevel of the 5E manifold that results from the trigonal splitting of the LFT ${}^5T_{2g}(t_{2g}^4 e_g^2)$ state. This is confirmed by the Mulliken population analysis and calculated net charges summarised in Table 4.1 for the calculations performed at the PBE/TZP and RPBE/TZP levels, and in Table S2 for the other calculations. As for the LS state, the Voronoi and Mulliken net charges show that the molecular charge is basically found on the iron atom. The Mulliken populations of the AOs of the iron atom also still agree with the [Ar]3d⁶ configuration of the free Fe²⁺ ion, the difference of the total (spin-up and spin-down) atomic populations with their free ion values being due to the covalence of the metal-ligand bond. Lastly, the spin density is located almost entirely on the Fe atom and comes nearly exclusively from the difference between the spin-up and spin-down populations of the Fe(3d) AOs, as expected for the HS 5E state.

The characterisation of the HS 5A_1 component could be performed with both software packages. The electronic structure of the complex in this state is depicted in Figure 4.6 by the diagram of the frontier KS MOs constructed from the PBE/TZP results. The representation of the MOs is again limited to the ones with noticeable metallic character. A comparison between this diagram and the diagram obtained for the HS 5E state (Figure 4.5) illustrates that, in essence, the two HS states differ by the nature of the highest occupied spin-down KS level of octahedral Fe(t_{2g}) parentage: namely, the $44e$ level for the 5E state and the $25a_1$ level for the 5A_1 state. One notes that, when passing from the HS 5E state to the HS 5A_1 state, the $25a_1$

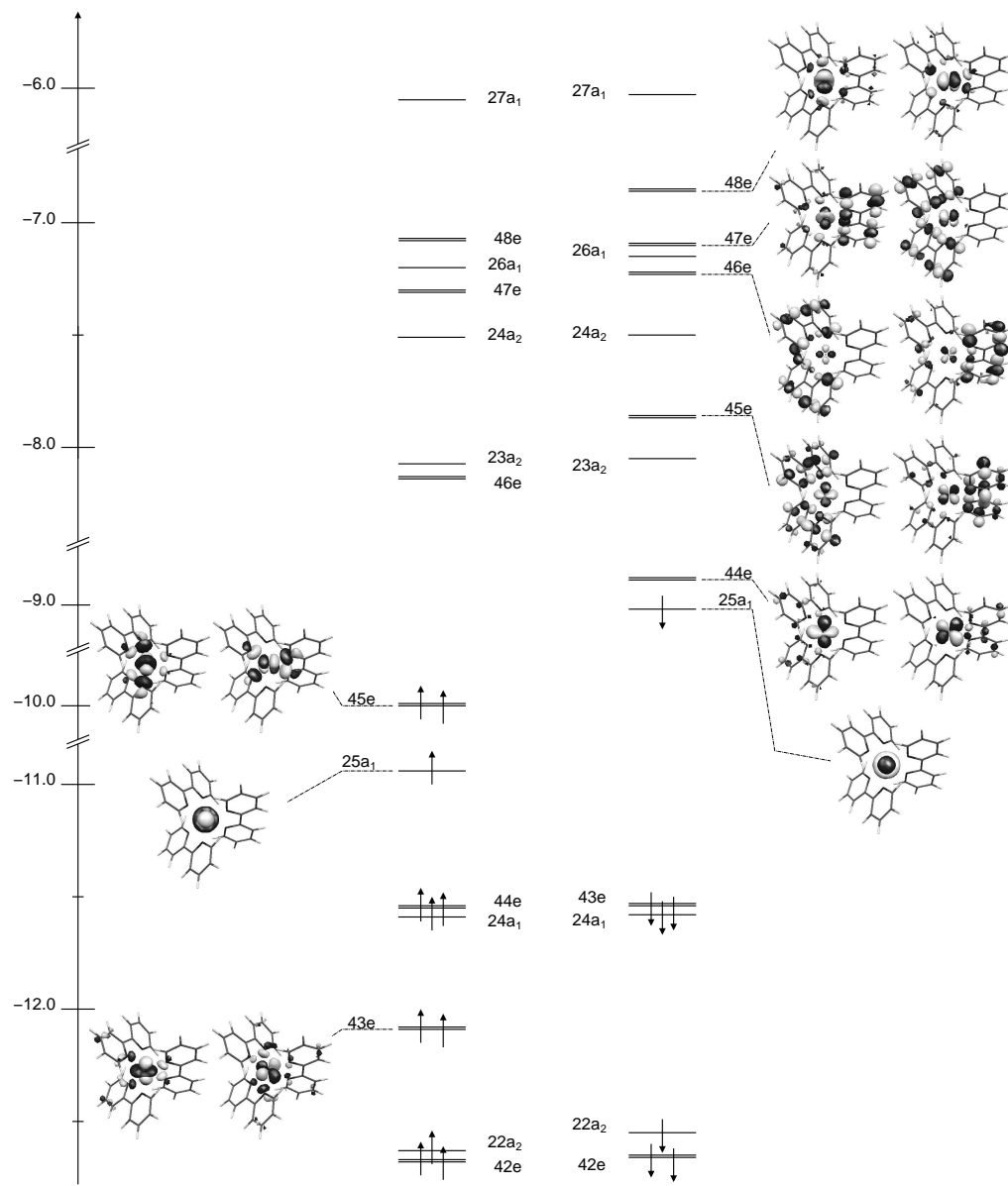


FIGURE 4.6: Frontier KS MOs of $[Fe(bpy)_3]^{2+}$ in the 5A_1 state: for clarity, MOs with noticeable metallic character only are represented (PBE/TZP results; eigenvalues in eV).

spin-down level is slightly stabilised in energy whereas the $44e$ spin-down level is comparatively more destabilised. The opposite trend is observed for their spin-up counterparts which are labelled $43e$ and $24a_1$ for the 5E state, and $43e$ and $25a_1$ for the 5A_1 state: the e level shows a moderate stabilisation and the a_1 level undergoes a very strong destabilisation. As for the anti-bonding e levels of Fe(e_g) parentage, namely the occupied $47e$ spin-up level and the virtual $47e$ spin-down level for the 5E state, and the $48e$ spin-down level for the 5A_1 state, they become moderately destabilised. An explanation for the way these orbital levels evolve on going from the HS 5E state to the HS 5A_1 state is far from being straightforward. Nevertheless the comparison of the two diagrams makes it obvious that the frontier KS levels with a metallic character are the ones which suffer the largest changes, and more especially that the non-bonding spin-down and spin-up levels of Fe(t_{2g}) parentage are the most affected metallic frontier levels. This is also emphasised by the results for the iron atom of the population analysis performed for the complex in the 5A_1 state (Tables 4.1 and S3). Indeed the populations of the spin-up and spin-down AOs given per l -values, as well as the values of the spin density and of the net charge found for the iron atom are identical to the ones reported in Table 4.1 (and Table S2) for the complex in the 5E state. This similarity, combined with the lack of major variations in the AO populations, spin densities and net charges of the N, C and H atoms of the ligands (data not shown), is consistent with the fact that the difference in the electronic structure of $[Fe(bpy)_3]^{2+}$ in the two HS states is mainly located in the metal-centred non-bonding levels of octahedral Fe(t_{2g}) parentage.

B Optimised geometries

1 Geometries in the LS state

The X-ray crystal structure of the $[Fe(bpy)_3]^{2+}$ cation has been reported twice so far [96, 32]. In the following we exclusively refer to the experimental data published by Dick, who solved the crystal structure of $[Fe(bpy)_3](PF_6)_2$ at 293 K [32]. The compound crystallises in the space group $P\bar{3}c1$ and the experimental metal-ligand bond lengths of 1.967 Å are typical for the complex in the LS ground state. It possesses a D_3 site symmetry. For this experimental structure, selected distances and values of the angles β , γ , τ and θ which characterise the arrangement of the ligands around the Fe centre (see Figure 4.7), are summarised in Table 4.2.

Table 4.2

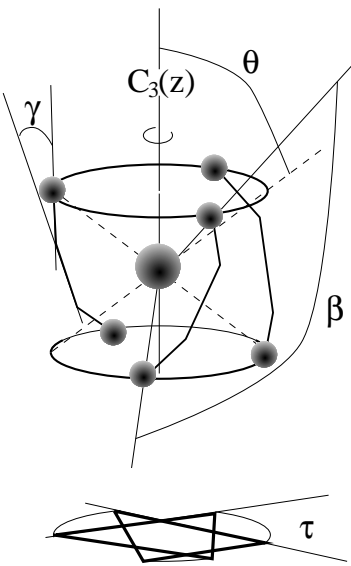


FIGURE 4.7: Angles characterising the spatial arrangement of the ligands around the metal centre in $[Fe(bpy)_3]^{2+}$. β is the bite angle ($\beta = N\text{-}Fe\text{-}N'$), γ the dihedral angle between the ligand moieties ($\gamma = N\text{-}C_2\text{-}C'_2\text{-}N$), τ the twist angle, and θ the angle between the z -axis and the generator of the cone on which the nitrogen atoms are located.

The values obtained for the same structural parameters of the optimised ground-state geometries from DFT are also reported in Table 4.2. The calculated geometries are all similar to one another irrespective of the functional and the quality of the basis set, and compare well with the experimental structure. For instance, all calculations led to a N-C₂ bond which is longer than the N-C₆ bond in agreement with experiment. However, the optimised geometries prove to be more expanded than the experimental geometry since, with the exception of the C₂-C'₂ and Fe-N bonds, the bond lengths found for the calculated structures tend to be systematically larger than the ones found experimentally. Given that our study is performed in the gas phase and therefore does not account for the packing and counter-ion effects present in the solid state, there is no reason as to why the experimental and calculated geometries should strictly match.

A more detailed analysis shows that the tendency of the optimised bond lengths of the pyridinyl rings to be larger than experimentally observed is most pronounced for the double- ζ STO DZ basis set and less pronounced for the GTO 6-311+G** basis set. It is least pronounced for the triple- ζ polarised GTO TZVP and STO TZP basis sets which give identical results when used with the PBE functional. This trend corresponds to a shrinking of the aromatic rings with the quality of the basis set. With the exception of the dihedral angle γ , the calculated values of the angular

parameters are close to those found for the X-ray structure to within ~ 1 degree, reflecting analogous arrangements of the ligands in the experimental and calculated structures. The γ values are larger for the GTO basis sets than for the STO basis sets. This basis set dependence and the important differences of about 3 to 6 degrees between the experimental and calculated γ values can be explained by the fact that the deformations along this angular coordinate are associated with floppy modes. The influence of the basis sets on γ and on the bond lengths of the aromatic rings is also observed for the optimised geometries of the free ligand [97]. On the whole, the best agreement between the calculated and experimental geometries of the ligands is observed for the hybrid functionals, in line with the acknowledged good performance of the hybrids for the description of the molecular structures of covalently bound main group elements [38, Sec. 8.1].

The optimised metal-ligand bond lengths increase with the quality of the basis sets used. Thus the shortest Fe-N distances are obtained for the DZ basis set as this allows the lack of flexibility of this basis set for describing the Fe atom (especially with regard to the important electron correlation in d -space) to be compensated for by the use of basis functions centred on the neighbouring N atoms. Longer Fe-N distances result from the use of the larger basis sets, but the Fe-N distances obtained for the 6-311+G^{**} basis set are still slightly shorter than those obtained for the TZP and TZP basis sets, presumably for the same reason as for the DZ basis set. The comparable quality of the TZP and TZVP basis sets is also illustrated by the fact that they lead to equal Fe-N distances when used with the PBE functional. With regard to the different functionals used in this study, the values of the optimised Fe-N bond length are lower for the BP86, PW91 and PBE GGAs than for the RPBE GGA and the hybrids. One also notes that the increase of the exact-exchange contribution from 15% in the B3LYP* functional to 20% in the B3LYP functional is accompanied by a lengthening of the Fe-N distance of 0.014 Å. Similarly, the admixture of 25% exact-exchange to the PBE functional as in the PBE1PBE hybrid gives rise to an increase of the Fe-N distance by 0.022 Å. We thus conclude that hybrid functionals tend to give longer metal-ligand bond lengths than do GGAs, and that the more important the exact-exchange contribution the longer the metal-ligand bond. Figure 4.8 illustrates this by showing the evolution of the Fe-N bond length in the LS state as a function of the amount a_0 of exact exchange in the B3LYP (Eq. (4.22)) and the PBE1PBE (Eq. (4.23)) functionals using the TZVP basis set. The effect is somewhat less pronounced for the PBE1PBE functional. This behaviour is reminiscent of the tendency of the HF method to systematically predict metal-ligand bonds which are too long [38, page 127].

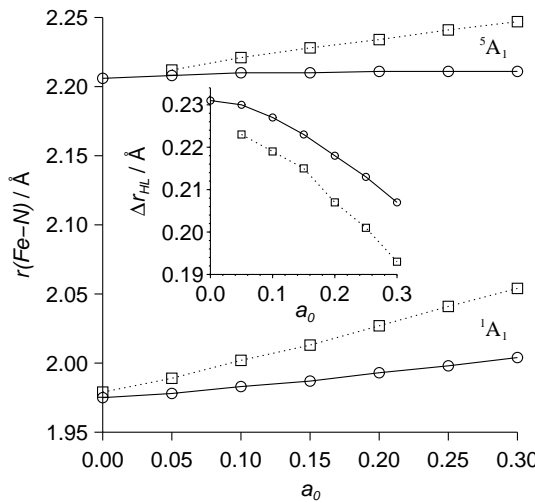


FIGURE 4.8: Evolution of the Fe-N bond length in the LS and HS 5A_1 state with the value of the a_0 coefficient of the exact-exchange contribution in the PBE1PBE (circles) and B3LYP (squares) hybrids; the inset gives the a_0 dependence of Δr_{HL} ; (results of geometry optimisations done using the TZVP basis set).

2 Geometries in the HS states

Tables 4.3 and 4.4 show selected distances and the values of the angles β, γ, τ and θ which characterise the geometry of the complex in the 5E and 5A_1 state, respectively.

Table 4.3

Table 4.4

For either HS state, the values of the selected structural parameters for the series of calculations predict a similar arrangement of the ligands around the Fe centre. Despite the lack of experimental data, the consistency of the computational results inspires confidence in the quality of the predicted HS geometries. Closer inspection of the Tables shows that, as observed for the LS geometries, there is a lengthening of the Fe-N bond along with a shrinking of the aromatic rings with increasing quality of the basis set. As also observed for the LS geometries, for the 5A_1 geometries the use of the hybrids leads to the least expanded pyridinyl rings and the longest Fe-N bonds are obtained for the RPBE and hybrid functionals. Again for the hybrids the Fe-N bond lengthens with the amount a_0 of the exact-exchange contribution (see Figure 4.8). One notes (i) that the dependence is more pronounced for the B3LYP functional than for the PBE1PBE functional; and (ii) that, for both functionals, the Fe-N bond length varies with a_0 slightly less rapidly for the complex in the HS state than for the complex in the LS state, as shown by the plots of Δr_{HL} against

a_0 in the inset of Figure 4.8. As a whole, the influence of the basis sets and of the functionals on the calculated geometries is the same whenever one considers either the LS geometries or the HS geometries. It follows that any bias due to the methods used will have a limited impact on the results of the comparison between the predicted geometries of the complex in the different states.

Thus, irrespective of the theoretical level considered, the main structural difference when going from the 5E state to the 5A_1 state turns out to be the lengthening of $\sim 0.02 \text{ \AA}$ of the Fe-N bond which little affects the bond lengths within the ligands (Tables 4.3 and 4.4). The $^5E \rightarrow ^5A_1$ change of state foremost consists in the depopulation of the $44e$ spin-down level in favour of the $25a_1$ spin-down level (Figures 4.5 and 4.6). These levels of Fe(t_{2g}) parentage being non-bonding is the reason as to why the geometries of the ligands hardly vary. The lengthening of the Fe-N bond may be explained by the fact (*i*) that there is a transfer of electron density from the xy plane to along the z axis and (*ii*) that the increase of the density along z tend to repel the ligands.

C Structural changes with regard to the analysis of the low-temperature relaxation dynamics

Comparison of Tables 4.2-4.4 shows that the most important structural change upon the LS \rightarrow HS transition is found for the Fe-N bond which lengthens by about 0.2 \AA . Table 4.5 gives for all the considered theoretical levels the estimated Δr_{HL} values.

Table 4.5

This increase of the Fe-N distance is due to the promotion of two electrons from the non-bonding metallic levels of octahedral Fe(t_{2g}) parentage into the anti-bonding level of octahedral Fe(e_g) parentage. It entails an important spatial rearrangement of the ligands illustrated by the relatively large variations of the angles β , γ , τ , and the θ . Within the ligands, the C₂-C'₂ distance between the pyridinyl moieties gets longer by about 0.02 \AA , probably because it allows - along with the modification of the angle values - to keep the metal-ligand interactions optimal despite the lengthening of the Fe-N bond. The other C-C bonds and the C-H bonds are hardly affected. The N-C distances become shorter by $\sim 0.01 \text{ \AA}$; however the N-C₂ bond remains longer than the N-C₆ bond as in the experimental LS geometry and in the optimised geometry of the free ligand [97]. The shortening of both N-C bonds with increasing metal-ligand distance can be assigned to a decrease of π -backbonding involving ligand-centred orbitals with anti-bonding character at the level of the N-C bonds. Nevertheless,

the changes in bond lengths observed for the ligands are globally quite limited and this actually is in agreement with the known rigidity of the 2,2'bipyridine ligand. The difference of $\sim 0.2 \text{ \AA}$ for the metal-ligand bond between the LS and the HS states agrees remarkably well with the experimental values found for iron(II) spin-crossover compounds with the same $[FeN_6]$ first coordination sphere as $[Fe(bpy)_3]^{2+}$ and, in particular, it validates the assumption $\Delta r_{HL} \approx 0.2 \text{ \AA}$ central to the analysis of the relaxation dynamics.

The molecular volume variation, ΔV_{HL} , also plays an important role because it governs the influence of an exerted pressure on the relaxation dynamics. In order to probe this value, the molecular volume of the complex in the LS and HS states was calculated as the volume defined by the isodensity surface $0.0004 \text{ e}/\text{bohr}^3$. This charge density value was used as it is known to yield for organic compounds volumes that compare well with the observed molar volumes in the liquid phase [98, 99]. Calculations were done for the complex in the 1A_1 , 5E and 5A_1 states using the STO DZ and TZP basis sets and the BP86, PW91, PBE and RPBE functionals. The results are reported in Table 4.6.

Table 4.6

One notes that the LS and HS molecular volumes obtained using the DZ basis set are systematically larger than the corresponding ones obtained with the TZP basis sets by ~ 50 and $\sim 40 \text{ \AA}^3$, respectively. This can be explained by the previously noticed fact that the geometries found for the ligands using the DZ basis set are more expanded than those found using the TZP basis set. Nevertheless, the ΔV_{HL} values calculated using either basis set are comparable. Depending on the functional used it is between 26 and 30 \AA^3 for the DZ basis set and between 21 and 24 \AA^3 for the TZP basis sets. These values are in the 15 - 30 \AA^3 range observed experimentally for spin-crossover systems and they agree remarkably well with the model value of 25 \AA^3 estimated from the pressure dependence of the HS \rightarrow LS relaxation in $[Fe(bpy)_3]^{2+}$ under the assumption that $\Delta r_{HL} \approx 0.2 \text{ \AA}$.

D The HS-LS energy gap

The zero-point energy difference ΔE_{HL}° of $[Fe(bpy)_3]^{2+}$ doped into different crystalline hosts has been estimated in Sec. II from the low-temperature HS \rightarrow LS relaxation dynamics to lie in the range of 2500 - 5000 cm^{-1} based on the now validated assumption that $\Delta r_{HL} \approx 0.2 \text{ \AA}$. The purely electronic energy difference between the potential wells of the lowest component of the HS state and the LS state is given by $\Delta E_{HL}^{\text{el.}} = \Delta E_{HL}^\circ - \Delta E_{HL}^{\text{vib.}}$. The vibrational contribution, $\Delta E_{HL}^{\text{vib.}}$, was estimated

to be -875 cm^{-1} from a vibrational analysis performed at the TZVP/PBE level for the LS $^1\text{A}_1$ and the HS $^5\text{A}_1$ states [100]. The sign reflects the weakening of the metal-ligand bond when passing from the LS to the HS state [101]. Thus the best experimental estimate of $\Delta E_{\text{HL}}^{\text{el}}$ for $[\text{Fe}(\text{bpy})_3]^{2+}$ is in the range of $3500\text{-}6000 \text{ cm}^{-1}$. The comparison of the calculated values of $\Delta E_{\text{HL}}^{\text{el}}$ with this estimate will provide a stringent test of the performance of the functionals used in this study.

Table 4.7 summarises the calculated values of the electronic energy difference between the HS and the LS state, $\Delta E_{\text{HL}}^{\text{el}}$, of $[\text{Fe}(\text{bpy})_3]^{2+}$ for the STO DZ and TZP basis sets (ADF) and for the GTO 6-311+G ** and TZVP basis sets (GAUSSIAN), and Figure 4.9 shows a graphic representation of the calculated values of $\Delta E_{\text{HL}}^{\text{el}}$ versus the respective calculated Fe-N bond lengths.

Table 4.7

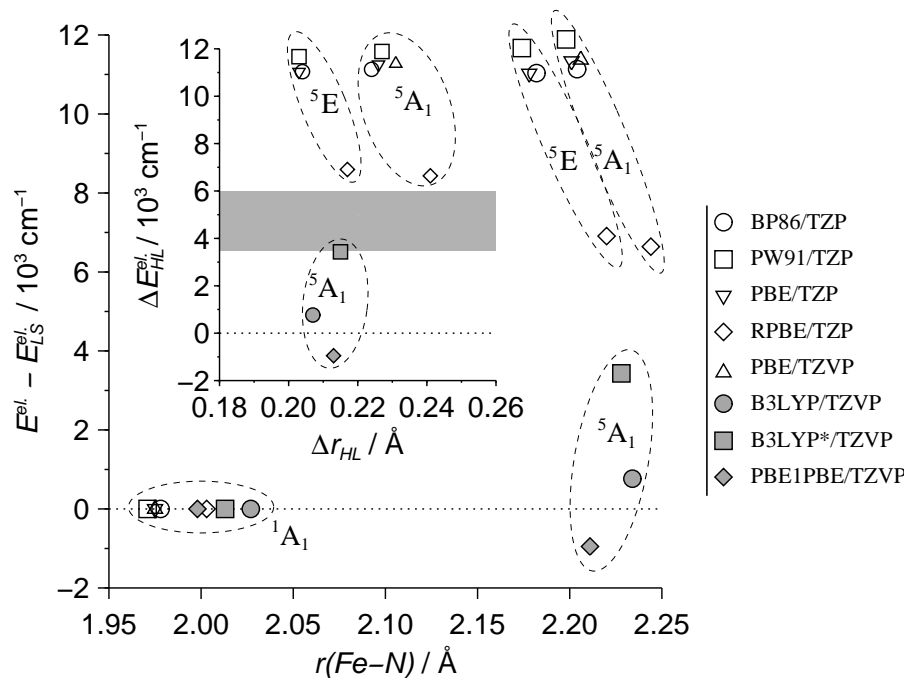


FIGURE 4.9: Comparison of best DFT estimates of the relative positions of the LS $^1\text{A}_1$ and HS ^5E and $^5\text{A}_1$ states of $[\text{Fe}(\text{bpy})_3]^{2+}$ along the Fe-N distance coordinate: results are for ADF and GAUSSIAN calculations with the STO TZP and GTO TZVP basis sets. The electronic energy is given relative to the energy of the LS state. Inset: HS-LS electronic energy difference $\Delta E_{\text{HL}}^{\text{el}}$ as a function of the Fe-N bond length change; the shaded region indicates the $3500\text{-}6000 \text{ cm}^{-1}$ experimental range.

Results obtained using GAUSSIAN are restricted to the $^5\text{A}_1$ component of the HS state. ADF permits calculations on both components of the HS state, which show

that the energy difference between the 5A_1 and the 5E components is comparatively small, irrespective of the quality of the basis set and the functional used. The calculated values for ΔE_{HL}° range from -1000 to 16000 cm^{-1} . Even though the experimental estimate lies within this range, this large spread is clearly not satisfactory and needs further discussion. In principle, the performance of different density functionals can only be judged in the limit of a complete basis set. In practice, one is often obliged to test functionals using incomplete basis sets. Before discussing the functionals, let us focus on the influence of the basis set on the evaluation of $\Delta E_{HL}^{\text{el}}$. For a given functional the DZ basis set results in values of $\Delta E_{HL}^{\text{el}}$ for the 5E and the 5A_1 components which are systematically higher by ~ 3400 and $\sim 4000\text{ cm}^{-1}$, respectively, compared to the values obtained with the TZP basis set. The improvement of the quality of the basis set actually lowers the energy of $[Fe(bpy)_3]^{2+}$ in either spin-state, however, the effect is more pronounced for the complex in the HS state than in the LS state. This is due to the limitations tied to the use of the smaller DZ basis set becoming more important as the metal-ligand bond lengthens. Thus the decrease in $\Delta E_{HL}^{\text{el}}$ of $\sim 3400\text{ cm}^{-1}$ for the 5E component is associated with the lengthening of the metal-ligand bond by $0.19\text{-}0.22\text{ \AA}$. Similarly, the Fe-N bond in the 5A_1 state being $\sim 0.02\text{ \AA}$ longer than in the 5E state, the change of basis set lowers the HS-LS energy gap by another $\sim 600\text{ cm}^{-1}$. These variations illustrate the effect of cancellation of errors tied to the use of finite basis sets. That is, the cancellation of errors is more effective (*i*) the smaller the difference in metal-ligand bond lengths in given geometries, and (*ii*) the more flexible the basis set is for the description of the valence electrons hence of chemical bonding. In addition, the $^5A_1\text{-}^1A_1$ electronic energy difference evaluated with the PBE functional and using the STO TZP and the GTO TZVP basis sets in ADF and GAUSSIAN, respectively, differ by only 36 cm^{-1} . This firmly establishes the previously noted equivalence of the STO TZP and the GTO TZVP basis sets and the order of increasing quality as

$$\text{DZ} \ll \text{TZP} \equiv \text{TZVP}. \quad (4.24)$$

For the two GTO basis sets, $\Delta E_{HL}^{\text{el}}$ is typically $\sim 440\text{ cm}^{-1}$ larger for the 6-311+G** basis set than for the TZVP basis set, irrespective of the functional. As the 6-311+G** basis set offers a larger flexibility for the description of the valence electrons than the TZVP basis set, this suggests that the use of basis sets larger than those we have used would mainly result in a slight stabilisation of the LS state with respect to the HS state, *i.e.* in a slight increase of $\Delta E_{HL}^{\text{el}}$ as observed when passing from the TZVP to the 6-311+G** basis set. Finally, the comparison of the sizes of the basis

sets and of the results they lead to indicates that, among the basis sets used, the TZVP and the TZP basis set offer the best tradeoff between size and flexibility.

The above discussion shows that the quality of the basis set influences the calculations quite considerably and therefore in the following the discussion of the performance of the functionals is restricted to results obtained using the two high-quality TZVP and TZP basis sets and to the comparison of $\Delta E_{\text{HL}}^{\text{el}}$ for the ${}^5\text{A}_1$ component as only this one is accessible with GAUSSIAN. We note that the GGA functionals BP86, PW91 and PBE give values for $\Delta E_{\text{HL}}^{\text{el}}$ of $11000\text{-}12000\text{ cm}^{-1}$, thus systematically overestimating it by more than 5000 cm^{-1} compared to the experimental value. On the other hand the hybrid functionals B3LYP and PBE1PBE underestimate $\Delta E_{\text{HL}}^{\text{el}}$ by at least 3000 cm^{-1} , in fact falsely predicting $[\text{Fe}(\text{bpy})_3]^{2+}$ to be a spin-crossover or even a high-spin complex. Two of the functionals, namely the RPBE GGA and the B3LYP* hybrid with calculated values of $\Delta E_{\text{HL}}^{\text{el}}$ of 6640 and 3430 cm^{-1} , respectively, approach the range of the experimental estimate. In contrast to the optimised geometries, the nature of the functional used has an even greater influence on the calculated values of $\Delta E_{\text{HL}}^{\text{el}}$ than the basis set, and therefore the energetics provide a much more stringent test of the performance of a given functional than the geometry optimisation. Based on this criterion, the RPBE GGA and the B3LYP* hybrid functionals show the best performance.

The disparity in performance of the XC functionals for predicting $\Delta E_{\text{HL}}^{\text{el}}$ of the $[\text{Fe}(\text{bpy})_3]^{2+}$ complex points to the inherent difficulty of XC functionals to correctly predict the relative energies of states of different spin multiplicities, particularly for spin-crossover systems [56, 66, 67, 68, 27] but also for spin-forbidden chemical reactions [102]. This is emphasised by the fact that for the TZP basis set the ${}^5\text{E}$ and the ${}^5\text{A}_1$ components of the quintet state are consistently predicted to be nearly degenerate, that is within the chemical accuracy of 350 cm^{-1} , by functionals which behave quite differently when it comes to evaluating the HS-LS energy gap. Given that the PBE, RPBE and PBE1PBE functionals have the same correlation contribution but differ in the exchange contribution, the remarkable divergence between their estimates of $\Delta E_{\text{HL}}^{\text{el}}$ must be due to the difficulty in correctly treating the exchange contribution in the approximate functionals. The key point is that the approximate exchange functionals have to correctly account for the variation of the exchange interaction (Fermi correlation), hence of $|E_x|$, with increasing or decreasing spin polarisation as in the case of a change of spin-state. For the GGA functionals, this implies that the exchange enhancement factor F_x intervening in the definition of E_x^{GGA} (Eq. (4.19)) has to increase correctly with the reduced spin-density gradients $s_\sigma(\mathbf{r})$ (Eq. (4.20)) so as to rapidly depart from its LDA value

of $F_x(0) = 1$ and thus to overcome the underestimation of the exchange energy inherited from their LDA component for both spin-unpolarised and spin-polarised systems. For spin-unpolarised systems with $\rho_\uparrow(\mathbf{r}) = \rho_\downarrow(\mathbf{r}) = \rho(\mathbf{r})/2$, Figure 4.10 allows the comparison of the enhancement factors of the B88, PW91, PBE and RPBE exchange functionals. Therein F_x is plotted against the reduced charge-density gra-

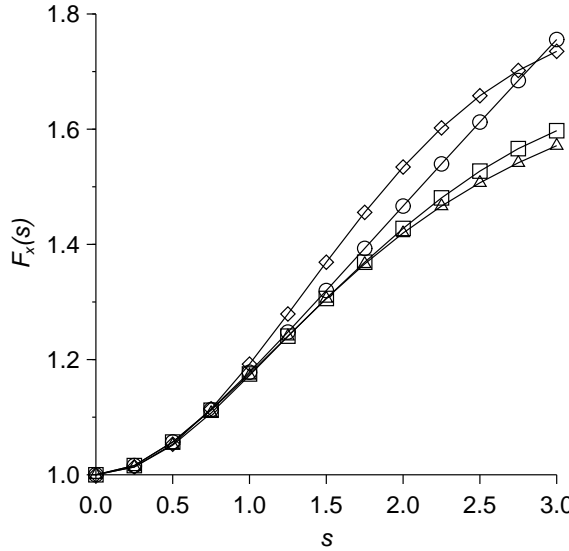


FIGURE 4.10: Plot of the exchange enhancement factors F_x for the B88 (circles), PW91 (squares), PBE (triangles) and RPBE (lozenges) exchange functionals against the reduced charge-density gradient $s(\mathbf{r}) = |\nabla\rho(\mathbf{r})| / (2(3\pi^2)^{1/3}\rho^{4/3}(\mathbf{r}))$ (results for the spin-unpolarised case).

dient, $s(\mathbf{r}) = |\nabla\rho(\mathbf{r})| / (2(3\pi^2)^{1/3}\rho^{4/3}(\mathbf{r}))$, for $s \in [0, 3]$, that is, for s in the range which is energetically important for atomic and molecular systems [49]. For the purpose of our discussion, it suffices to note that (i) the four F_x functions increase with s and are almost superimposable for $0 \lesssim s \lesssim 0.7$, (ii) in the most significant interval $0.7 \lesssim s \lesssim 2$, the F_x^{PW91} , F_x^{PBE} and even the F_x^{B88} enhancement factors still behave quite similarly, but F_x^{RPBE} is found to be larger than the three other functions everywhere in this range. Of the four GGA exchange functionals, the RPBE thus provides the largest nonlocal corrections to the LDA exchange energy for the spin-unpolarised case.

For spin-polarised systems, the gradient correction is even more important since the exchange interactions increase with the spin polarisation $\zeta(\mathbf{r})$ (Eq. (4.18)). The dependence of E_x^{GGA} on $\zeta(\mathbf{r})$ is made more obvious by recasting Eq. (4.19) in the form

$$E_x^{\text{GGA}}[\rho_\uparrow, \rho_\downarrow] = C_x \int d\mathbf{r} \rho^{4/3}(\mathbf{r}) F_x(\zeta(\mathbf{r}), s(\mathbf{r})). \quad (4.25)$$

The exchange enhancement factor $F_x(\zeta, s)$, derived by setting $\rho_\uparrow = \rho(1 + \zeta)/2$ and $\rho_\downarrow = \rho(1 - \zeta)/2$ in Eq. (4.19) and by neglecting contributions in $\nabla\zeta$ [49], reads

$$F_x(\zeta, s) = \frac{1}{2}(1 + \zeta)^{4/3}F_x(s/(1 + \zeta)^{1/3}) + \frac{1}{2}(1 - \zeta)^{4/3}F_x(s/(1 - \zeta)^{1/3}). \quad (4.26)$$

$F_x(\zeta, s)$ is represented in Figure 4.11, along with the gradient correction $F_x(\zeta, s) - F_x(\zeta, s = 0)$, for the B88, PW91, PBE and RPBE exchange functionals as function of ζ for $s = 0.0, 0.5, 1.0, 1.5, 2$. In all cases, the enhancement factor increases with

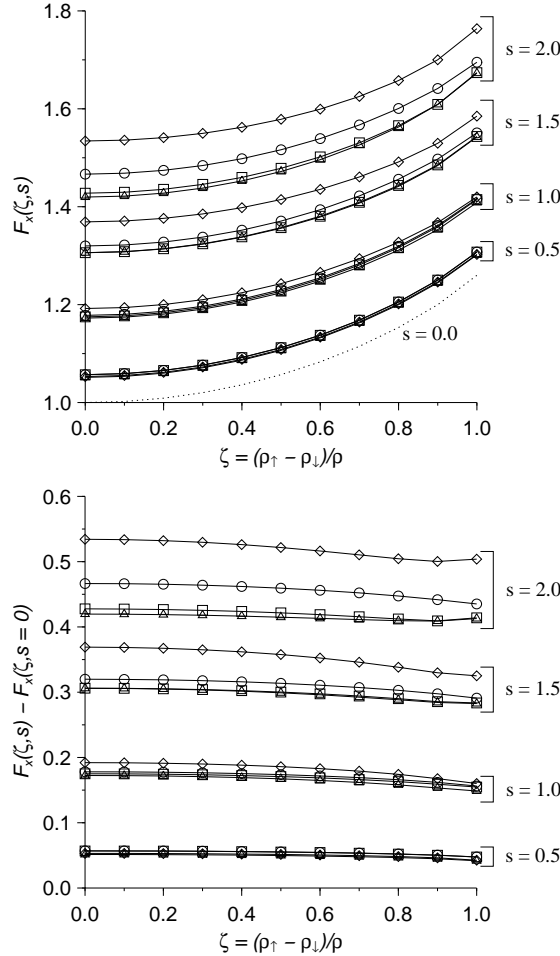


FIGURE 4.11: (Top) Exchange enhancement factor $F_x(\zeta, s)$ (Eq. (4.26)) for the B88 (circles), PW91 (squares), PBE (triangles) and RPBE (lozenges) exchange functionals as function of ζ for fixed s values. (Bottom) Plots of the gradient corrections $F_x(\zeta, s) - F_x(\zeta, s = 0)$.

the spin polarisation. For $s = 0$, that is in LDA, it reduces to $F_x(\zeta, s = 0) = \frac{1}{2}[(1 + \zeta)^{4/3} + (1 - \zeta)^{4/3}]$. The gradient corrections increase with increasing values of s . For small values of s they are quite similar for the four functionals considered.

At higher values of s , that is for $s \approx 1.5$, the F_x^{RPBE} is again found to give the largest gradient correction. Therefore the success of the RPBE XC functional correctly predicting the HS-LS energy difference in $[Fe(bpy)_3]^{2+}$ can be ascribed to an improved gradient correction to the LDA exchange energy for both spin-unpolarised and spin-polarised systems as compared to PBE, PW91 and BP86 GGAs, thus allowing a more reliable description of the change in exchange energy which accompanies the spin-state change. The requirement of correctly rendering the variation of the exchange energy upon the change of spin-state is also important because of the large metal-ligand bond length difference between the two states as the reduced gradient s increases when bonds stretch and exchange turns on with increasing s values [47, 49].

As a cautious note, we believe at this point that it is worth insisting upon the fact that the success met with the RPBE functional for the evaluation of the HS-LS energy difference in $[Fe(bpy)_3]^{2+}$, or even in $[Fe(H_2O)_6]^{2+}$ as in Ref. [27], does not imply that this GGA is *the* functional of choice for the description of iron(II) complexes. For instance, for the $[Fe(NH_3)_6]^{2+}$ complex investigated in Ref. [28], although the RPBE functional outperforms the BP86, BLYP, PW91 and PBE GGAs and performs as well as more recent functionals, it still underestimates the best *ab initio* estimate of the HS-LS energy difference, the best overall agreement for the energetics of the studied simple $[Fe(H_2O)_6]^{2+}$ and $[Fe(NH_3)_6]^{2+}$ complexes being found for the PBE1PBE functional.

For the hybrid functionals B3LYP (Eq. (4.22)) and PBE1PBE (Eq. (4.23)), the contribution a_0 of the exact-exchange energy E_x^{KS} , Eq. (4.14), has a substantial influence on the evaluation of the HS-LS energy gap. Figure 4.12 gives $\Delta E_{\text{HL}}^{\text{el}}$ plotted against a_0 for $0 \leq a_0 \leq 0.3$. In this interval $\Delta E_{\text{HL}}^{\text{el}}$ for the two functionals are decreasing functions of a_0 . They cross the 3500-6000 cm⁻¹ range of the experimental $\Delta E_{\text{HL}}^{\text{el}}$ values for a_0 values of between 0.10 and 0.15, the value $a_0 = 0.15$ being actually used in the B3LYP* functional by Reiher *et al.* [66, 67]. For an exact-exchange contribution smaller than 10%, the HS-LS energy gap is overestimated as a consequence of the underestimation of the exchange energy. This is best illustrated by considering the $a_0 = 0$ limit. Using the PBE1PBE formula, the exchange contribution reduces to the PBE exchange functional which was shown above to not provide sufficient gradient corrections to the LDA exchange energy. With the B3LYP expression, the exchange contribution becomes $E_x^{\text{LDA}} + a_x \Delta E_x^{\text{B}}$ with $a_x = 0.72$. It also underestimates exchange since its GGA part consists in a drastic reduction to 72% of the Becke's 1988 nonlocal correction ΔE_x^{B} which was already found to be too small. With regard to the issue of the amount of the exact exchange to be included in hybrids, the above results support the idea that, for the energetics of transition

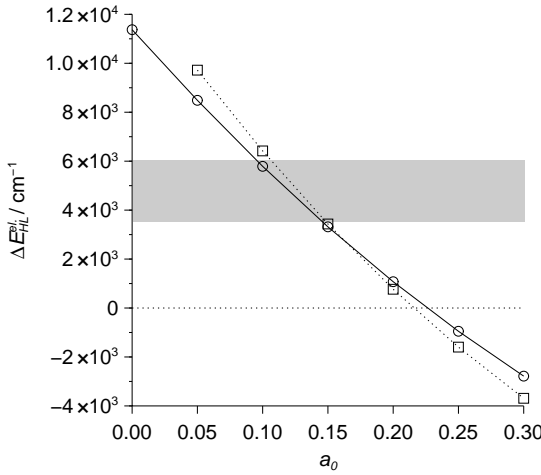


FIGURE 4.12: Dependence of the electronic energy difference $\Delta E_{\text{HL}}^{\text{el}}$ between the HS ${}^5\text{A}_1$ and LS ${}^1\text{A}_1$ states on the a_0 coefficient of the exact-exchange contribution in the B3LYP (squares, Eq. (4.22)) and PBE1PBE (circles, Eq. (4.23)) hybrids; (results of geometry optimisations done with the TZVP basis set). The shaded region indicates the range of the experimental values (see text).

metal complexes, it must be further reduced relative to its generally admitted value of about 1/4. A contribution of $\sim 10\%$ seems to be the more appropriate.

We end our discussion by reconsidering the remarks made in Section B that the use of the RPBE GGA and of the hybrids yields the longest metal-ligand bonds for the complex in a given spin-state, and that the Fe-N bond obtained with a hybrid is longer the larger the contribution of the exact exchange. From the analysis of the results obtained for the energetics and the trend of the HF method to give too long metal-ligand bonds due to the lack of correlation, it actually appears that both phenomena can be explained by the fact that correlation turns off relative to exchange with an increase of the latter [49], since (i) as compared to the other GGAs there is with the RPBE a relative enhancement of exchange provided by significant gradient corrections to the LDA exchange energy and, similarly, (ii) the admixture of exact-exchange energy in hybrids is at the origin of an increase of exchange.

VI Concluding remarks

We have examined the extension of the HS \rightarrow LS relaxation model used for spin-crossover systems to the LS complex $[\text{Fe}(\text{bpy})_3]^{2+}$. For this purpose, $[\text{Fe}(\text{bpy})_3]^{2+}$ has been characterised in the LS and HS states using density-functional approaches. The BP86, PW91, PBE and RPBE GGAs and the B3LYP, B3LYP* and PBE1PBE hybrids have been employed in combination with the STO DZ and TZP and the

GTO TZVP and 6-311+G^{**} basis sets. The main results and conclusions obtained are summarised below.

$\langle 1 \rangle$ By applying the relaxation model to $[Fe(bpy)_3]^{2+}$, a zero-point energy difference ΔE_{HL}° of between 2500 and 5000 cm⁻¹ was estimated for the complex embedded in different crystalline hosts and a molecular volume change of $\Delta V_{HL} \approx 25 \text{ \AA}^3$ was deduced from the pressure study of its relaxation dynamics. The assumption central to this approach of a Fe-N bond length change of $\Delta r_{HL} \approx 0.2 \text{ \AA}$ was validated at all the considered theoretical levels, and the calculations furthermore gave ΔV_{HL} values in good agreement with the experimental estimate. These results therefore establish the validity of the extension of the relaxation model used for the spin-crossover complexes to the LS complex $[Fe(bpy)_3]^{2+}$.

$\langle 2 \rangle$ The density-functional calculations led to the characterisation of the D_3 complex in the 1A_1 , 5E and 5A_1 states which were shown to correspond to the octahedral ligand-field LS $^1A_{1g}(t_{2g}^6)$ and HS $^5T_{2g}(t_{2g}^4 e_g^2)$ states, the quintet states resulting from the trigonal splitting of the octahedral HS state. The spin-state change from the LS state to any of the HS component schematically corresponds the promotion of two electrons from the frontier non-bonding a_1 and e KS levels of octahedral $Fe(t_{2g})$ parentage into the frontier anti-bonding KS e level of octahedral $Fe(e_g)$ parentage. This explains the large increase of the Fe-N bond distance of about 0.2 Å upon the change of spin-states which constitutes the main structural evolution in the complex. With regard to the HS geometries, they are quite similar as the difference in their electronic structure essentially involves an electronic rearrangement within the frontier non-bonding KS levels of octahedral $Fe(t_{2g})$ parentage.

$\langle 3 \rangle$ The STO TZP and GTO TZVP bases proved to be of similar quality for the description of the geometry and the energetics of $[Fe(bpy)_3]^{2+}$. They outperform the small STO DZ basis set and constitute thus the best basis sets used.

$\langle 4 \rangle$ Whereas the XC functionals consistently describe the LS and HS geometries, they perform very differently with respect to the energetics. For the calculations with the most flexible and equivalent TZP and TZVP basis sets, the HS-LS electronic energy difference that comes closest to the best experimental estimate of 3500-6000 cm⁻¹ is obtained with the RPBE GGA ($\Delta E_{HL}^{\text{el}} = 6640 \text{ cm}^{-1}$). This energy gap is overestimated when the BP86, PW91 and PBE GGAs are used (11000-12000 cm⁻¹) and it is underestimated with the hybrids. With the B3LYP ($\Delta E_{HL}^{\text{el}} = 766 \text{ cm}^{-1}$) and PBE1PBE (-951 cm⁻¹) hybrids, $[Fe(bpy)_3]^{2+}$ is wrongly predicted as a spin-crossover or HS complex. The result improves with the B3LYP* hybrid ($\Delta E_{HL}^{\text{el}} = 3432 \text{ cm}^{-1}$) which incorporates less exact-exchange contribution than the B3LYP. We ascribe the difficulties met with the DFT methods for the evaluation of the HS-LS

energy gap in $[\text{Fe}(\text{bpy})_3]^{2+}$ to the fact that the exchange functionals do not properly take into account the variation of exchange when the spin polarisation and the metal-ligand bond length significantly vary as is the case upon the change of spin-state in our system. This deficiency is emphasised by the fact that the HS ^5E and $^5\text{A}_1$ states of a same spin multiplicity are consistently given by all the GGAs as being nearly degenerate to within 350 cm^{-1} (4 kJ/mol). The overestimation of $\Delta E_{\text{HL}}^{\text{el}}$ with the GGAs is due to the fact that, despite the nonlocal corrections, the B88, PW91 and PBE exchange GGAs still present the underestimation of exchange inherited from their LDA component. The larger gradient correction of the RPBE exchange GGA allows a better description of exchange which is at the origin of the very good result achieved for the determination of $\Delta E_{\text{HL}}^{\text{el}}$ with this functional. With the hybrids exchange is overestimated and this explains the severe underestimation of $\Delta E_{\text{HL}}^{\text{el}}$ with the B3LYP and PBE1PBE functionals. For the hybrids, the determination of the dependence of the HS-LS energy difference on the exact-exchange contribution shows that the contribution in both the B3LYP and PBE1PBE functionals should be reduced to an amount of about 10% to achieve a good description of the energetics of $[\text{Fe}(\text{bpy})_3]^{2+}$.

Our results show that a reliable characterisation of the $[\text{Fe}(\text{bpy})_3]^{2+}$ complex in the LS and HS states can be achieved using density-functional approaches but also that there is still room for improving the XC functionals. With regard to the correlation functionals, although their formal properties differ [103, 61, 62], we cannot distinguish between them. Given that exchange dominates the high-density limit [69, 70], the evaluation of the energy difference between states of different multiplicities for electron-rich system such as iron(II) complexes suffers mainly from the limitation of the exchange functionals. The difficulties encountered for the energetics suggest that the relative spin-state energies of a number of systems should be incorporated into the data sets which serve as benchmarks for XC functionals or as training sets for their empirical design. To further improve our understanding of the photophysical properties of $[\text{Fe}(\text{bpy})_3]^{2+}$ and, in particular with regard to the dynamics of the photo-induced HS \rightarrow LS relaxation, the role of the environment must now be thoroughly investigated. In that respect, we have extended our study so as to account for the influence of solvation effects on the HS-LS energy gap and on the optical and chirooptical properties of the complex [104].

Acknowledgements

We would like to thank Nabil Berkaïne and Georg Ganzenmüller for helpful discussions. AH, AV and LMLD thank the *Centro Svizzero di Calcolo Scientifico* (CSCS) for the calculation resources allocated in the framework of the CSCS project entitled "Photophysics and Photochemistry of Transition Metal Compounds: Theoretical Approaches" and the *Swiss National Science Foundation* for financial support. This is part of a contribution by AF and MEC to the *groupe de recherche* in "density functional theory" (DFT) and the *COST* working group D26/0013/02. AF thanks the french *Ministère de l'Education Nationale et de la Recherche* for a *Bourse de Mobilité*. MEC and AF thank the support team of the LEDSS and the *Centre d'Experimentation pour le Calcul Intensif en Chimie* (CECIC) and they acknowledge supercomputer time at the *Institut du Développement et des Ressources en Informatique Scientifique* (IDRIS project number 021576).

Supporting Information available

AO populations and net charge found for the iron atom in the LS 1A_1 and the HS 5E and 5A_1 states of $[Fe(bpy)_3]^{2+}$ (Tables S1-S3).

Bibliography

- [1] P. Gütlich, H. A. Goodwin, editors. *Spin Crossover in Transition Metal Compounds I*. **2004**, volume 233 of *Topics in Current Chemistry*. Springer-Verlag, Heidelberg.
- [2] P. Gütlich, H. A. Goodwin, editors. *Spin Crossover in Transition Metal Compounds II*. **2004**, volume 234 of *Topics in Current Chemistry*. Springer-Verlag, Heidelberg.
- [3] P. Gütlich, H. A. Goodwin, editors. *Spin Crossover in Transition Metal Compounds III*. **2004**, volume 235 of *Topics in Current Chemistry*. Springer-Verlag, Heidelberg.
- [4] P. Gütlich, H. A. Goodwin. *Spin Crossover in Transition Metal Compounds I* [1], pages 1–47.
- [5] M. A. Hoselton, L. J. Wilson, R. S. Drago. *J. Am. Chem. Soc.* **1975**, 97, 1722–1729.

- [6] B. A. Katz, C. E. Strouse. *J. Am. Chem. Soc.* **1979**, 101, 6214–6221.
- [7] M. Mikami-Kido, Y. Saito. *Acta Cryst.* **1982**, B38, 452–455.
- [8] R. A. Binstead, J. K. Beattie. *Inorg. Chem.* **1986**, 25, 1481–1484.
- [9] M. Konno, M. Mikami-Kido. *Bull. Chem. Soc. Jpn.* **1991**, 64, 339–345.
- [10] J.-F. Létard, P. Guionneau, L. Rabardel, J. A. K. Howard, A. E. Goeta, D. Chasseau, O. Kahn. *Inorg. Chem.* **1998**, 37, 4432–4441.
- [11] P. J. Koningsbruggen, Y. Garcia, O. Kahn, L. Fournès, H. Kooijman, A. L. Spek, J. G. Haasnoot, J. Moscovici, K. Provost, A. Michalowicz, F. Renz, P. Gütlich. *Inorg. Chem.* **2000**, 39, 1891–1900.
- [12] L. Wiehl, G. Kiel, C. P. Köhler, H. Spiering, P. Gütlich. *Inorg. Chem.* **1986**, 25, 1565–1571.
- [13] P. Adler, A. Hauser, A. Vef, H. Spiering, P. Gütlich. *Hyperfine Interactions.* **1989**, 47, 343–356.
- [14] L. Wiehl, H. Spiering, P. Gütlich, K. Knorr. *J. Appl. Cryst.* **1990**, 23, 151–160.
- [15] A. Hauser, N. Amstutz, S. Delahaye, A. Sadki, S. Schenker, R. Sieber, M. Zerara. *Structure and Bonding.* **2004**, 106, 81–96.
- [16] J. J. McGarvey, I. Lawthers. *J. Chem. Soc., Chem. Comm.* **1982**, pages 906–907.
- [17] I. Lawthers, J. J. McGarvey. *J. Am. Chem. Soc.* **1984**, 106, 4280–4282.
- [18] S. Decurtins, P. Gütlich, C. P. Köhler, H. Spiering, A. Hauser. *Chem. Phys. Lett.* **1984**, 105, 1–4.
- [19] S. Decurtins, P. Gütlich, K. M. Hasselbach, H. Spiering, A. Hauser. *Inorg. Chem.* **1985**, 24, 2174–2178.
- [20] A. Hauser. Gütlich and Goodwin [2], pages 155–198.
- [21] E. Buhks, G. Navon, M. Bixon, J. Jortner. *J. Am. Chem. Soc.* **1980**, 102, 2918–2923.
- [22] C.-L. Xie, D. N. Hendrickson. *J. Am. Chem. Soc.* **1987**, 109, 6981–6988.
- [23] A. Hauser. *Comments Inorg. Chem.* **1995**, 17, 17–40. And references therein.

- [24] A. Vef, U. Manthe, P. Gütlich. *J. Chem. Phys.* **1994**, 101, 9326–9332.
- [25] P. Gütlich, A. Hauser, H. Spiering. *Angew. Chem. Int. Ed. Engl.* **1994**, 33, 2024–2054.
- [26] A. Hauser. Gütlich and Goodwin [1], pages 49–58.
- [27] A. Fouqueau, S. Mer, M. E. Casida, L. M. Lawson Daku, A. Hauser, T. Mineva. *J. Chem. Phys.* **2004**, 120, 9473–9486.
- [28] A. Fouqueau, M. E. Casida, L. M. Lawson Daku, A. Hauser, F. Neese. *J. Chem. Phys.* **2004**. in press.
- [29] A. Hauser. *Chem. Phys. Lett.* **1990**, 173, 507–512.
- [30] S. Deisenroth, A. Hauser, H. Spiering, P. Gütlich. *Hyperfine Interactions.* **1994**, 93, 1573–1577.
- [31] S. Schenker, A. Hauser, W. Wang, I. Y. Chan. *Chem. Phys. Lett.* **1998**, 297, 281–286.
- [32] S. Dick. *Zeitschrift für Kristallographie - New Crystal Structures.* **1998**, 213, 356.
- [33] A. Hauser, A. Vef, P. Adler. *J. Chem. Phys.* **1991**, 95, 8710–8717.
- [34] J. Ferguson, F. Herren, G. M. McLaughlin. *Chem. Phys. Lett.* **1982**, 89, 376–380.
- [35] S. Schenker, A. Hauser, W. Wang, I. Y. Chan. *J. Chem. Phys.* **1998**, 109, 9870–9878.
- [36] R. G. Parr, W. Yang. *Density-Functional Theory of Atoms and Molecules.* **1989**. Oxford University Press, New York.
- [37] R. M. Dreizler, E. K. U. Gross. *Density Functional Theory, An Approach to the Quantum Many-Body Problem.* **1990**. Springer-Verlag, New York.
- [38] W. Koch, M. C. Holthausen. *A Chemist's Guide to Density Functional Theory.* **2000**. Wiley-VCH, New York.
- [39] P. Hohenberg, W. Kohn. *Phys. Rev.* **1964**, 136, B864–B871.
- [40] W. Kohn, L. J. Sham. *Phys. Rev.* **1965**, 140, A1133–A1138.

- [41] O. Gunnarsson, B. I. Lundqvist. *Phys. Rev. B.* **1976**, 13, 4274–4298.
- [42] W. Kohn. Density Functional Theory: Fundamentals and Applications. F. Bassani, F. Fumi, M. P. Tosi, editors, *Highlights of Condensed Matter Theory*, page 1, North-Holland, Amsterdam, **1985**.
- [43] In the HF approach, the orbitals result from a nonlocal potential which only accounts for exchange effect, whereas they are determined in the KS method by a local potential which incorporates exchange and correlation effects.
- [44] D. M. Ceperley, B. J. Alder. *Phys. Rev. Lett.* **1980**, 45, 566–569.
- [45] S. H. Vosko, L. Wilk, M. Nusair. *Can. J. Phys.* **1980**, 58, 1200–1211.
- [46] J. P. Perdew, M. Ernzerhof, A. Zupan, K. Burke. *J. Chem. Phys.* **1998**, 108, 1522–1531.
- [47] A. Zupan, K. Burke, M. Ernzerhof, J. P. Perdew. *J. Chem. Phys.* **1997**, 106, 10184–10293.
- [48] K. Burke, J. P. Perdew, M. Ernzerhof. *J. Chem. Phys.* **1998**, 109, 3760–3771.
- [49] J. P. Perdew, S. Kurth. C. Fiolhais, F. Nogueira, M. Marques, editors, *A primer in density functional theory*. **2003**, volume 620 of *Lecture Notes in Physics*, pages 1–55. Springer, Berlin.
- [50] A. D. Becke. *J. Chem. Phys.* **1993**, 98, 1372–1377.
- [51] A. D. Becke. *J. Chem. Phys.* **1993**, 98, 5648–5652.
- [52] J. Harris, R. O. Jones. *J. Phys. F.* **1974**, 4, 1170–1186.
- [53] J. P. Perdew, M. Ernzerhof, K. Burke. *J. Chem. Phys.* **1996**, 105, 9982–9985.
- [54] K. Burke, M. Ernzerhof, J. P. Perdew. *Chem. Phys. Lett.* **1997**, 265, 115–120.
- [55] M. Ernzerhof. *Chem. Phys. Lett.* **1996**, 263, 499–506.
- [56] H. Paulsen, L. Duelund, H. Winkler, H. Toftlund, A. X. Trautwein. *Inorg. Chem.* **2001**, 40, 2201–2204.
- [57] A. D. Becke. *Phys. Rev. A.* **1988**, 38, 3098–3100.
- [58] C. Lee, W. Yang, R. G. Parr. *Phys. Rev. B.* **1988**, 37, 785–789.

- [59] J. P. Perdew, J. A. Chevary, S. H. Vosko, K. A. Jackson, M. R. Pederson, D. J. Singh, C. Fiolhais. *Phys. Rev. B.* **1992**, 46, 6671–6687.
- [60] J. P. Perdew, J. A. Chevary, S. H. Vosko, K. A. Jackson, M. R. Pederson, D. J. Singh, C. Fiolhais. *Phys. Rev. B.* **1993**, 48, 4978. Erratum.
- [61] J. P. Perdew, K. Burke, Y. Wang. *Phys. Rev. B.* **1996**, 54, 16533–16539.
- [62] J. P. Perdew, K. Burke, Y. Wang. *Phys. Rev. B.* **1998**, 57, 14999. Erratum.
- [63] G. Baranović. *Chem. Phys. Lett.* **2003**, 369, 668–672.
- [64] J. P. Perdew. *Phys. Rev. B.* **1986**, 33, 8822–8824.
- [65] Gaussian NEWS, v. 5, no. 2, summer 1994, p. 2. “Becke3LYP Method References and General Citation Guidelines”.
- [66] M. Reiher, O. Salomon, B. A. Hess. *Theor. Chem. Acc.* **2001**, 107, 48–55.
- [67] O. Salomon, M. Reiher, B. A. Hess. *J. Chem. Phys.* **2002**, 117, 4729–4737.
- [68] M. Reiher. *Inorg. Chem.* **2002**, 41, 6928–6935.
- [69] J. P. Perdew, K. Burke, M. Ernzerhof. *Phys. Rev. Lett.* **1996**, 77, 3865–3868.
- [70] J. P. Perdew, K. Burke, M. Ernzerhof. *Phys. Rev. Lett.* **1997**, 78, 1396. Errata.
- [71] B. Hammer, L. B. Hansen, J. K. Nørskov. *Phys. rev. B.* **1999**, 59, 7413–7421.
- [72] F. Neese. *J. Chem. Phys.* **2003**, 119, 9428–9443.
- [73] C. Adamo, V. Barone. *J. Chem. Phys.* **1999**, 110, 6158–6170.
- [74] M. Ernzerhof, G. E. Scuseria. *J. Chem. Phys.* **1999**, 110, 5029–5036.
- [75] “Amsterdam Density Functional program”, Theoretical Chemistry, Vrije Universiteit, Amsterdam, the Netherlands, <http://www.scm.com>.
- [76] Gaussian 03, Revision B.03/B.04, M. J. Frisch, G. W. Trucks, H. B. Schlegel, G. E. Scuseria, M. A. Robb, J. R. Cheeseman, J. A. Montgomery, Jr., T. Vreven, K. N. Kudin, J. C. Burant, J. M. Millam, S. S. Iyengar, J. Tomasi, V. Barone, B. Mennucci, M. Cossi, G. Scalmani, N. Rega, G. A. Petersson, H. Nakatsuji, M. Hada, M. Ehara, K. Toyota, R. Fukuda, J. Hasegawa, M. Ishida, T. Nakajima, Y. Honda, O. Kitao, H. Nakai, M. Klene, X. Li, J. E. Knox, H. P. Hratchian, J. B. Cross, C. Adamo, J. Jaramillo, R. Gomperts, R. E.

- Stratmann, O. Yazyev, A. J. Austin, R. Cammi, C. Pomelli, J. W. Ochterski, P. Y. Ayala, K. Morokuma, G. A. Voth, P. Salvador, J. J. Dannenberg, V. G. Zakrzewski, S. Dapprich, A. D. Daniels, M. C. Strain, O. Farkas, D. K. Malick, A. D. Rabuck, K. Raghavachari, J. B. Foresman, J. V. Ortiz, Q. Cui, A. G. Baboul, S. Clifford, J. Cioslowski, B. B. Stefanov, G. Liu, A. Liashenko, P. Piskorz, I. Komaromi, R. L. Martin, D. J. Fox, T. Keith, M. A. Al-Laham, C. Y. Peng, A. Nanayakkara, M. Challacombe, P. M. W. Gill, B. Johnson, W. Chen, M. W. Wong, C. Gonzalez, and J. A. Pople, Gaussian, Inc., Pittsburgh PA, 2003.
- [77] A. Schäfer, C. Huber, R. Ahlrichs. *J. Chem. Phys.* **1994**, 100, 5829–5835.
- [78] K. Raghavachari, J. S. Binkley, R. Seeger, J. A. Pople. *J. Chem. Phys.* **1980**, 72, 650–654.
- [79] A. J. H. Wachters. *J. Chem. Phys.* **1970**, 52, 1033–1036.
- [80] P. J. Hay. *J. Chem. Phys.* **1977**, 66, 4377–4384.
- [81] K. Raghavachari, G. W. Trucks. *J. Chem. Phys.* **1989**, 91, 1062–1065.
- [82] K. N. Kudin, G. E. Scuseria, E. Cancès. *J. Chem. Phys.* **2002**, 116, 8255–8261.
- [83] MOLEKEL 4.0, P. Flükiger, H.P. Lüthi, S. Portmann, J. Weber, Swiss Center for Scientific Computing, Manno (Switzerland), 2000.
- [84] G. Schaftenaar, J.H. Noordik. *J. Comput.-Aided Mol. Design.* **2000**, 14, 123–134.
- [85] G. te Velde, F. M. Bickelhaupt, E. J. Baerends, C. Fonseca Guerra, S. J. A. van Gisbergen, J. G. Snijders, T. Ziegler. *J. Comp. Chem.* **2001**, 22, 931–967.
- [86] J. P. Foster, F. Weinhold. *J. Am. Chem. Soc.* **1980**, 102, 7211–7218.
- [87] J. E. Carpenter, F. Weinhold. *J. Mol. Struct. (Theochem).* **1988**, 169, 41–62.
- [88] A. E. Reed, L. A. Curtiss, F. Weinhold. *Chem. Rev.* **1988**, 88, 899–926.
- [89] M. E. Casida, K. C. Casida, D. R. Salahub. *Int. J. Quant. Chem.* **1998**, 70, 933–941.
- [90] A. Savin, C. J. Umrigar, X. Gonze. *Chem. Phys. Lett.* **1998**, 288, 391–395.
- [91] M. Grüning, O. V. Gritsenko, S. J. A. van Gisbergen, E. J. Baerends. *J. Chem. Phys.* **2001**, 114, 652–660.

- [92] M. E. Casida In *Accurate description of low-lying molecular states and potential energy surfaces, ACS Symposium Series* 828; Hoffmann, M. R.; Dyall, K. G., Eds; ACS Press: Washington, D. C., 2002, (Proceedings of ACS Symposium, San Diego, Calif., 2001), 199-220.
- [93] J. P. Perdew, R. G. Parr, M. Levy, J. L Baldz, Jr. *Phys. rev. Lett.* **1982**, 49, 1691–1694.
- [94] C.-O. Almbladh, U. von Barth. *Phys. Rev. B.* **1985**, 31, 3231–3244.
- [95] S. Hamel, P. Duffy, M. E. Casida, D. R. Salahub. *J. Electr. Spectr. and Related Phenomena.* **2002**, 123, 345–363.
- [96] M. E. García Posse, M. A. Juri, P. J. Aymonino, O. E. Piro, H. A. Negri, E. E. Castellano. *Inorg. Chem.* **1984**, 23, 948–952.
- [97] Selected distances (\AA) and dihedral angle γ (deg) characterising the geometry of C_2 symmetry of the free ligand. Results of calculations using the PBE functional and the DZ, TZP, TZVP and 6-311+G ** basis sets. DZ: N-C₂ = 1.364; N-C₆ = 1.354; C₂-C'₂ = 1.493; C₂-C₃ = 1.410; C₃-C₄ = 1.400; C₄-C₅ = 1.401; C₅-C₆ = 1.401; γ = 3.6. TZP: N-C₂ = 1.348; N-C₆ = 1.337; C₂-C'₂ = 1.497; C₂-C₃ = 1.408; C₃-C₄ = 1.393; C₄-C₅ = 1.395; C₅-C₆ = 1.398; γ = 9.5. TZVP: N-C₂ = 1.348; N-C₆ = 1.338; C₂-C'₂ = 1.493; C₂-C₃ = 1.406; C₃-C₄ = 1.394; C₄-C₅ = 1.395; C₅-C₆ = 1.399; γ = 38.5. 6-311+G ** : N-C₂ = 1.349; N-C₆ = 1.340; C₂-C'₂ = 1.495; C₂-C₃ = 1.408; C₃-C₄ = 1.397; C₄-C₅ = 1.397; C₅-C₆ = 1.401; γ = 37.6. The values found for the γ angle strongly depend on the basis set used for the calculations. There is also a noticeable shrinking of the aromatic rings when passing from the geometry obtained with the DZ basis set to the one obtained with the more flexible TZP basis set. This is also verified in a lesser extent when going from the “6-311+G ** ” structure to the “TZVP” structure. Besides the differences in the γ values, the geometries found using the TZP and TZVP basis sets are very similar.
- [98] K. B. Wiberg, P. R. Rablen, D. J. Rush, T. A. Keith. *J. Am. Chem. Soc.* **1995**, 117, 4261–4270.
- [99] K. B. Wiberg, T. A. Keith, M. J. Frish, M. Murcko. *J. Phys. Chem.* **1995**, 99, 9072.
- [100] No imaginary frequency was obtained for the vibrational analysis performed at the PBE/TZVP level for the complex in the 1A_1 and 5A_1 states, thus showing

that the geometries calculated at the PBE/TZVP level for the complex in both spin-states correspond to real minima. Vibrational analysis were not performed systematically because of their computational cost; in addition, analytical second derivatives are so far only available in GAUSSIAN. Still the consistency of our results provides evidences for the fairly good quality of the convergence achieved by the optimisation processes.

- [101] It must be precised that the negative contribution to $\Delta E_{\text{HL}}^{\text{vib}}$ due to the frequency shifts of the vibrational modes involving the metal-ligand bond is partly counterbalanced by the increase of the frequencies of vibrational modes affecting the N-C and C-C bonds of the ligands. The increase of the frequencies of these vibrational modes centered on the aromatic rings is indicative of the diminishing with the lengthening of the Fe-N bond distance of π -backbonding interactions that imply ligand-centered anti-bonding orbitals.
- [102] R. Poli, J. N. Harvey. *Chem. Soc. Rev.* **2003**, 32, 1–8.
- [103] J. P. Perdew, K. Burke. *Int. J. Quant. Chem.* **1996**, 57, 309–319.
- [104] A. Vargas, L. M. Lawson Daku, A. Hauser. In preparation.

	1A_1		5E		5A_1	
	PBE	RPBE	PBE	RPBE	PBE	RPBE
<i>Mulliken populations</i>						
s-pop.	5.9	5.9	3.1/3.0	3.1/3.0	3.1/3.0	3.1/3.0
p-pop.	12.4	12.4	6.3/6.2	6.3/6.2	6.3/6.2	6.3/6.2
d-pop.	6.7	6.7	5.0/1.3	5.0/1.3	5.0/1.4	5.0/1.4
<i>Spin density</i>						
Mulliken	0.0	0.0	+3.9	+3.9	+3.8	+3.8
<i>Net charge</i>						
Mulliken	+1.0	+1.0	+1.1	+1.1	+1.0	+1.0
Voronoi	+1.1	+1.1	+1.2	+1.2	+1.2	+1.2

	1A_1		5A_1	
	PBE	B3LYP*	PBE	B3LYP*
<i>Natural populations</i>				
s-pop.	6.2	6.2	3.1/3.1	3.1/3.1
p-pop.	12.0	12.0	6.0/6.0	6.0/6.0
d-pop.	7.2	7.0	4.9/1.4	5.0/1.3
<i>Spin density</i>				
Natural	0.0	0.0	+3.5	+3.7
<i>Net charge</i>				
Natural	+0.6	+0.8	+1.5	+1.5

TABLE 4.1: AO populations, spin density and net charge found for the iron atom in the LS 1A_1 and HS 5E and 5A_1 states of the $[Fe(bpy)_3]^{2+}$ complex (populations are given per l -values). For the HS states, the spin-up/spin-down AO populations are indicated. Top: ADF results obtained using the TZP basis set, bottom: GAUSSIAN results obtained using the TZVP basis set. (Results for the other functionals and basis sets are given in Tables S1-S3).

	Exp. [32]	BP86		PW91		PBE		RPBE	
		DZ	TZP	DZ	TZP	DZ	TZP	DZ	TZP
Bond lengths (Å)									
Fe-N	1.967	1.956	1.978	1.954	1.971	1.955	1.975	1.979	2.003
N-C ₂	1.359	1.384	1.369	1.380	1.365	1.382	1.367	1.388	1.373
N-C ₆	1.338	1.367	1.354	1.364	1.351	1.366	1.353	1.372	1.359
C ₂ -C' ₂	1.471	1.462	1.463	1.459	1.461	1.460	1.462	1.469	1.471
C ₂ -C ₃	1.377	1.402	1.400	1.400	1.397	1.401	1.399	1.408	1.406
C ₃ -C ₄	1.374	1.399	1.392	1.397	1.390	1.398	1.391	1.404	1.397
C' ₄ -C ₅	1.380	1.403	1.397	1.401	1.395	1.402	1.396	1.407	1.401
C ₅ -C ₆	1.358	1.396	1.392	1.394	1.389	1.396	1.391	1.401	1.396
Angles (deg)									
β	81.8	82.2	81.2	82.1	81.5	82.1	81.3	81.7	80.8
γ	6.4	0.1	1.3	0.2	1.6	0.2	1.5	0.8	1.5
τ	53.6	54.1	53.1	54.1	53.3	54.1	53.1	54.0	53.1
θ	57.8	57.8	58.0	57.8	58.0	57.8	58.0	58.1	58.4

	PBE		B3LYP		B3LYP*		PBE1PBE	
	TZVP	6-311+G**	TZVP	6-311+G**	TZVP	6-311+G**	TZVP	6-311+G**
Bond lengths (Å)								
Fe-N	1.975	1.971	2.027	2.022	2.013	2.008	1.998	1.993
N-C ₂	1.369	1.371	1.356	1.358	1.359	1.361	1.350	1.352
N-C ₆	1.353	1.356	1.342	1.344	1.344	1.347	1.337	1.339
C ₂ -C' ₂	1.464	1.466	1.473	1.475	1.471	1.473	1.468	1.470
C ₂ -C ₃	1.400	1.402	1.394	1.396	1.395	1.397	1.389	1.391
C ₃ -C ₄	1.392	1.394	1.387	1.389	1.388	1.390	1.384	1.386
C ₄ -C ₅	1.397	1.399	1.389	1.391	1.390	1.393	1.386	1.388
C ₅ -C ₆	1.391	1.394	1.386	1.389	1.387	1.390	1.383	1.386
Angles (deg)								
β	81.5	81.6	80.3	80.5	80.6	80.8	80.9	81.0
γ	3.3	3.0	3.4	3.1	3.4	3.0	3.3	2.8
τ	54.2	54.4	53.1	53.3	53.4	53.6	53.7	53.9
θ	58.3	58.3	58.7	58.7	58.6	58.6	58.6	58.5

TABLE 4.2: Comparison between experimental and theoretical ${}^1\text{A}_1$ $[\text{Fe}(\text{bpy})_3]^{2+}$ geometries. Top: ADF, bottom: GAUSSIAN.

	BP86		PW91		PBE		RPBE	
	DZ	TZP	DZ	TZP	DZ	TZP	DZ	TZP
Bond lengths (Å)								
Fe-N	2.158	2.182	2.148	2.174	2.158	2.178	2.192	2.220
N-C ₂	1.375	1.361	1.373	1.359	1.374	1.360	1.380	1.366
N-C ₆	1.363	1.349	1.360	1.347	1.362	1.348	1.368	1.354
C ₂ -C' ₂	1.477	1.479	1.476	1.478	1.476	1.479	1.486	1.489
C ₂ -C ₃	1.405	1.401	1.403	1.399	1.404	1.401	1.411	1.408
C ₃ -C ₄	1.400	1.393	1.398	1.391	1.399	1.393	1.404	1.398
C ₄ -C ₅	1.403	1.397	1.401	1.394	1.402	1.396	1.407	1.401
C ₅ -C ₆	1.397	1.392	1.395	1.389	1.396	1.391	1.401	1.397
Angles (deg)								
β	76.5	75.4	76.7	75.6	76.4	75.5	75.7	74.6
γ	4.5	4.6	4.0	5.1	4.4	5.0	4.3	5.8
τ	46.6	46.0	47.4	46.5	46.6	46.1	46.2	46.1
θ	58.8	59.3	58.9	59.3	58.9	59.2	59.1	59.9

TABLE 4.3: Optimised $[\text{Fe}(\text{bpy})_3]^{2+}$ geometries in the HS ${}^5\text{E}$ state. ADF results.

	BP86		PW91		PBE		RPBE	
	DZ	TZP	DZ	TZP	DZ	TZP	DZ	TZP
Bond lengths (Å)								
Fe-N	2.180	2.204	2.169	2.198	2.171	2.201	2.207	2.244
N-C ₂	1.373	1.359	1.370	1.357	1.371	1.358	1.378	1.364
N-C ₆	1.360	1.347	1.358	1.345	1.359	1.346	1.365	1.352
C ₂ -C' ₂	1.483	1.483	1.482	1.481	1.483	1.483	1.492	1.492
C ₂ -C ₃	1.404	1.400	1.402	1.398	1.403	1.400	1.409	1.407
C ₃ -C ₄	1.402	1.394	1.400	1.392	1.402	1.394	1.407	1.399
C ₄ -C ₅	1.402	1.395	1.400	1.393	1.401	1.395	1.406	1.400
C ₅ -C ₆	1.399	1.393	1.396	1.391	1.398	1.392	1.403	1.398
Angles (deg)								
β	75.5	74.4	75.8	74.6	75.7	74.5	74.9	73.6
γ	5.8	5.9	5.9	6.2	6.2	6.2	6.2	6.8
τ	45.6	44.6	46.3	46.5	46.3	44.7	46.1	44.9
θ	59.1	59.4	59.1	59.5	59.2	59.4	59.7	60.1

	PBE		B3LYP		B3LYP*		PBE1PBE	
	TZVP	6-311+G**	TZVP	6-311+G**	TZVP	6-311+G**	TZVP	6-311+G**
Bond lengths (Å)								
Fe-N	2.206	2.203	2.234	2.232	2.228	2.225	2.211	2.207
N-C ₂	1.359	1.361	1.350	1.352	1.352	1.354	1.344	1.346
N-C ₆	1.347	1.349	1.339	1.341	1.341	1.343	1.334	1.336
C ₂ -C' ₂	1.484	1.487	1.486	1.488	1.486	1.488	1.481	1.483
C ₂ -C ₃	1.401	1.403	1.394	1.397	1.396	1.398	1.390	1.392
C ₃ -C ₄	1.395	1.397	1.388	1.391	1.389	1.392	1.385	1.388
C ₄ -C ₅	1.395	1.398	1.388	1.391	1.390	1.392	1.385	1.388
C ₅ -C ₆	1.394	1.396	1.387	1.389	1.388	1.391	1.384	1.386
Angles (deg)								
β	74.5	74.6	73.7	73.7	73.9	74.0	74.0	74.1
γ	8.9	7.5	7.1	6.1	7.2	6.2	7.2	5.8
τ	46.1	46.1	45.3	45.2	45.4	45.4	45.6	45.6
θ	59.9	59.9	60.1	60.1	60.1	60.0	60.0	60.0

TABLE 4.4: Optimised $[Fe(bpy)_3]^{2+}$ geometries in the HS 5A_1 state. Top: ADF, bottom: GAUSSIAN.

	Δr_{HL} 5E		Δr_{HL} 5A_1	
BP86/DZ	0.202	0.224	PBE/TZVP	0.231
BP86/TZP	0.204	0.224	PBE/6-311+G**	0.232
PW91/DZ	0.194	0.215	B3LYP/TZVP	0.207
PW91/TZP	0.203	0.227	B3LYP/6-311+G**	0.210
PBE/DZ	0.203	0.216	B3LYP*/TZVP	0.215
PBE/TZP	0.203	0.226	B3LYP*/6-311+G**	0.217
RPBE/DZ	0.213	0.228	PBE1PBE/TZVP	0.213
RPBE/TZP	0.217	0.241	PBE1PBE/6-311+G**	0.214
Exp.: $\Delta r_{HL} \cong 0.16-0.22$				

TABLE 4.5: Comparison between calculated Fe-N bond length differences $\Delta r_{HL} = r_{HS} - r_{LS}$ (Å), (where r_{HS} and r_{LS} are the Fe-N bond lengths in the HS (5E or 5A_1) and LS (1A_1) states, respectively), and experimental Δr_{HL} values for spin-crossover systems with $[FeN_6]$ coordination [5, 6, 7, 8, 9, 10, 11].

	V_{LS}	V_{HS}	ΔV_{HL}		
		5E	5A_1	5E	5A_1
BP86/DZ	720	748	749	28	29
BP86/TZP	670	691	693	21	23
PW91/DZ	717	743	744	26	27
PW91/TZP	666	688	689	22	23
PBE/DZ	718	747	745	29	27
PBE/TZP	668	689	690	21	22
RPBE/DZ	725	755	753	30	28
RPBE/TZP	671	693	695	22	24
Exp: $\Delta V_{HL} \approx 15\text{-}30$					

TABLE 4.6: Comparison between calculated differences in molecular volume, $\Delta V_{HL} = V_{HS} - V_{LS}$ (in \AA^3), (where V_{HS} and V_{LS} are the molecular volumes in the HS (5E or 5A_1) and LS (1A_1) states, respectively), and measured changes of crystal volume *per* molecular unit, $\Delta V_{HL}^{\text{exp}}$ [8, 12, 13, 14].

	$\Delta E_{HL}^{\text{el.}}$	5E	5A_1	$\Delta E_{HL}^{\text{el.}}$	5A_1
BP86/DZ	14397	15169	PBE/TZVP	11373	
BP86/TZP	11034	11135	PBE/6-311+G**	11849	
PW91/DZ	15055	15879	B3LYP/TZVP	766	
PW91/TZP	11699	11887	B3LYP/6-311+G**	1211	
PBE/DZ	14431	15313	B3LYP*/TZVP	3432	
PBE/TZP	11022	11337	B3LYP*/6-311+G**	3907	
RPBE/DZ	10463	10853	PBE1PBE/TZVP	-951	
RPBE/TZP	6909	6640	PBE1PBE/6-311+G**	-466	
Exp.: $\Delta E_{HL}^{\text{el.}} \approx 3500\text{-}6000$					

TABLE 4.7: Calculated and experimental (see text) electronic energy differences $\Delta E_{HL}^{\text{el.}}$, (in cm^{-1}).

4-7 Comparison of Density Functionals for Energy and Structural Differences Between the High $[^5T_{2g} : (t_{2g})^4(e_g)^2]$ and Low $[^1A_{1g} : (t_{2g})^6(e_g)^0]$ Spin States of Iron(II) Coordination Compounds : IV. Comparison of Density-Functional and Experimental Results for the Ferrous Complexes $[Fe(L)('NHS_4')]$, where

$'NHS_4'$ = 2,2'-*Bis*(2-mercaptophenylthio)diethylamine Dianion, and L = NH₃, N₂H₄, PMe₃, CO, and NO⁺

Comparison of Density Functionals for Energy and Structural

Differences Between the High [$^5T_{2g}$: (t_{2g})⁴(e_g)²] and
Low [$^1A_{1g}$: (t_{2g})⁶(e_g)⁰] Spin States of Iron(II) Coordination Compounds:

IV. Comparison of Density-Functional and Experimental Results

for the Ferrous Complexes $[Fe(L)('NHS_4')]$, where

'NHS₄' = 2,2'-Bis(2-mercaptophenylthio)diethylamine Dianion,
and L = NH₃, N₂H₄, PMe₃, CO, and NO⁺

Georg Ganzenmüller, Nabil Berkaïne, Antony Fouqueau, Mark E. Casida¹

Institut de Chimie Moléculaire de Grenoble (ICMG, FR-2607),
Laboratoire d'Études Dynamiques et Structurales de la Sélectivité (LÉDSS),
UMR CNRS/UJF 5616, Équipe de Chimie Théorique (LÉDSS-ECT),
Université Joseph Fourier (Grenoble I), F38041 Grenoble, FRANCE

Markus Reiher

Lehrstuhl für Theoretische Chemie der Universität Bonn, Wegelerstrasse 12,
D-53115 Bonn, GERMANY

¹Mark.Casida@ujf-grenoble.fr

Abstract

Previous work testing density-functionals for use in calculating high spin-low spin energy differences, ΔE_{HL} , for iron(II) spin-crossover transitions has tended to conclude that only properly reparameterized hybrid functionals can predict ΔE_{HL} since it seems to depend critically on a correct description of the electron pairing energy governed by the exchange term. Exceptions to this rule are the previous three papers (I, II, and III in the present series of papers.) Papers I and II compared different functionals for their ability to calculate high- and low-spin properties for the simple compounds $[Fe(H_2O)]^{2+}$ and $[Fe(NH_3)]^{2+}$ against the results of high-quality *ab initio* calculations. It was found that modern generalized gradient approximations (GGAs) and meta-GGAs could do as well as hybrid functionals, if not better, for this type of problem. However, the results of Papers I and II were necessarily limited to small complexes because of the desire to compare against *ab initio* gas phase calculations. Paper III extended these previous studies to the *tris*(2,2'-bipyridine) complex, $[Fe(bpy)_3]^{2+}$ which is in a size range typical of spin-transition complexes of practical interest. For a complex of this size, high quality *ab initio* calculations are impractical and so comparison was against an experimental estimate of ΔE_{HL} obtained by analysis of the low-temperature dynamics of the high-spin \rightarrow low-spin relaxation rate following the photo-induced population of the high-spin state. In the present paper, we extend these previous studies to five more molecules which are too large to treat with high quality *ab initio* calculations, namely the series, $[Fe(L)('NHS_4')]$, where ' NHS_4' = 2,2'-bis((2-mercaptophenylthio)diethylamine dianion, and $L = NH_3$, N_2H_4 , PMe_3 , CO , and NO^+ . Since we know of no reliable experimental estimate of ΔE_{HL} , we content ourselves with a comparison against the experimentally-determined groundstate spin-symmetry including, in so far as possible, finite temperature effects. Together with the results of Papers I, II, and III, this paper provides a test of a large number of functionals against the high-spin/low-spin properties of a diverse set of Fe(II) compounds, making it possible to draw some particularly interesting conclusions. Trends among different classes of functionals are discussed and it is pointed out there is at least one functional, namely the OLYP generalized gradient approximation, which is able to give a reasonably good description of the delicate spin energetics of Fe(II) coordination compounds without resorting to hybrid functionals which require the relatively more expensive calculation of a Hartree-Fock-like exchange term.

I Introduction

Transition metal compounds often exhibit a variety of spin states and a knowledge of their relative energetics can be critical for describing the chemical and physical properties of these compounds [1]. Nowadays density-functional theory (DFT) is often the method of choice for the theoretical modeling of transition metal compounds involving more than just a few atoms [1, 2]. However theoretical modeling of the relative spin-state energetics in this type of system is far from straightforward, since the energy differences can be rather small and electron correlation can be both critical and difficult to describe with even the best available methods. It is thus important to study the ability of DFT to describe relative spin energetics with different choices of density functionals. We are particularly interested in finding functionals which yield an acceptable description of the low-spin $^1A_{1g}$ – high-spin $^5T_{2g}$ energetics in octahedral iron(II) compounds [3, 4, 5]. This is certainly in keeping with a recent interest in spin-crossover compounds [6], but interest in finding density-functionals capable of giving a correct description of spin energetics is by no means limited to spin-crossover compounds, as Harvey makes clear in his recent review article [1]. The present paper is the fourth in a series of papers testing functionals for the description of the relative spin energetics in octahedral iron(II) compounds. It should be pointed out in this context that the issue of whether density functionals should be assessed by comparison against experimental data or against the results of *ab initio* calculations is not entirely clear. The advantage of comparison with *ab initio* calculations is that direct comparisons can be made with features of the Born-Oppenheimer surfaces of isolated molecules, without having to worry about the vibrational, environmental, and finite temperature effects which are unavoidably involved in comparing with experimental data. Paper I [3] consisted of a comparison of DFT results with *ab initio* results for the hexaquoferrrous cation, $[Fe(H_2O)_6]^{2+}$. Paper II [4] extended this comparison to additional functionals and the hexaminoferrous cation, $[Fe(NH_3)_6]^{2+}$. These studies indicated that, of the functionals studied, the PBE0 hybrid functional and the VSXC meta-GGA gave the best description of spin energetics. A limitation of comparing with *ab initio* calculations is that good *ab initio* calculations are only possible for the smallest iron(II) complexes. Paper III [5] extended these previous studies to the *tris*(2,2'-bipyridine) complex, $[Fe(bpy)_3]^{2+}$ which is in a size range typical of spin-transition complexes of practical interest. For a complex of this size, high quality *ab initio* calculations are impractical and so comparison was against an experimental estimate of ΔE_{HL} obtained by analysis of the low-temperature dynamics of the high-spin → low-spin relaxation rate following the photo-induced population of the high-spin state. The present paper goes even

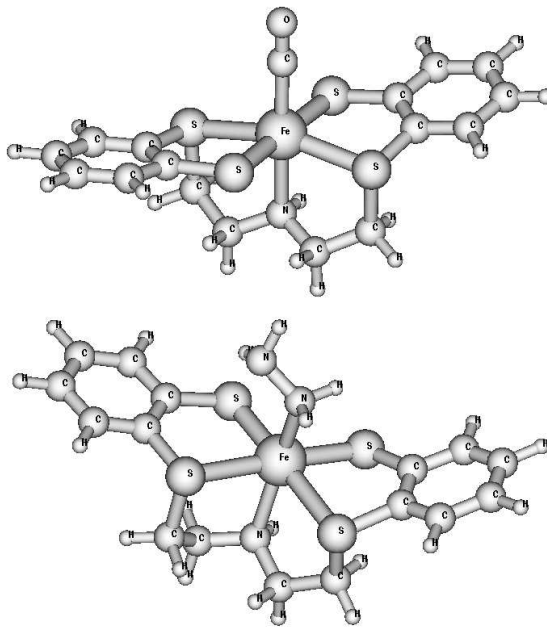


FIGURE 4.13: Examples of $[\text{Fe}(\text{L})(\text{'NHS4'})]$ complexes. Above: the *trans*- NO^+ -complex. Below: the *cis*- N_2H_4 - complex. NH_3 , CO , and PMe_3 are also treated in this article.

further by comparing DFT results for an interesting set of large octahedral iron(II) complexes (Fig. 4.13) for which experimental data is available regarding the ground spin state. These complexes have the generic formula $[\text{Fe}(\text{L})(\text{'NHS4'})]$, where 'NHS₄' is short-hand notation for the 2,2'-bis(2-mercaptophenylthio)diethylamine dianion and L is one of NH_3 , N_2H_4 , PMe_3 [i.e. $\text{P}(\text{CH}_3)_3$], NO^+ or CO . They show an energy difference between the low-spin and high-spin electronic states as small as only a few 1000 cm^{-1} (roughly 3 kcal/mol), in particular for the PMe_3 compound. This level of accuracy can now be achieved in many instances with high-quality *ab initio* calculations for small molecules but not for molecules of the size considered here. It is a challenging test set for a DFT approach which aims at extending *ab initio* accuracy to molecules in a size range of practical interest. The *cis* isomers of the $[\text{Fe}(\text{L})(\text{'NHS4'})]$ complexes with $\text{L} = \text{NH}_3$ and N_2H_4 have been experimentally determined to have a quintet high-spin ground state ($S = 2$) [7], whereas the *trans* isomers with $\text{L} = \text{PMe}_3$, NO^+ , and CO are known to have an electronic ground state with $S = 0$ [8, 9]. Special care is taken in the present study to include, in so far as possible, vibrational, environmental, and finite temperature effects in our comparison with the available experimental data. This point is further discussed below.

Apart from Papers I and II, almost all previous work on density-functionals for spin-crossover compounds consisted of comparisons with experimental data [10]. (We have only recently become aware of the very interesting pioneering article of Bolvin [11] where DFT results were compared with the results of *ab initio* calculations remarkably similar to those reported in Papers I and II, albeit for different compounds. Rather than seeking the best functional, it was simply concluded in Ref. [11] that DFT calculations gave results which were too erratic to be useful. Of course, we feel that our results show that systematic results may be obtained provided once the functionals have been carefully screened for their treatment of the DFT spin-pairing energy problem.) It was found that the local density approximation (LDA) seriously underestimated electron pairing energies, artificially stabilizing low-spin states with respect to high-spin states. That means that the electronic high-spin (HS) — low-spin (LS) energy difference,

$$\Delta E_{HL}^{el} = E_{HS}^{el} - E_{LS}^{el}, \quad (4.27)$$

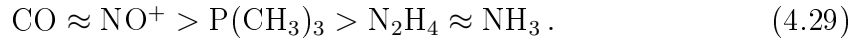
is artificially high when $E_{HS}^{el} > E_{LS}^{el}$ and artificially low when $E_{LS}^{el} > E_{HS}^{el}$. (Through out this paper, the notation,

$$\Delta X_{HL} = X_{HS} - X_{LS}, \quad (4.28)$$

refers to the difference between the HS and LS values of X.) The ground spin state may even be incorrectly predicted to be LS when it is really HS. The usual explanation given is that the LDA underestimates exchange by more than 10%, leading to serious errors in describing parallel spin (i.e. Fermi) correlation [12]. In particular it is often reasoned that exchange between parallel-spin electron pairs keeps the electrons apart, thereby reducing their electron repulsion, so that underestimating exchange will overestimate electron repulsion leading to an energetic destabilization of HS states. (This point is discussed in more detail in Paper I.) Traditional generalized gradient approximations (GGAs), such as BP, PW91, PBE, and BLYP, were found to reduce the pairing energy error, but not to eliminate it. (The nomenclature of the different functionals used in this article is the same as that in the GAUSSIAN 03 manual. This notation is reviewed in Appendix VII.) Hybrid functionals either overcorrect (most works) or undercorrect (papers I and II), but the pairing energy error appeared to be directly proportional to the amount of Hartree-Fock exchange [13] and good results could be obtained in many cases by simply tuning the amount of exact exchange. In particular, the B3LYP* functional with 15% exact

exchange was found to work well for calculating ΔE_{HL}^{el} [14]. Interestingly enough Papers I and II seem to indicate that this good behavior of the B3LYP* functional does not extrapolate to the small molecules $[\text{Fe}(\text{H}_2\text{O})_6]^{2+}$ and $[\text{Fe}(\text{NH}_3)_6]^{2+}$. It was also found that newer highly parameterized GGAs, such as the HTCH functionals, could do roughly as well as conventional hybrid functionals for these small molecules, but without exact exchange. The VSXC meta-GGA was found to be one of the better functionals for this particular property, while retaining the advantage that it has been well tested in a number of molecules [15, 16] and found to give reasonable results for a variety of properties. Note however the dramatic failure of the VSXC functional for describing torsion potentials in π -conjugated systems [17]. Given that the experience obtained from testing functionals on larger molecules did not seem to extrapolate well to the small molecules $[\text{Fe}(\text{H}_2\text{O})_6]^{2+}$ and $[\text{Fe}(\text{NH}_3)_6]^{2+}$, we wanted to see if our small molecule experience would extrapolate to the treatment of larger molecules of more practical interest.

The only way to do this seems to be to accept the idea of comparing with experiment. One way to do this was described in Paper III. A good experimental estimate of ΔE_{HL}^{el} is available for the *tris*(2,2'-bipyridine) ferrous cation, $[\text{Fe}(\text{bpy})_3]^{2+}$, on the basis of the low-temperature dynamics of the HS \rightarrow LS relaxation rate [5]. In this paper we make use of a second source of experimental data in our assessment of density-functionals, namely the series of 2,2'-*bis*(2-mercaptophenylthio)diethylamine dianion ferrous compounds, $[\text{Fe}(\text{L})(\text{'NHS}_4^{\prime})]$ with L = NH₃, N₂H₄, PMe₃, CO, and NO⁺. In this case it is the ground spin state which is known experimentally and which must be correctly predicted all along the series in order for a functional to be regarded as acceptable. This was the basis of the earlier work by Reiher which resulted in the B3LYP* functional [14]. The energy difference, ΔE_{HL}^{el} , decreases for these compounds along the spectrochemical series,



On the left hand end of this series, ΔE_{HL}^{el} , is positive. It is negative on the right hand end. In fact, a more careful comparison with experiment must take into account finite temperature effects and involve the calculation of the free energy difference, ΔG_{HL} .

Our paper is divided into the following sections. The next section discusses the problem of calculating ΔG_{HL} for these compounds. Some of the issues distinguishing candidate functionals for applications to spin-crossover ferrous compounds are reviewed in Sec. III. (An appendix summarizes abbreviations for the different func-

tionals used in this study.) The technical details of our calculations are given in Sec. IV. In Sec. V we give our results. Section VI summarizes.

II Thermodynamic Calculations

Most of the results in this paper will be given in terms of the quantity ΔE_{HL}^{el} which is the difference between the HS and LS electronic energies [Eq. (4.27)]. This quantity is convenient in that it is relatively straightforward to calculate and facilitates comparison with results of previous studies. But comparing ΔE_{HL}^{el} against experiment involves certain assumptions, not all of which are completely justified. This is why our final comparisons for the $[Fe(L)('NHS_4')]$ complexes will be based upon the free energy difference, ΔG_{HL} , though this involves additional, rather computer resource intensive, calculations. The relation between ΔG_{HL} and ΔE_{HL}^{el} is discussed in detail here.

If γ_{HS} denotes the fraction of complexes in the HS state, then the HS-LS equilibrium constant,

$$K_{HL} = \frac{\gamma_{HS}}{1 - \gamma_{HS}} = \frac{[HS]}{[LS]}, \quad (4.30)$$

is determined by the free energy difference according to the well-known relation,

$$\Delta G_{HL} = -RT \ln K_{HL}. \quad (4.31)$$

The complex is LS when ΔG_{HL} is positive and HS when ΔG_{HL} .

The free energy difference is a macroscopic property which we would like to be able to calculate from molecular level information which we can calculate. In principle, this molecular level information contains not just information internal to the iron complexes but also information about interactions between these complexes and the other molecules around them. Our first approximation is to neglect the effects of these interactions. This approximation can be justified by looking at the individual terms in

$$\Delta G_{HL} = \Delta H_{HL} - T\Delta S_{HL}. \quad (4.32)$$

Lindoy and Livingstone [18] have estimated that the electronic contribution, ΔH_{HL}^{el} is $\sim 1000 \text{ cm}^{-1}$, the intramolecular vibrational contribution, $\Delta H_{HL}^{vib(intra)}$ is $\sim 100 \text{ cm}^{-1}$, and the intermolecular vibrational contribution, $\Delta H_{HL}^{vib(inter)}$ is $\sim 10 \text{ cm}^{-1}$ [18]. Thus neglecting the intermolecular contribution to the enthalpy difference is justified and that ΔH_{HL} is dominated by the electronic contribution. As regards the entropy

difference, ΔS_{HL} , suffice it to say that our calculated intramolecular vibrational contribution to the entropy difference are in the range $T\Delta S_{HL} = 1500 - 2000 \text{ cm}^{-1}$ at 298 K (Table 4.10) which may be compared with a measured vibrational contribution to the entropy difference of $4.3 - 7.2 \text{ cm}^{-1}\text{K}^{-1}$ ($T\Delta S_{HL} = 1280 - 2140 \text{ cm}^{-1}$ at 298 K) measured by Sorai and Seki [19] using infrared spectroscopy and calorimetric methods for $[\text{Fe}(\text{phen})_2(\text{NCX})_2]$ (with X = S, Se). It is thus relatively safe to neglect intermolecular effects unless a major change of crystal structure is expected to be associated with the change of spin state.

Many quantum chemistry programs, such as GAUSSIAN 03[20], calculate free energies using well-established formulae based upon an ideal gas (particle in the box) treatment of translations, a rigid rotor treatment of rotations, a harmonic oscillator treatment of vibrations, and the assumption that only a single electronic state is thermally accessible (see, for example, Ref. [21], pp. 136-138.) It turns out that these also provide a reasonable approach to calculating ΔG_{HL} in the condensed phase. This is because translational effects completely cancel when taking the difference and the only rotational effects left after taking the difference are in the entropic term and are small enough to neglect. Let us examine the relative magnitudes of the different terms contributing to ΔG_{HL} .

Both vibrational and electronic effects make significant contributions to the entropy difference, ΔS_{HL} . Remember that we are assuming that only a single electronic state is thermally accessible at any given time (an assumption which may be questioned but which is very difficult to avoid in practical calculations, since taking it into account means calculating information about the potential energy surfaces of electronic excited states.) This means that the electronic contribution to the entropy difference is completely determined by spin degeneracy,

$$\Delta S_{HL}^{el.} = R \ln \frac{2S_{HS} + 1}{2S_{LS} + 1} = R \ln 5. \quad (4.33)$$

This leads to a stabilization of $1.12 \text{ cm}^{-1}\text{K}^{-1}$ for the high-spin state. This is a significant contribution to ΔS_{HL} , but not as significant as the vibrational contribution to ΔS_{HL} . For the $[\text{Fe}(\text{L})(\text{'NHS}_4^{\prime})]$ complexes studied here, we have explicitly calculated both S_{HS} and S_{LS} using all degrees of freedom and found S_{HS} to be always larger than S_{LS} , resulting in an entropic difference between high-spin and low spin states of $\Delta S_{HL} \approx 5 - 7 \text{ cm}^{-1}\text{K}^{-1}$. This results in an entropic stabilization of the high-spin state of approximately $T\Delta S_{HL} = 1500 - 2000 \text{ cm}^{-1}$ at 298 K. This is quite reasonable in comparison with the estimate of typical ΔS_{HL} given in [22], including both vibrational and electronic contributions, of $4 - 7 \text{ cm}^{-1}\text{K}^{-1}$.

TABLE 4.8: Typical thermodynamic data for the $[Fe(L)('NHS4')]$ complexes at 298.15 K and 1 bar. All values are in cm^{-1} (See also Table 4.10.)

Term	Typical Value (cm^{-1})
$\Delta E_{HL}^{\text{ZPVE}}$	-700
$\int_{T=0K}^{298K} \Delta C_{HL}^V(T')dT'$	400
$-T\Delta S_{HL}$	-1800
$p\Delta V_{HL}$	< 0.1
Total ^a	-2100

$$^a \Delta G_{HL} - \Delta E_{HL}^{el} = \Delta E_{HL}^{\text{ZPVE}} + \int_{T=0K}^{298K} \Delta C_{HL}^V(T')dT' - T\Delta S_{HL}$$

The enthalpy difference, ΔH_{HL} , may be decomposed into the sum of the electronic energy difference, ΔE_{HL}^{el} , the zero-point vibrational energy difference, $\Delta E_{HL}^{\text{ZPVE}}$,

$$\Delta H_{HL}(T, p) = \Delta E_{HL}^{el} + \Delta E_{HL}^{\text{ZPVE}} + \int_0^T \Delta C_{HL}^V(T')dT' + p\Delta V_{HL}. \quad (4.34)$$

Note that the method used to calculate free energies is derived for the ideal gas model of translational motions. In this model, the constant pressure and constant volume heat capacities are related by the product of the number of moles of gas, n , and the ideal gas constant, R ,

$$C_p = C_V + nR. \quad (4.35)$$

In a liquid or solid, it is a good approximation to take,

$$C_p = C_V. \quad (4.36)$$

(See for example Ref. [23].) In either case,

$$\Delta C_{HL}^p = \Delta C_{HL}^V. \quad (4.37)$$

As previously mentionned, neither translations nor rotations contribute to the enthalpy energy difference. Table 4.8 provides a summary of typical values for these terms. The electronic energy difference, ΔE_{HL}^{el} , is usually the dominating quantity in Eq. (4.34). However other terms in Eq. (4.34) become important for ΔE_{HL}^{el} on the order of 2000 cm^{-1} . The next most important term is the zero-point vibrational energy difference, $\Delta E_{HL}^{\text{ZPVE}}$. We have always found it to be a negative quantity, thus

stabilizing the HS state. This makes sense because antibonding e_g orbitals are occupied in the HS state which are not occupied in the LS state. This results in weaker longer bonds with smaller force constants in the HS than in the LS state and hence smaller zero-point vibrational energies. For finite temperatures, excited vibrational states are populated. This is taken into account via an integration over the constant volume heat capacity difference, $\int_0^T \Delta C_{HL}^V(T')dT'$, which is entirely vibrational in the approximations mentionned above. In our calculations, we have always found this quantity to be positive, hence stabilizing the LS state. Finally the term, $p\Delta V_{HL}$, is the work exerted on the atmosphere due to a macroscopic volume change, ΔV_{HL} . If no dramatic change in crystal structure occurs, this can be estimated from the change in molecular volume. The spin transition in octahedral ferrous compounds leads to a very large change in the iron-ligand bond length (typically around 0.2 Å). Experimental values for ΔV_{HL} [24, 25, 26, 27] are in the range of 15-30 Å³ per molecule. However, this results in a work exerted against atmospheric pressure of less than 0.1 cm⁻¹, which can be neglected.

In summary, ΔE_{HL}^{el} is only a first approximation to the free energy difference ΔG_{HL} , which is the quantity which should really be obtained from experiment. Given ΔE_{HL}^{el} one can obtain an improved estimate of ΔG_{HL} by subtracting the typical value of 2000 cm⁻¹ given in Table 4.8,

$$\Delta G_{HL} \approx \Delta E_{HL}^{el} - 2000 \text{ cm}^{-1}. \quad (4.38)$$

In this paper we actually do much better than this by explicitly calculating the free energy correction term to the electronic energy difference for the OLYP and BP86 functionals so as to have specific molecule-dependent estimates, thereby allowing a rigorous comparison of DFT results with experiment.

III Density Functionals

This section reviews the general types of functionals used in this study. We employ the notion of ‘Jacob’s Ladder’ introduced by Perdew and Schmidt [28] as a helpful classification scheme. More general background information about density-functional theory (DFT) may be found in Refs. [29, 12, 30]. We also point out the importance of the exchange contribution to the DFT spin-pairing energy problem in metal complexes.

TABLE 4.9: Jacob's Ladder for DFT. Spin has been suppressed for simplicity of notation.

Heaven (Chemical Accuracy)		
orbital-dependent functionals	$\rho, \vec{\nabla}\rho$ τ, ψ_i^d	B3LYP, B3LYP* PBE0
meta-GGAs	$\rho, \vec{\nabla}\rho, \tau^c$	VSXC
GGAs	$\rho, \vec{\nabla}\rho^b$	BP86, OLYP HCTH93, HCTH147, HCTH407
LDA	ρ^a	LDA
Hartree World		

^a The density, $\rho_\sigma(\mathbf{r}) = \sum_i n_i |\psi_i(\mathbf{r})|^2$.

^b The reduced density, $x(\mathbf{r}) = |\vec{\nabla}\rho(\mathbf{r})/\rho^{4/3}(\mathbf{r})|$ and other derivatives of the density.

^c The kinetic energy density, $\tau(\mathbf{r}) = (1/2) \sum_i n_i |\vec{\nabla}\psi_i(\mathbf{r})|^2$.

^d Indicates a more general dependence on the orbitals, $\psi_i(\mathbf{r})$.

A Jacob's Ladder

Jacob's Ladder (Table 4.9) groups functionals into families, depending upon which ingredients are used in making the functionals. For the lowest three rungs on this ladder, a general formula for the exchange-correlation functional is given by,

$$E_{xc}[\rho] = \int \epsilon_{xc}(\rho(\mathbf{r}), \vec{\nabla}\rho(\mathbf{r}), \tau(\mathbf{r})) \rho d\mathbf{r}. \quad (4.39)$$

The quantity ρ is the electron density, $\vec{\nabla}\rho$ is the gradient of the electron density and τ is the local kinetic energy density which for the interacting system is given by

$$\tau(\mathbf{r}) = \frac{1}{2} \sum_i^{\text{occup}} |\nabla\psi_i(\mathbf{r})|^2. \quad (4.40)$$

In general, the exchange-correlation energy density, ϵ_{xc} , depends explicitly on the two spin components of each of the variables ($\rho_\uparrow, \rho_\downarrow, \vec{\nabla}\rho_\uparrow, \vec{\nabla}\rho_\downarrow, \tau_\uparrow, \tau_\downarrow$). This spin dependence has been suppressed for simplicity of notation.

The local density approximation (LDA) constitutes the first rung of the ladder. It corresponds to neglecting τ and $\vec{\nabla}\rho$ in Eq. (4.39). This approximation, which is based on the homogeneous electron gas, works remarkably well for predicting equilibrium geometries, although molecular charge densities are far from being homogeneous. In fact, the exchange-correlation energy only depends on the spherically-averaged exchange-hole which shares several common features in molecules and the

homogeneous electron gas. These include satisfying certain sum rules, the behavior for vanishing inter-electronic distances of the exchange part,

$$h_x(\mathbf{r}_2 \rightarrow \mathbf{r}_1) = -\rho(\mathbf{r}_1), \quad (4.41)$$

and the correlation part, and the constraint that the exchange hole be everywhere negative [30].

The second rung is reached by including the gradient of the charge density $\vec{\nabla}\rho$. This is a promising way to include the effect of the rapidly varying electron density common in molecules by only including information about the local rate of variation of the charge density. A natural way to include the gradient of the charge density is the gradient expansion approximation (GEA) obtained via a truncated Taylor series expansion,

$$E_{xc}^{GEA}[\rho] = \int \epsilon_{xc}(\rho(\mathbf{r}))\rho(\mathbf{r}) d\mathbf{r} + \int C_{xc}(\rho(\mathbf{r}))x(\mathbf{r}) d\mathbf{r}. \quad (4.42)$$

Unfortunately, the GEA gives worse rather than better results than the LDA. The reason for this poor performance is that the GEA fails to satisfy many of the exact constraints satisfied by the LDA. The most important violations of these constraints are the sum rules and that the exchange hole is no longer restricted to be negative for any pair of charges $\mathbf{r}_1, \mathbf{r}_2$. A further approximation can be made, which enforces all these constraints by setting to zero those contributions from the GEA exchange-correlation functional that result in a positive exchange hole and by approximating the exchange and the correlation holes such that $h_x(\mathbf{r}_1, \mathbf{r}_2)$ and $h_c(\mathbf{r}_1, \mathbf{r}_2)$ contain exactly one and zero electron charges, respectively [30]. The resulting generalized gradient functionals (GGA) outperform the LDA. Among the most recent GGAs are the highly parametrized functionals by Handy and coworkers [31], HCTH93, HCTH147 and HCTH407. These employ 15 parameters and yield very satisfactory results for many properties. Another recent GGA functional is the OPTX exchange functional [32] also by Handy and Cohen. This exchange functional differs from other GGA exchange integrals as it has been parametrized to reproduce Hartree-Fock exchange only for atoms. Handy and Cohen argue that this allows the functional to take better account of static correlation effects than would be the case had parameterization included molecular data. In particular, it is argued that exact exchange and density-functional exchange will always differ in molecules because some left-right correlation will always be present in the density functional which is absent in Hartree-Fock exchange. For atoms, however, there is no left-right correlation and so the two types of exchange energies are comparable.

The third rung of Jacob's ladder is composed of meta GGAs. While the GGA approach has been found to work quite well, it also has some inherent shortcomings. In particular, it cannot usually account for the fact that the exact exchange hole, $h_x(\mathbf{r}_1, \mathbf{r}_2)$, in molecules is spread out over several centers, meaning that its structure at any given point \mathbf{r}_1 should have an explicit dependence on the coordinates of other points, \mathbf{r}_2 . Such behavior cannot be correctly described by functionals employing only $\rho(\mathbf{r}_1)$ and $\nabla\rho(\mathbf{r}_1)$ [33]. An illustrative example is the stretched H_2^+ molecule. In this one-electron system, the only duty of the exchange hole is to take care of the self-interaction. The exchange hole is given by

$$h_x(\mathbf{r}_1, \mathbf{r}_2) = -\frac{|\sum_i^{occ.} \psi_i(\mathbf{r}_1)\psi_i^*(\mathbf{r}_2)|^2}{\rho(\mathbf{r}_1)} \quad (4.43)$$

and because there is only one electron in this system, the exchange hole is static and equal to the negative of half the σ_g density, $-|\psi(\mathbf{r}_2)|^2$. This exchange hole is independent of the position of \mathbf{r}_1 and is equally split between the two nuclei, even at large distances when H_2^+ is strongly stretched. Thus the exact exchange hole removes only half of the charge at each nucleus and the other half of the charge at the other nucleus. Unfortunately a local functional always assumes a localized hole and thus removes one charge at each nucleus, overestimating the exchange energy contribution and overlooking that the fact that the exchange hole has been fractured into separate parts, each containing only a fraction of an electron. This problem can be overcome by making use of the kinetic energy density τ as a probe of fractional exchange-correlation hole occupancy. In particular, Becke has shown [33] that the quotient,

$$t = \frac{\tau^{LDA}}{\tau}, \quad (4.44)$$

is a good measure of the delocalization of the exchange hole if t has a value significantly less than one. Here τ^{LDA} is the expression of the kinetic energy density in the local spin approximation and can be conveniently expressed as $\tau^{LDA} = \frac{3}{5}(6\pi^2)^{\frac{2}{3}}\rho^{\frac{5}{3}}$. Thus, by probing the quantity t , even a non hybrid functional should be able to eliminate the overestimation of the exchange energy present in the LDA and GGAs. A different approach to employing the kinetic energy density τ is a high-order density matrix expansion (DME). Van Voorhis and Scuseria proposed one of the first meta-GGAs using this technique [15]. They approximated Hartree-Fock exchange by means of a second order DME using Bessel functions and Legendre polynomials. Although this DME approximation does not explicitly evaluate the quantity t given

in Eq. (4.44), one can still expect the resulting exchange functional to correctly describe delocalized exchange holes in so far as it mimics exact exchange.

These methods outlined above make up the first three rungs on Jacob's Ladder. The fourth rung is not local anymore because it depends on the evaluation of expressions that are calculated using orbitals rather than the charge density, where the dependence on electron coordinates has already been removed by integration over all space. The fourth rung is constituted from the hybrid functionals which include a portion of exact (Hartree-Fock) exchange. Some of these functionals (such as B3LYP and PBE0) are among the most popular and most successful density functionals nowadays available.

Users of DFT have been described as the angels ascending and descending Jacob's ladder [28], free to choose the level of approximation which most suits them. This is a nontrivial point. Even if one might hope that ascending the ladder will improve precision, the inclusion of more and more ingredients in the density functionals means more complicated functionals and added computational expense. This is why it is also important to be able to descend Jacob's ladder.

B Exchange and the DFT Spin-Pairing Energy Problem

As pointed out in the introduction, the amount of admixed exact exchange will severely affect ΔE_{HL} in so far as a higher multiplicity state will be stabilized relative to a lower multiplicity state. This becomes obvious when the Hartree-Fock exchange energy is written down,

$$K = \sum_i \sum_j n_i n_j \times \iint \psi_i(\mathbf{x}_1) \psi_j^*(\mathbf{x}_1) \frac{1}{\mathbf{r}_{12}} \psi_i(\mathbf{x}_2) \psi_j^*(\mathbf{x}_2) d\mathbf{x}_1 d\mathbf{x}_2 \quad (4.45)$$

Here, $\mathbf{x} = (\mathbf{r}, \sigma)$ is shorthand for space and spin coordinates. Because of the spin integration, only terms with like spin contribute to K . As high spin states contain more spin orbitals of one spin type than the corresponding low spin state with the same number of electrons, K will tend to be greater for the HS state because more contributing terms enter into the summation. It follows, that an increase of the scaling parameter in hybrid functionals will stabilize the HS state relative to the LS state.

The situation for pure DFT exchange is completely different. In the Slater X α

exchange approximation, we have,

$$E_x[\rho] = -\alpha C_x \int \left(\sum_i n_i |\psi_i(\mathbf{r})|^2 \right)^{\frac{4}{3}} d\mathbf{r} \quad (4.46)$$

n_i is the occupation number of the i th orbital. Now, if we look at a d^6 atom in an octahedral ligand field and freeze the core electrons, the Slater exchange contribution will give for the singlet state,

$$E_x^{S=0}[\rho] = -\alpha C_x \int (6|t_{2g}(\mathbf{r})|^2)^{\frac{4}{3}} d\mathbf{r} \quad (4.47)$$

For the quintet state, the same expression yields,

$$\begin{aligned} E_x^{S=2}[\rho] &= -\alpha C_x \int (4|t_{2g}(\mathbf{r})|^2 + 2|e_g(\mathbf{r})|^2)^{\frac{4}{3}} d\mathbf{r} \\ \end{aligned} \quad (4.48)$$

The answer to the question of whether this stabilizes the HS or the LS state depends upon the relative size of the magnitudes of $E_x^{S=0}$ and $E_x^{S=2}$. Since the e_g orbitals are typically more diffuse than the t_{2g} orbitals, the magnitude of $E_x^{S=2}[\rho]$ is typically smaller than that of $E_x^{S=0}[\rho]$. Consequently the LS state will be stabilized relative to the HS state when α is increased. This is exactly the opposite behavior from exact exchange and certainly seems counter-intuitive when it is recalled that Slater wanted to approximate the complicated Hartree-Fock expression. If we extend our argument to allow for orbital relaxation effects, the situation is of course more complicated, since the electron-electron repulsion term J , the kinetic energy of the electrons, and the core-electron electrostatic energy are all implicit functions of $E_x[\rho]$.

Nevertheless the answer remains the same for octahedral Fe(II) complexes. To see this, we calculated ΔE_{HL} with a variable factor α which scales the total contribution of the exchange functional to the total energy,

$$\begin{aligned} E &= \frac{1}{2} \sum_{i=1}^N \int |\nabla \psi_i|^2 d^3\mathbf{r} + \int \rho V_{ext.} d^3\mathbf{r} \\ &+ \frac{1}{2} \int \int \frac{\rho(\mathbf{r}_1)\rho(\mathbf{r}_2)}{r_{12}} d^3\mathbf{r}_1 d^3\mathbf{r}_2 + \alpha E_x[\rho_\uparrow, \rho_\downarrow] \end{aligned} \quad (4.49)$$

Note that we decided not to include a correlation functional so as not to complicate our analysis of exchange effects.

Figure 4.14 shows results for the totally symmetric octahedral molecule, FeH_6 ,

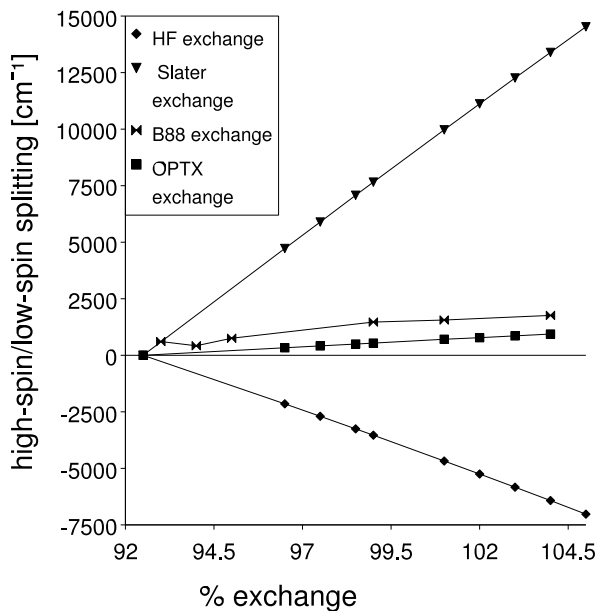


FIGURE 4.14: Influence of the admixture of HF, Slater and GGA exchange on ΔE_{HL} . In order to keep everything on a single graph, the quantity ΔE_{HL} has been arbitrarily displaced so that it is zero for a scaling parameter of 92.5%.

using HF, Slater, OPTX and B88 exchange functionals. As expected, the HF results show a negative slope ($-564 \text{ cm}^{-1}/\%$ exchange) with respect to the scaling parameter. Rather unexpectedly, Slater exchange behaves oppositely to HF exchange, showing a positive slope ($1161 \text{ cm}^{-1}/\%$ exchange). This means that increased amounts of Slater exchange actually stabilizes the LS state relative to the HS state even though HF exchange destabilizes the LS state relative to the HS state. We also tested Becke's B88 exchange functional and the OPTX exchange functional in order to see if this counterintuitive behavior of Slater exchange would still be present for GGAs. Indeed the corresponding slopes are positive ($125 \text{ cm}^{-1}/\%$ exchange and $82 \text{ cm}^{-1}/\%$ exchange) but are much smaller. The fact that the GGA slopes lie between the HF and LDA slopes might be interpreted as being consistent with the GGAs giving a better than LDA description of HF exchange. Nevertheless the sign of the LDA and GGA slopes are surprising given the simple idea that DFT exchange should be describing Pauli exclusion effects which one would, naively, think would favor the HS state over the LS state by keeping like spin electrons physically separated in space and thus reducing their mutual electronic repulsion.

We also verified that these results are not an artifact of the simple model system FeH_6 . For the *trans*-[Fe(CO)(‘NHS₄’)] variation of Slater exchange from 92% to 105% yielded a slope of $141 \text{ cm}^{-1}/\%$ exchange.

In fact, not only ΔE_{HL} , but also E_{HS} and E_{LS} , were observed to show a linear dependance on the amount of LDA or GGA exchange included in the functional. This is very similar to the linear dependance of ΔE_{HL} observed by Reiher on the relative amount of HF to GGA exchange included in hybrid functionals [14]. We conclude that increasing the relative amount of HF to GGA exchange stabilizes the HS state relative to the LS state, not only because the amount of HF exchange is increased but also because the amount of GGA exchange is decreased, since both effects actually individually favor the HS over the LS state.

We have also studied ideal tetrahedral Fe(II) complexes, and although the above argument, that high multiplicity states will profit less from Slater exchange, can be extended to tetrahedral and square planar complexes, we have found a stabilization of the HS state relative to the LS state in tetrahedral Fe(II) complexes with an increase in α , just as would be expected for exact exchange.

Previous studies have tended to emphasize the importance of the fourth rung of Jacob's Ladder for a correct description of the relative energetics and the HS and LS states in octahedral Fe(II) complexes. Our goal is to make a more thorough study and to see if we cannot find functionals which allow us to descend Jacob's Ladder will still giving an adequate treatment of the high-spin/low-spin energy splittings in octahedral Fe(II) complexes.

IV Computational Details

The DFT calculations reported here were carried out with GAUSSIAN 03 [20] using the TZVP basis set of Ahlrichs [34]. We note that computational demand for the $[Fe('NHS_4')(L)]$ and the $[Fe(bpy)_3]^{2+}$ complexes is quite high. Some single-point calculations needed more than 24 hours to converge on a 2.3 GHz BiXeon machine. SCF convergence was set to 10^{-6} hartrees. The resolution of the identity technique (RI) with the default density fitting basis set was always used for the LDA and GGA density functionals but not for hybrid functionals as there was no significant improvement over the standard coulomb term evaluation method. The accuracy of the RI method compared to the standard technique was assesed in some single point calculations and found to be sufficient, with deviations between both methods smaller than 0.1 cm^{-1} . The default integration grid was always used. Frequency and thermodynamic data calculations were also performed with GAUSSIAN 03 using the TZVP basis set and the RI technique.

TABLE 4.10: Thermodynamic data for the $[\text{Fe}(\text{'NHS}_4^{\prime})(\text{L})]$ complexes at $T = 298\text{K}$. All values are in cm^{-1}

Complex	$\Delta E_{HL}^{\text{ZPVE}}$	$-T\Delta S_{HL}$	$\int_0^T C_{HL}^v(T') dT'$	$\Delta G_{HL} - \Delta E_{HL}$
OLYP at OLYP optimized geometries:				
cis- N_2H_4	-525	-1778	402	-1901
cis- NH_3	-643	-1974	452	-2165
trans- PMMe_3	-707	-2126	477	-2356
trans- NO^+	-856	-1452	391	-1917
trans- CO	-900	-1954	498	-2356
aver. value	-726	-1857	444	-2139
BP86 at BP86 optimized geometries:				
cis- N_2H_4	-572	-2355	594	-2333
cis- NH_3	-650	-1982	460	-2172
trans- PMMe_3	-665	-1208	261	-1612
trans- NO^+	-807	-1418	370	-1855
trans- CO	-865	-1993	487	-2371
aver. value	-712	-1791	433	-2069

V Results

This section is organized as follows: We start by giving thermodynamic data for the $[\text{Fe}(\text{'NHS}_4^{\prime})(\text{L})]$ medium-sized compounds in order to estimate a value for ΔG_{HL} from ΔE_{HL} . We then compare ΔE_{HL} results of different density functionals against experimental data. First, we give results for the $[\text{Fe}(\text{'NHS}_4^{\prime})(\text{L})]$ medium-sized compounds calculated with different density functionals but always at the B3LYP* optimized geometries. This allows us to focus on trends among different functionals, while keeping the number of degrees of freedom in the problem to a minimum. The B3LYP* optimized geometries used are in good agreement with crystal structures for these complexes [14]. *Please note that we will henceforth drop the superscript in $\Delta E_{HL}^{\text{el}}$ and just denote it by ΔE_{HL} .* Full geometry optimizations and estimates of ΔG_{HL} are then given for the density functionals which are found to work best at the B3LYP* geometries. Finally we compare these functionals against quantitative ΔE_{HL} values for $[\text{Fe}(\text{H}_2\text{O})]^{2+}$ [3], $[\text{Fe}(\text{NH}_3)]^{2+}$ [4], and $[\text{Fe}(\text{bpy})_3]^{2+}$ [5] from *ab initio* calculations or experiments measuring tunneling relaxation rates which permit direct access to ΔE_{HL} instead of ΔG_{HL} .

A Thermodynamic Data

As discussed in the introduction, it is necessary to know ΔG_{HL} when one compares against experimental data. In order to calculate ΔG_{HL} as given by equations 4.32 and 4.34, one needs to know $\Delta E_{HL}^{\text{ZVPE}}$, $-T\Delta S$ and $\int_0^T \Delta C_{HL}^V(T') dT'$ in addition to ΔE_{HL} . We have explicitly calculated zero-point vibrational energy differences ($\Delta E_{HL}^{\text{ZVPE}}$) as well as finite temperature effects at the OLYP level and at the BP86 level. Results are given in Table 4.10. Interestingly, although the results for both functionals are similar to some extent, a large deviation of 744 cm^{-1} between the two functionals occurs for $\Delta G_{HL} - \Delta E_{HL}$ with the trans-PMe₃ complex. As the BP86 functional has been proven to be one of the better functionals for calculating vibrational frequencies [30] and there is less experience with the newer OLYP functional, we will focus on the results given by BP86 and propose that combining the BP86 value of $\Delta G_{HL} - \Delta E_{HL}$ with the ΔE_{HL} calculated by any density functional can be used to obtain a reasonable estimate of ΔG_{HL} . Table 4.10 makes it clear that ΔG_{HL} has only to be considered when ΔE_{HL} is smaller than about 2100 cm^{-1} . This is typically the case only for the $[Fe('NHS_4')(L)]$ complex with L=PMe₃.

B Hartree-Fock and Half-And-Half Functionals

We begin by looking at how Hartree-Fock performs for these complexes. One would intuitively expect that the high-spin state is strongly favoured because Fermi correlation is included in the HF picture while all other correlation is totally neglected. In Fig 4.15 shows that this expectation is justified. ΔE_{HL} is negative for all complexes although the complexes with the ligands PMe₃, NO⁺ and CO are experimentally known to have a positive ΔE_{HL} (LS ground state). We also included the half-and-half density functionals BHandH and BHandHLYP here because they contain 50% HF exchange and show the same behaviour as HF in so far as that the HS state is favoured in all cases. Note that this overstabilization will only be accentuated by including thermodynamic corrections [Eq. (4.38)]. This strong overstabilization of the HS state demonstrates once again that a good density functional will need to make less use of exact exchange in order to correctly describe ΔE_{HL} [35].

C Hybrid Functionals

We have tested a variety of popular hybrid functionals containing between 25% and 15% exact exchange. For the $[Fe('NHS_4')(L)]$ medium-sized compounds, we have noticed that these hybrid functionals show a distinctive trend in ΔE_{HL} that can be

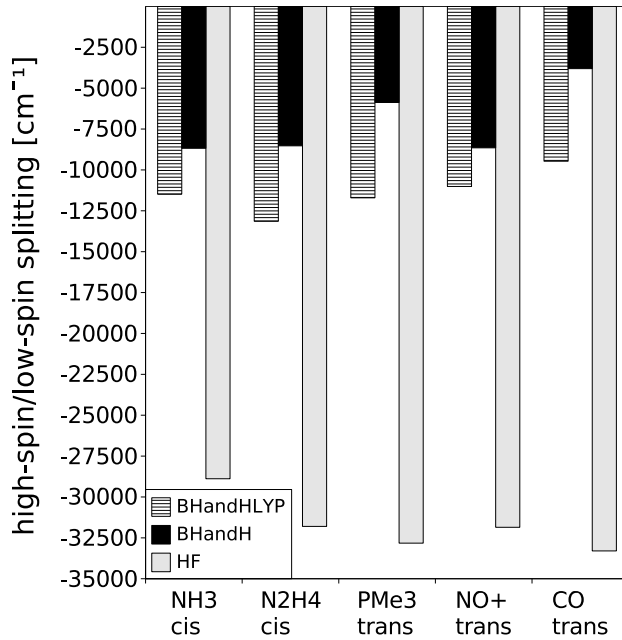


FIGURE 4.15: ΔE_{HL} for Hartree-Fock and half-and-half functionals for the $[\text{Fe}(\text{L})(\text{'NHS}_4)]$ complexes.

related to the amount of exact Hartree-Fock exchange contained in each functional. This is consistent with the previous observation that the dependence of ΔE_{HL} on the exact exchange is linear for the B3LYP functional [14] within a certain range, but is more general in that our observation applies to other hybrid functionals as well. In Fig. 4.16 we show results for five different hybrid functionals. The lines that connect ΔE_{HL} values can be thought of as the functionals' prediction for the spectrochemical series when ligand field strength is increased from left to right. The most striking difference among the functionals is that these spectrochemical series are shifted vertically on this graph according to the amount of exact exchange, indicating that all functionals correctly calculate the relative strengths of the ligands. However a curve containing more exact exchange is always below all other curves with less exact exchange, regardless of the correlation functional part, confirming that Fermi correlation is much more important than Coulomb correlation for calculating ΔE_{HL} .

Only the B3LYP* functional succeeds in assigning a positive ΔE_{HL} to the *trans*-PMe₃ complex. This latter point is not really surprising because the B3LYP* functional was developed by varying the coefficient of HF-exchange so as to produce values for ΔE_{HL} that produce the known experimental groundstates of the $[\text{Fe}(\text{L})(\text{'NHS}_4)]$ complexes, based upon the implicit assumption that ΔE_{HL} was an adequate approximation to ΔG_{HL} . According to Eq. (4.38) shifting all of the curves down by about 2000 cm⁻¹ will provide a better estimate of ΔG_{HL} . When this is

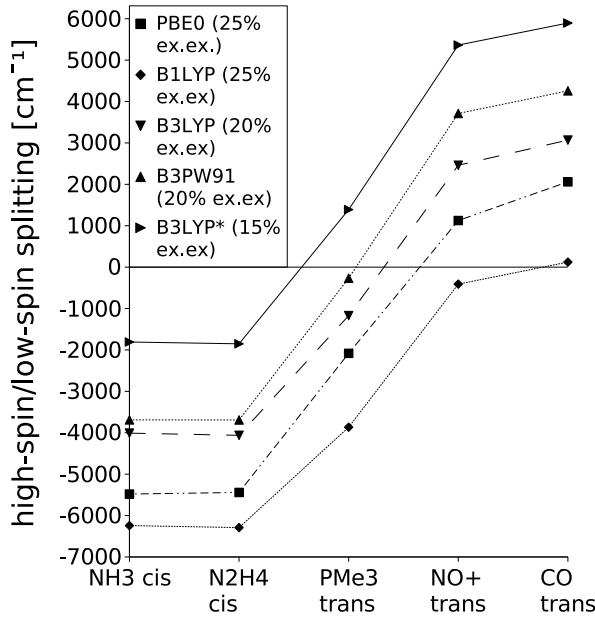


FIGURE 4.16: ΔE_{HL} for hybrid functionals for the $[Fe(L)('NHS_4')]$ complexes. The percentage of exact exchange for each functional is given in parentheses in the figure legend. Note that the B1LYP data point for the *trans*-NO⁺ complex is only a best estimate of the converged result because of difficulty obtaining completely satisfactory convergence for the HS state.

done, it is seen that none of the hybrid functionals is able to predict the known experimental groundstates simultaneously for the entire series of these compounds. Of these functionals the B3LYP* comes the closest to a correct description of ΔG_{HL} over the entire series, although the estimated ΔG_{HL} for the *trans*-PMe₃ complex is slightly negative when it should be positive. Alternatively, this may be viewed as evidence confirming the argument given in Ref. [35], that the amount of exact exchange in the B3LYP functional should be still further reduced below the 15% present in the B3LYP* functional.

D LDA, GGA and meta-GGA Functionals

The Hartree-Fock and half-and-half results presented in Sec. B represent one extreme, strongly favoring the HS state. The other extreme is marked by the LDA which strongly favors the LS states. The popular GGA functionals PBEPBE and BP86 show a similar behaviour to that of the LDA (Fig. 4.17). Even after inclusion of the thermodynamic correction [Eq. (4.38)], the LDA, PBEPBE, and BP86 functionals all incorrectly predict LS groundstates for the entire series of $[Fe(L)('NHS_4')]$ complexes. We conclude that the poor performance of these functionals is due to

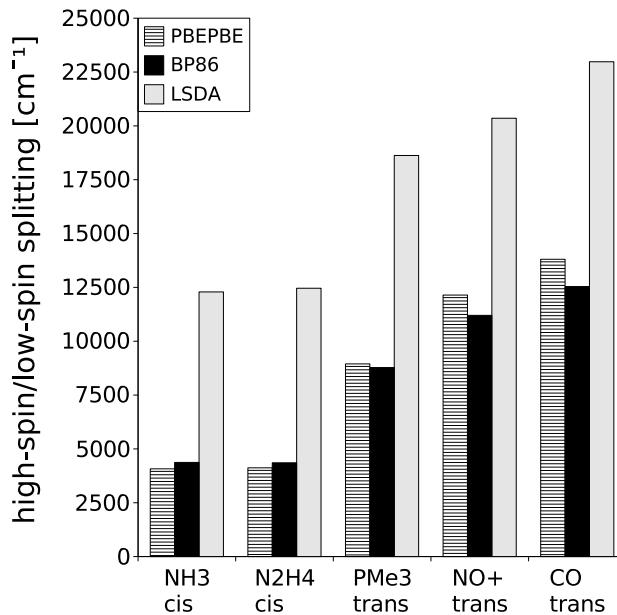


FIGURE 4.17: LDA and GGA ΔE_{HL} 's for the $[\text{Fe}(\text{L})(\text{'NHS}_4\text{'})]$ complexes.

the poor ability of the respective pure density-dependent exchange-correlation part to describe the spin-pairing problem.

This, however, is not a good reason to give up hope that GGA or meta-GGA functionals will be able to give a correct description of the pairing energy in these complexes. Recent developments on the second rung of Jacob's Ladder include the highly-parametrized functionals HCTH407, HCTH147 and HCTH93. As shown in Fig. 4.18, these functionals all give very similar results. They succeed in predicting negative values for ΔE_{HL} for the $[\text{Fe}(\text{L})(\text{'NHS}_4\text{'})]$ complexes with $\text{L}=\text{NH}_3, \text{N}_2\text{H}_4$ and positive values for ΔE_{HL} when L is one of CO, PMe₃, NO⁺. Nevertheless, ΔE_{HL} for the PMe₃-complex is too small to predict a low-spin ground state once thermodynamic corrections are applied. That is ΔG_{HL} will be negative for this complex, indicating a HS ground state as opposed to the observed LS ground state.

Another example of recent advancement on the second rung is the OPTX exchange functional by Handy and coworkers [32]. This functional, combined with Lee, Yang and Parr's correlation functional LYP gave very satisfactory results for the $[\text{Fe}(\text{'NHS}_4\text{'})(\text{L})]$ complexes. Together with the meta-GGA VSXC which belongs to the third rung on Jacob's Ladder, these do indeed seem to be density functionals that can treat the difficult spin-pairing energy problem in octahedral Fe(II) complexes without resorting to the use of exact exchange. In Fig. 4.19 we show the results for these two functionals. VSXC and OLYP correctly assign a negative ΔE_{HL} to the *cis* isomers and a positive ΔE_{HL} to the *trans* isomers with ΔE_{HL} being sufficiently

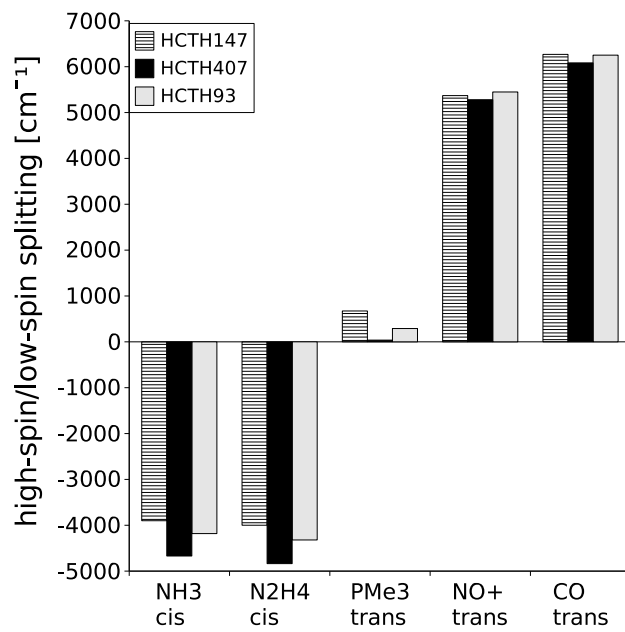


FIGURE 4.18: ΔE_{HL} for highly parametrized functionals and the $[Fe(L)('NHS_4')]$ complexes.

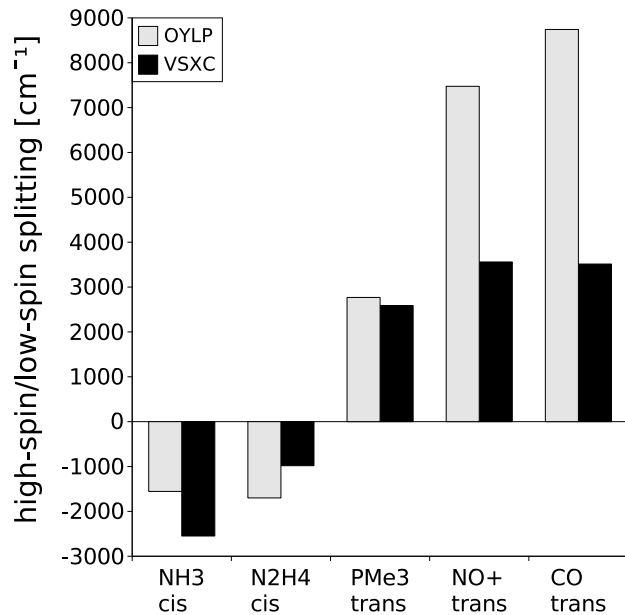


FIGURE 4.19: ΔE_{HL} for OPTX in combination with LYP (OLYP) and the meta-GGA VSXC.

large that a LS groundstate will still be obtained for the *trans*-PM₃ complex after application of the thermodynamic correction is applied to obtain ΔG_{HL} .

E Geometry optimization

Up to this point, all the results for ΔE_{HL} were calculated at a given geometry, i.e. no geometry optimizations but single point calculations were done. This has allowed us to compare functionals without the additional complication of different geometries and to determine that the B3LYP*, VSXC, and OLYP functionals are best for the calculation of ΔE_{HL} . In the end, however, what matters for first principles predictions is how these functionals perform at the HS and LS geometries optimized with the same functional used to calculate ΔE_{HL} .

Figure 4.20 shows ΔG_{HL} for the B3LYP*, VSXC, and OLYP functionals obtained after geometry optimization. We point out again, that ΔG_{HL} is the quantity that has to be compared to finite-temperature experimental data, while ΔE_{HL} can only serve as an approximation. ΔG_{HL} has been calculated using the BP86 results given in Table 4.10. As expected, based upon our previous discussion, the B3LYP* functional predicts the groundstates of the different complexes correctly, except for that of the $[\text{Fe}(\text{PMe}_3)(\text{'NHS}_4^{\prime})]$ complex where ΔG_{HL} is ever so slightly negative thus incorrectly predicting a HS groundstate for this complex. Although the VSXC functional had predicted a LS groundstate for the $[\text{Fe}(\text{PMe}_3)(\text{'NHS}_4^{\prime})]$ complex at the B3LYP* geometry, it now fails dramatically and incorrectly predicts a HS groundstate for this complex. Only the OLYP functional is able to give values of ΔG_{HL} consistent with all experimental findings.

This behaviour of the VSXC functional is quite striking. One might normally expect the results from geometry optimizations to improve when compared against the artificial situation of results obtained from single point calculations at a fixed geometry. As this is not the case, we took a closer look at the structures predicted by the VSXC functional and found them to be unphysically twisted. This twisting might be because VSXC overestimates long range bonding effects like hydrogen bonding or π - π interactions [17]. In Fig. 4.21 we compare predicted structures for the $[\text{Fe}(\text{PMe}_3)(\text{'NHS}_4^{\prime})]$ complex. While OPTX and B3LYP* structures are very similar, it is clearly seen that the structure predicted by the VSXC functional is strongly twisted, falsely indicating a possible interaction between the phosphane hydrogens and the phenyl rings. The shortest measured distances between phosphane hydrogens and phenyl carbon atoms are around 2.5 Å. Also, for the VSXC optimized $[\text{Fe}(\text{NO}^+)(\text{'NHS}_4^{\prime})]$ complex we noticed a strong bending of the NO^+ ligand towards one of the phenyl rings. In this arrangement π - π interactions between the NO^+ - π -orbitals and the phenyl π -system seems possible.

In Table 4.11 we give bond lengths between the central atom Fe and the first ligand sphere atoms. Refer to Fig. 4.21 for the labelling of the atoms. We note that

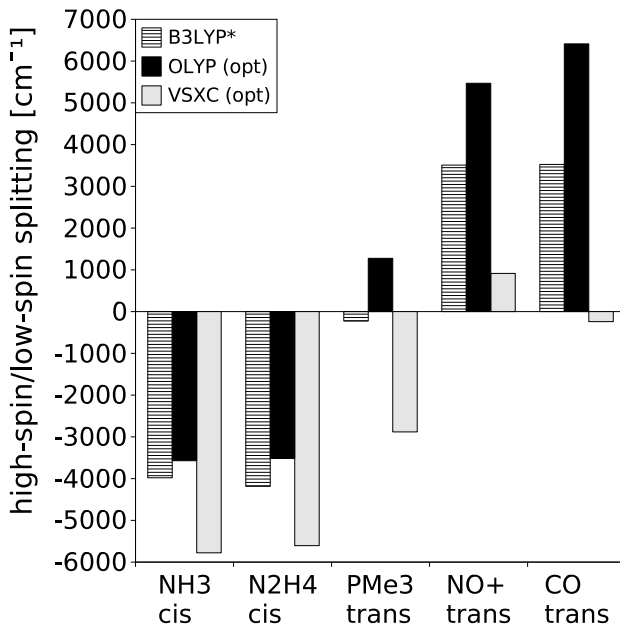


FIGURE 4.20: ΔG_{HL} calculated at optimized geometries with the functionals B3LYP*, VSXC and OLYP. The thermodynamic correction is that of Table 4.10 for the BP86 functional.

the performance of the hybrid functional B3LYP* and the GGA functional OLYP is more or less equal. B3LYP* deviates less for the *cis* complexes, OLYP deviates less for the *trans* complexes. OLYP overestimates the axial Fe-L bond lengths in the *cis* complexes more than B3LYP*.

F Quantitative Assessment of Functionals: Comparison of ΔE_{HL}^{DFT} vs. $\Delta E_{HL}^{ab initio}$ and $\Delta E_{HL}^{exp.}$

We would also like to give a more quantitative description of the high-spin / low-spin splitting phenomenon and the performance of DFT in this field. One might think that *ab initio* zero temperature gas phase results would be the best comparison candidates for DFT calculations since the additional complications of finite temperature condensed matter effects are avoided. However, because of the computationally demanding nature of sophisticated *ab initio* calculations, results are only available for much smaller molecules than the $[Fe('NHS_4')(L)]$ complexes discussed above. For the $[Fe(bpy)_3]^{2+}$ complex, accurate quantitative comparison data is available from quantum tunneling experiments [5]. Although we might rather prefer gas-phase comparison data for consistency reasons, we still include the $[Fe(bpy)_3]^{2+}$ complex but point again out the caveat that we are using an energy estimate obtained from

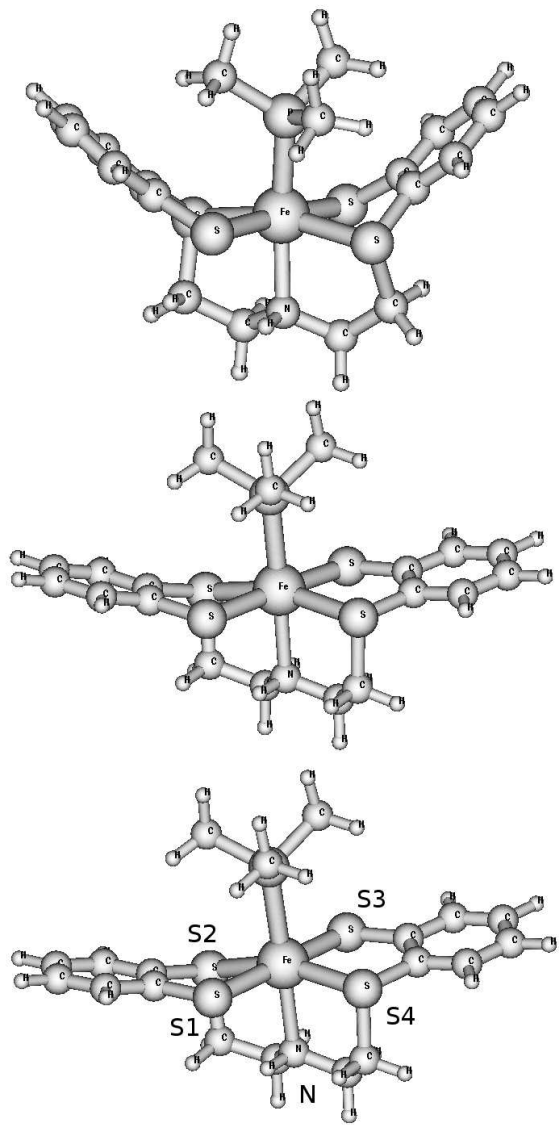


FIGURE 4.21: Optimized geometries for the $[\text{Fe}(\text{PMe}_3)(\text{'NHS}_4)]$ complex: Top VSXC, middle B3LYP*, bottom OLYP.

TABLE 4.11: Bond lengths (\AA) between Fe and first-sphere ligands.

L=NH ₃ (S=2)	OLYP dev.	B3LYP* dev. [14]	Exp. [7]
Fe-S1	-0.048	-0.013	2.397
Fe-S2	+0.127	+0.116	2.588
Fe-S3	+0.169	+0.149	2.586
Fe-S4	-0.027	+0.009	2.394
Fe-N	+0.143	+0.069	2.244
Fe-NH ₃	+0.103	+0.048	2.189
MAE	0.102	0.067	

L=N ₂ H ₄ (S=2)	OLYP dev.	B3LYP* dev. [14]	Exp. [7]
Fe-S1	-0.056	-0.018	2.402
Fe-S2	+0.081	+0.092	2.602
Fe-S3	+0.169	+0.141	2.602
Fe-S4	-0.001	+0.034	2.381
Fe-N	+0.121	+0.054	2.255
Fe-N ₂ H ₄	+0.136	+0.058	2.192
MAE	0.094	0.066	

L=CO (S=0)	OLYP dev.	B3LYP* dev. [14]	Exp. [8]
Fe-S1	+0.031	+0.073	2.225
Fe-S2	+0.024	+0.051	2.298
Fe-S3	+0.002	+0.046	2.251
Fe-S4	+0.029	+0.050	2.305
Fe-N	+0.053	+0.039	2.072
Fe-CO	-0.017	+0.024	1.753
MAE	0.026	0.047	

L=PM ₃ (S=0)	OLYP dev.	B3LYP* dev. [14]	Exp. [9]
Fe-S1	+0.019	+0.065	2.229
Fe-S2	+0.031	+0.048	2.307
Fe-S3	+0.009	+0.064	2.231
Fe-S4	+0.010	+0.057	2.309
Fe-N	+0.060	+0.045	2.067
Fe-PM ₃	+0.052	+0.086	2.215
MAE	0.030	0.061	

condensed phase experimental results. However, this does not pose a great problem in this case, because a $\Delta E_{HL}^{\text{ZPVE}}$ -corrected ΔE_{HL} is directly available from the tunneling experiment so this is a good candidate for comparison against $\Delta E_{HL}^{\text{DFT}}$. For $[\text{Fe}(\text{H}_2\text{O})]^{2+}$ and $[\text{Fe}(\text{NH}_3)]^{2+}$ sophisticated *ab initio* calculations are available [3, 4]. based on these calculations, best estimates for ΔE_{HL} are in the range from -12347 cm^{-1} to -13660 cm^{-1} (with a mean value of -13004 cm^{-1}) for the hexaqua iron(II) complex and ΔE_{HL} is in the range from -9125 cm^{-1} to -11230 cm^{-1} (with a mean value of -10178 cm^{-1}) for the hexamino iron(II) complex. For $[\text{Fe}(\text{bpy})_3]^{2+}$, experimental estimate of ΔE_{HL} to be within 3500 cm^{-1} to 6000 cm^{-1} (mean value is 4750 cm^{-1}). The mean experimental and *ab initio* high-spin/low spin splittings form the reference values for the following comparison.

Table 4.12 gives results for $\Delta E_{HL}^{\text{DFT}}$ calculated with the functionals B3LYP*, VSXC and OLYP at geometries optimized with the same functionals. While B3LYP* predicts in all cases the correct sign for ΔE_{HL} , it deviates by almost 7000 cm^{-1} for the hexamino ferrous cation. VSXC predicts a negative ΔE_{HL} for the $[\text{Fe}(\text{bpy})_3]^{2+}$ complex which is experimentally known to have a positive ΔE_{HL} . Interestingly, there are again π - π interactions in the complex that VSXC does not work very well for. OLYP performs slightly better than B3LYP*, with a largest deviation of -3485 cm^{-1} or -10 kcal/mol ($[\text{Fe}(\text{NH}_3)]^{2+}$). Although reasonable expectations for good *ab initio* calculations on this type of compound is an accuracy of only about 5 kcal/mol \approx 1800 cm^{-1} , it is also conceivable that the error in our best estimates could be as large as 10 kcal/mol. Nevertheless, regardless of our ability to make precise estimates of the intrinsic errors in our best estimates of ΔE_{HL} , the results reported here provide a strong indication that the OLYP functional gives not only qualitatively correct results but also works quite well for giving quantitative results.

VI Conclusion

We have assessed 16 different density functionals on their performance for predicting high-spin/low-spin splitting energies in octahedral Fe(II) complexes. We have shown that it is necessary to explicitly take into account entropic and zero-point vibrational contributions when comparing against finite temperature experimentally-determined equilibria. In these cases, the quality of a density functional has to be assessed by comparing ΔG_{HL} rather than ΔE_{HL} . We found that it is not necessarily a functional from one of the higher rungs of Jacob's Ladder that gives overall best results. Rather, we found the GGA-functional OLYP to work remarkably well for the compounds studied here, outperforming most classic hybrid functionals. While the meta-GGA

functional VSXC works quite well for predicting energies at equilibrium structures, we cannot recommend it for geometry optimizations since this functional seems to overestimate long-range $\pi - \pi$ interactions. It is good news to us that new approximate density functionals are overcoming the need for exact exchange in order to describe correctly delicate spin pairing energetics. For all practical purposes, when it comes to the application of DFT to large transition metals complexes, a GGA functional like OLYP, with no explicit orbital dependence, is much to be preferred over hybrid functionals. This is because, in comparison with hybrid functionals, GGAs can take much better advantage resolution-of-the-identity techniques using auxiliary functions, leading to a significant decrease in necessary computational requirements.

Acknowledgments

This study was carried out in the context of the *Groupe de Recherche en Commutateurs Optiques Moléculaires à l'Etat Solide* (COMES), *groupe de recherche en density functional theory* (DFT) and the working group COST D26/0013/02. AF would like to acknowledge the French *Ministère d'Education* for a *Bourse de Mobilité*. GG would like to thank the *Freunde der Universität Freiburg im Breisgau* for their generous sponsoring. MEC, GG and AF would like to thank Pierre Vatton, Denis Charapoff, Régis Gras, Sébastien Morin, and Marie-Louise Dheu-Andries for technical support of the LEDSS and *Centre d'Expérimentation le Calcul Intensif en Chimie* (CECIC) computers used for the calculations reported here. We would also like to thank Max Latévi Lawson Daku for helpful comments on the manuscript.

Bibliography

- [1] J.N. Harvey, in *Principles and Applications of Density Functional Theory in Inorganic Chemistry I*, Structure and Bonding Vol. 112, edited by N. Kaltsoyannis and J.E. McGrady (Springer-Verlag, Heidelberg, 2004) p. 151.
- [2] T. Ziegler, Chem. Rev . **91**, 651 (1991)
- [3] A. Fouqueau, S. Mer., M.E. Casida, L.M. Lawson Daku, A. Hauser, T. Mineva, F. Neese, J.Chem Phys. **120**, 9473 (2004).
- [4] A. Fouqueau, M.E. Casida, L.M. Lawson Daku, A. Hauser, F. Neese, J. Chem. Phys, accepted

- [5] L.M. Lawson Daku, A. Vargas, A. Hauser, A. Fouqueau, and M. Casida, *ChemPhysChem submitted.*
- [6] P. Gütlich, H.A. Goodwin, *Topics in Current Chemistry* **233**, **234**, **235**.
- [7] D. Sellmann, W. Soglowek, F. Knoch, G. Ritter, J. Dengler, *Inorg. Chem* **31**, 3711 (1992)
- [8] D. Sellmann, H. Kunstmann, F. Knoch, M. Moll, *Inorg. Chem.* **27**, 4183 (1988)
- [9] D. Sellmann, T. Hofmann, F. Knoch, *Inorg. Chim Acta* **224**, 61 (1994)
- [10] H. Paulsen, L. Duelund, H. Winkler, H. Toftlund, and A.X. Trautwein, *Inorg. Chem.* **40**, 2201 (2001).
- [11] H. Bolvin, *J. Phys. Chem. A* **102**, 7525 (1998)
- [12] R.M. Dreizler and E.K.U. Gross, *Density Functional Theory, An Approach to the Quantum Many-Body Problem* (Springer-Verlag: New York, Springer-Verlag, 1990).
- [13] O. Salomon, M. Reiher, and B.A. Hess, *J. Chem. Phys.* **117**, 4729 (2002).
- [14] M. Reiher, O. Salomon, and B.A. Hess, *Theor. Chem. Acc.* **107**, 48 (2001).
- [15] T. Van Voorhis, G. E. Scuseria, *J. Chem. Phys.* **109**, No. 2, 400 (1998)
- [16] J. Jaramillo, G. E. Scuseria, *Chem. Phys. Lett.* **312**, 269 (1999)
- [17] J. C. Sacho-García, J. Cornil *J. Chem. Phys.* **121**, 3096 (2004)
- [18] L.F. Lindoy and S.E. Livingstone, *Coord. Chem. Rev.* **2**, 173 (1967).
- [19] M. Sorai and S. Seki, *J. Phys. Chem. Solids* **35**, 555 (1974).
- [20] A.1, M. J. Frisch, G. W. Trucks, H. B. Schlegel, G. E. Scuseria, M. A. Robb, J. R. Cheeseman, J. A. Montgomery, Jr., T. Vreven, K. N. Kudin, J. C. Burant, J. M. Millam, S. S. Iyengar, J. Tomasi, V. Barone, B. Mennucci, M. Cossi, G. Scalmani, N. Rega, G. A. Petersson, H. Nakatsuji, M. Hada, M. Ehara, K. Toyota, R. Fukuda, J. Hasegawa, M. Ishida, T. Nakajima, Y. Honda, O. Kitao, H. Nakai, M. Klene, X. Li, J. E. Knox, H. P. Hratchian, J. B. Cross, C. Adamo, J. Jaramillo, R. Gomperts, R. E. Stratmann, O. Yazyev, A. J. Austin, R. Cammi, C. Pomelli, J. W. Ochterski, P. Y. Ayala, K. Morokuma, G. A. Voth, P. Salvador, J. J. Dannenberg, V. G. Zakrzewski, S. Dapprich, A. D. Daniels,

- M. C. Strain, O. Farkas, D. K. Malick, A. D. Rabuck, K. Raghavachari, J. B. Foresman, J. V. Ortiz, Q. Cui, A. G. Baboul, S. Clifford, J. Cioslowski, B. B. Stefanov, G. Liu, A. Liashenko, P. Piskorz, I. Komaromi, R. L. Martin, D. J. Fox, T. Keith, M. A. Al-Laham, C. Y. Peng, A. Nanayakkara, M. Challacombe, P. M. W. Gill, B. Johnson, W. Chen, M. W. Wong, C. Gonzalez, and J. A. Pople, Gaussian 03, Revision A.1, Gaussian, Inc., Pittsburgh PA, 2003.
- [21] D.A. McQuarrie, *Statistical Thermodynamics* (Harper and Row: New York, 1973).
- [22] G. Brehm, M. Reiher, S. Schneider, *J. Phys. Chem. A* **102**, 12024 (2002)
- [23] G.W. Castellan, *Physical Chemistry*, 2nd Ed. (Addison-Wesley Publishing Company: Reading, Massachusetts, 1971) p. 127.
- [24] R. A. Binstead, J. K. Beattie, *Inorg. Chem.* **25**, 1481 (1986)
- [25] L. Wiehl, K. Kiel, C. P. Köhler, H. Spiering, G. Gütlich *Inorg. Chem.* **25**, 1565 (1986)
- [26] P. Adler, A. Hauser, A. Vef, H. Spiering, P. Gütlich *Hyperfine. Int.* **47**, 343 (1989)
- [27] L. Wiehl, H. Spiering, P. Gütlich, K. Knorr *J. Appl. Cryst.* **23**, 151 (1990)
- [28] J.P. Perdew, K. Schmidt, *Density Functional Theory and Its Applications to Materials*, edited by V. VanDoren, C. Van Alsenoy, and P. Geerling (American Institute of Physics, New York, 2001)
- [29] R.G. Parr and W. Yang, *Density-Functional Theory of Atoms and Molecules* (Oxford University Press: New York, 1989).
- [30] W. Koch and M.C. Holthausen, *A Chemist's Guide to Density Functional Theory* (Wiley-VCH: New York, 2000).
- [31] F. A. Hamprecht, A. J. Cohen, D. J. Tozer, N. C. Handy, *J. Chem. Phys.* **109**, No. 15, 6264 (1998)
- [32] N.C. Handy, A.J. Cohen, *Molec. Phys.* **99**, No.5, 403 (2000)
- [33] Axel D. Becke, *J. Chem. Phys.* **112**, 4020 (2000).
- [34] A. Schäfer, C. Huber, and R. Ahlrichs, *J. Chem. Phys.* **100**, 5829 (1994).

- [35] M. Reiher, Inorg. Chem. **41**, 6928 (2002)
- [36] J. P. Perdew, K. Burke, and M. Ernzerhof, Phys. Rev. Lett. **77**, 3865 (1996)
- [37] A. D. Becke, J. Chem. Phys. **104**, 1040 (1996)
- [38] C. Lee, W. Yang, and R.G. Parr, Phys. Rev. B **37**, 785 (1988).
- [39] Gaussian NEWS, v. 5, no. 2, summer 1994, p. 2.
- [40] A.D. Becke, Phys. Rev. A **38**, 3098 (1988).
- [41] J.P. Perdew, J.A. Chevary, S.H. Vosko, K.A. Jackson, M.R. Pederson, D.J. Singh, and C. Fiolhais, Phys. Rev. B **46**, 6671 (1992); Erratum, Phys. Rev. B **48**, 4978 (1993).
J.P. Perdew, K. Burke, and Y. Wang, Phys. Rev. B **54**, 16533 (1996); Erratum, Phys. Rev. B **57**, 14999 (1998).
- [42] J.P. Perdew, Phys. Rev. B **33**, 8822 (1986).
- [43] J.P. Perdew, K. Burke, and M. Ernzerhof, Phys. Rev. Lett. **77**, 3865 (1996); Erratum: Phys. Rev. Lett. **78**, 1386 (1997).

VII Appendix : Density Functionals

The abbreviations of the density-functionals used in this study are the same as those given in the Gaussian 03 [20] manual:

- BHandH: The hybrid functional $0.5 \times E_x^{HF} + 0.5 \times E_x^{LSDA} + E_c^{LYP}$ [20].
- BHandHLYP: The hybrid functional $0.5 \times E_x^{HF} + 0.5 \times E_x^{LSDA} + 0.5 \times E_x^{Becke88} + E_c^{LYP}$ [20].
- PBE0: A hybrid functional containing exactly 25% HF exchange. This value has been derived by a perturbation theory argument rather than empirically [36].
- B1LYP: B1 is the one-parameter Becke exchange functional containing exact exchange [37]. LYP is the correlation functional of Lee, Yang, and Parr [38].
- B3LYP: A three-parameter hybrid functional composed of Becke's 1988 exchange functional combined with the LYP correlation functional [39]. It contains 20% exact exchange.
- B3LYP*: A reparametrized version of the B3LYP functional. The amount of exact exchange has been reduced to 15% [14].
- B3PW91: Becke's original 3-parameter hybrid functional involving Becke's 1988 exchange functional [40] combined with Perdew and Wang's 1991 gradient-corrected correlation functional [41]
- VSXC: Van Voorhis and Scuseria's 1998 meta-GGA with an explicit dependence on the kinetic energy density [15].
- BP86: B is Becke's 1988 gradient corrected exchange functional [40] and P86 is Perdew's 1986 correlation functional [42].
- OLYP: This is the OPTX functional of Handy and coworkers [32] combined with the LYP correlation functional.
- PBEPBE: The nonempirical GGA of J.P. Perdew, K. Burke, and M. Ernzerhof [43]
- HCTH147, HCTH93, HCTH407: These are the highly-parametrized GGA functionals of Handy and coworkers [31].

TABLE 4.12: Quantitative comparison of density functionals at optimized geometries. All values are in cm^{-1}

	ΔE_{HL} calculated by DFT	Deviation from the interval mean
$[\text{Fe}(\text{bpy})_3]^{2+}$: $\Delta E_{HL}^{\text{exp.}} = 3500 - 6000$		
OLYP	2684	2066
VSXC	-1822	6572
B3LYP*	3332	1418
$[\text{Fe}(\text{NH}_3)]^{2+}$: $\Delta E_{HL}^{ab \text{ initio}} = -11230 - -9125$		
OLYP	-6693	3485
VSXC	-5928	4250
B3LYP*	-3226	6952
$[\text{Fe}(\text{H}_2\text{O})]^{2+}$: $\Delta E_{HL}^{ab \text{ initio}} = -13360 - -12347$		
OLYP	-16284	3431
VSXC	-13975	1122
B3LYP*	-10456	2398

Conclusion

Nous avons donc étudié les limites d'application de la théorie de la Fonctionnelle de la Densité (DFT) aux complexes de métaux de transition dans le but de décrire le phénomène de piégeage d'états excités de spin induit par la lumière (LIESST). Pour ce faire, nous avons procédé essentiellement en deux étapes.

Dans un premier temps, nous avons étudié des "petits" complexes afin d'être en mesure de comparer nos résultats DFT avec des estimations provenant de la théorie du champs de ligands (LFT) et des calculs *ab initio* très poussés étant à la limite de ce qui est possible de faire actuellement sur les machines mises à notre disposition. Même si ces complexes ne peuvent pas subir une Transition de Spin, ils furent de très bons candidats pour tester ces différentes méthodes. En effet, les complexes pouvant subir une transition de spin sont beaucoup plus grands et rendent donc les calculs beaucoup plus longs. Il s'est avéré que même ce type de calcul nécessitait une correction empirique. Cette correction est attribuable au manque de flexibilité de la base utilisée. La comparaison *ab initio*/DFT a mis en évidence le problème d'énergie d'appariement de spin en DFT. Il est essentiellement lié à une mauvaise description de l'échange. Nous avons alors cherché les meilleures fonctionnelles pour pallier ce problème. Il est apparu que des fonctionnelles assez récentes comme VSXC, HCTH_x en souffraient beaucoup moins et avaient même tendance à le sur-corriger.

Dans un deuxième temps, nous avons étudié des complexes d'intérêts pratiques. Le premier complexe étudié a été le 2,2'-trisbi-pyridine fer (II). L'hypothèse expérimentale selon laquelle la différence de distance Métal-Ligand entre les états HS et LS, Δr_{HL} , était de 0.2 Å a pu être vérifiée. Ainsi la différence d'énergie entre les deux états *High-Spin* (HS) et *Low-Spin* (LS), ΔE_{HL}^{el} , a pu être déterminée. En considérant que la relaxation *HS* \rightarrow *LS* est gouvernée par un processus multiphonon adiabatique, il est possible d'estimer ΔE_{HL}^{el} compris dans l'intervalle 3500-6000 cm⁻¹. Cette estimation nous a permis une nouvelle fois de tester les différentes fonctionnelles. Le meilleur accord fut trouvé avec la fonctionnelle GGA RPBE et la fonctionnelle hybride B3LYP*. Contrairement aux petits complexes modèles, la proportion d'échange Hartree-Fock doit être diminuée afin de bien décrire cette différence éner-

gétique. Les fonctionnelles B3LYP et PBE0 la sous-estiment d'autant plus que la proportion d'échange exacte est importante. En effet, dans ce cas, l'échange est sur-estimé et l'état HS est ainsi favorisé ce qui diminue ΔE_{HL}^{el} .

D'autre part, nous avons étudié une famille de complexes, $[Fe(L)('NHS_4')]$, dont l'état fondamental est connu expérimentalement. Nous avons donc pris en compte les corrections thermodynamiques afin de comparer ΔG_{HL} avec l'expérience plutôt que ΔE_{HL} . En effet, une correction de 2000 cm^{-1} ($\sim 7 \text{ kcal.mol}^{-1}$) est à appliquer pour comparer les résultats de nos calculs avec l'expérience. Nous avons obtenu le meilleur accord avec la fonctionnelle B3LYP* et la fonctionnelle GGA OLYP. De nouveau, une fonctionnelle GGA permet de décrire correctement nos complexes au niveau énergétique. Ce résultat est très intéressant car ce type de fonctionnelle est très bien adapté pour utiliser la technique de la résolution de l'identité. Ainsi le coût des calculs peut-être fortement réduit.

Nous avons montré que le principal problème des fonctionnelles d'échange-corrélation provient de la partie d'échange, la partie corrélation ayant peu d'influence. Les améliorations permanentes apportées aux fonctionnelles d'échange sont nécessaires pour prédire de manière sûre l'état fondamental d'un complexe de fer(II).

Maintenant qu'une méthodologie est à notre disposition pour étudier les états fondamentaux de ce type de complexes, nous pouvons envisager d'en étudier les états excités à l'aide de la théorie de la fonctionnelle de la densité dépendante du temps (TDDFT, pour l'anglais *Time-dependent Density Functional Theory*).

Annexes

1 Processus multiphonon non-adiabatique

La constante de relaxation HS → BS s'écrit dans la théorie multiphonon non-adiabatique :

$$k_{HL}(T) = \frac{2\pi}{\hbar^2\omega} \beta_{HL}^2 F_p(T). \quad (4.50)$$

β_{HL} est l'élément de la matrice électronique de $\langle \Phi_{LS} | H | \Phi_{HS} \rangle$ estimé à 150 cm^{-1} en considérant le couplage spin-orbite par l'intermédiaire de l'état triplet ${}^3\text{T}_1$, $\hbar\omega$ est la fréquence de respiration des entités FeN₆. Dans le cas de puits de potentiels décrits dans l'approximation harmonique avec des constantes de force et des fréquences de vibration égales dans les deux états HS et BS, le facteur Franck-Condon prend la forme :

$$F_p(T) = \frac{\sum_m |\langle \chi_{m+p} | \chi_m \rangle|^2 e^{-m\hbar\omega/k_B T}}{\sum_m e^{-m\hbar\omega/k_B T}}. \quad (4.51)$$

La relaxation se produit entre les niveaux vibrationnels n de l'état initial (HS) et le niveau vibrationnel m de l'état final (LS), avec $n = m + p$. L'énergie réduite $p = \Delta E_{LH}^0 / \hbar\omega$ est une mesure du déplacement vertical relatif des deux puits de potentiel de l'état initial et final. A haute température, le facteur Franck-Condon $F_p(T)$ est proportionnel à $\exp(-\Delta E_{LH}^0 / k_B T)$, c'est-à-dire de type Arrhénius. Ce régime est atteint lorsque la température devient supérieure à 100-150 K. Le régime basse température correspond au cas simplifié où $T \rightarrow 0$. A $T \rightarrow 0$, le facteur $F_p(T)$ peut se simplifier par les expressions 4.52 et 4.53. La relaxation est décrite comme un processus d'ordre zéro entre deux états de spin différents.

$$k_{HL}^0 = \frac{2\pi}{\hbar^2\omega} \beta_{HL}^2 \frac{S^p e^{-S}}{p!} \quad (4.52)$$

où

$$S = \frac{1}{2} f \frac{\Delta Q^2}{\hbar\omega} \quad \text{avec} \quad \Delta Q = \sqrt{6} \Delta r_{HL} \quad (4.53)$$

2 Conversion d'énergies

	hartree	eV	cm^{-1}	kcal.mol^{-1}	kJ.mol^{-1}
hartree	1	27.2107	219474.63	627.503	2625.5
eV	0.0367502	1	8065.73	23.0609	96.4869
cm^{-1}	4.55633×10^{-6}	1.23981×10^{-4}	1	0.00285911	0.0119627
kcal.mol^{-1}	0.00159362	0.0433634	349.757	1	4.18400
kJ.mol^{-1}	0.00038088	0.01036410	83.593	0.239001	1

TAB. 4.13: Conversion d'énergies

3 *Size consistency et size extensivity*

Considérons une supermolécule composé de deux unités monomères séparées par une grande distance. Ces deux monomères peuvent donc être considéré sans interaction. L'énergie de ces deux monomères sera exactement le double de l'énergie d'une unité monomère. Une méthode permettant ceci sera dite *size consistent*.

La méthode Hartree-Fock et la méthode full-CI sont *size consistent*. Mais les méthodes d'interaction de configuration tronquées ne le sont pas. Prenons l'exemple de la méthode CISD. Par définition, la fonction d'onde, de cette méthode, appliquée sur un monomère contient des doubles excitations. En la multipliant par 2, la fonction d'onde des 2 monomères contiendra des quadruples excitations qui ne sont pas incluses dans le calcul CISD du dimère. Cette méthode n'est donc pas *size consistent*.

La notion de *size consistency* est défini pour 2 fragments non-interagissant alors que la notion de *size extensivity* s'applique pour des fragments interagissant ou non et signifie que le coût de la méthode augmente avec le nombre de particules. La méthode full-CI est *size consistent* et *size extensive* mais les formes tronquées ne le sont pas. Le manque de *size extensivity* implique une récupération de l'énergie de corrélation de plus en plus petite quand le système devient de plus en plus grand.

4 Fonction et fonctionnelle

Une fonction transforme un nombre en un autre nombre

$$x \xrightarrow{f(x)} y. \quad (4.54)$$

Par exemple, prenons la fonction $f(x) = 2x^2 + 1$. Pour $x = 1$, cette fonction donne $y = 3$.

Une fonctionnelle transforme une fonction en un nombre

$$f(x) \xrightarrow{F[f]} y. \quad (4.55)$$

Par exemple, prenons la fonctionnelle définie par l'intégrale

$$F[f] = \int_0^1 f(x) dx \quad (4.56)$$

Nous avons alors, pour $f(x) = 2x^2 + 1$,

$$F[f] = \int_0^1 (2x^2 + 1) dx = \frac{5}{3} \quad (4.57)$$

Afin de pouvoir différencier ces deux concepts, des parenthèses sont utilisées pour les fonctions alors que des crochets sont utilisés pour les fonctionnelles.

Liste des tableaux

1.1	Paramètres empiriques pour estimer Δ_0 (tiré de [4] p.218-219)	17
1.2	Estimations de Δ_0 et $\Delta E_{HL}^{\text{vert}}$ pour les complexes $[\text{Fe}(\text{H}_2\text{O})_6]^{2+}$ et $[\text{Fe}(\text{NH}_3)_6]^{2+}$	17
2.1	Unités atomiques.	38
3.1	Summary of basis sets used in this work.	87
3.2	$^5\text{T}_{2g}$ $[\text{Fe}(\text{H}_2\text{O})_6]^{2+}$ bond lengths. Our notation is based upon the idea of a pseudo D_{4h} structure since, neglecting the hydrogens, since this is what we find in our best calculations. Footnotes indicate geometries which, neglecting the hydrogens, are better described as D_{3d} and give the OFeO C_{3v} angle.	89
3.3	$^5\text{T}_{2g}$ $[\text{Fe}(\text{H}_2\text{O})_6]^{2+}$ bond angles. Our notation is based upon the idea of a pseudo D_{4h} structure since, neglecting the hydrogens, since this is what we find in our best calculations. Footnotes indicate geometries which, neglecting the hydrogens, are better described as D_{3d} and give the OFeO C_{3v} angle. The abbreviation NA appears in the table for these entries to indicate that the D_{4h} angles are “not applicable.” . . .	90
3.4	Experimental $[\text{Fe}(\text{H}_2\text{O})_6]^{2+}$ geometries. Bond distances in Å, bond angles in degrees.	106
3.5	$^1\text{A}_{1g}$ $[\text{Fe}(\text{H}_2\text{O})_6]^{2+}$ geometry. A D_{3d} geometry has been assumed, neglecting hydrogens. The OFeO angle given is between oxygens related by the C_{3v} symmetry operation. The complex geometry becomes O_h when this angle is 90°	107
3.6	$[\text{Fe}(\text{H}_2\text{O})_6]^{2+}$ LS-HS energy differences as calculated directly and after shifting the asymptotes of the dissociation curves to match the known experimental atomic Fe^{2+} ${}^5D \rightarrow {}^1I$ energy difference.	108
3.7	Comparison of atomic excitation energies.	109

3.8	Calculated bond length and energy differences between high and low state structures for selected basis sets and functionals. The results for basis set "E" were obtained by multiplying the ΔR_{HL} results for basis set C" by 1.08 and the ΔE_{HL} results for basis set C" by 1.07.	110
3.9	Summary of functionals used in the present study.	117
3.10	Parameters entering into and results of the simple model described in the text. Experimental data and corresponding results are given in parentheses.	120
3.11	Vertical and Adiabatic transition energies calculated with the SORCI method for the $[Fe(NH_3)_6]^{2+}$ complex at the B3LYP/TZVP optimized HS and LS geometries	126
3.12	Summary of basis sets used in this work.	128
3.13	$[Fe(NH_3)_6]^{2+}$ and $[Fe(H_2O)_6]^{2+}$ HS-LS energy differences	135
3.14	$[Fe(NH_3)_6]^{2+}$ and $[Fe(H_2O)_6]^{2+}$ HS-LS energy differences	143
4.1	AO populations, spin density and net charge found for the iron atom in the LS 1A_1 and HS 5E and 5A_1 states of the $[Fe(bpy)_3]^{2+}$ complex (populations are given per l -values). For the HS states, the spin-up/spin-down AO populations are indicated. Top: ADF results obtained using the TZP basis set, bottom: GAUSSIAN results obtained using the TZVP basis set. (Results for the other functionals and basis sets are given in Tables S1-S3).	194
4.2	Comparison between experimental and theoretical 1A_1 $[Fe(bpy)_3]^{2+}$ geometries. Top : ADF, bottom : GAUSSIAN.	195
4.3	Optimised $[Fe(bpy)_3]^{2+}$ geometries in the HS 5E state. ADF results. .	195
4.4	Optimised $[Fe(bpy)_3]^{2+}$ geometries in the HS 5A_1 state. Top : ADF, bottom : GAUSSIAN.	196
4.5	Comparison between calculated Fe-N bond length differences $\Delta r_{HL} = r_{HS} - r_{LS}$ (\AA), (where r_{HS} and r_{LS} are the Fe-N bond lengths in the HS (5E or 5A_1) and LS (1A_1) states, respectively), and experimental Δr_{HL} values for spin-crossover systems with $[FeN_6]$ coordination [5, 6, 7, 8, 9, 10, 11].	196
4.6	Comparison between calculated differences in molecular volume, $\Delta V_{HL} = V_{HS} - V_{LS}$ (in \AA^3), (where V_{HS} and V_{LS} are the molecular volumes in the HS (5E or 5A_1) and LS (1A_1) states, respectively), and measured changes of crystal volume <i>per</i> molecular unit, ΔV_{HL}^{\exp} [8, 12, 13, 14]. .	197
4.7	Calculated and experimental (see text) electronic energy differences $\Delta E_{HL}^{\text{el.}}$, (in cm^{-1}).	197

4.8	Typical thermodynamic data for the [Fe(L)(‘NHS ₄ ’)] complexes at 298.15 K and 1 bar. All values are in cm ⁻¹ (See also Table 4.10.)	208
4.9	Jacob’s Ladder for DFT. Spin has been suppressed for simplicity of notation.	210
4.10	Thermodynamic data for the [Fe(‘NHS ₄ ’)(L)] complexes at <i>T</i> = 298K. All values are in cm ⁻¹	217
4.11	Bond lengths (Å) between Fe and first-sphere ligands.	226
4.12	Quantitative comparison of density functionals at optimized geometries. All values are in cm ⁻¹	233
4.13	Conversion d’énergies	238

Table des figures

1.1	Influence du champ cristallin octaédrique sur les niveaux d'énergies 3d.	9
1.2	Diagramme de Tanabe-Sugano pour une configuration d^6 avec $B = 1080 \text{ cm}^{-1}$ et $C/B = 4.42$. (Tiré de [4] page 139.)	16
1.3	Diagramme schématique proposé pour les effets LIESST et reverse-LIESST. Les flèches rectilignes représentent les excitations électroniques et les flèches ondulées symbolisent les processus de relaxation non-émissifs (tiré de la Ref [52]).	26
3.1	Correlation diagram for the highest-lying occupied and lowest-lying unoccupied molecular orbitals found in our DFT singlet calculations (not to scale). Also shown are pictures of the highest occupied molecular orbitals (HOMOs) and lowest unoccupied molecular orbitals (LUMOs) showing the d - π bonding nature of the former and the anti-bonding nature of the latter. Note that e_g Fe(II) orbitals correlate with e_g $6\text{H}_2\text{O}$ orbitals, t_{2g} Fe(II) orbitals correlate with t_{2g} $6\text{H}_2\text{O}$ orbitals, but that there is an absence of t_{1g} Fe(II) orbitals to correlate with the $6\text{H}_2\text{O}$ orbitals of the same symmetry representation.	85
3.2	The two pseudosymmetries found for $[\text{Fe}(\text{H}_2\text{O})_6]^{2+}$ in our calculations. Arrows have been added to the D_{4h} structure to indicate a Jahn-Teller distortion. Dotted lines have been added to the D_{3d} structure to indicate the presence of weak H-bonding interactions. The distortion of the D_{3d} structure has been exaggerated for clarity.	88
3.3	Superposition of the HS (single color) and LS (multicolor) $[\text{Fe}(\text{H}_2\text{O})_6]^{2+}$ minima found at the BP86/B' level of calculation.	92

3.4 Comparison of <i>ab initio</i> and DFT best estimates for bond length and energy differences between the high and low spin states of $[\text{Fe}(\text{H}_2\text{O})_6]^{2+}$. Results of atomic calculations have been used to empirically correct our CASPT2(12,10) energy difference for an insufficiently large basis set. DFT results are for GAUSSIAN calculations with the E basis set and ADF calculations with the fictitious “E” basis set. (PW91 results shown only for the GAUSSIAN calculations.) In particular, ADF results with the C" basis set have been empirically scaled in order to estimate what they would be with the better E basis set. See text for further details.	96
3.5 Representation of the potential wells for the quintet and singlet states with the different quantities cited in the text	121
3.6 Diagram of the SORCI algorithm (based on Fig. 1 of Ref. [38]), showing the principle steps and the three thresholds, T_{pre} , T_{nat} and T_{sel}	124
3.7 Superposition of the LS (light) and HS (dark) $[\text{Fe}(\text{NH}_3)_6]^{2+}$ geometries optimized at the PBE0/B level of calculation.	129
3.8 Comparison of metal-ligand bond length for the high- and low-spin states of $[\text{Fe}(\text{NH}_3)_6]^{2+}$ with the 2 basis sets A and B (with the 2 basis sets A" and C" for the ADF calculations)	129
3.9 Comparison of metal-ligand bond length for the high- and low-spin states of $[\text{Fe}(\text{H}_2\text{O})_6]^{2+}$ with the basis set B (with the basis set C" for the ADF calculations)	130
3.10 Comparison of metal-ligand bond length for the high- and low-spin states of $[\text{Fe}(\text{NH}_3)_6]^{2+}$ with the basis set B (with the basis set C" for the ADF calculations)	130
3.11 $\Delta E_{\text{LH}}^{\text{adia}}$ for $[\text{Fe}(\text{H}_2\text{O})_6]^{2+}$ (dark bar) and $[\text{Fe}(\text{NH}_3)_6]^{2+}$ (light bar).	132
3.12 Difference of $\Delta E_{\text{LH}}^{\text{adia}}$ between $[\text{Fe}(\text{H}_2\text{O})_6]^{2+}$ and $[\text{Fe}(\text{NH}_3)_6]^{2+}$ with the basis set B	133
4.1 Configurational coordinate diagram along the totally symmetric breathing mode for an iron(II) complex with a LS ${}^1\text{A}_{1g}(t_{2g}^6)$ ground state. Only the potential wells of the ground state and the first excited state, namely the ${}^5\text{T}_{2g}(t_{2g}^4 e_g^2)$ HS state are explicitly shown, higher excited ligand-field and MLCT states are indicated schematically. The potential wells of the LS and HS states are plotted assuming equal vibrational frequencies, $\hbar\omega$, for the two states. Quantum efficiencies for the light-induced population of the HS state are generally close to unity [20].	151

4.2 View of the X-ray structure [32] of $[\text{Fe}(\text{bpy})_3]^{2+}$ in the LS state: the complex possesses a D_3 site symmetry. The atom labelling used in the manuscript is indicated.	153
4.3 The low-temperature tunnelling rate constant, $k_{\text{HL}}(T \rightarrow 0)$, on a logarithmic scale as a function of $\Delta E_{\text{HL}}^\circ$. Theoretical curves were calculated using the model values as described in the text with an average value of $S = 45$ (solid line) and the limiting values 40 and 50 (dashed line). The lozenges, circles and squares represent experimental values for a series of spin-crossover compounds with a $[\text{FeN}_6]$ first coordination sphere according to Ref. [20]. The range of experimental values for the LS complex $[\text{Fe}(\text{bpy})_3]^{2+}$ doped into different crystalline host lattices [15] is also indicated (shaded area).	155
4.4 Frontier KS MOs of $[\text{Fe}(\text{bpy})_3]^{2+}$ in the $^1\text{A}_1$ state (PBE/TZP results; eigenvalues in eV).	166
4.5 Frontier KS MOs of $[\text{Fe}(\text{bpy})_3]^{2+}$ in the ^5E state: for clarity, MOs with noticeable metallic character only are represented (PBE/TZP results; eigenvalues in eV).	168
4.6 Frontier KS MOs of $[\text{Fe}(\text{bpy})_3]^{2+}$ in the $^5\text{A}_1$ state: for clarity, MOs with noticeable metallic character only are represented (PBE/TZP results; eigenvalues in eV).	170
4.7 Angles characterising the spatial arrangement of the ligands around the metal centre in $[\text{Fe}(\text{bpy})_3]^{2+}$. β is the bite angle ($\beta = \text{N}-\text{Fe}-\text{N}'$), γ the dihedral angle between the ligand moieties ($\gamma = \text{N}-\text{C}_2-\text{C}'_2-\text{N}$), τ the twist angle, and θ the angle between the z -axis and the generator of the cone on which the nitrogen atoms are located.	172
4.8 Evolution of the Fe-N bond length in the LS and HS $^5\text{A}_1$ state with the value of the a_0 coefficient of the exact-exchange contribution in the PBE1PBE (circles) and B3LYP (squares) hybrids; the inset gives the a_0 dependence of Δr_{HL} ; (results of geometry optimisations done using the TZVP basis set).	174
4.9 Comparison of best DFT estimates of the relative positions of the LS $^1\text{A}_1$ and HS ^5E and $^5\text{A}_1$ states of $[\text{Fe}(\text{bpy})_3]^{2+}$ along the Fe-N distance coordinate: results are for ADF and GAUSSIAN calculations with the STO TZP and GTO TZVP basis sets. The electronic energy is given relative to the energy of the LS state. Inset: HS-LS electronic energy difference $\Delta E_{\text{HL}}^{\text{el}}$ as a function of the Fe-N bond length change; the shaded region indicates the 3500-6000 cm ⁻¹ experimental range.	177

4.10 Plot of the exchange enhancement factors F_x for the B88 (circles), PW91 (squares), PBE (triangles) and RPBE (lozenges) exchange functionals against the reduced charge-density gradient $s(\mathbf{r}) = \nabla\rho(\mathbf{r}) / (2(3\pi^2)^{1/3}\rho^{4/3}(\mathbf{r}))$ (results for the spin-unpolarised case).	180
4.11 (Top) Exchange enhancement factor $F_x(\zeta, s)$ (Eq. (4.26)) for the B88 (circles), PW91 (squares), PBE (triangles) and RPBE (lozenges) exchange functionals as function of ζ for fixed s values. (Bottom) Plots of the gradient corrections $F_x(\zeta, s) - F_x(\zeta, s = 0)$	181
4.12 Dependence of the electronic energy difference $\Delta E_{HL}^{\text{el}}$ between the HS ${}^5\text{A}_1$ and LS ${}^1\text{A}_1$ states on the a_0 coefficient of the exact-exchange contribution in the B3LYP (squares, Eq. (4.22)) and PBE1PBE (circles, Eq. (4.23)) hybrids; (results of geometry optimisations done with the TZVP basis set). The shaded region indicates the range of the experimental values (see text).	183
4.13 Examples of $[\text{Fe}(\text{L})(\text{'NHS}_4)]$ complexes. Above: the <i>trans</i> -NO ⁺ - complex. Below: the <i>cis</i> -N ₂ H ₄ - complex. NH ₃ , CO, and PMe ₃ are also treated in this article.	203
4.14 Influence of the admixture of HF, Slater and GGA exchange on ΔE_{HL} . In order to keep everything on a single graph, the quantity ΔE_{HL} has been arbitrarily displaced so that it is zero for a scaling parameter of 92.5%.	215
4.15 ΔE_{HL} for Hartree-Fock and half-and-half functionals for the $[\text{Fe}(\text{L})(\text{'NHS}_4)]$ complexes.	219
4.16 ΔE_{HL} for hybrid functionals for the $[\text{Fe}(\text{L})(\text{'NHS}_4)]$ complexes. The percentage of exact exchange for each functional is given in parentheses in the figure legend. Note that the B1LYP data point for the <i>trans</i> -NO ⁺ complex is only a best estimate of the converged result because of difficulty obtaining completely satisfactory convergence for the HS state.	220
4.17 LDA and GGA ΔE_{HL} 's for the $[\text{Fe}(\text{L})(\text{'NHS}_4)]$ complexes.	221
4.18 ΔE_{HL} for highly parametrized functionals and the $[\text{Fe}(\text{L})(\text{'NHS}_4)]$ complexes.	222
4.19 ΔE_{HL} for OPTX in combination with LYP (OLYP) and the meta-GGA VSXC.	222
4.20 ΔG_{HL} calculated at optimized geometries with the functionals B3LYP*, VSXC and OLYP. The thermodynamic correction is that of Table 4.10 for the BP86 functional.	224

Index

- B3LYP, 66
- B88, 63
- CASPT2, 52
- CASSCF, 51
- CI, 47, 50
- CID, 51
- CISD, 51
- CISDT, 51
- CISDTQ, 51
- complete CI, 50
- ERI, 46
- full CI, 50
- GEA, 63
- GGA, 63
- HF, 46
- HOMO, 51
- KS, 57
- LCAO, 42
- LD-LISC, 21
- LDA, 61
- LIESST, 2
- LSDA, 61
- LUMO, 51
- LYP, 64
- MBPT, 47
- MCSCF, 47, 51
- mGGA, 64
- MP2, 47
- NIESST, 22
- ODA, 72
- OEP, 67
- OM, 40
- OPTX, 63
- PBE, 64
- PW86, 63
- PW91, 63
- reverse-LIESST, 25
- RHF, 41
- SOXIESST, 22
- UHF, 41
- VSXC, 65
- VWN, 62